



**HAL**  
open science

# Microcrystalline silicon deposited from SiF<sub>4</sub>/H<sub>2</sub>/Ar plasmas and its application to photovoltaics

Jean-Christophe Dornstetter

► **To cite this version:**

Jean-Christophe Dornstetter. Microcrystalline silicon deposited from SiF<sub>4</sub>/H<sub>2</sub>/Ar plasmas and its application to photovoltaics. Materials Science [cond-mat.mtrl-sci]. Ecole Polytechnique, 2014. English. NNT: . tel-01111141

**HAL Id: tel-01111141**

**<https://pastel.hal.science/tel-01111141>**

Submitted on 29 Jan 2015

**HAL** is a multi-disciplinary open access archive for the deposit and dissemination of scientific research documents, whether they are published or not. The documents may come from teaching and research institutions in France or abroad, or from public or private research centers.

L'archive ouverte pluridisciplinaire **HAL**, est destinée au dépôt et à la diffusion de documents scientifiques de niveau recherche, publiés ou non, émanant des établissements d'enseignement et de recherche français ou étrangers, des laboratoires publics ou privés.



Distributed under a Creative Commons Attribution 4.0 International License



Doctoral thesis in Materials Science

# **Microcrystalline silicon deposited from $\text{SiF}_4/\text{H}_2/\text{Ar}$ plasmas and its application to photovoltaics**

Jean-Christophe Dornstetter





Doctoral thesis in Materials Science

# Microcrystalline silicon deposited from SiF<sub>4</sub>/H<sub>2</sub>/Ar plasmas and its application to photovoltaics

Jean-Christophe Dornstetter

Ph.D. thesis defended on the 19<sup>th</sup> of November, 2014.

Prof. Laifa Boufendi	GREMI	Referee
Prof. Bernd Rech	HZB	Referee
Dr. Friedhelm Finger	Jülich FZ	Examiner
Dr. Bruno Delahaye	TOTAL	Examiner
Dr. Franz-Josef Haug	EPFL - PV Lab	Examiner
Dr. Edward Hamers	HyET Solar	Examiner
Prof. Pere Roca i Cabarrocas	LPICM	Supervisor



## Acknowledgements

Passage incontournable, les Remerciements marquent la fin de trois longues et merveilleuses années de thèse et achèvent de mettre un point final à un manuscrit que l'on a rédigé avec cœur. Les Remerciements c'est aussi et surtout la seule partie de cet ouvrage rédigée « à chaud » sans la censure académique (légitime et bienvenue, il va sans dire). C'est donc naturellement l'occasion de remercier directement, sincèrement et chaleureusement tous ceux qui m'ont entouré durant ma thèse.

Je tiens tout d'abord à remercier ma famille pour son soutien inconditionnel durant ces trois laborieuses – et laborantines, années de thèse.

Je pense ensuite à Marc et Lars. Merci de m'avoir permis de réaliser cette thèse au sein de la R&D Solaire de TOTAL, dont je remercie par ailleurs tous les membres. Un grand merci en particulier à Caroline pour son aide infaillible dans la gestion des OM faits à la dernière minute. Je n'oublie évidemment pas mes divers « n+1 » successifs : Samir, Loïc, Fabrice, et – pour finir en beauté, Nada. Merci Samir de m'avoir initié à ce beau sujet de thèse, de m'avoir enseigné l'art de faire plein de manips en parallèle (mon record personnel étant désormais de trois réacteurs en simultané, avec toutes les caractérisations matériaux/cellules afférentes) et concomitamment de m'avoir appris à organiser mes journées au quart d'heure près ! Merci à Antoine, Patricia, Samir, Nada, Jean-François, Ludovic, Gilles, Jara, Sergej, Céline, Ahmed, Martin, et Etienne, bref à tous les « expats » de Palaiseau pour leur compagnie et leur bonne humeur, que j'ai pu apprécier au cours des (trop nombreuses ?) pauses café.

Passons maintenant au LPICM qui m'a accueilli pendant ces trois années. Je commence évidemment par Pere, qui a dirigé ma thèse avec un optimisme constant (et rarement égalé) : merci pour toutes ces réunions passées à dodeliner de la tête pour me pousser à mieux expliquer, à mieux présenter, et à mieux argumenter mes résultats scientifiques. Merci également pour ton sourire toujours bienveillant. Merci à tout le LPICM et spécialement à toute l'équipe administrative du premier étage pour votre efficacité et votre sympathie. Merci à Cyril, Fred, GG, Nacib, et François du BEER et désolé pour toutes les pompes cassées et les innombrables joints DN40 utilisés. Merci au duo Fred et Eric pour tout le support informatique lié à mon Windows XP (et oui on est en 2014...). Merci à toute l'équipe PVSIXT. Merci Rymounette pour ton sourire et tes fous rires contagieux. Merci à l'équipe TEM du LPICM et en particulier à Ileana pour ses magnifiques images qui ont « sauvé » mon modèle phénoménologique. Merci à Joaquim pour les discussions magistrales sur la physique des semi-conducteurs et sur la subtile physique de la jonction P-N et des quasi-niveaux de Fermi (même après trois années de thèse, cela fait toujours beaucoup de bien de revenir aux fondamentaux). Encore 谢谢 à Joaquim, grâce à qui j'ai pu découvrir la Chine (et sa soupe aux limaces de mer). Merci à mes deux stagiaires, Junkang et Miao, pour leur travail. Enfin merci à Pavel pour son aide toujours prompte et efficace sur les manips ainsi que pour toutes discussions franches sur les plasmas. Elles furent précieuses et essentielles pour le cheminement intellectuel de ma thèse.

Pour finir, je remercie tous les doctorants que j'ai eu la chance de côtoyer, à commencer par les « anciens » : James, Coralie et Guillaume. Je remercie les doctorants de ma « génération » : Bastien (tu me ferais pas une cellule ?), Romain (sans rancune !), Sofia, Soumyadeep, ainsi que mes acolytes des Student Chapters, Barbara, Nicolas, et Florence. Je remercie également la « nouvelle » génération en leur souhaitant bonne chance pour leur thèse : Ronan (tu verras, c'est cool le SiF<sub>4</sub>), Paul (high five !), Jian, Junkang, Gwenaëlle (bon coup d'œil, hein !), et Fabien. Je termine mes remerciements avec celui qui fut mon co-bureau (et le meilleur que j'eusse pu avoir) pendant ces trois longues années. J'ai été surpris de constater que deux personnalités aussi opposées que les nôtres ont été paradoxalement aussi compatibles. Merci Igor pour les discussions, les raftings (road-trips inclus), les hymnes, et les KD...

Merci à tous pour ce moment !



**Epigraphe pour un livre condamné.**

Lecteur paisible et bucolique,  
Sobre et naïf homme de bien,  
Jette ce livre saturnien,  
Orgiaque et mélancolique.

Si tu n'as fait ta rhétorique  
Chez Satan, le rusé doyen,  
Jette ! tu n'y comprendrais rien,  
Ou tu me croirais hystérique.

Mais si, sans se laisser charmer,  
Ton œil sait plonger dans les gouffres,  
Lis-moi pour apprendre à m'aimer ;

Ame curieuse qui souffres  
Et vas cherchant ton paradis,  
Plains-moi !... sinon, je te maudis !

Charles Baudelaire



# Table of Contents

<b>1. Context</b>	<b>15</b>
<b>1.1 From the issue of energy to SiF<sub>4</sub>/H<sub>2</sub>/Ar plasmas</b>	<b>16</b>
1.1.1 From global energy to solar energy	16
1.1.2 From solar energy to silicon technology	19
1.1.3 From silicon technology to SiF <sub>4</sub> /H <sub>2</sub> /Ar plasmas	20
1.1.4 Beyond the production of energy	21
<b>1.2 Framework of this thesis</b>	<b>22</b>
1.2.1 Focus on microcrystalline silicon	22
1.2.2 Research topic at LPICM	23
1.2.3 Deposition and characterization techniques	24
1.2.4 Structure of the thesis	26
<b>2. Plasma chemistry of SiF<sub>4</sub>/H<sub>2</sub>/Ar gas mixtures</b>	<b>27</b>
<b>2.1 Hydrogen depletion and HF formation</b>	<b>28</b>
2.1.1 Black box approach coupled with RGA	28
2.1.2 Detection of HF molecules	29
2.1.3 Depletion and consumption of H <sub>2</sub>	32
2.1.4 Effect of the Ar flow rate	34
<b>2.2 Hydrogen flow rate series</b>	<b>36</b>
2.2.1 Amorphous to microcrystalline transition	36
2.2.2 Depletion of H <sub>2</sub> and production of HF molecules	38
2.2.3 Optical emission spectroscopy	39
2.2.4 H <sub>2</sub> consumption	40
2.2.5 Discussion	41
<b>2.3 Phenomenological model</b>	<b>42</b>
2.3.1 Description of the model	42
2.3.2 Solving model equations	43
2.3.3 Comparison with experimental results	44
2.3.4 Discussion on OES and V <sub>DC</sub> measurements	47
2.3.5 Comparison with literature	48
<b>2.4 Transfer from PHILIX reactor to CLUSTER-PL8 reactor</b>	<b>49</b>
2.4.1 Getting amorphous and microcrystalline films	49
2.4.2 Optimizing the H <sub>2</sub> consumption	50
2.4.3 SiF <sub>4</sub> consumption	52
<b>2.5 Chapter key results</b>	<b>54</b>
<b>3. Plasma-generated nanoparticles</b>	<b>55</b>
<b>3.1 Plasma studies</b>	<b>56</b>

3.1.1	Effect of gas temperature.....	56
3.1.2	Early stage of deposition .....	58
3.1.3	Metallic grid .....	61
<b>3.2</b>	<b>Effect of pressure and inter-electrode distance.....</b>	<b>64</b>
3.2.1	Inter-electrode distance series .....	64
3.2.2	Where is my silicon? .....	67
3.2.3	Dust model.....	68
3.2.4	Geometrical model .....	69
3.2.5	P-di series for different plasma conditions.....	71
3.2.6	Pros and cons of dust and geometrical models.....	74
3.2.7	Perspectives.....	75
<b>3.3</b>	<b>Surface versus plasma crystallization.....</b>	<b>76</b>
3.3.1	Beyond the phenomenological model .....	76
3.3.2	Crystallization of plasma-generated nanoparticles .....	77
3.3.3	Mapping of plasma-generated nanoparticle crystallinity .....	78
3.3.4	Morphology of nanoparticles .....	88
<b>3.4</b>	<b>Self-sustained plasma oscillations .....</b>	<b>90</b>
3.4.1	Overview.....	90
3.4.2	Detailed analysis of the OES oscillations .....	92
3.4.3	Toy model .....	96
3.4.4	Forced oscillations .....	102
<b>3.5</b>	<b>Chapter key results .....</b>	<b>103</b>
<b>4.</b>	<b>Material properties .....</b>	<b>105</b>
<b>4.1</b>	<b>Crystalline silicon.....</b>	<b>106</b>
4.1.1	Bragg Brentano XRD .....	106
4.1.2	Grazing Incidence XRD.....	106
<b>4.2</b>	<b>Raman spectroscopy.....</b>	<b>107</b>
4.2.1	Overview.....	107
4.2.2	Deconvolution.....	108
4.2.3	Definitions of crystallinity-related fractions.....	112
4.2.4	Mapping of the crystallinity with Raman measurements .....	113
<b>4.3</b>	<b>Hydrogen incorporation.....</b>	<b>114</b>
4.3.1	FTIR and exodiffusion .....	114
4.3.2	H <sub>2</sub> flow rate series.....	118
4.3.3	RF power series.....	121
<b>4.4</b>	<b>Material quality.....</b>	<b>122</b>
4.4.1	SIMS .....	122
4.4.2	Defect density from FTPS measurements .....	125

4.5 Chapter key results .....	127
<b>5. Solar cells .....</b>	<b>129</b>
5.1 Description of the P-I-N stacks.....	130
5.1.1 Solar cell stack .....	130
5.1.2 ZnO.....	131
5.1.3 TEM cross section picture of the PIN solar cells.....	131
5.1.4 Metallization.....	134
5.1.5 Plasma conditions for the intrinsic microcrystalline silicon layer .....	135
5.1.6 Solar cell characterizations.....	135
<b>5.2 Correlation between solar cell characteristics and material properties .....</b>	<b>135</b>
5.2.1 Fully crystallized versus partially crystallized I-layer .....	135
5.2.2 $V_{OC}$ versus $X_C$ and $X_{cry}$ .....	139
5.2.3 $V_{OC}$ & $J_0$ versus $X_{GB}$ at $X_C=100\%$ .....	140
5.2.4 Spectral response at 800 nm versus the I-layer thickness for $X_C=100\%$ I-layer .....	142
<b>5.3 Focus on our record solar cells .....</b>	<b>143</b>
5.3.1 Thick intrinsic microcrystalline layer: 3.8 $\mu\text{m}$ with $X_C<100\%$ .....	143
5.3.2 High efficiency solar cell: 3.4 micron-thick with $X_C<100\%$ .....	144
5.3.3 Highest efficiency solar cell: 1.8 micron-thick with $X_C=100\%$ .....	145
5.3.4 Summary of the solar cells.....	145
<b>5.4 Chapter key results .....</b>	<b>146</b>
<b>6. Conclusions and perspectives .....</b>	<b>147</b>
6.1 Achievements.....	148
6.2 Perspectives on $\text{SiF}_4/\text{H}_2/\text{Ar}$ plasmas.....	149
6.3 Strategies to improve microcrystalline silicon solar cell efficiencies.....	149
<b>7. Publications.....</b>	<b>151</b>
7.1 Leading author .....	151
7.2 Co-author .....	151
<b>8. Bibliography .....</b>	<b>153</b>



## Table of Symbols:

AFM	Atomic Force Microscopy.
amu	Atomic mass unit.
at	Atom. Unit representing a number of atoms.
a.u.	Arbitrary unit.
BB-XRD	XRD in Bragg-Brentano configuration.
$d_i$	Inter-electrode distance.
$D_r$	Deposition rate.
$\eta$	Solar cell efficiency (expressed in %).
EELS	Electron energy loss spectroscopy.
FF	Fill factor (expressed in %).
FTIR	Fourier transform infrared spectroscopy.
FTPS	Fourier transform photocurrent spectroscopy.
GI-XRD	XRD in grazing incidence configuration.
HR-TEM	High Resolution TEM.
$J_0$	Dark saturation current density (expressed in mA/cm <sup>2</sup> ).
$J_{sc}$	Short-circuit current density (expressed in mA/cm <sup>2</sup> ).
mol	One mole is $6.02 \times 10^{23}$ atoms (Avogadro constant).
$n_e$	Electron density. The order of magnitude is $10^9$ - $10^{10}$ cm <sup>-3</sup> for RF capacitively coupled plasmas.
RF	Radio-frequency.
$R_{sc}$	Differential resistance $\partial V/\partial J$ at the short-circuit condition (expressed in $\Omega \cdot \text{cm}^2$ ).
$T_e$	Electron temperature. The order of magnitude is few electron-volt (eV).
TEM	Transmission Electron Microscopy.
$V_{DC}$	DC bias voltage measured between the RF electrode and the grounded electrode.
$V_{OC}$	Open-circuit voltage (expressed in mV).
$V_{RF}$	RF voltage applied to the RF electrode of the plasma reactor. The frequency is 13.56 MHz and $V_{RF}$ represents the root-mean-square (RMS) amplitude of the sinus wave.
XRD	X-ray diffraction.



# 1. Context

## Contents

---

<b>1.1 From the issue of energy to SiF<sub>4</sub>/H<sub>2</sub>/Ar plasmas .....</b>	<b>16</b>
1.1.1 From global energy to solar energy.....	16
1.1.2 From solar energy to silicon technology.....	19
1.1.3 From silicon technology to SiF <sub>4</sub> /H <sub>2</sub> /Ar plasmas .....	20
1.1.4 Beyond the production of energy.....	21
<b>1.2 Framework of this thesis.....</b>	<b>22</b>
1.2.1 Focus on microcrystalline silicon .....	22
1.2.2 Research topic at LPICM .....	23
1.2.3 Deposition and characterization techniques.....	24
1.2.4 Structure of the thesis .....	26

---

## 1.1 From the issue of energy to SiF<sub>4</sub>/H<sub>2</sub>/Ar plasmas

The industrial revolution is the starting point of an unprecedented sustained growth of energy demand. It was made possible by the invention of steam engines which required coal as fuel. From the eighteenth century the energy demand did not stop to increase and other sources of energy have been found to match the world's growing appetite for energy. Today, 200 years later, the technology for energy production is varied and complex (gas, nuclear, hydro, geothermal, wind, etc.). Consequently the effort of researchers working on the improvement of production efficiency has shifted from individual scientists (as James Watt who patented in 1769 his invention of a separated condensation chamber for steam engine) to collective efforts (plenty of dedicated laboratories around the world).

### 1.1.1 From global energy to solar energy

Energy can be found in many forms: kinetic, potential, thermal, chemical, nuclear, etc. Meanwhile the production of energy is classified into categories according to the fuel used (hydroelectricity is also a “renewable energy” but is separated because of its higher capacity for the time being):

- | Energy fuels: |                  |
|---------------|------------------|
| ➤             | Coal             |
| ➤             | Oil              |
| ➤             | Natural gas      |
| ➤             | Nuclear          |
| ➤             | Hydroelectricity |
| ➤             | Renewables       |

The repartition of the energy consumption (as a function of the fuel type) in the world in year 2013 is given in Figure 1. The data are taken from the “BP Statistical Review of World Energy – June 2014” available on [www.bp.com/statisticalreview](http://www.bp.com/statisticalreview). The three main types of fuel used in 2013 were oil, coal and natural gas.

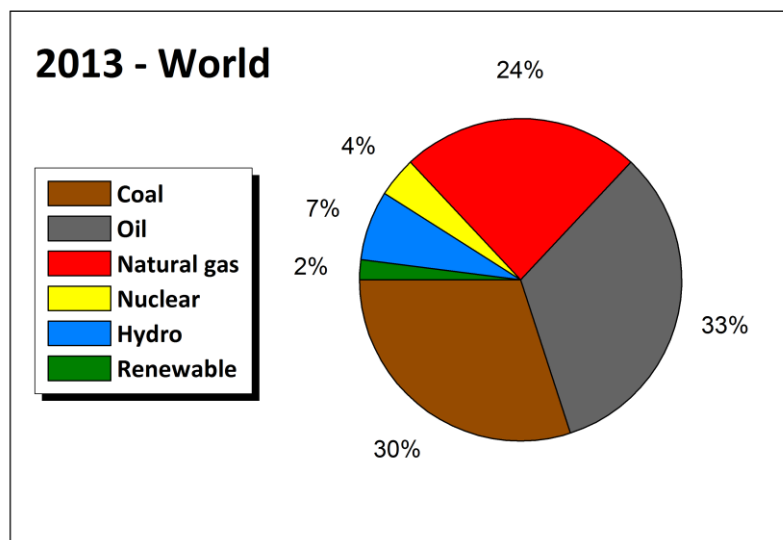


Figure 1: World energy consumption in 2013 by types of fuels.

However the distribution of the energy consumption in each category depends strongly on the countries as depicted in Figure 2 where the repartition is given for the USA, China, Brazil, and France (according again to the BP Statistical Review of World Energy). We note that the USA mainly use oil

and natural gas whereas China primarily uses coal. In Brazil, oil is used but hydroelectricity is noteworthy above 30% of the total share. For the case of France, nuclear power is the principal source of energy.

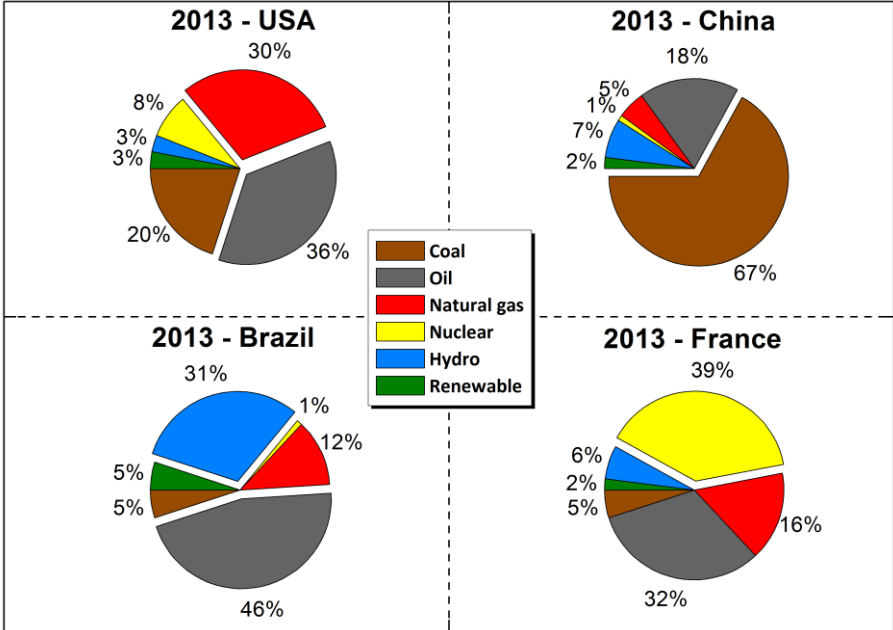


Figure 2: Energy consumption in 2013 by types of fuels for USE, China, Brazil, and France.

The reason of such differences between countries is multifactorial. It depends on the natural resources of the country and of its energy policy (diversification to reduce dependency from foreign countries, reduction of CO<sub>2</sub> emission, etc.). For example, China has one of the biggest resource of coal (the same argument applies for Poland with a coal share of 56%) and the geography of Brazil is adequate for dams on the Amazon River (a similar geographical argument applies for Norway with a hydroelectricity share of 65%). However the explanation for the high nuclear share in France is based on an energy policy: after the Second World War the French government decided to create a French nuclear industry with both military and civil applications. The 1973 oil crisis has accelerated the development of the civil nuclear power (Messmer Plan) to reduce the energy dependency of France.

The evolution of the repartition of the production (by fuel type) depends on the type of new installed production capacities. These new installations are required to match the growing demand. Figure 3 shows the increase of the world energy consumption (expressed in Mtoe where “toe” stands for tons of oil equivalent) over one decade. From 2003 to 2013 the increase was of 28%. It is worth noticing that the demand has increased almost linearly during this decade. Increasing of the production capacity may be more or less easy depending on the type of fuel. For example, the construction of a nuclear power plant is a long term project (for the construction as well as for the dismantling). The installation of new hydroelectricity capacity depends on the countries: from 2003 to 2013 China has driven the increase of hydroelectricity power from a production of 64.2 Mtoe to a production of 206.3 Mtoe (Three Gorges Dam, etc.). This increase represents more than 50% of the world increase over this decade.

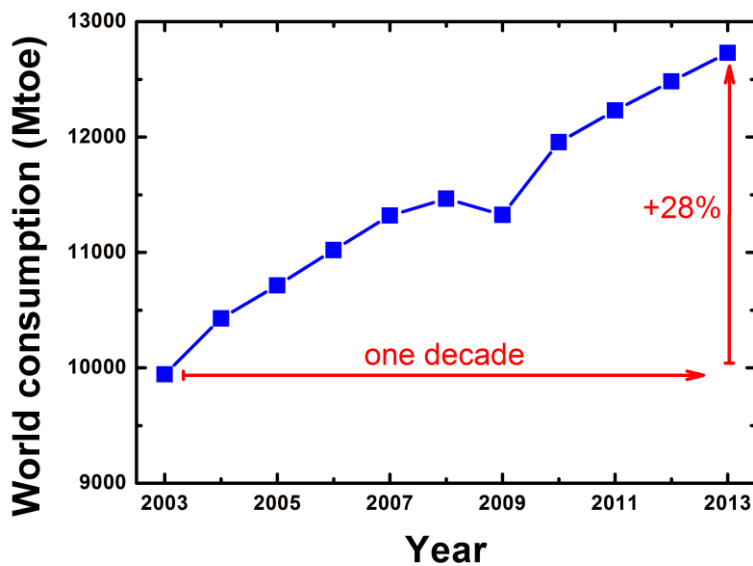


Figure 3: Growth of the world consumption of energy between 2003 and 2013.

Among the new installed capacity, renewable energies are taking more and more shares. Figure 4 shows the rapid growth of such energies over the decade. The increase represents a tripling over the decade and the growth is more than linear. However the corresponding volumes are few hundred Mtoe compared to ten thousand Mtoe of the total world consumption.

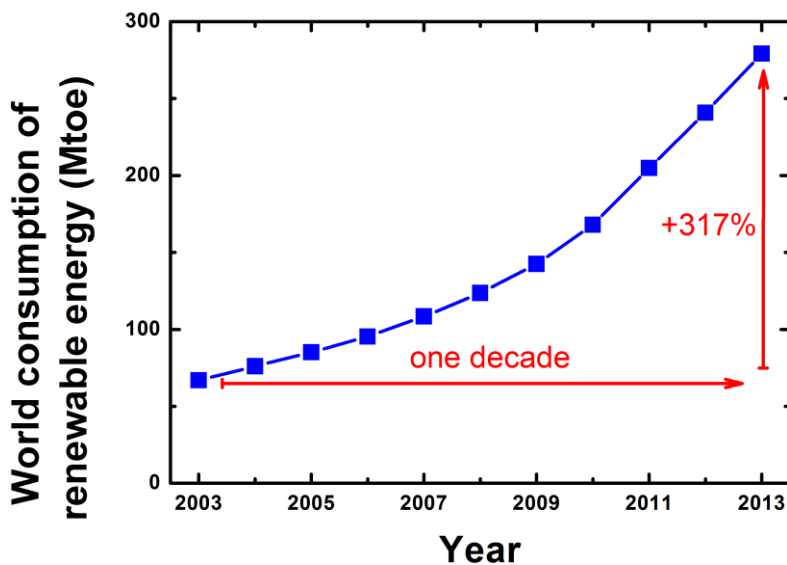


Figure 4: Growth of the world consumption of renewable energy between 2003 and 2013.

The assets of renewable energies are their low greenhouse gas emissions combined with the specificity of their “fuels” (tidal force, wind, geothermal energy, and sun photons): they are free and available directly at the production sites (no importation of raw material). However renewable energies have to face challenges: they are capital intensive, their return on investment (ROI) is long, they are intermittent and have to compete with already well-established, mature, and profitable conventional technologies.

The “fuel” of the solar energy is the sunlight, and more specifically its photons. Each photon has an energy which depends on its color. This energy can be used to heat water. In that case it is named solar thermal energy. The purpose can be water heating either for residential buildings or for steam generation used in a turbine which produces electricity. Instead of converting the light energy into heat, photons can directly produce electrons: the technology based on this process is called photovoltaics (PV).

- Solar:**
- Solar thermal
  - Photovoltaics

The distribution of sunlight over the world is not uniform. The intensity of the sunlight is measured by the Direct Normal Irradiance, which represents the photon energy per time unit arriving on a surface of 1 m<sup>2</sup> perpendicular to the sun direction. The irradiation is the irradiance cumulated over a period of time. Figure 5 shows a map of the Direct Normal Irradiation (DNI) over one year. Globally the DNI is higher between the tropic of Cancer and the tropic of Capricorn. However the altitude is beneficial to the DNI as for the Andes cordillera and the Himalayas. The highest DNIs are found in Chili and Australia, whereas the lowest DNIs are found in east of China (for anthropological reason...). The development of solar renewable energy is and will be different from country to country.

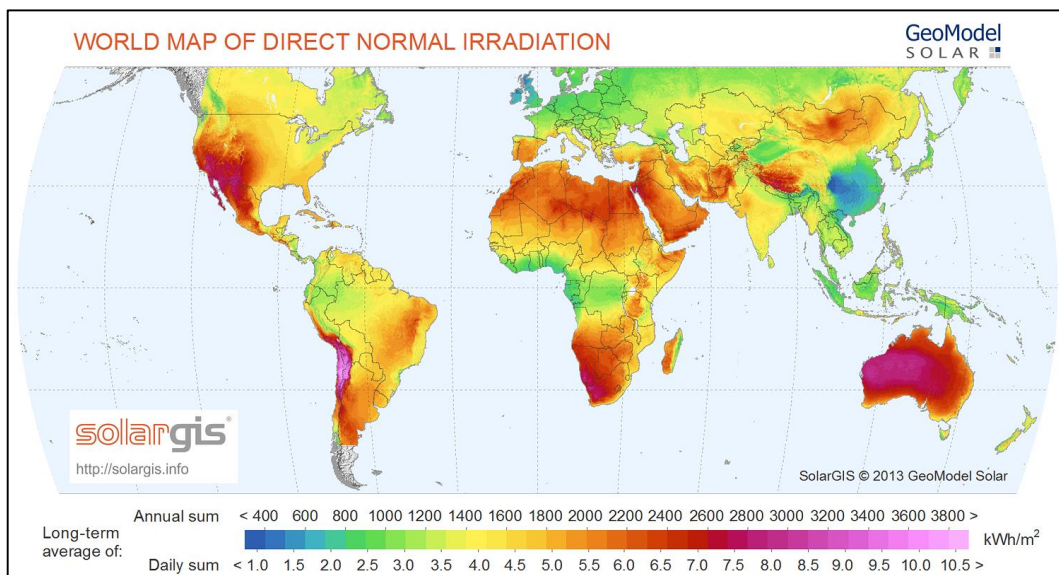


Figure 5: World map of the DNI (SolarGIS © 2014 GeoModel Solar).

### 1.1.2 From solar energy to silicon technology

The main component of a photovoltaics power plant is a module. Its standard shape is a rectangle of 1x1.5 m<sup>2</sup> and it is composed of few tens of smaller units called cells. The cell is the photovoltaic device which converts photons into electrons. The module is not only a connection in series or in parallel of the cells, it also protects the cells from the weather (water, dust, etc.). The frame of the module provides a rigid structure to transport and to install it. Around the module, there is the system which encompasses the mounting of the modules, their cabling, and the conversion of the DC electricity from the module to AC electricity thanks to inverters. In some cases, the modules are mounted on a tracking system. The system can also solve the problem of the Maximum Power Point Tracking (MPPT) by finding the adequate load of a module to optimize its production (a PV device can either produce high current with low voltage (low load) or high voltage with low current (high load): an intermediate load maximizes the output power of the device). To summarize, photovoltaics is organized in three research fields: the system, the modules, and the solar cells.

**Photovoltaics:**

- System
- Module
- Cell

The research field of solar cells is vast. To give an idea of the variety of technologies, the famous NREL chart of record efficiency cells is displayed in Figure 6. The chart is available on [www.nrel.gov/ncpv/images/efficiency\\_chart.jpg](http://www.nrel.gov/ncpv/images/efficiency_chart.jpg). The records are sorted out by the semiconductor material: silicon, GaAs, CIGS, CdTe, organics, and perovskites.

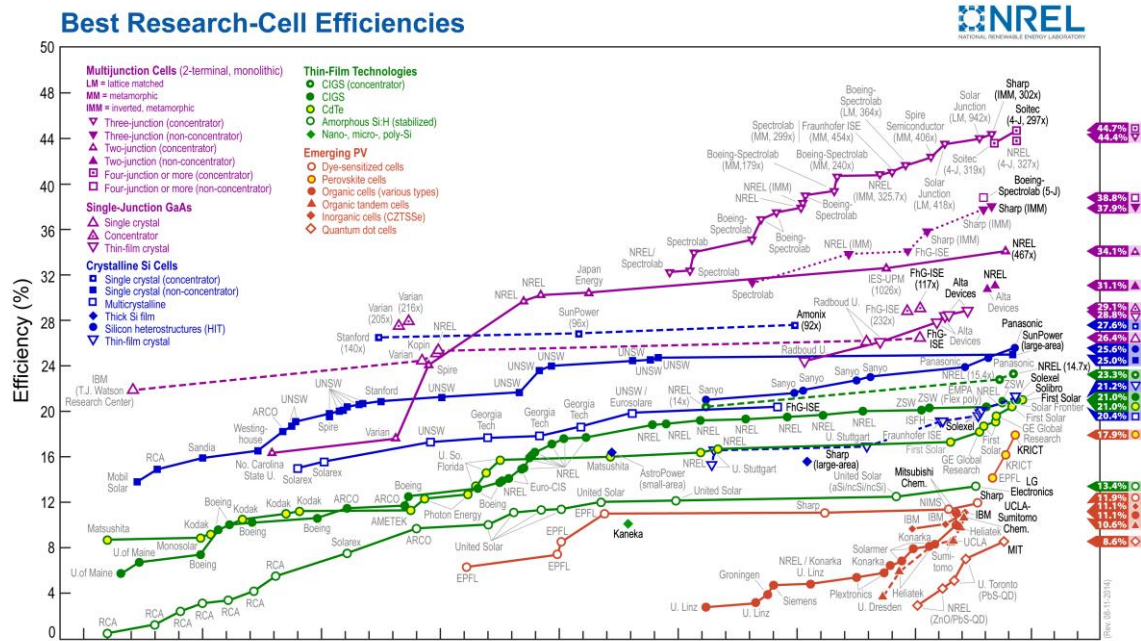


Figure 6: Historic of record cell efficiencies by NREL.

Each technology has its own history and this graph only gives the efficiency records obtained in laboratories. It does not give insight about the feasibility of a mass production of the corresponding solar cells (price, supply of raw material, aging, etc.). In addition to the semiconductor type, there is the structure type of the solar cell. For a single junction solar cells there is a balance between covering as much visible sun spectra as possible (achieved by low bandgap semiconductor) and reducing the energy losses by thermalization (achieved by high bandgap semiconductor). The tradeoff is achieved by multi-junction solar cells where each junction deals with one portion of the solar spectrum thus reducing thermalization losses and improving the solar cell efficiency.

**Cell technologies:**

- GaAs
- CdTe
- CIGS
- Organics
- Perovskites
- Silicon

**1.1.3 From silicon technology to SiF<sub>4</sub>/H<sub>2</sub>/Ar plasmas**

The world of silicon solar cells is split in two parts: crystalline silicon and thin films. Crystalline silicon solar cells are made of a silicon wafer which can be either fully crystalline or multicrystalline. On the one hand, Czochralski and float-zone are two processes used to produce silicon ingot. The crystalline

structure is made by heating the silicon at its melting temperature and then cooling down slowly. Wafer thicknesses are typically of few hundreds of microns. On the other hand, in thin film technology, a silicon film with a thickness of a few hundreds of nanometers up to microns is directly deposited on substrates without a melting step. For example, Plasma Enhanced Chemical Vapor Deposition (PECVD) can be used to deposit hydrogenated amorphous or microcrystalline silicon. This technology is low cost and has other assets such as the fabrication of flexible solar cells. However silicon based thin film solar cells are less efficient than the ones based on crystalline silicon. The latter are often named “high efficiency solar cells”. Single junction silicon thin film solar cell efficiency is in the range of 10-11% (depending on the structure of the material: amorphous or microcrystalline) whereas single junction crystalline silicon solar cell efficiency is about 25%.

However there is a synergy between the crystalline silicon world and the thin film world. A silicon wafer is not a solar cell and thin films can be used to form a PN junction (e.g. in heterojunctions), to passivate surface (e.g. with hydrogenated amorphous silicon), or to make an antireflection coating (e.g. with Indium Tin Oxide). Moreover in order to reduce costs, the general trend in crystalline silicon industry is to use thinner and thinner wafers. However, the sawing technique is limiting to achieve such low thickness. An efficiency above 20% has been reported with the use of a 40  $\mu\text{m}$  thick monocrystalline silicon wafer [1]. To obtain such a thickness, thin film techniques can be used to grow crystalline silicon thanks to an epitaxial growth.

- |   |
|---|
| <p><b>Silicon:</b></p> <ul style="list-style-type: none"><li>➤ Crystalline silicon</li><li>➤ Thin epitaxial crystalline silicon</li><li>➤ <b>Silicon thin films</b></li></ul> |
|---|

Moreover, the PECVD technique can be used to grow hydrogenated amorphous or microcrystalline silicon. Plasmas of  $\text{SiH}_4/\text{H}_2$  gas mixtures are usually used. Another gas mixture can be used to deposit such layers: the silane is replaced by  $\text{SiF}_4$ . The  $\text{SiF}_4$  is mixed with  $\text{H}_2$  and Ar. The  $\text{SiF}_4/\text{H}_2/\text{Ar}$  gas chemistry can be an alternative for the  $\text{SiH}_4/\text{H}_2$  gas chemistry.

- |  |
|--|
| <p><b>Silicon thin films:</b></p> <ul style="list-style-type: none"><li>➤ <math>\text{SiH}_4/\text{H}_2</math> plasmas</li><li>➤ <b><math>\text{SiF}_4/\text{H}_2/\text{Ar}</math> plasmas</b></li></ul> |
|--|

This thesis is dedicated to the study of  $\text{SiF}_4/\text{H}_2/\text{Ar}$  plasmas. Single junction silicon thin film solar cells will be used to demonstrate the benefits of such fluorinated gas chemistry.

#### 1.1.4 Beyond the production of energy

The development of renewable energies is increasing. Their deployment has been driven by public policies but they are already profitable and competitive in some countries, in a world where their cost decreases year after year and where the cost of other energy sources increases. The cost of PV energy is the key factor for its development but beyond this single value, renewable energy must tackle the challenge of the redesign of the energy mix.

The past paradigm of the balance between production and consumption was that the supply should match the demand. However this paradigm is shifting towards load management, i.e. during consumption peaks, instead of adding production capacity, a part of the demand is not fulfilled. That changes the mentality on the side of the demand (individuals, industries, etc.). On the side of utilities the intermittency of renewable calls also for a change in the strategy, which is a real challenge. That will be a long yet progressive revolution in the problematic field of energy.

## 1.2 Framework of this thesis

### 1.2.1 Focus on microcrystalline silicon

Hydrogenated microcrystalline silicon was reported for the first time in 1968 by Vepřek and Mareček [2]. Hydrogenated amorphous silicon (a-Si:H) and hydrogenated microcrystalline silicon ( $\mu\text{-Si:H}$ ) are two materials which can be deposited by Plasma Enhanced Chemical Vapor Deposition (PECVD). Usually the film precursor is silane ( $\text{SiH}_4$ ) diluted in hydrogen ( $\text{H}_2$ ), and there is a consensus [3] stipulating that the microcrystallinity is mediated by atomic hydrogen during the growing process (via surface and sub-surface reactions [4]). Plasma conditions leading to hydrogenated amorphous and microcrystalline silicon are similar. The key parameter, which controls the transition, is the silane concentration (SC) [5] and from a practical point of view a high dilution of silane into hydrogen is required for microcrystalline growth. However microcrystalline silicon can also be obtained at high SC values if the silane depletion is increased [6]. In  $\text{SiH}_4/\text{H}_2$  plasmas, the promotion of crystalline phase is hindered by the recombination reaction  $\text{H}+\text{SiH}_4\rightarrow\text{H}_2+\text{SiH}_3$  happening in the plasma phase: one  $\text{SiH}_3$  growth precursor is created while one atomic hydrogen, catalyzing the microcrystallinity, is lost. To overcome this issue, high pressure depletion regime has been studied [7][8]: the silane is depleted such as the recombination reaction cannot occur anymore. In addition, deposition rate as high as  $28 \text{ \AA/s}$  has been achieved [8].

As a matter of fact microcrystalline silicon covers a wide range of material structures. It is generally characterized by a crystalline fraction, an amorphous fraction and a void fraction. This structure depends on the plasma conditions and especially on the silane concentration [5][9]. From a semiconductor point of view the microcrystalline silicon has the low indirect bandgap of crystalline silicon at  $\approx 1.1 \text{ eV}$  which should be compared to the high bandgap of amorphous silicon of  $\approx 1.7 \text{ eV}$ , which can be shifted to higher energies depending on the hydrogen content of the amorphous silicon [10]. The advantage of a low bandgap is counterbalanced by a low absorption coefficient of the microcrystalline silicon compared to amorphous silicon [11]. Few micron-thick layers are usually required to absorb a sufficient fraction of sunlight, in comparison to  $300 \text{ nm}$  for a-Si:H. In addition to the crystalline/amorphous/void fractions, grain boundaries and column boundaries have been identified [12][13].

The growth mechanism of microcrystalline silicon has been studied with a layer-by-layer (LBL) technique, which has revealed four steps in the growth [14][15]: (i) the incubation, where the material is amorphous and its porosity increases with the thickness, (ii) the nucleation, where first yet small crystalline phase appears and where the void fraction is maximum, (iii) crystalline growth, where crystalline fraction increases whereas the void fraction and the amorphous fraction decrease, (iv) the stationary growth, where the composition is constant. There is a consensus on the need of atomic hydrogen to achieve a crystalline phase, however there is no consensus on the detailed mechanism. Several models have been proposed such as selective etching model, surface diffusion model, and chemical annealing model [3].

Besides the structure of the  $\mu\text{-Si:H}$ , the quality of the material is of importance. Impurities, such as oxygen, nitrogen, or carbon, can migrate in grain boundaries. Moreover the density of states (DOS) within the bandgap is problematic as it is responsible for electron-hole pair recombination. Every source of recombination will limit the lifetime and the mobility of carriers. The transport mechanism in microcrystalline silicon is very complex because of the heterogeneity of the material and its anisotropy. A homogeneous model has been proposed in [16] where the transport is assumed to be limited by potential barriers at grain boundaries (model developed for polycrystalline silicon). Other groups claimed that the transport mechanism in microcrystalline is similar to that in amorphous silicon [17]. Finally some investigations have shown that the transport is indeed limited by defects inside the crystallites [18] thus advising a reduction of the ion bombardment during the growth. The defect density is the most critical parameter determining the carrier transport as was shown in [19].

Intrinsic microcrystalline silicon can be used as the absorber layer in a solar cell. The collection of generated electrons and holes is performed by a P- and an N-layer. For this application, the general consensus is that the structure of the microcrystalline should be optimized so that it is close to the amorphous-to-microcrystalline transition (meaning that the crystalline fraction around 70%). Indeed, the general trend is a decrease of the open-circuit voltage ( $V_{oc}$ ), when the crystalline fraction increases (the material becomes more crystallized) [9][20]. The main invoked reason was the passivation of grain boundaries and of crystallites by amorphous silicon (under the assumption that recombination is predominant mechanism degrading the  $V_{oc}$ ). In crystalline silicon technology, the dominant recombination process does not happen in the bulk of the material (the wafer) but on the surfaces (the two sides of the wafer and the edges too), and that is the reason why passivation layers are used ( $SiN_x$  or a-Si:H for instance).

Microcrystalline silicon single junction PIN solar cells have been achieved by EPFL with a certified efficiency of 10.7% [21]. In order to achieve such a high efficiency, adequate layers have to be used (in particular doped microcrystalline silicon oxide), the cell design should be adapted, careful study of cracks should be performed and post treatments should be done [22]. Based on Green et al. [23], world record efficiencies are:

- 11.0% for  $\mu c$ -Si:H single junction solar cell by AIST [24]
- 12.3% for a-Si:H/ $\mu c$ -Si:H tandem solar cell by Kaneka
- 13.4% for a-Si:H/ $\mu c$ -Si:H/ $\mu c$ -Si:H triple junction solar cell by LG Electronics

Silicon-Germanium alloys have been used to produce a a-Si:H/a-SiGe:H/ $\mu c$ -Si:H triple junction solar cells with an initial efficiency of 16.3% [25]. A detailed discussion of the use of high quality  $\mu c$ -Si:H in single-, tandem-, and triple-junctions can be found in [26].

### 1.2.2 Research topic at LPICM

In 1978, Madan and Ovshinsky suggested to use  $SiF_4$  instead of  $SiH_4$  [27][28]. Ever since then,  $SiF_4/H_2$  mixtures have been studied to grow amorphous and microcrystalline silicon. Research efforts have been supported around the world by (non-exhaustive list) Madan and Ovshinsky in USA [27][28], Shimizu, Oda, and coworkers in Japan [29][30], and Bruno, Capezzuto, Cicala, and coworkers in Italy [31][32][33]. Detailed description of their publications will be presented later on and compared with the new results of this thesis. Other halogens than F have also been studied such as  $SiCl_4$  [34][35].

At the end of the 90's, we introduced in LPICM  $SiF_4/H_2/Ar$  plasmas to deposit microcrystalline and more specifically for the application of Thin Film Transistors (TFT) [36]. The first tests with  $SiF_4$  have been performed by Romain Brenot during his Ph.D. thesis in LPICM. Later on, two other Ph.D. candidates dedicated their thesis on that topic: Samir Kasouit on the growth and transport mechanisms in fluorinated microcrystalline silicon (2003) and Yassine Djeridane on the synthesis of nanoparticles and the study of their role in the growth of fluorinated microcrystalline silicon (2008). Afterwards, the  $SiF_4$  thematic in our laboratory shifted to photovoltaic application with the study of epitaxial silicon from  $SiF_4/H_2/Ar$  plasmas on c-Si and GaAs substrates by Mario Moreno (postdoc) [37] and on FeNi42 substrates by Alfonso Torres Rios (Ph.D. candidate) [38]. This thesis is dedicated to the photovoltaic application of  $SiF_4/H_2/Ar$  plasmas, with the fabrication of microcrystalline silicon single junction solar cells.

The current paradigm to obtain the highest solar cell efficiency is to use a material deposited under plasma conditions at the transition between amorphous and microcrystalline silicon [9][20]. A decrease of the open-circuit voltage ( $V_{oc}$ ) is encountered when the crystalline fraction is increased. Moreover, the short-circuit current density ( $J_{sc}$ ) increases with the thickness of the layer. However carrier collection decreases when the I-layer is too thick [39]. That the reason why thicknesses around 2  $\mu m$  are generally used [22]. We propose a new paradigm for microcrystalline solar cells where a negligible fraction of amorphous silicon is present but the material still has a better defect passivation of grain boundaries and of crystallites. By doing so, thicker layers (more than 4  $\mu m$ ) can be used

because a higher crystalline fraction means better carrier transport and therefore less carrier collection issues for a given thickness. As it will be shown in this manuscript, we can afford this new paradigm because microcrystalline silicon deposited from  $\text{SiF}_4/\text{H}_2/\text{Ar}$  gas mixtures has shown better properties: very low defect density, fully crystallized material, large grain sizes, and low impurity content.

The aim of this thesis is to put our principles into actions and into concrete fabrication of PIN solar cells. In addition, the goal of this thesis is to deepen the understanding of such complex plasma chemistry to answer following questions as:

- How can I achieve a high quality microcrystalline silicon at high deposition rate?
- What is the gas consumption of the process?
- Is the process easy to transfer to industrial reactors?
- How good is the microcrystalline silicon in terms of defect density?
- What is the structure of the material and its composition (H, F and impurities)?
- Can we produce high efficiency cells with a fully crystallized material?

### 1.2.3 Deposition and characterization techniques

The following gives information about equipment used during this thesis.

- Deposition reactors:
  - PHILIX

That is the main PECVD equipment used for this thesis, consists of a monochamber RF capacitive reactor excited at 13.56 MHz. A picture of the reactor is given in Figure 7, when the chamber is opened for unloading/loading. The plasma fills the volume between the RF electrode and the substrate holder (grounded electrode). The plasma confinement box is a cylinder which is grounded and has several holes to allow for *in situ* spectroscopic ellipsometry (SE), as well as optical emission spectroscopy (OES) measurements. The pumping occurs through these holes. To close the chamber, the bottom flange is rotated by  $90^\circ$  such that the substrate holder closes the cylinder. The gases are injected through a shower head embedded in the RF electrode. The RF electrode and the substrate holder are both heated.

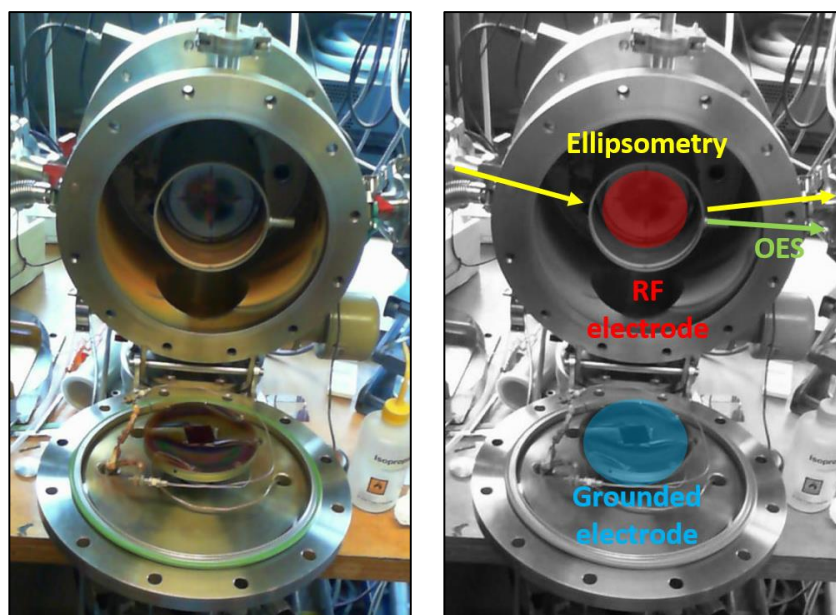


Figure 7: Picture of PHILIX reactor with the chamber is opened.

- ARCAM

In order to fabricate solar cells, P- and N-doped layers (amorphous or microcrystalline) are required and have been deposited in ARCAM which is a multiplasma monochamber reactor described in [40].

- ATOS

This is another PECVD reactor in which the excitation source can be either RF or MDECR [41]. ATOS has been used because its geometry allows the installation of a Quadrupole Mass Spectrometer (QMS) (which is not the case of PHILIX).

- CLUSTER

This is a brand new system with six PECVD chambers from MVSystems ([www.mvsystemsinc.com](http://www.mvsystemsinc.com)). One chamber is dedicated to SiF<sub>4</sub>/H<sub>2</sub>/Ar plasmas and the goal was to transfer the recipe from PHILIX to CLUSTER. Other chambers are used to deposit doped layers which were usually deposited on ARCAM. During this thesis, (p)μc-Si:H and (n)a-Si:H have also been developed on CLUSTER. Solar cells presented in this thesis were done with PHILIX and ARCAM. Some other solar cells have been fabricated with PHILIX and CLUSTER with a current cell efficiency of 7.4% but are not shown here (further optimization is required). The launching and the maintenance of this new cluster tool has taken significant amount of effort and time, despite the relatively small impact on the results shown in this thesis.

- Plasma diagnostics:

- RGA

The residual gas analyzer is a “Microvision 2” from MKS ([www.mksinst.com](http://www.mksinst.com)). In this thesis, it has been mainly used to detect HF molecules and to measure the depletion of H<sub>2</sub>.

- QMS

A quadrupole mass spectrometer has been installed to understand the chemistry of SiF<sub>4</sub>/H<sub>2</sub>/Ar plasma. It is an “EQP300 system” (up to 300 amu) from Hiden Analytical ([www.hidenanalytical.com](http://www.hidenanalytical.com)). In this thesis, it has been used to measure the dissociation cross sections and to identify detected species (for example discriminate between HF<sup>+</sup> and Ar<sup>++</sup> detected at the same 20 amu mass).

- OES

Optical emission spectroscopy has been recorded thanks to a “Maya 2000 Pro” spectrometer from Ocean Optics ([www.oceanoptics.com](http://www.oceanoptics.com)). A fiber (UV and visible range) has been installed to collect the light from the reactor viewport into the spectrometer device.

- V<sub>RF</sub>

The measurements of RF electrical signals (current, voltage and impedance) have been performed by an “Octiv” probe from Impedans ([www.impedans.com](http://www.impedans.com)).

- Material characterizations:

- Spectroscopic Ellipsometry

*In situ* and *ex situ* spectroscopy ellipsometry measurements have been done by “UVISEL” equipment from Horiba Jobin Yvon ([www.horiba.com](http://www.horiba.com)).

- Raman Spectroscopy

A “LabRAM ARAMIS” Raman setup from Horiba Scientific ([www.horiba.com](http://www.horiba.com)) has been used to characterize the microcrystalline silicon layers. Four lasers can be used 785 nm, 633 nm, 532 nm, and 473 nm.

- FTIR

A “Nicolet 6700” from Thermo Scientific ([www.thermoscientific.com](http://www.thermoscientific.com)) has been used in transmission mode. A nitrogen flush is installed to reduce the CO<sub>2</sub> absorption lines.

- Exodiffusion (Thermal Diffusion Spectroscopy)

The thermal diffusion spectroscopy is performed by an oven pumped down to 10<sup>-7</sup> mbar where the temperature is increased at a rate of 10°C·min<sup>-1</sup>. The partial pressure of H<sub>2</sub> is measured by a QMS.

- XRD

Grazing Incidence X-ray Diffractions have been performed with a “D8 Discover” system from Bruker ([www.bruker.com](http://www.bruker.com)).

#### **1.2.4 Structure of the thesis**

This manuscript is organized into six parts: the introduction, four chapters, and the conclusion. The four chapters represent all the topics which have been investigated starting from fundamental understandings of plasma and ending with the realizations of solar devices:

- Plasmas chemistry of SiF<sub>4</sub>/H<sub>2</sub>/Ar
- Dusty plasmas: the role of nanoparticles
- Material
- Devices

The aim of this thesis is to make the bridge between the deposition processes and corresponding materials and solar cell properties.

## 2. Plasma chemistry of SiF<sub>4</sub>/H<sub>2</sub>/Ar gas mixtures

### Contents

---

<b>2.1 Hydrogen depletion and HF formation .....</b>	<b>28</b>
2.1.1 Black box approach coupled with RGA.....	28
2.1.2 Detection of HF molecules.....	29
2.1.3 Depletion and consumption of H <sub>2</sub> .....	32
2.1.4 Effect of the Ar flow rate .....	34
<b>2.2 Hydrogen flow rate series .....</b>	<b>36</b>
2.2.1 Amorphous to microcrystalline transition.....	36
2.2.2 Depletion of H <sub>2</sub> and production of HF molecules.....	38
2.2.3 Optical emission spectroscopy .....	39
2.2.4 H <sub>2</sub> consumption .....	40
2.2.5 Discussion .....	41
<b>2.3 Phenomenological model.....</b>	<b>42</b>
2.3.1 Description of the model.....	42
2.3.2 Solving model equations .....	43
2.3.3 Comparison with experimental results .....	44
2.3.4 Discussion on OES and V <sub>DC</sub> measurements.....	47
2.3.5 Comparison with literature .....	48
<b>2.4 Transfer from PHILIX reactor to CLUSTER-PL8 reactor .....</b>	<b>49</b>
2.4.1 Getting amorphous and microcrystalline films .....	49
2.4.2 Optimizing the H <sub>2</sub> consumption.....	50
2.4.3 SiF <sub>4</sub> consumption .....	52
<b>2.5 Chapter key results .....</b>	<b>54</b>

---

## 2.1 Hydrogen depletion and HF formation

### 2.1.1 Black box approach coupled with RGA

Plasma physics and chemistry is a discipline in itself. Plasmas have been studied in many ways. They can be seen as objects which have electrical and optical properties. Accordingly, various diagnostics such as RF voltage, RF current, impedance, harmonics, and self-bias DC voltage as well as optical emission spectroscopy (OES) measurements are helpful to understand them. However since the physics of plasmas is complex, there is no direct and simple correspondence between what is measured and intrinsic plasma parameters. A good example of this statement is the estimation of the electron density, the electron temperature, and the concentration of reactive species by actinometry: the electron density and the electron temperature are generally involved but those two parameters remain difficult to precisely measure.

Another approach would be to consider the plasma as a “black box” where (for a given pressure, RF power, temperature, etc.) the inputs are the injected gas flows and the outputs are the pumped gas flows (going to the exhaust line). Based on this black box approach, the plasma will be studied by looking at the changes it produces in the composition of the passing gas mixture. If the plasma is not ignited, the outputs are expected to be identical to the inputs. This approach, however, is not very adapted for simple plasmas: a pure Ar plasma, an H<sub>2</sub> plasma, or an H<sub>2</sub>/Ar plasma. Indeed, the zoology of the species which can be synthesized in these plasmas is extraordinary rich (H, H<sup>+</sup>, H<sub>2</sub><sup>+</sup>, H<sub>3</sub><sup>+</sup>, Ar<sup>\*</sup>, ArH<sup>+</sup>, Ar<sub>2</sub>, ...) but none of these species are stable. Therefore within the exhaust line only Ar and H<sub>2</sub> will be found and from the point of view of the black box the plasma has no action on this gas mixture. The black box approach is however very powerful for reactive gas mixtures such as SiF<sub>4</sub>/H<sub>2</sub>/Ar for example, as corresponding plasmas are more complex. The objective of the black box approach is to provide a simple correlation between the process parameters (pressure, RF power, temperature, etc.) and the product of the reactions taking place, and in our case the deposition rate of the silicon thin films and – if possible – their structure (amorphous or microcrystalline).

Differentially-pumped mass spectrometry is an ideal tool to study the gas composition at the output of the “black box”. It can be done by installing a Residual Gas Analyzer (RGA) in the exhaust line of the process as sketched in Figure 8. The operating principle of an RGA is based on the detection of positive ions with specific mass. They are created via the ionization of neutral background gas molecules by electron impact. Electrons are continuously emitted from a heated filament and accelerated to a certain pre-set energy before the impact. The determination of the mass is performed by a quadrupole mass analyzer which acts as a mass filter: ions travel in between four parallel cylindrical rods on which an oscillating RF electric field is applied. Depending on the mass-to-charge ratio of the ion, its trajectory will be stable or not for a given RF frequency. Only ions that pass through the rods are selected and detected. The selected species are the ones with specific mass-to-charge “m/q” ratio. In practice, the frequency of the oscillating field is continuously varied to scan all the wanted mass-to-charge ratios.

The energy of the electrons coming out of the filament is of importance as they are responsible for the ionization of gas molecules which will be eventually selected and detected. Without ionization, no signal is detected. The electron energy of the ionization stage is tunable such that it can be chosen above any given ionization threshold (or dissociation ionization threshold) or below a given threshold to avoid unnecessary ionizations and dissociations. The ionization filament, the filter and the detection stage have to run under high vacuum; therefore a sampling orifice (about 30-100 μm) is present to allow a differential pumping of the RGA enclosure.

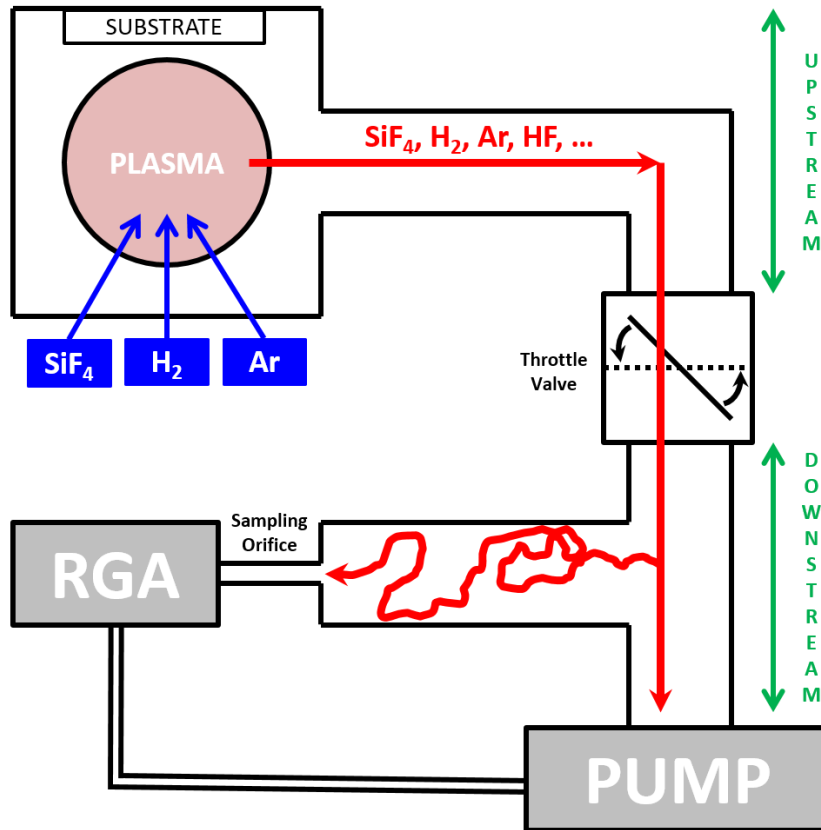


Figure 8: Schematic of PHILIX reactor with the RGA.

Process pressure is controlled by a throttle valve. RGA is installed in the exhaust line – between the throttle valve and the pump.

### 2.1.2 Detection of HF molecules

The unit used to denote the mass of elements is the Atomic Mass Unit (amu): one unit corresponds to the mass of one nucleon (neutrons and protons have approximately the same mass). The mass of an argon atom is 40 amu. The ions detected at mass 40 are  $\text{Ar}^+$  produced by the ionization of neutral Ar by electron impact (electrons emitted by the filament). Equation (1) shows this ionization reaction. A quadrupole mass spectrometer (QMS) has been used to look at the number of detected ions at mass 40 as a function of the energy of the incident electron. The result is displayed in Figure 9 by a green line and is similar to the ionization cross section curve of argon: the signal drastically drops to zero below the threshold of 15.8 eV (first ionization energy of argon). As indicated above, the signals with plasma ON and OFF are identical. The RGA is not helpful for inert gases.



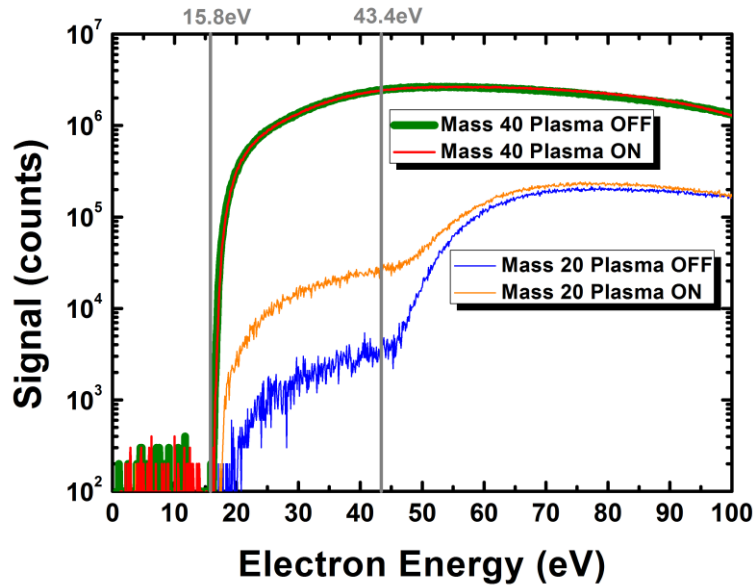


Figure 9: Signals detected by QMS at 40 amu ( $\text{Ar}^+$ ) and 20 amu ( $\text{Ar}^{++}$  and  $\text{HF}^+$ ). Above 43.4 eV mainly  $\text{Ar}^{++}$  is detected at 20 amu but below this value only  $\text{HF}^+$  is monitored.

The situation is different at 20 amu. Two species can be detected at this mass.  $\text{HF}^+$  because the mass of atomic hydrogen is 1 and atomic fluorine is 19, and  $\text{Ar}^{++}$  because the mass of argon is 40 but when the ion is double-charged the mass-to-charge ratio of 20.  $\text{Ar}^{++}$  is detected if an argon atom has undergone reaction (3). This reaction is the double ionization of argon by electron impact. It can be seen as the reaction (1) followed by the reaction (2). The first ionization energy of argon is 15.8 eV and corresponds to reaction (1). The second ionization energy of argon is 27.6 eV and corresponds to reaction (2). Therefore the threshold energy of reaction (3) is simply the sum of those two energies which is 43.4 eV. The pressure in the RGA is so small (below  $10^{-6}$  mbar) that a stepwise ionization (reaction (1) followed by reaction (2)) is very unlikely to occur. In Figure 9 the blue curve represents the signal of ions detected at 20 amu when the plasma is off. The signal is high between 70 eV and 100 eV but drops when electron energy is close to 43.4 eV. Consequently above this energy we attribute the signal to  $\text{Ar}^{++}$  ions to reaction (3).

The orange curve of Figure 9 represents the signal at 20 amu when the plasma is on and  $\text{HF}^+$  is expected to be produced. The signal above 43.4 eV is always dominated by  $\text{Ar}^{++}$  ion signal: in this electron energy range the orange curve (plasma on) is close to the blue curve (plasma off) because the gas mixture is mainly composed of argon. Below 43.3 eV only  $\text{HF}^+$  ions contribute to the signal. These ions are the products of the reaction (4) where the first ionization level of  $\text{HF}$  is 16.0 eV thus explaining the drop of the signal at this electron energy. When the plasma is off, no  $\text{HF}$  is created and no  $\text{HF}^+$  ions should be detected. However, as it can be seen on the blue curve, a residual signal is measured. One can attribute this residue to remaining  $\text{HF}$  molecules sticking to the wall of the QMS: it is well known that molecules having a high sticking coefficient are difficult to pump. That stands for water molecules as well as for fluorinated molecules. In the example of Figure 9 this background signal is about one order of magnitude lower than the signal when plasma ignited.

The  $\text{Ar}^+$  signal does not change with the ignition of the plasma: in Figure 9 the red curve (plasma on) overlaps the green curve (plasma off). Therefore the concentration of argon in the gas mixture is not altered by the plasma, and for the same reason the  $\text{Ar}^{++}$  signal should not be altered by the plasma. Consequently, looking at 20 amu, by subtracting the blue curve (plasma off) from the orange curve (plasma on) one should obtain the  $\text{HF}^+$  signal, i.e. the  $\text{HF}$  produced in the plasma. The subtraction is shown in Figure 10. The noise increases above 43.4 eV due to the noise of the higher  $\text{Ar}^{++}$  signal. It is the reason why electron energy below 43.4 eV should be preferred.

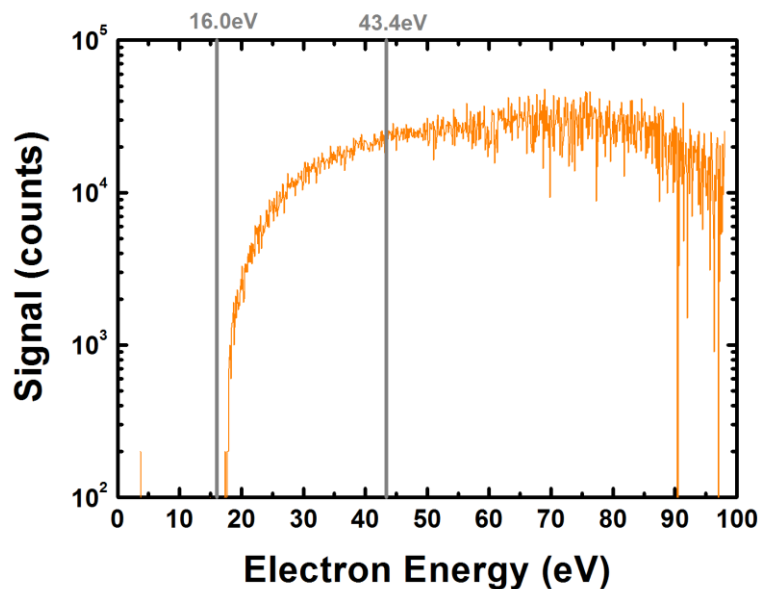


Figure 10: HF<sup>+</sup> signal detected by QMS.

It is computed by removing the contribution of Ar<sup>+</sup> signal. The first ionization level of HF is 16.0 eV.

Figure 11 shows RGA signals at 40, 20 and 2 amu as a function of time. Signals are expressed in terms of partial pressures. The electron energy has been set to 20 eV. The plasma is started after few tens of seconds of turning the RGA on. The argon signal at 40 amu is stable because it does not react to form new species. The HF signal at 20 amu is below  $2 \times 10^{-4}$  before the ignition. It cannot be due to Ar<sup>+</sup> because electron energy is below the threshold energy of reaction (3), but to residual HF within the reactor or the RGA equipment. After plasma ignition and a delay of several seconds, the HF signal starts to increase until it reaches a value of  $3.5 \times 10^{-3}$ . The RGA is connected in the exhaust line of the process, which means that gases are passing by towards the pumps. However between the plugging point and the RGA sampling orifice, only diffusion takes place as sketched in Figure 8 by the red line. Moreover, a high sticking coefficient of the molecules on the walls will delay their transport by successive adsorption/desorption events. It is consistent with the fact that HF (fluorinated element) is detected at mass 20 amu and that the delay in Figure 11 at 20 amu is higher than the one at 2 amu corresponding to H<sub>2</sub> (higher diffusion coefficient and lower sticking coefficient compared to HF).

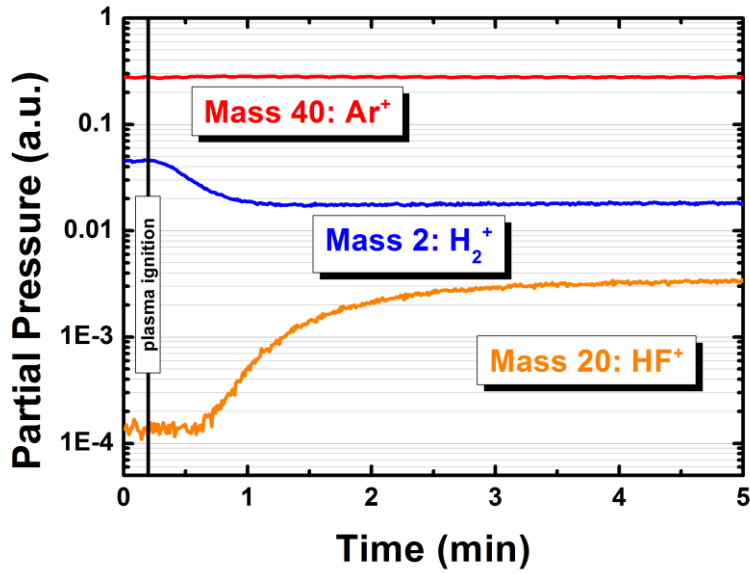


Figure 11: RGA signals at 40, 2 and 20 amu as a function of time. They are attributed respectively to Ar, H<sub>2</sub> and HF concentrations of the gas mixtures. Argon is stable, H<sub>2</sub> is consumed (to produce HF) and HF is produced in the plasma.

### 2.1.3 Depletion and consumption of H<sub>2</sub>

The concentration of hydrogen in the gas mixtures can be estimated by RGA with the H<sub>2</sub><sup>+</sup> ions (detected at the mass-to-charge ratio 2) thanks to the ionization reaction of hydrogen (5).

However, with the SiH<sub>4</sub>/H<sub>2</sub> chemistry, H<sub>2</sub><sup>+</sup> ions can also result from the dissociation-ionization reaction (6). Therefore there are two contributions of the 2 amu signal – one from H<sub>2</sub> and one from SiH<sub>4</sub> – thus leading to a difficult interpretation of it. On the contrary, with SiF<sub>4</sub>/H<sub>2</sub>/Ar chemistry only H<sub>2</sub> molecules can contribute to the signal at 2 amu. The interpretation is then simple: H<sub>2</sub> molecules are dissociated by the plasma and are used to form new species (Si<sub>x</sub>F<sub>y</sub>H<sub>z</sub> with x,y,z integers). The H<sub>2</sub> gas is said to be “depleted” by the plasma. If there are no H<sub>2</sub> molecules at the output of the process, then the depletion is 100%. If there is the same amount of H<sub>2</sub> molecules at the output gas mixture than in the input gas mixture, then the depletion is 0% (hydrogen is not consumed in the process).



Figure 11 shows that the ignition of the plasma is responsible for an absolute decrease of the H<sub>2</sub><sup>+</sup> (partial pressure) signal from 4.5x10<sup>-2</sup> to 2x10<sup>-2</sup>. The relative decrease is 56%, meaning that 56% of the H<sub>2</sub> has been used by the process. The depletion is calculated from Equation (7) where “P” designs the partial pressures measured by the RGA.

$$D_{\text{H}_2} = \frac{P_{\text{H}_2^+}^{\text{off}} - P_{\text{H}_2^+}^{\text{on}}}{P_{\text{H}_2^+}^{\text{off}}} \quad (7)$$

Another way to express the depletion of hydrogen is to compute the consumption which represents the absolute amount of hydrogen which has been lost. The consumption is given in flow rate units (sccm). It can be calculated by Equation (8) where “Φ” stands for the flow rate. For instance, if the depletion is 25% and the H<sub>2</sub> flow rate is 4 sccm then the consumption is 1 sccm. However a depletion of 25% with a H<sub>2</sub> flow rate of 12 sccm corresponds to a consumption of 3 sccm. Therefore to compare

several plasma conditions, depletion is relevant and useful when  $H_2$  flow rate is constant. However consumption should be preferred when  $H_2$  flow rate is changed.

$$C_{H_2} = D_{H_2} \cdot \Phi_{H_2} \quad (8)$$

In  $SiF_4/H_2/Ar$  plasmas, the  $H_2$  depletion is a fast and absolute measurement. On the contrary the detection of HF is slower (as seen previously in Figure 11 with the delay and the long stabilization time of mass 20 signal) and relative: the signal is an estimation of the HF amount which depends on the gas pressure just before the sampling orifice of the RGA. If from one process to another this pressure is changed, then the comparison of the two HF signals is intricate. The pressure inside the reactor (PHILIX) is controlled by a throttle valve (see Figure 8): the pumping rate below the throttle valve is constant and the throttle valve is opened or closed to reach the desired pressure upstream. The RGA has been plugged downstream this throttle valve such that the downstream pressure only depends on the total gas flow rate and does not depend on the upstream pressure. For instance, the change of the inter-electrode distance, of the RF power and of the (upstream) pressure has no impact on the downstream pressure and therefore HF signal variations truly represent the fluctuations of the HF molecules produced by the plasma.

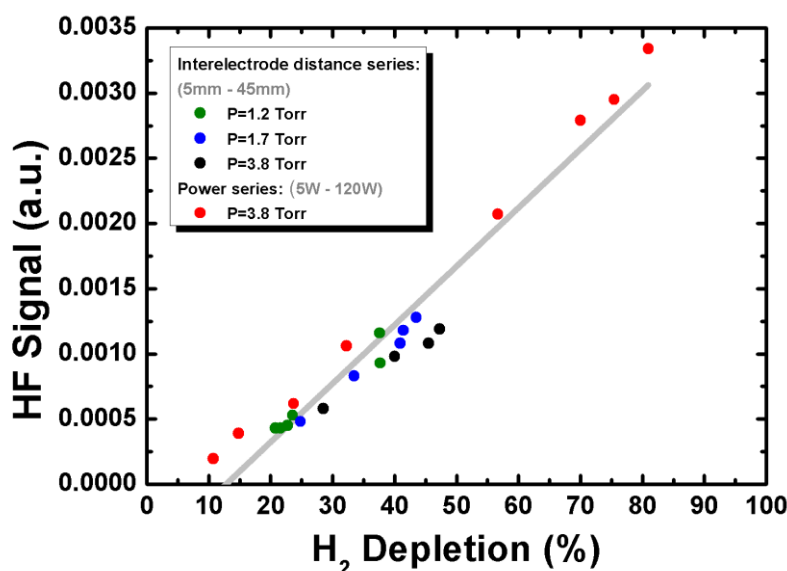


Figure 12: HF signal versus  $H_2$  depletion for many different plasma conditions. A linearity is clearly seen, explaining the depletion of  $H_2$  by the formation of HF molecules.

Several plasma parameters have been varied and both  $H_2$  depletion and HF signal have been recorded. Inter-electrode distance, RF power and pressure have been varied and as mentioned above it is relevant to compare HF signals. Moreover, as the  $H_2$  flow rate is not changed, depletion can be used to monitor the  $H_2$  loss instead of  $H_2$  consumption. In Figure 12, the HF signal has been plotted as function of the  $H_2$  depletion for all plasma conditions. The inter-electrode distance and the pressure both have an impact on the depletion which varies between 20% and 50%.  $H_2$  depletion seems to be more sensitive to the RF power parameter: depletion can be as low as 10% at 5 W and as high as 80% at 120 W. It is worth noticing that the HF signal increases linearly with the  $H_2$  depletion. The meaning is simple but fundamental: the role of  $H_2$  is to provide the hydrogen to form HF molecules. But to form HF both hydrogen and fluorine are required. Fluorine must result from the dissociation of  $SiF_4$  by electron impact. Several hypothesis can be made regarding the chemical reaction producing HF molecules. One can reasonably assume that three-body reactions are very unlikely. Molecules ( $SiF_4$  or  $H_2$ ) and radicals ( $SiF_x$ , F, or H which exist thanks to the plasma) can be reactants of the reaction producing HF. Several chemical reactions may happen (non-exhaustive list):

- a. SiF<sub>4</sub> and H<sub>2</sub>
- b. SiF<sub>4</sub> and H
- c. SiF<sub>x</sub> and H<sub>2</sub>
- d. SiF<sub>x</sub> and H
- e. F and H<sub>2</sub>
- f. F and H

The first reaction (a) is clearly irrelevant since there is no chemical reaction in a SiF<sub>4</sub>/H<sub>2</sub> gas mixture without plasma assistance. In capacitively coupled RF plasmas, radical concentrations are much lower than the gas density (in our case of SiF<sub>4</sub>/H<sub>2</sub>/Ar gas mixture, is mainly composed of argon atoms). Therefore reaction (b), involving atomic hydrogen, cannot account for the depletion of 80% at 120 W. The same argument applies for reaction (c) with SiF<sub>x</sub> radicals. Reactions (d) and (f) can be discarded because both reactants are radicals and the probability of meeting each other is small. However reaction (e) does not suffer from above-mentioned considerations: fluorine atoms are present as byproducts of the dissociation of SiF<sub>4</sub>, and H<sub>2</sub> is an input gas (not a radical) - therefore in substantial concentration within the plasma. Reaction (e) is written in Equation (9). It is thermodynamically favored and exothermic: this reaction has been reported to have an activation energy barrier of only 0.04 eV [32][42]. It does account for a high H<sub>2</sub> depletion due to the strong reactivity of atomic F on H<sub>2</sub> molecules.



Thanks to RGA, we have been able to measure the H<sub>2</sub> depletion and to estimate the amount of HF molecules produced in SiF<sub>4</sub>/H<sub>2</sub>/Ar plasmas. A strong correlation has been found between the consumption of H<sub>2</sub> molecules and the formation of HF molecules, whatever the plasma parameters changed (inter-electrode distance, pressure, or RF power). Taking the example of the RF power series, an increase of the power leads to an increase of the H<sub>2</sub> depletion and a proportional increase of the created HF molecules. The advantage of the RF power parameter is the “intuitive” understanding of its meaning: an increase of the power generally and consensually means higher deposition rate. What we have found with the RGA is: more power leads to more H<sub>2</sub> depletion and to more HF. Let us use now the RGA (H<sub>2</sub> depletion and/or HF formation) as a tool to diagnose SiF<sub>4</sub>/H<sub>2</sub>/Ar plasmas and to investigate the chemistry of such processes.

#### 2.1.4 Effect of the Ar flow rate

In this section, the effect of argon in SiF<sub>4</sub>/H<sub>2</sub>/Ar plasmas is addressed. The easiest study consists in changing the argon flow rate while keeping all other plasma parameters constant (named below as “the basic argon study”). By doing so, one could argue that increasing the argon flow rate at constant total pressure leads to a decrease of partial pressures of SiF<sub>4</sub> and H<sub>2</sub>, and of their residence time. From previous section, we know that some chemical reactions take place to form HF molecules, and the kinetics of these reactions depend on concentration of each reactant. The concentrations are given by the partial pressure of the corresponding species. Reactions are promoted by higher reactant partial pressures. Therefore “the basic argon study” suffers from the variation of SiF<sub>4</sub> and H<sub>2</sub> partial pressures.

To overcome this issue, the partial pressure of SiF<sub>4</sub> and H<sub>2</sub> can be kept constant while the argon flow is increased. However the total pressure should be increased as well, because the partial pressure of argon inevitably increases. A series of samples have been deposited on glass substrates where the partial pressure of SiF<sub>4</sub> plus H<sub>2</sub> has been kept constant at 400 mTorr. Plasmas have been run during half an hour. The argon flow rate has been varied between 0 sccm and 88 sccm while the total pressure ranged from 400 mTorr to 3800 mTorr as shown in Table 1 where the process conditions are specified and lead to the deposition of hydrogenated microcrystalline silicon.

$T_{\text{sub}}$	$T_{\text{RF}}$	$d_i$	Pr	SiF <sub>4</sub>	H <sub>2</sub>	Ar	Pw	$t_d$
(°C)	(°C)	(mm)	(Torr)	(sccm)	(sccm)	(sccm)	(W)	(min)
150	200	30	0.40	3.6	5.3	0	20	30
			1.55			22		
			2.38			44		
			3.12			66		
			3.80			88		

Table 1: Plasma conditions for the argon flow rate series.

For this argon flow rate series, H<sub>2</sub> depletions have been measured and deposition rates have been calculated from ellipsometry spectra. Both are displayed in Figure 13. The plasma of pure SiF<sub>4</sub>/H<sub>2</sub> gas mixture depleted only 7% of the injected H<sub>2</sub>. By adding argon, the plasma is able to deplete almost 40% of the H<sub>2</sub>, despite the fact that the RF power was kept constant at 20 W. Moreover, the growth rate is as low as 0.25 Å/s without argon in the gas mixture, but exceeds 2 Å/s at 88 sccm of argon.

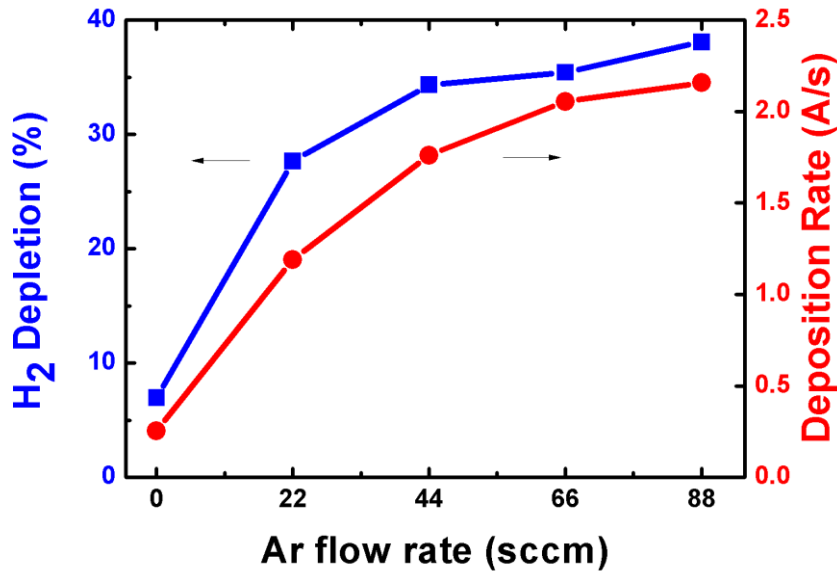


Figure 13: H<sub>2</sub> depletion and deposition rate for argon flow rate series.

The same trend is observed for both the H<sub>2</sub> depletion and the deposition rate curves. This correlation is not fortuitous. As said above “intuitively”, the higher the power the higher the deposition rate, but here the RF power was kept constant. However, experimentally (see Figure 12) with increasing RF power, a higher H<sub>2</sub> depletion has been found. We demonstrated here, with the argon flow rate series, that a high H<sub>2</sub> depletion correlates with high deposition rate.

We have shown that the depletion was due to the formation of HF molecules and that this happens probably through Equation (9). The partial pressure of H<sub>2</sub> has been kept constant. The increase of the H<sub>2</sub> depletion is then explained by a higher atomic fluorine concentration. And only more dissociation of SiF<sub>4</sub> can account for more atomic fluorine. This leads us to propose that the role of argon is to help the dissociation of SiF<sub>4</sub> molecules. In the literature, many papers have addressed the crucial role of metastable argon atoms [43][44]. The exact pathway of the assistance of SiF<sub>4</sub> dissociation is not revealed by the depletion technique, nevertheless the latter has given precious information of the plasma chemistry.

The addition of argon to the gas mixture does change both the plasma properties and the plasma chemistry. Unfortunately, plasma physics is complex because plasma properties and chemistry are intrinsically linked: plasma properties (like  $n_e$  or  $T_e$ ) rule the species dissociation and thus the plasma chemistry, but plasma chemistry (mostly in the case of electronegative gas such as SiF<sub>4</sub> and dusty

plasma such as our conditions) can influence the plasma properties through electron-attachment for instance. This is illustrated by the electrical measurements of  $V_{RF}$  and  $V_{DC}$  shown in Figure 14. Both potentials strongly decrease with the argon flow rate. The large variation of  $V_{DC}$  reflects a significant change in plasma properties: the role of the self-established  $V_{DC}$  is to balance flux of the positive and negative charge to the electrodes such that no DC current flows through the circuit. The RF power of the plasma is kept constant at 20 W but  $V_{RF}$  varies from 221 V down to 100 V. Therefore either the plasma impedance (at 13.56 MHz) or the RF current should vary, proving again that plasma properties are really changed between a pure  $\text{SiF}_4/\text{H}_2$  plasma or mixed with 88 sccm of argon.

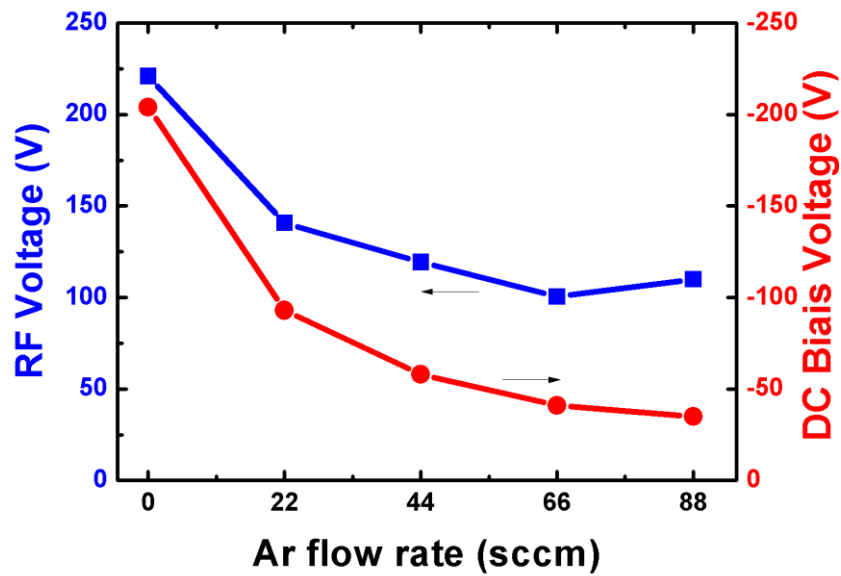


Figure 14:  $V_{RF}$  and  $V_{DC}$  for argon flow rate series.

Potentials encounter dramatic changes between no argon and 88 sccm of argon flow rate.

Figure 14 shows a strong correlation between the electrical properties of the plasma and the corresponding deposition rate on the substrate (Figure 13), without providing any clear and direct explanation. However Figure 13 gives a partial yet clear insight on what is happening in  $\text{SiF}_4/\text{H}_2/\text{Ar}$  plasmas: the increase of the deposition rate is concomitant to the increase of the  $\text{H}_2$  depletion. And the increase of the depletion is enhanced by the argon.  $\text{H}_2$  depletion measurement is a powerful tool to investigate the plasma chemistry and has been used to demonstrate the role of metastable argon as a catalyzer of the  $\text{SiF}_4$  dissociation.

## 2.2 Hydrogen flow rate series

### 2.2.1 Amorphous to microcrystalline transition

There is a general consensus saying that for thin film silicon solar cell applications, the best material is a microcrystalline silicon composed of a mixture of amorphous and crystalline phase (30% and 70% respectively). That consensus stands for  $\text{SiH}_4/\text{H}_2$  gas mixtures. It is therefore interesting to study the amorphous to microcrystalline transition in the case of  $\text{SiF}_4/\text{H}_2/\text{Ar}$  gas mixtures.

A series of layers was deposited on glass substrates at a constant  $\text{SiF}_4$  flow rate of 10 sccm and constant RF power of 40 W. The  $\text{H}_2$  flow rate was varied from 1 sccm to 8 sccm. The conditions are shown in Table 2. The composition and thickness of each layer was obtained from spectroscopic ellipsometry measurements. Figure 15 shows the composition of the layers in terms of amorphous, crystalline and void fractions. For  $\text{H}_2$  flows below 4.5 sccm, the layers are amorphous, and above they are microcrystalline. The crystalline fraction sharply increases to 50% at 5 sccm, and then stabilizes around 65% for 6, 7, and 8 sccm. The amorphous-to-microcrystalline transition is very abrupt and the

void fraction of all the layers is about 10%, independent of the amorphous or microcrystalline nature of the film.

$T_{\text{sub}}$	$T_{\text{RF}}$	$d_i$	Pr	$\text{SiF}_4$	$\text{H}_2$	Ar	Pw	$t_d$
(°C)	(°C)	(mm)	(Torr)	(sccm)	(sccm)	(sccm)	(W)	(sec)
150	200	30	3.8	10	1→8	88	40	1800

Table 2: Plasma conditions for the  $\text{H}_2$  flow rate series.

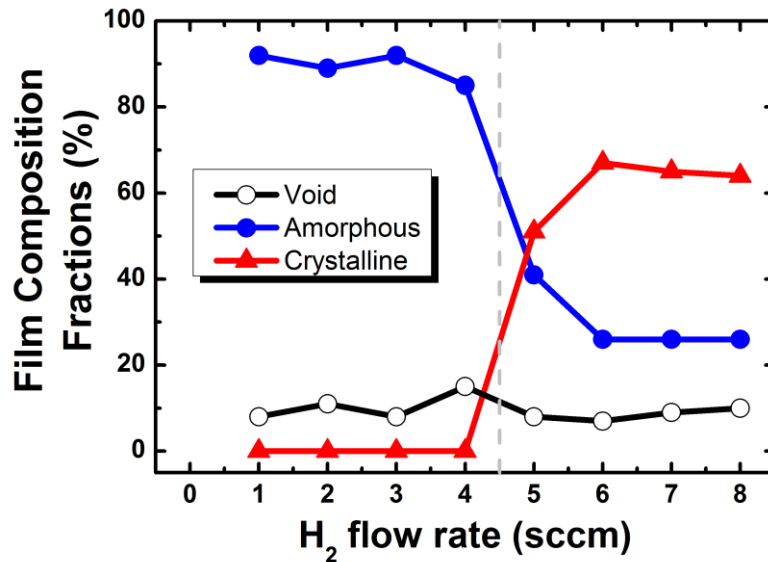


Figure 15: Film composition deduced by ellipsometry as a function of the  $\text{H}_2$  flow rate. Notice the sharp amorphous-to-microcrystalline transition at 4.5 sccm, indicated by the dashed line.

Although from ellipsometry measurements, one can extract the film thickness, to correctly estimate the deposition rate, one should take into account the incubation time for the growth, especially for microcrystalline deposition at high  $\text{H}_2$  flow rates. To account for this effect, the ellipsometry spectra were acquired in-situ at intervals of ten minutes (plasma was off during the measurements). After modelling the films for each spectrum and extracting the thickness, the deposition rate is then computed as the difference of the two sequential thicknesses divided by 600 s. Figure 16 shows that the deposition rate increases linearly with the  $\text{H}_2$  flow rate up to 4 sccm, at which value the deposition reaches its maximum of 4.5 Å/s. Then, at the amorphous-to-microcrystalline transition (between 4 and 5 sccm), the deposition rate stays constant and finally, it slowly decreases to 4 Å/s for a hydrogen flow rate of 8 sccm.

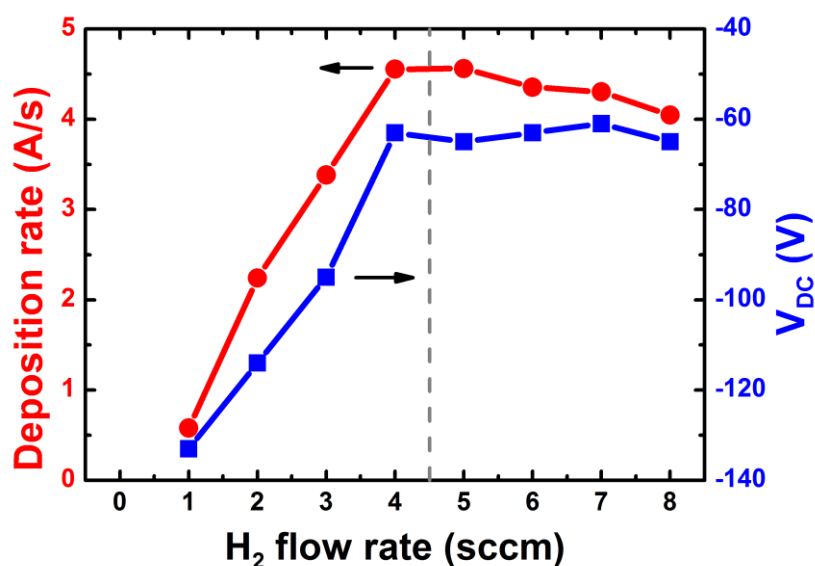


Figure 16: Deposition rate and  $V_{DC}$  as functions of the  $H_2$  flow rate. Note that the deposition rate is constant at the transition.

As the reactor used in this study is geometrically asymmetric (the grounded electrode has a larger surface than the RF electrode), a large self-bias ( $V_{DC}$ ) is usually developed on the capacitively coupled RF electrode.  $V_{DC}$  is negative and its absolute value strongly decreases when the  $H_2$  flow rate is increased. As shown in Figure 16, the self-bias changes from -133 V to -63 V when the  $H_2$  flow rate increases from 1 to 4 sccm. Then, for flows between 4 and 8 sccm, the  $V_{DC}$  is nearly constant. Interestingly the features in  $V_{DC}$  mimic those of the deposition rate.

### 2.2.2 Depletion of $H_2$ and production of HF molecules

In order to gain more insight into the changes in the plasma chemistry for various process conditions, we have performed RGA measurements. RGA is used to estimate the  $H_2$  depletion and the production of HF molecules under the same conditions of the  $H_2$  flow rate series as shown in Figure 16. The results presented in Figure 17a show that between 1 and 5 sccm, a very high  $H_2$  depletion (above 90 %) is achieved. However, a constant depletion does not indicate a constant  $H_2$  consumption, as  $H_2$  flow rate is varied. Indeed, the hydrogen consumption corresponding to the depletion curve of Figure 17a is displayed on Figure 17b. Between 1 and 5 sccm, where the  $H_2$  depletion is roughly constant (above 90%), there is a linear increase in  $H_2$  consumption. The more  $H_2$  is injected, the more is used, despite the fact that the total pressure and RF power are kept constant.

However, above 4.5 sccm, the  $H_2$  depletion begins to decrease, reaching 55% at 8 sccm, suggesting that only 4.4 sccm of the 8 sccm  $H_2$  feed gas is used in the process. As a matter of fact, this consumption is relatively constant in the range of 6 to 8 sccm: 4.38 sccm of  $H_2$  is used among the 6 sccm (depletion 73%) of injected  $H_2$  flow rate, and 4.42 sccm of  $H_2$  is used among the 7 sccm (depletion 63%) of feed  $H_2$  flow rate. It should be noted that this constant  $H_2$  consumption is found for a  $SiF_4$  flow rate of 10 sccm and a RF power of 40 W.

As an indication of the molecule formation pathway that is consuming  $H_2$ , on the right axis of Figure 17a we plot the amount of HF (in arbitrary units) produced by the process and measured by RGA. The production of HF is proportional to the hydrogen flow rate for hydrogen flows up to 5 sccm and stays constant above this value, meaning that HF formation is governed by  $H_2$  addition and not by RF power.

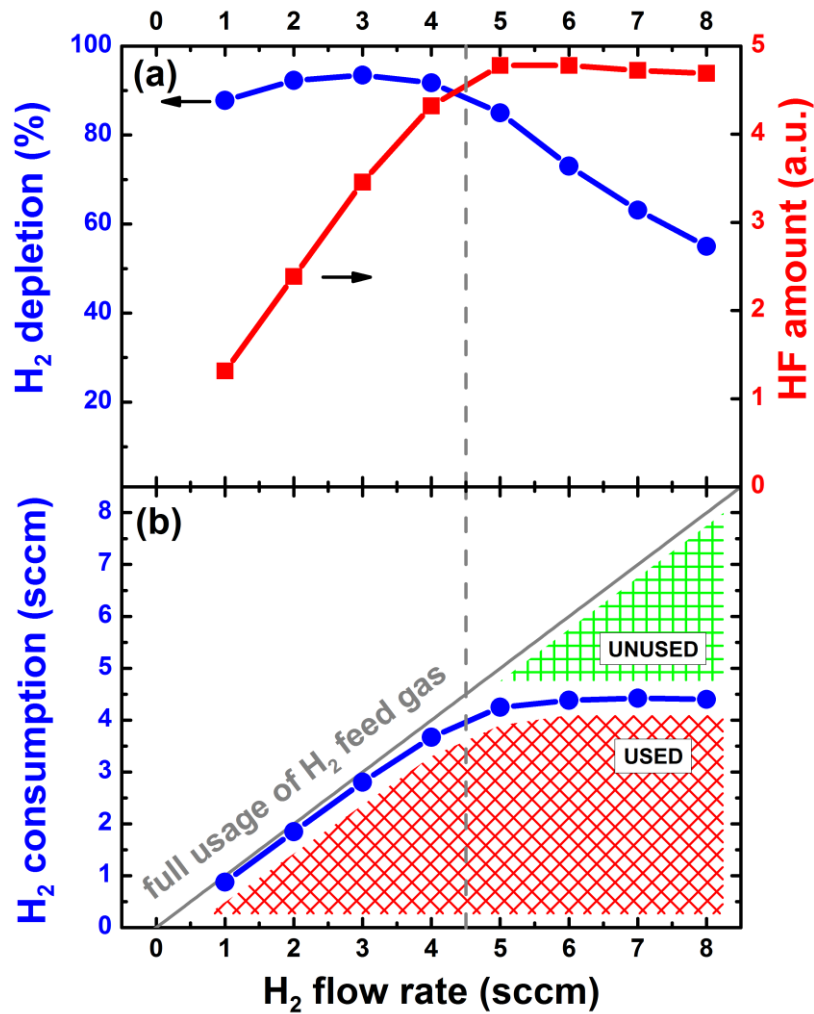


Figure 17: (a) Depletion of H<sub>2</sub> and production of HF and (b) the hydrogen consumption as a function of the H<sub>2</sub> flow rate.

The total pressure and RF power are kept constant at 3.8 Torr and at 40 W respectively. At low H<sub>2</sub> flow rate, consumption is close to the full usage of injected H<sub>2</sub>. At high H<sub>2</sub> flow rate, the H<sub>2</sub> consumption is constant.

### 2.2.3 Optical emission spectroscopy

Figure 18 shows the variation in the intensity of the optical emission spectroscopy lines of Ar, SiF, and H as functions of the H<sub>2</sub> flow rate. It should be pointed out that RGA and OES probe plasma properties at different location: OES is taken from the plasma whereas the RGA is plugged in the exhaust line of the reactor. The H<sub>α</sub> line increases monotonically with the H<sub>2</sub> flow rate. In contrast with the RGA measurements, no sharp transition is observed at 4.5 sccm. Between 0 and 1 sccm of H<sub>2</sub> flow rate, an abrupt increase of the SiF line is seen, as the addition of a small amount of H<sub>2</sub> to the SiF<sub>4</sub>/Ar plasma strongly increases the SiF intensity [45]. However, the SiF line decreases continuously for H<sub>2</sub> flows above 1 sccm. Interestingly, the argon signal increases between 0 sccm and 4.5 sccm, then it slowly decreases.

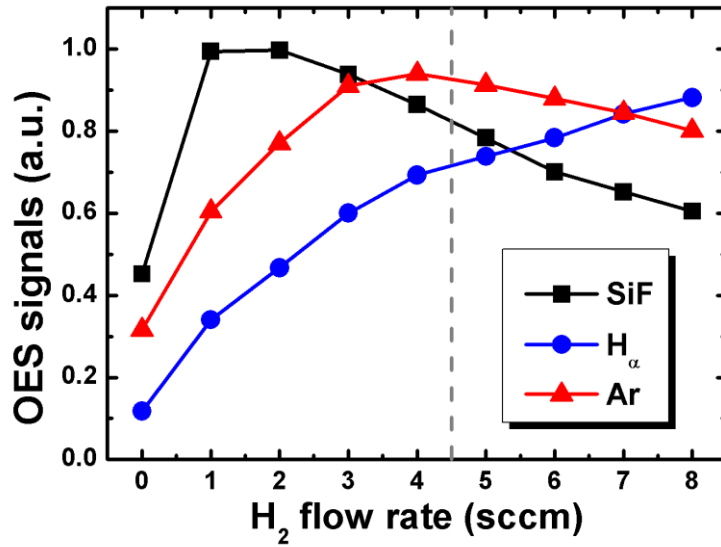


Figure 18: OES signals of SiF (440nm), H $\alpha$  (656nm), and Ar (750nm) as functions of the H<sub>2</sub> flow rate. Except for the hydrogen flow rate, all process parameters are kept constant.

#### 2.2.4 H<sub>2</sub> consumption

So far we have focused on a H<sub>2</sub> flow rate series where the SiF<sub>4</sub> flow rate was kept constant at 10 sccm and the RF power at 40 W. To gain more insight into SiF<sub>4</sub>/H<sub>2</sub>/Ar plasmas, the effect of the H<sub>2</sub> flow rate has been studied for various values of the SiF<sub>4</sub> flow rate (3.6, 10 and 20 sccm) and of the RF power (10, 20 and 40 W). Conditions are given in Table 3.

T <sub>sub</sub>	T <sub>RF</sub>	d <sub>i</sub>	Pr	SiF <sub>4</sub>	H <sub>2</sub>	Ar	Pw
(°C)	(°C)	(mm)	(Torr)	(sccm)	(sccm)	(sccm)	(W)
150	200	30	3.8	3.6	1→10	88	10
							20
							40
				10			20
							40
							40
20	40						

Table 3: Plasma conditions for study of H<sub>2</sub> consumption.

For this set of processing conditions, the resulting H<sub>2</sub> consumption is plotted in Figure 19. For each process condition, a behavior similar to that of Figure 17b can be seen. For all the curves, one can outline two regimes. The first regime corresponds to the full consumption of H<sub>2</sub> feed gas, and the second to a constant H<sub>2</sub> consumption. Moreover, the H<sub>2</sub> flow rate at which the transition between the two regimes takes place increases with the SiF<sub>4</sub> flow rate for a given RF power, and also with the RF power for a fixed SiF<sub>4</sub> flow rate. In other words, the higher the dissociation of SiF<sub>4</sub>, the higher the hydrogen flow rate at which the transition takes place.

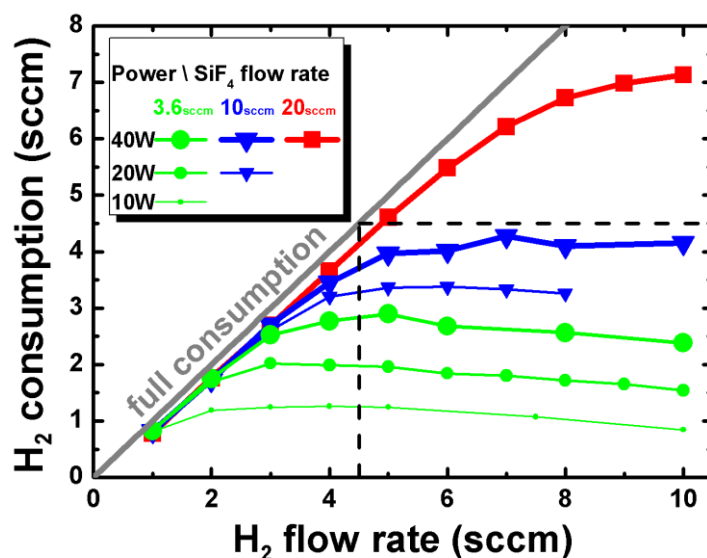


Figure 19: H<sub>2</sub> consumption as a function of the H<sub>2</sub> flow rate for various values of the RF power and SiF<sub>4</sub> flow rate.

### 2.2.5 Discussion

The results on plasma and film properties presented above reveal that in SiF<sub>4</sub>/H<sub>2</sub>/Ar plasma chemistries, the amorphous-to-microcrystalline transition is linked to the consumption of hydrogen molecules. As shown in Figure 15, the material transition occurs at 4.5 sccm of H<sub>2</sub> – a flow rate which separates the two regimes of H<sub>2</sub> consumption found in Figure 17b. The initial conclusion is that for this chemistry, amorphous films are deposited when H<sub>2</sub> is completely consumed, whereas microcrystalline layers are grown when the H<sub>2</sub> feed gas is not fully depleted. This point is coherent with the fact that microcrystalline silicon growth requires excess hydrogen. Furthermore, below the transition, the deposition rate is proportional to the H<sub>2</sub> flow rate (as shown in Figure 16). These results suggest that the H<sub>2</sub> flow rate is the limiting factor for the deposition rate in the amorphous silicon deposition regime. The reason for that could be the etching by excess atomic F. Above the transition, the deposition rate is quite independent of the H<sub>2</sub> flow rate and the films are microcrystalline.

In a previous section, we have shown that in the case of a constant H<sub>2</sub> flow rate, the depletion of H<sub>2</sub> is strongly correlated to the formation of HF molecules, even when the RF power, the total pressure and inter-electrode distance were varied. This is consistent with the measurements displayed in Figure 17a, which show the quantity of HF molecules detected by the RGA as a function of hydrogen flow rate. It increases until the H<sub>2</sub> flow reaches 4.5 sccm and stays constant above this value. This trend can be compared to that of the deposition rate (Figure 16) and of the H<sub>2</sub> consumption (Figure 17b), both of which display similar trends. Interestingly, the production of HF molecules is proportional to the consumption of H<sub>2</sub>, irrespective of the nature (amorphous or microcrystalline) of the deposited layers. Therefore, the production of HF molecules is a signature of the formation of the growth precursors but it cannot be held responsible for the amorphous or crystalline structure of the films.

In summary, as shown in Figures 15, 16, and 17, for the whole range of H<sub>2</sub> flow rates, and independently of the nature of the layers, the deposition rate, the production of HF and the consumption of H<sub>2</sub> are strongly correlated. In the amorphous growth regime, the deposition rate is limited by the H<sub>2</sub> gas flow rate and practically all H<sub>2</sub> molecules are used to form growth precursors and HF molecules as a byproduct. In the microcrystalline growth regime, a constant amount of H<sub>2</sub> is used to form precursors and all the F is scavenged. The remaining hydrogen contributes to processes leading to crystalline layer growth.

The dissociation of SiF<sub>4</sub> molecules produces SiF<sub>x</sub> and F and their concentration increases with the SiF<sub>4</sub> flow rate and the RF power. Under the conditions of reactor geometry, temperature, pressure,

argon dilution, RF power (40 W) and SiF<sub>4</sub> flow rate (10 sccm) used for the experiments of Figure 17, a maximum of 4.4 sccm of H<sub>2</sub> (55% depletion at 8 sccm) plays a role in HF and precursor production. As shown in Figure 16, the upper limit of the deposition rate is obtained at this maximal 4.4 sccm consumption of H<sub>2</sub>.

Concerning the dominant growth precursor(s) for this plasma chemistry, studies in the literature have proposed many species: SiF<sub>x</sub>H<sub>y</sub> radicals [30], SiF<sub>2</sub> reacting at the surface with an impinging H [33], and even silicon nanoparticles [46]. In any case, SiF<sub>x</sub> radicals are required to form growth precursors. However this is not sufficient because no deposition is found with a pure SiF<sub>4</sub>/Ar plasma despite the presence of SiF<sub>x</sub> species in such plasma. The creation of SiF<sub>x</sub> molecules is associated with the release of atomic F. Whatever the growth precursor, it requires SiF<sub>x</sub> as well as the removal of the corresponding atomic F. This removal is performed, given the presence of H<sub>2</sub> molecules, by the formation of HF via Equation (9). The amorphous to microcrystalline transition happens precisely when all F is scavenged.

The H<sub>2</sub> flow rate at which the transition occurs therefore only depends on the concentration of free atomic F to scavenge. Consequently, we can conclude that by increasing the SiF<sub>4</sub> flow rate or the RF power, more F has to be scavenged. Therefore more SiF<sub>4</sub> molecules are dissociated and the transition occurs at higher H<sub>2</sub> flow rate, as shown in Figure 19. Accompanying this transition shift, higher deposition rates can be obtained.

## 2.3 Phenomenological model

### 2.3.1 Description of the model

The detailed physical modeling of the SiF<sub>4</sub>/H<sub>2</sub>/Ar plasma is out of the scope of this thesis. Rather, we propose a phenomenological model which accounts for the experimental data. The simplicity of the model is meant to provide intuitive insights into the plasma process as its predictions match experimental trends. The model consists of three kinetic equations based on previous findings. The first equation accounts for the dissociation of SiF<sub>4</sub> into SiF<sub>3</sub> and atomic F (Equation (10)). The second equation is the dissociation of H<sub>2</sub> into atomic H (Equation (11)). The third equation is the formation of HF molecules from atomic H and atomic F (Equation (12)). As discussed above, atomic F can directly react with H<sub>2</sub> molecules; the kinetic equation corresponding to reaction of Equation (9) is equivalent to a combination of Equations (11) and (12).



The model is composed of only six species: SiF<sub>4</sub>, SiF<sub>3</sub>, F, H<sub>2</sub>, H and HF. The initial concentrations are set to zero for all species, except for SiF<sub>4</sub> and H<sub>2</sub>. The initial concentration of SiF<sub>4</sub> in the model is denoted as "A"; it represents the maximum amount of SiF<sub>4</sub> which can be dissociated within the plasma. It is expected to increase with RF power and with SiF<sub>4</sub> flow rate. The initial concentration of H<sub>2</sub> is denoted as "B" and is representative the H<sub>2</sub> flow rate. The equilibrium concentrations of the six species represent the simplified plasma chemistry of the deposition process. The equilibrium constants of reactions corresponding to Equations (10), (11) and (12) are named respectively K<sub>a</sub>, K<sub>b</sub>, and K<sub>c</sub>. The equilibrium equations are the following (square brackets indicate equilibrium concentrations):

$$K_a \cdot [\text{SiF}_4] = [\text{SiF}_3] \cdot [\text{F}] \quad (13)$$

$$K_b \cdot [\text{H}_2] = [\text{H}]^2 \quad (14)$$

$$K_c \cdot [\text{H}] \cdot [\text{F}] = [\text{HF}] \quad (15)$$

These constants depend on the plasma parameters (electron density and electron temperature, for example) as some reactions (such as the dissociation of SiF<sub>4</sub>) are assisted by electron impact. Three more equations can be written based on the conservation of matter for elemental Si (Equation (16)), F (Equation (17)) and H (Equation (18)):

$$[\text{SiF}_4] + [\text{SiF}_3] = A \quad (16)$$

$$[\text{SiF}_4] + [\text{F}] + [\text{HF}] = A \quad (17)$$

$$2 \cdot [\text{H}_2] + [\text{H}] + [\text{HF}] = 2 \cdot B \quad (18)$$

In the model SiF<sub>3</sub> is assumed to be the growth precursor but only SiF<sub>3</sub> production accompanied by the effective removal of the produced atomic F can contribute to the growth. Therefore the deposition rate is given by [SiF<sub>3</sub>]-[F]. This statement is consistent with the fact that no deposition is obtained in pure SiF<sub>4</sub>/Ar plasma where the concentration of SiF<sub>3</sub> is equal to that of F.

Concerning hydrogen, all the atomic H present in the discharge can recombine inside or outside the plasma to form H<sub>2</sub> molecules. Within the model (in which there are only six species), the only way for hydrogen to bind into something else than H<sub>2</sub> is to form HF. Therefore the depletion is given by the ratio [HF]/(2.B). The linear relationship between the amount of produced HF molecules and the H<sub>2</sub> consumption in the process is intrinsic to the model. Finally, the nature of the deposition (amorphous or microcrystalline) is assumed to depend on the ratio between the concentration of free atomic H and the concentration of growth precursors [47]. This ratio is given by [H]/([SiF<sub>3</sub>]-[F]).

### 2.3.2 Solving model equations

In order to solve the six equations (from Equation (13) to Equation (18)) with the six unknown (concentrations of SiF<sub>4</sub>, SiF<sub>3</sub>, F, H<sub>2</sub>, H, and HF), many calculations should be carried out.

- Equation (16) is rewritten in Equation (19).

$$[\text{SiF}_3] = A - [\text{SiF}_4] \quad (19)$$

- By combining Equation (13) with Equation (19), Equation (20) is obtained.

$$[\text{SiF}_4] = \frac{A}{1 + \frac{K_a}{[\text{F}]}} \quad (20)$$

- Equation (21) is identical to Equation (15).

$$[\text{HF}] = K_c \cdot [\text{H}] \cdot [\text{F}] \quad (21)$$

- Equation (14) is rewritten in Equation (22).

$$[\text{H}_2] = \frac{[\text{H}]^2}{K_b} \quad (22)$$

- At this stage of the solving, the concentrations of the four species SiF<sub>4</sub>, SiF<sub>3</sub>, HF and H<sub>2</sub> are expressed with the concentrations of F and H. By using Equation (17), one can easily get Equation (23) giving the H concentration from the F concentration.

$$[\text{H}] = \frac{A \cdot K_a - K_a \cdot [\text{F}] - [\text{F}]^2}{K_c \cdot [\text{F}] \cdot (K_a + [\text{F}])} \quad (23)$$

- Now, all the concentrations of the species can be calculated from the F concentration. The last equation to use is the continuity equation of hydrogen given by Equation (18). After laborious

calculations, one can find that F concentration is root of a polynomial of fifth degree. The polynomial is written in Equation (24) and its coefficients are given by Equation (25) where a compact notation has been used and is explained in Equation (26).

$$Q_0 + Q_1 \cdot [F] + Q_2 \cdot [F]^2 + Q_3 \cdot [F]^3 + Q_4 \cdot [F]^4 + Q_5 \cdot [F]^5 = 0 \quad (24)$$

$$\begin{cases} Q_0 = 2 \cdot A^2 \cdot K_a^2 \\ Q_1 = A \cdot K_a^2 \cdot b c & -4 \cdot A \cdot K_a^2 \\ Q_2 = 2 \cdot K_a^2 & -K_a^2 \cdot b c^2 & +A \cdot K_a^2 \cdot b c^2 & -2 \cdot B \cdot K_a^2 \cdot b c^2 & +A \cdot K_{abc} & -4 \cdot A \cdot K_a \\ Q_3 = -K_a^2 \cdot b c^2 & +A \cdot K_{abc}^2 & +4 \cdot K_a & -2 \cdot K_{abc} & -4 \cdot B \cdot K_{abc}^2 \\ Q_4 = -2 \cdot K_{abc}^2 & -2 \cdot B \cdot K_{bc}^2 & +2 & -K_{bc} \\ Q_5 = -K_{bc}^2 \end{cases} \quad (25)$$

$$K_a^p b^q c^r = K_a^p \cdot K_b^q \cdot K_c^r \quad (26)$$

- To numerically solve the F concentration (i.e. to numerically determine a root of a polynomial), dichotomy can be used. The lower bound of F concentration is 0 and the upper bound is A. At each iteration, one bit of precision is gained. After calculating the polynomial coefficients, only 100 iterations are performed to estimate the F concentration.

Figure 20 shows the results of a simulation where  $K_a$ ,  $K_b$ , and  $K_c$  are set to 10, and the A parameter is set to 80. The B parameter ( $H_2$  flow rate) is varied from 0 to 100. The concentrations of the six species are plotted. The concentration of HF increases up to a value of B about 40. Above 40, the HF stabilizes at 80 which is the maximum reachable value given by A parameter. Below 40, the  $H_2$  and H concentrations are very low and they start to increase only above  $B=40$ . This means that below  $B=40$ , the depletion of  $H_2$  is very high. The concentration of free F atoms is the highest at low values of B. With the increase of the B parameter, more HF is produced via reaction (12) and accordingly less free atomic F is available. Above 40, almost no F can be found.

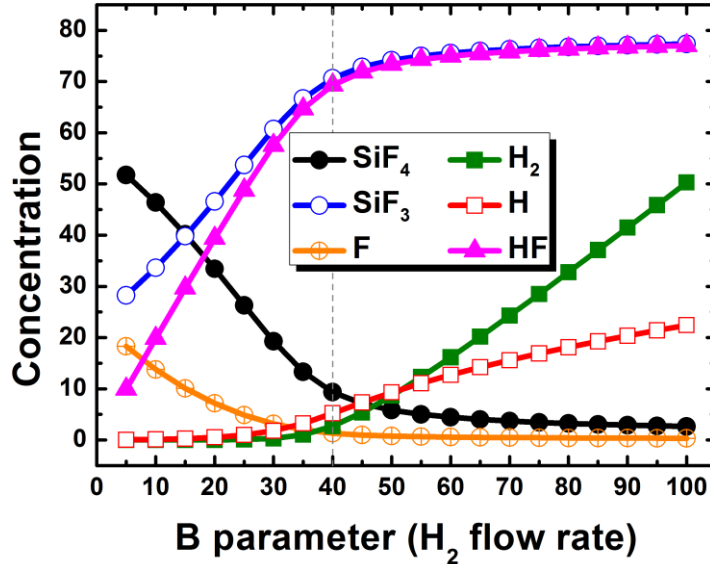


Figure 20: Concentrations of the six species included in the phenomenological model as functions of the B parameter.  $K_a$ ,  $K_b$ ,  $K_c$ , and A parameters have been set to 10, 10, 10, and 80, respectively. Concentrations have been computed by solving Equations (10) to (18)

### 2.3.3 Comparison with experimental results

As explained in the previous subsection, the deposition rate should be proportional to  $[SiF_3] \cdot [F]$  and the crystalline fraction of the deposited material should depend on the ratio between atomic hydrogen

and silicon film precursor  $[H]/([SiF_3]-[F])$ . Those two quantities are plotted in Figure 21. The  $[SiF_3]-[F]$  concentration follows the same trend as the deposition rate shown in Figure 16: when the  $H_2$  flow rate is increased, first a linear increase is encountered, and then a plateau is reached above the value  $B=40$ . Moreover, the transition from amorphous to microcrystalline silicon (Figure 15) can be explained by the ratio  $[H]/([SiF_3]-[F])$  plotted in blue in Figure 21; the ratio starts to increase when the deposition rate starts to saturate around  $B=40$ . The threshold ratio for crystallization is reached at the transition. Note that contrary to the experimental results (Figure 15), the ratio does not present an abrupt increase. However the model results are consistent with OES data (Figure 18) which do not show an abrupt increase on the  $H_\alpha$  line, and this is rather an indication that the process leading to crystalline growth has a very sharp threshold in H concentration.

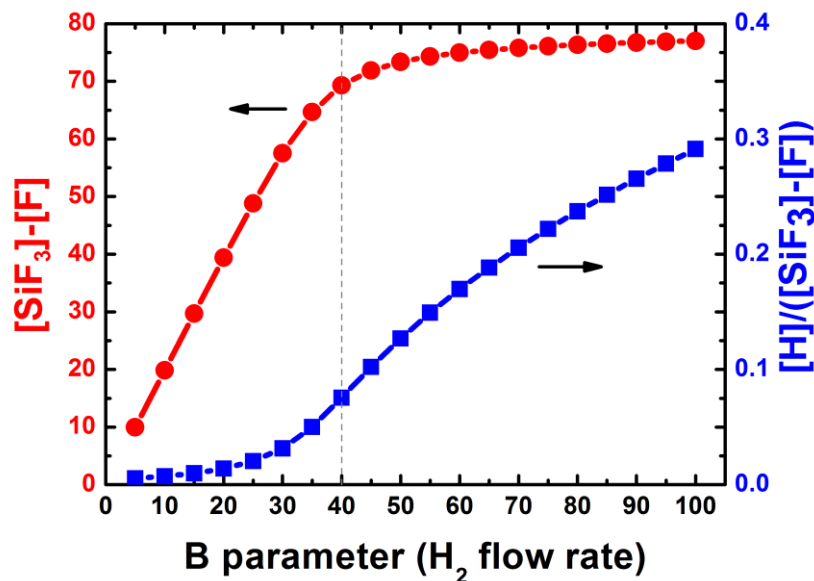


Figure 21:  $[SiF_3]-[F]$  concentration and  $[H]/([SiF_3]-[F])$  ratio versus the B parameter.  $[SiF_3]-[F]$  represents the deposition rate, and  $[H]/([SiF_3]-[F])$  the process determining crystalline fraction.

We found experimentally that the consumption of  $H_2$  is proportional to the production of HF molecules. In the model, the depletion is computed from  $[HF]/(2.B)$ . Consequently the linear relationship between  $H_2$  consumption and HF formation is inherent in the model.

The model can also reproduce the experimental behavior of the  $H_2$  consumption shown in Figure 19. Increasing the RF power or the  $SiF_4$  rate is equivalent to increasing the parameter A, which is the maximal amount of  $SiF_4$  which can be dissociated within the plasma. The consumption of  $H_2$  is simply computed in the model by  $[HF]/2$ . The consumption is plotted in Figure 22 as a function of the B parameter and for different values of A. As found experimentally (Figure 19),  $H_2$  is fully consumed up to a certain value of the  $H_2$  flow rate and then becomes constant. Those two regimes coincide with the transition from amorphous to microcrystalline silicon deposition and the transition is shifted to higher values of the  $H_2$  flow rate (B values) when the dissociation of  $SiF_4$  (A value) is increased.

The phenomenological model has been built up from  $H_2$  flow rate series, i.e. using a B parameter series. However the model can be used to make predictions on an A parameter series (where B parameter is kept constant). The easiest way to change A parameter is to vary the RF power. Three RF power series have been carried out to verify the model. The first series is with 2 sccm of  $H_2$  flow rate; the second series with 3 sccm, and the third series with 10 sccm. For each plasma conditions, a deposition of 30 min has been made on glass and the thickness has been estimated by ex-situ ellipsometry. The deposition conditions are given in Table 4.

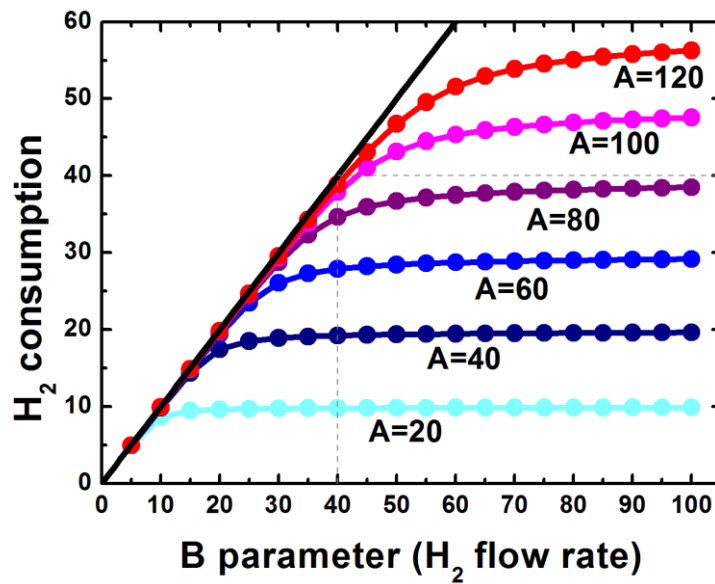


Figure 22: Modeled H<sub>2</sub> consumption as a function of the parameter B.  
Note the similarity with the experimental data shown in Figure 19.

T <sub>sub</sub>	T <sub>RF</sub>	d <sub>i</sub>	Pr	SiF <sub>4</sub>	H <sub>2</sub>	Ar	Pw	t <sub>d</sub>
(°C)	(°C)	(mm)	(Torr)	(sccm)	(sccm)	(sccm)	(W)	(sec)
150	80	30	3.8	3.3	2,3,10	88	5→45	1800

Table 4: Plasma conditions for study of RF power series to test the prediction of the model.

Figure 23 shows the deposition rate as a function of the RF power for the three H<sub>2</sub> flow rates. Generally speaking, we confirm that more power leads to higher deposition rate. We have shown that more power also leads to a higher H<sub>2</sub> consumption which was linked to higher SiF<sub>4</sub> dissociation (higher A parameter value). Consequently, we can conclude from the model and Figure 23 that the deposition rate is really given by the A parameter (if not limited by a full depletion of H<sub>2</sub>). For 10 sccm, a linear increase in the deposition rate is found with the RF power. However for 2 sccm, a saturation is found at 25 W. In the scope of the model, the deposition rate does not increase from 25 W to 35 W because of a shortage in H<sub>2</sub>, or in other words an excess of atomic F which can lead to etching. At high RF power the process is H<sub>2</sub>-limited (B-limited), which should be compared to the H<sub>2</sub> flow rate series of Figure 19 where at high H<sub>2</sub> flow rate the process is limited by the absence of atomic F (A-limited, or limited by the SiF<sub>4</sub> dissociation). Both cases correspond to a shortage of one of the reactants in Equation 9. This equation is the crucial one which explains when we are either A-limited or B-limited. In Figure 19, the maximum H<sub>2</sub> consumption is around 2 sccm at 20 W and around 3 sccm at 40 W, which is consistent in Figure 23 with a saturation of the deposition rate at around 25 W at 2 sccm and around 35W at 3 sccm.

A similar behavior is found at 3 sccm: above 35 W the growth rate does not increase. The saturation takes place at higher RF power compared to the 2 sccm case because more atomic F should be produced to scavenge more H<sub>2</sub>. The maximum deposition rate at 3 sccm is 3 Å/s whereas at 2 sccm it is 2.25 Å/s.

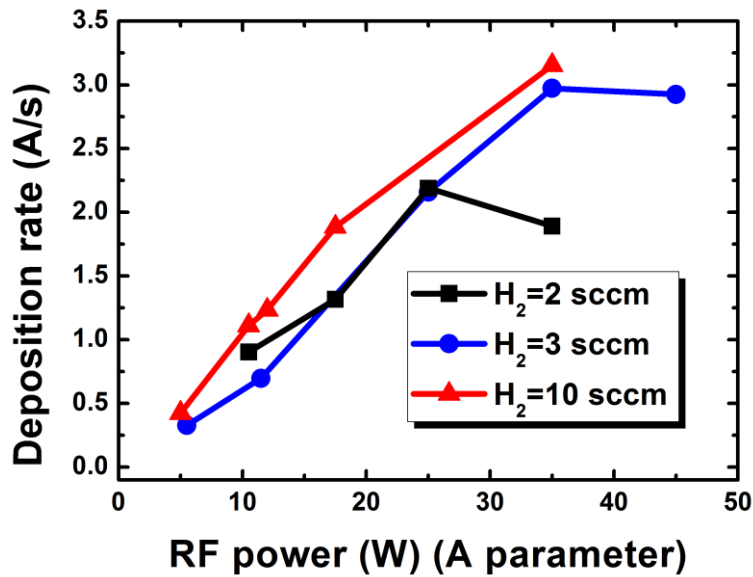


Figure 23: Deposition rate as a function of the RF power.

The deposition rate saturates at 25 W for 2 sccm of H<sub>2</sub> flow rate and at 35 W for 3 sccm.

### 2.3.4 Discussion on OES and V<sub>DC</sub> measurements

In Figure 18, the hydrogen signal in OES increases with the H<sub>2</sub> flow rate, and the SiF signal decreases. In light of the model, no explanation can be proposed to these experimental observations. The increase in hydrogen signal might be understood as the quantity of H<sub>2</sub> increases with the H<sub>2</sub> feed gas flow rate.

We have shown in Figure 18 that the Ar signal was maximal at the transition. It increases a lot by the addition of H<sub>2</sub> in the amorphous regime (below the transition) and slowly decreases in the microcrystalline regime (above the transition). From a practical point of view, OES via the Ar signal can be used to locate the transition in H<sub>2</sub> flow rate parameter. Indeed, the trend of the Ar signal is general and can be found on all other plasma conditions, as displayed in Figure 24 where SiF<sub>4</sub> flow rate and RF power have been changed. The reference conditions are 10 sccm and 40 W as shown in Figure 18. By decreasing the RF power down to 20 W, the OES argon signal globally decreases and its optimum shifts to lower H<sub>2</sub> flow rate value. The same trend has been found with H<sub>2</sub> consumption in Figure 19. By increasing the SiF<sub>4</sub> flow rate up to 20 sccm, the OES argon signal globally decreases and its optimum shifts to a higher H<sub>2</sub> flow rate value, in accordance with Figure 19.

Like OES argon signal, the self-bias voltage V<sub>DC</sub> has been found to be useful to locate the transition, as plotted in Figure 16. In the amorphous regime, V<sub>DC</sub> decreases (in absolute value from 160 V to 80 V) and stays constant in the microcrystalline regime. This behavior is also found for the 20 sccm and 40 W series as shown in Figure 24 (right axis).

We can try to explain the argon line as well as the V<sub>DC</sub> behavior in light of the phenomenological model. Our plasma conditions are known to be dusty, therefore a lot of nanoparticles are generated in the plasma. Electron attachment is very easy on these particles, leading to negatively charged nanoparticles [48]. The electron attachment involves a free electron and consequently the presence of nanoparticles reduces the electron density n<sub>e</sub>. To balance the electron loss, the electronic temperature T<sub>e</sub> increases. Based on the model, below the transition, the addition of H<sub>2</sub> increases the formation of growth precursors (SiF<sub>3</sub> in the model). The increase of T<sub>e</sub> accounts for the rise of the OES argon signal. Low V<sub>DC</sub> values (in absolute value) have been correlated to the formation of nanoparticles [49]. Therefore the decrease of V<sub>DC</sub> (in absolute value) is consistent with the increase of the number of nanoparticles when H<sub>2</sub> flow rate is increased below the transition.

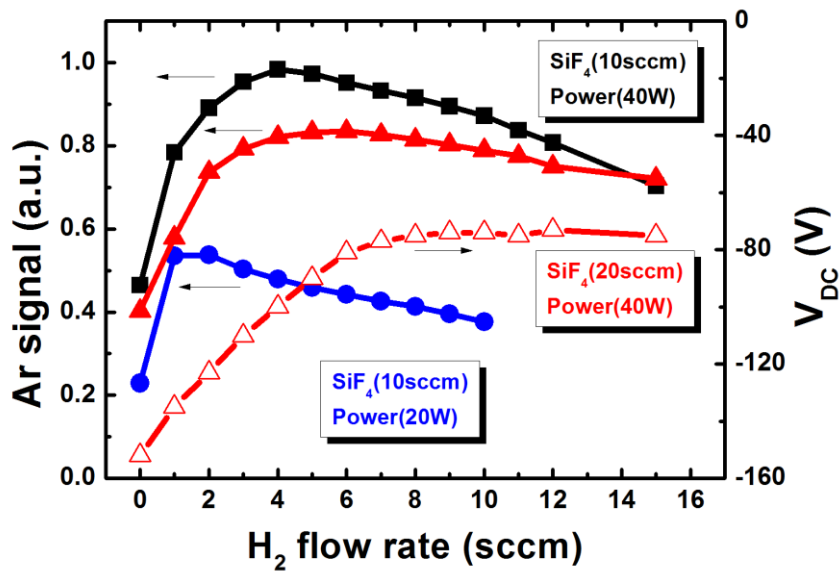


Figure 24: OES argon signal and  $V_{DC}$  as functions of the  $H_2$  flow rate for different plasma conditions.

In addition to this explanation, a remark can be raised based on the phenomenological model as well: the concentration of atomic fluorine decreases with the increase of the  $H_2$  flow rate. The fluorine is known to possess the highest electron affinity ( $SiF_4$  plasmas are known as electronegative discharges). Therefore the electron density of the plasma can be reduced by the formation of  $F^-$  anions. It might be possible that this effect takes place in our plasmas but that the electron attachment on nanoparticles presented above is stronger than electron attachment on  $F$  (the two having opposite trends in the  $H_2$  flow rate series).

### 2.3.5 Comparison with literature

Using our experimental results and our simple model to provide context, the abundant experimental results in the literature can now be coherently understood. In their early work [27], Ovshinsky and Madan reported on the deposition of amorphous a-Si:H,F films for an  $SiF_4/H_2$  ratio of 10/1, as expected from our model. Later on, they varied the  $SiF_4/H_2$  in the range of 10 to 99 [28] under a RF power of 50 W. One can reasonably assume that  $H_2$  was nearly fully depleted in their experiment conditions. Their plasma conditions would be equivalent to a low B and high A set of parameters. As seen on Figure 22, those kinds of values lead to a full consumption of  $H_2$  resulting in amorphous films, as reported by the authors.

In Shimizu's work [29], based on the use of a hydrogen radical enhanced CVD, the  $H_2$  flow rate was 30 sccm for microcrystalline deposition, whereas amorphous silicon was obtained at 10 sccm  $H_2$ . Since layers were amorphous at 10 sccm, at least 10 sccm of  $H_2$  were used to produce HF and growth precursors and, according to Figures 16 and 17a, one can expect that the depletion of the  $H_2$  was high. Then, the high growth rate ( $>20 \text{ \AA/s}$ ) can be understood under the assumption that the precursor contains one silicon atom, and that two  $H_2$  molecules are needed to react with one  $SiF_4$  to produce four HF molecules and one silicon atom. As 10 sccm were completely depleted to form HF and to deposit amorphous silicon, the plasma process should at least produce 5 sccm of growth precursors, consistent with the high deposition rate of 2 nm/s. Also, based on mass spectrometry studies, Shimizu's team proposed that the decomposition of  $SiF_4$  is greatly enhanced by addition of atomic hydrogen generated by a microwave plasma (and as we found in Figure 18, where SiF signal is enhanced at 1 sccm of  $H_2$  flow rate compared to the 0 sccm case). This observation can be compared to the model; in Figure 20, below the transition at  $B=40$ , the concentration of  $SiF_4$  is decreasing linearly with the addition of the hydrogen flow rate (B value). The formation of HF molecules is responsible for the scavenging of atomic F and consequently driving the dissociation of  $SiF_4$  to fulfill Equation (13).

Cicala, Capezzuto and Bruno reported on the amorphous and microcrystalline silicon growth from SiF<sub>4</sub>/H<sub>2</sub>/He gas mixtures [33][31]. Their model is based on a competition between deposition and etching. The promotion of crystalline phase was attributed to the etching of the amorphous phase by fluorine atoms. They found that by increasing the RF power, the deposition rate was increasing and the crystallinity was decreasing. Their results can be explained in the light of our model: by increasing the RF power and by keeping the H<sub>2</sub> flow rate constant, the A parameter is increased and the B parameter is constant (Figure 22). Therefore B/A is decreasing and the plasma condition shifts to amorphous deposition (Figure 21). As shown in Figure 22, to keep the crystallinity and increase the deposition rate, one should increase the RF power (parameter A) and compensate at the same time the increase of F concentration by scavenging it through the addition of the hydrogen. These authors compared the deposition rate and the crystallinity for two plasma excitation frequencies: 13.56 MHz and 75 MHz. The deposition rate at 75 MHz was three times higher than at 13.56 MHz, but the crystallinity was lower. This can be explained by a larger A value at 75 MHz as the dissociation is known to be enhanced by a high RF plasma excitation frequency. Therefore less crystallized films are expected at 75 MHz but at a higher deposition rate. Our phenomenological model is consistent with their results on the effects of the H<sub>2</sub> flow rate, the RF power, and the excitation frequency.

## 2.4 Transfer from PHILIX reactor to CLUSTER-PL8 reactor

### 2.4.1 Getting amorphous and microcrystalline films

Depositions from SiF<sub>4</sub>/H<sub>2</sub>/Ar plasmas were made in PHILIX reactor. Another reactor (chamber PL8 of a PECVD cluster tool, basically named CLUSTER) was available to grow intrinsic microcrystalline silicon from SiF<sub>4</sub> precursors. The geometry of the reactor is different: the RF electrode is larger and forms a square of 15x15 cm<sup>2</sup>. The direct transfer of plasma conditions from PHILIX reactor to CLUSTER-PL8 reactor was not successful as no deposition on glass was obtained. Many other attempts were unsuccessful.

The use of the RGA (Residual Gas Analyzer) was of precious help to understand such disappointing results. The first evaluation of the H<sub>2</sub> depletion reveals that we were far away from the transition (no more than 12% of depletion). Therefore the role of etching by atomic H was of paramount importance. Unfortunately the H<sub>2</sub> flow rate was already in the lower bound of the mass flow controller, meaning that it was not possible to play with the H<sub>2</sub> flow rate to come close to the transition. A H<sub>2</sub> flow rate series has been performed using the plasma conditions given by Table 5.

T <sub>HW</sub>	T <sub>RF</sub>	d <sub>i</sub>	Pr	SiF <sub>4</sub>	H <sub>2</sub>	Ar	Pw
(°C)	(°C)	(mm)	(Torr)	(sccm)	(sccm)	(sccm)	(W)
300	200	35	2	10	1→11	100	50

Table 5: Plasma conditions for the transfer from PHILIX to CLUSTER reactors.

The H<sub>2</sub> depletion and the H<sub>2</sub> consumption are displayed in Figure 25. The depletion is very high (above 90%) below 6 sccm and then decreases down to 50% at 11 sccm. This corresponds to a linear increase in the H<sub>2</sub> consumption below 6 sccm and then a constant consumption. This behavior is strictly similar to the one observed in PHILIX reactor as described in Figures 17a and 17b. Thus, the model is not specific to PHILIX reactor but, as expected, to the SiF<sub>4</sub>/H<sub>2</sub>/Ar chemistry. Moreover, two samples have been deposited at 6 sccm and 8 sccm. The one at 6 sccm was amorphous and the one at 8 sccm was microcrystalline: the amorphous-to-microcrystalline transition is around 7 sccm for our conditions. Again as in PHILIX reactor, microcrystalline layers are obtained when there is a H<sub>2</sub> flow rate excess compared to the H<sub>2</sub> consumption.

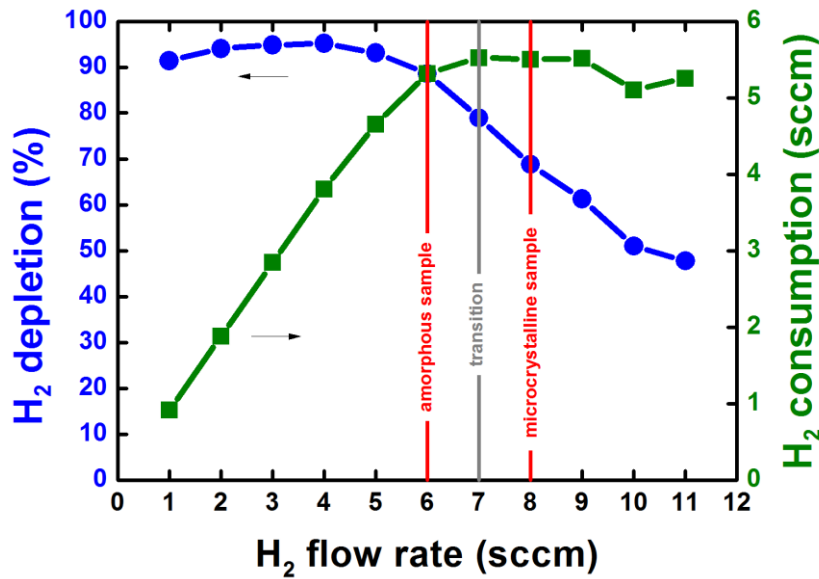


Figure 25: Depletion and consumption of H<sub>2</sub> as functions of the H<sub>2</sub> flow rate measured by RGA on CLUSTER-PL8 reactor.

Samples deposited at 6 sccm are amorphous, and those at 8 sccm are microcrystalline.

#### 2.4.2 Optimizing the H<sub>2</sub> consumption

From our model, we know that the deposition rate is given by the A parameter. Therefore if we want to increase the deposition rate, we should increase the A parameter value. Thanks to the RGA, this A parameter can be estimated: if H<sub>2</sub> flow rate is in excess, the H<sub>2</sub> consumption is constant and is equal to A/2 (but if the process is H<sub>2</sub> limited, the depletion is high and the consumption is approximately equal to the H<sub>2</sub> flow rate – or B). The factor 2 comes from the fact that in the model, one molecule of hydrogen can scavenge two F atoms and form two HF molecules. Therefore, after verifying that the depletion is not too high, the H<sub>2</sub> consumption is a good indicator of the deposition rate. As the measurement of the H<sub>2</sub> consumption is very fast – few minutes, the RGA is a very powerful tool to optimize our process conditions on the new CLUSTER-PL8 reactor allowing to save a significant amount of time.

##### i. Pressure series:

The pressure has been varied from 500 mTorr to 4 Torr and corresponding H<sub>2</sub> consumptions are displayed in Figure 26. The conditions are given in Table 6. At low pressure (500 mTorr) the consumption is around 2 sccm, and by increasing the pressure to 2 Torr, a consumption of 3.5 sccm is reached. By increasing even more the pressure, the consumption decreases down to 3 sccm. Thus, the pressure of 2 Torr is selected.

T <sub>HW</sub>	T <sub>RF</sub>	d <sub>i</sub>	Pr	SiF <sub>4</sub>	H <sub>2</sub>	Ar	Pw
(°C)	(°C)	(mm)	(Torr)	(sccm)	(sccm)	(sccm)	(W)
200	100	20	0.5→4	10	high	300	50

Table 6: Plasma conditions for the pressure series in the CLUSTER reactor.

##### ii. Ar flow rate series:

The easiest way to increase A parameter is by increasing the RF power, but other phenomena should be considered such as the material quality: high RF powers can be aggressive conditions to grow amorphous or microcrystalline layers. Therefore the RF power was fixed at 30 W, and an argon flow rate series was performed from the plasma conditions of Table 7.

$T_{HW}$	$T_{RF}$	$d_i$	Pr	SiF <sub>4</sub>	H <sub>2</sub>	Ar	Pw
(°C)	(°C)	(mm)	(Torr)	(sccm)	(sccm)	(sccm)	(W)
200	100	20	2	10	high	100→500	30

Table 7: Plasma conditions for the Ar flow rate series in the CLUSTER reactor.

The H<sub>2</sub> consumption is given in Figure 26 as a function of the Ar flow rate. The increase from 100 sccm to 300 sccm allows the H<sub>2</sub> consumption to increase from 1.8 sccm to 2.4 sccm. No more increase is obtained above 300 sccm up to 500 sccm.

iii. SiF<sub>4</sub> flow rate series:

A SiF<sub>4</sub> flow rate series has been carried out and H<sub>2</sub> consumptions are plotted in Figure 26. The plasma conditions are given in Table 8. At 5 sccm of SiF<sub>4</sub> flow rate, the H<sub>2</sub> consumption is as low as 1.5 sccm, but at 50 sccm the consumption is as high as 6 sccm. This high H<sub>2</sub> consumption is reached at the low power of 30 W, which is a little bit better than the maximal consumption of Figure 25 obtained with 50 W. We found here again that the A parameter is increasing with the SiF<sub>4</sub> flow rate, as in Figure 19.

$T_{HW}$	$T_{RF}$	$d_i$	Pr	SiF <sub>4</sub>	H <sub>2</sub>	Ar	Pw
(°C)	(°C)	(mm)	(Torr)	(sccm)	(sccm)	(sccm)	(W)
200	100	20	2	5→50	high	500	30

Table 8: Plasma conditions for the SiF<sub>4</sub> flow rate series in the CLUSTER reactor.

iv. RF power series:

Finally, irrespectively of material quality, the A parameter can be optimized by varying the RF power. A power series has been performed and is displayed in Figure 26 where the RF power was varied from 5 W to 40 W. The conditions are given in Table 9. At 40 W, a H<sub>2</sub> consumption of 7.5 sccm is reached.

$T_{HW}$	$T_{RF}$	$d_i$	Pr	SiF <sub>4</sub>	H <sub>2</sub>	Ar	Pw
(°C)	(°C)	(mm)	(Torr)	(sccm)	(sccm)	(sccm)	(W)
200	100	20	2.5	50	high	500	5→40

Table 9: Plasma conditions for the RF power series in the CLUSTER reactor.

All these series are easy and quick to perform. As an example, the four of them described above took less than 2 hours. The RGA was a valuable assistance for the transfer of SiF<sub>4</sub>/H<sub>2</sub>/Ar plasma from PHILIX reactor to CLUSTER-PL8 reactor. It allows the user to locate easily the transition and optimize the H<sub>2</sub> consumption (and the deposition rate). Starting from plasma conditions optimized that way, usual depositions should be performed to verify the deposition rate and to assess the quality of the material.

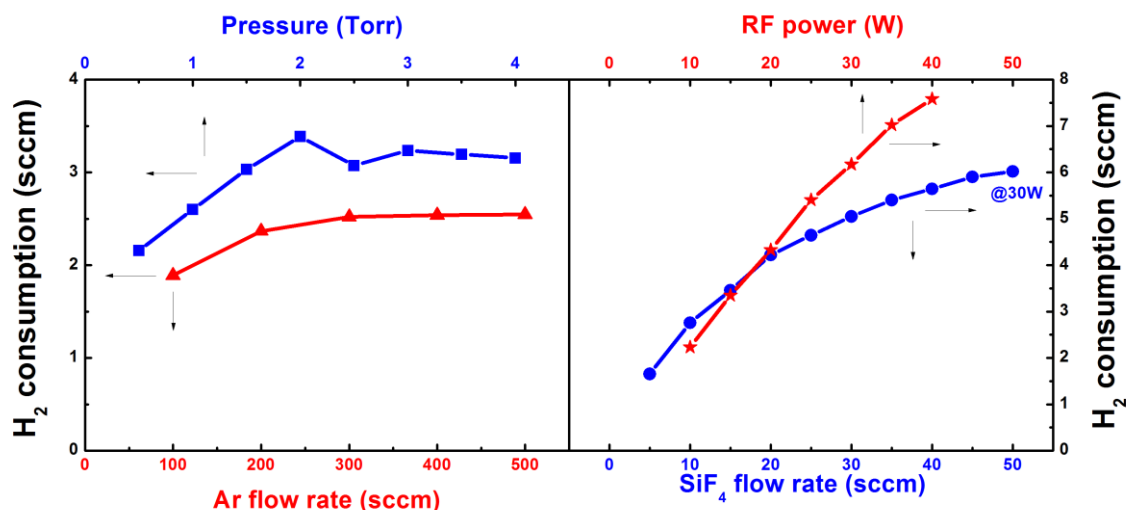


Figure 26: Optimization of the  $H_2$  consumption as a function of the Ar flow rate, the  $SiF_4$  flow rate, the RF power and the pressure.

### 2.4.3 $SiF_4$ consumption

We have shown that 50 sccm of  $SiF_4$  allow a high  $H_2$  consumption. By increasing the  $SiF_4$  flow rate and keeping all other parameters constant, the partial pressure of  $SiF_4$  increases. Therefore the probability of a free electron colliding and dissociating a  $SiF_4$  molecule increases, which could explain the increase of the  $H_2$  consumption. However, which amount of  $SiF_4$  is really dissociated by the plasma? The answer is given by the consumption of the  $SiF_4$ , defined similarly to the  $H_2$  consumption (Equations (7) & (8)).

In order to estimate the  $SiF_4$  consumption, one should know at which mass-to-charge ratio the  $SiF_4$  should be detected. Figure 27 shows the QMS signal as a function of the mass-to-charge ratio (up to 110 amu) in a  $SiF_4/H_2/Ar$  gas mixture (there is no plasma, just gas). The electron energy of the ionization stage of the QMS is set at 70 eV. Many ions are detected:  $H_2^+$  at 2 amu,  $Ar^+$  at 40 amu, and especially  $SiF_3^+$  at 85 amu and  $SiF_4^+$  at 104 amu.

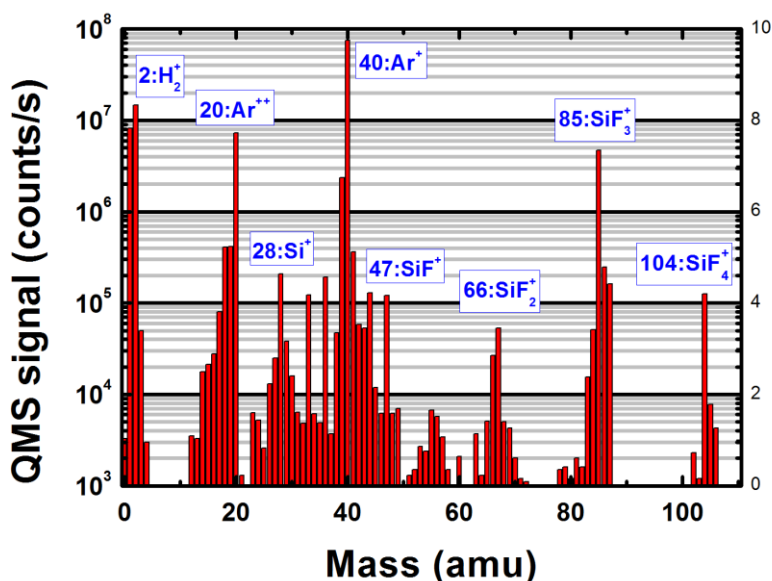


Figure 27: QMS signal at different mass-to-charge ratio in a  $SiF_4/H_2/Ar$  gas mixture.

The  $SiF_4^+$  ions are produced via Equation (27) representing the ionization of a  $SiF_4$  molecule. When the plasma is on, only  $SiF_4$  molecules can contribute to the signal at 104 amu. However the signal at

85 amu is much higher (by more than one order of magnitude). This is the advantage of the  $\text{SiF}_3^+$  signal; its drawback is the non-uniqueness of the reaction leading to this ion. What is detected at 85 amu in Figure 27 only comes from Equation (28) (or similar to, one can imagine that the atomic fluorine is negatively charged and only one electron is present as a byproduct instead of two). When the plasma is on, new species can be created within the plasma. It is worth mentioning that usually fluorinated radicals can have a long life time value and therefore can travel a few meters. The RGA is plugged outside the plasma, but such radical can reach the equipment. For example, by considering a neutral  $\text{SiF}_3$  radical arriving in the ionization stage of the RGA, one could obtain a  $\text{SiF}_3^+$  ion through Equation 29 which is simply the ionization of  $\text{SiF}_3$ . As a result, it is not possible to know the reaction pathway of a detected  $\text{SiF}_3^+$  ion at 85 amu. Indeed, in some plasma conditions, an increase in the signal at 85 amu has been detected when the plasma has been started. To summarize, to calculate the  $\text{SiF}_4$  depletion the signal at 104 amu should be monitored by RGA. Similarly, the  $\text{SiF}_4$  consumption can be computed from the  $\text{SiF}_4$  depletion.



For different plasma conditions,  $\text{SiF}_4$  consumptions have been calculated. They are plotted as a function of their corresponding  $\text{H}_2$  consumption in Figure 28. A linear correlation between  $\text{SiF}_4$  and  $\text{H}_2$  consumptions are found, which is in good agreement with the phenomenological model. More interestingly, the slope seems to be close to 1, i.e. that 3 sccm of  $\text{H}_2$  consumption corresponds to 3 sccm of  $\text{SiF}_4$  consumption. For example, in the  $\text{SiF}_4$  flow rate series in Figure 26, by increasing the  $\text{SiF}_4$  flow rate up to 50 sccm, an  $\text{H}_2$  consumption of 6 sccm was obtained. Therefore the  $\text{SiF}_4$  consumption should be 6 sccm as well, meaning that 44 sccm of  $\text{SiF}_4$  is wasted through the pumping.

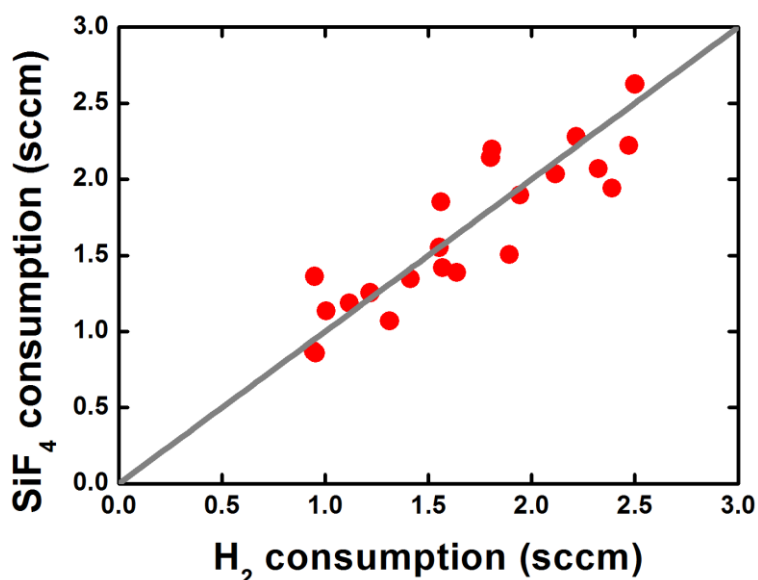


Figure 28:  $\text{SiF}_4$  consumption versus  $\text{H}_2$  consumption.

A linear correlation is found in agreement with the phenomenological model.

## 2.5 Chapter key results

We have demonstrated in this chapter that the  $\text{SiF}_4/\text{H}_2/\text{Ar}$  plasmas could be simplified by three kinetic equations forming our “phenomenological model”. The main event happening in such fluorinated chemistry, and distinguishing  $\text{SiF}_4/\text{H}_2/\text{Ar}$  plasmas from  $\text{SiH}_4/\text{H}_2$  plasmas, is the formation of HF molecules. The dissociation of  $\text{SiF}_4$  produces atomic fluorine which is scavenged by molecular hydrogen to form HF. The role of argon has been clearly identified: argon helps the dissociation of  $\text{SiF}_4$ . Two plasma regimes have been brought to light:

- **H<sub>2</sub>-limited regime** where the formation of HF is hindered by a low concentration of available hydrogen (high depletion of  $\text{H}_2$  flow rate). Atomic fluorine is in excess.
- **F-limited regime** where the formation of HF is hindered by a low concentration of available atomic fluorine (and thus by the dissociation of  $\text{SiF}_4$ ).  $\text{H}_2$  is in excess.

The amorphous-to-microcrystalline transition corresponds exactly to the frontier between  $\text{H}_2$ -limited regime and F-limited regime. Only in the F-limited regime, the atomic hydrogen is in excess on the substrate surface and sub-surface leading to the growth of microcrystalline silicon. In addition to the amorphous-to-microcrystalline transition, the deposition rate of the silicon films depends linearly on the  $\text{H}_2$  flow rate when the process is  $\text{H}_2$ -limited (and amorphous silicon is obtained) and does not depend on the  $\text{H}_2$  flow rate when the process is F-limited (and microcrystalline silicon is obtained). Conversely, in the  $\text{H}_2$ -limited regime, the growth rate does not depend on the RF power and in F-limited regime the growth rate does depend on the RF power. The phenomenological model summarizes the main lessons learnt throughout this chapter: it clarifies the close relationships between deposition rate, amorphous-to-microcrystalline transition, HF formation,  $\text{H}_2$  flow rate and RF power.

The phenomenological model has been experimentally verified on PHILIX reactor, however it occurred to be also valid on other PECVD reactors like CLUSTER, and it has developed into a powerful tool to transfer the  $\text{SiF}_4/\text{H}_2/\text{Ar}$  plasma process conditions between these reactors. Many tools could be used to perform the transfer: the Residual Gas Analyzer (which is an easier one), the Optical Emission Spectroscopy, and electrical measurements such as  $V_{\text{DC}}$ .

Beyond the simple phenomenological model, the fact is that our plasmas are dusty. This calls for a specific study of plasma-generated nanoparticles, which is the purpose of the next chapter.

# 3. Plasma-generated nanoparticles

## Contents

---

<b>3.1 Plasma studies.....</b>	<b>56</b>
3.1.1 Effect of gas temperature.....	56
3.1.2 Early stage of deposition .....	58
3.1.3 Metallic grid.....	61
<b>3.2 Effect of pressure and inter-electrode distance.....</b>	<b>64</b>
3.2.1 Inter-electrode distance series.....	64
3.2.2 Where is my silicon? .....	67
3.2.3 Dust model.....	68
3.2.4 Geometrical model .....	69
3.2.5 P-di series for different plasma conditions.....	71
3.2.6 Pros and cons of dust and geometrical models.....	74
3.2.7 Perspectives.....	75
<b>3.3 Surface versus plasma crystallization.....</b>	<b>76</b>
3.3.1 Beyond the phenomenological model .....	76
3.3.2 Crystallization of plasma-generated nanoparticles .....	77
3.3.3 Mapping of plasma-generated nanoparticle crystallinity .....	78
3.3.4 Morphology of nanoparticles .....	88
<b>3.4 Self-sustained plasma oscillations .....</b>	<b>90</b>
3.4.1 Overview.....	90
3.4.2 Detailed analysis of the OES oscillations .....	92
3.4.3 Toy model .....	96
3.4.4 Forced oscillations .....	102
<b>3.5 Chapter key results .....</b>	<b>103</b>

---

### 3.1 Plasma studies

#### 3.1.1 Effect of gas temperature

The effect of the gas temperature ( $T$ ) has been studied by carrying out depositions on glass substrates where the pressure ( $P$ ) and/or gas density ( $n$ ) have been changed. The deposition time was fixed at 30 min and the film thickness was estimated by spectroscopic ellipsometry. The RF power was kept at 20 W. One could easily admit that the increase of  $P$  or  $n$  will increase the deposition rate. However according to ideal gas law (Equation (30)) a modification in  $T$  will automatically change either  $P$  or  $n$ . The gas temperature is controlled by  $T_{RF}$  and the substrate temperature is kept constant at 150°C because the deposition rate may depend on the surface temperature. The gas is injected through a shower head in the RF electrode. Therefore we do the approximation that the gas temperature is given by  $T_{RF}$ .

$$P \cdot V = n \cdot R \cdot T \quad (30)$$

Our purpose when studying the effect of gas temperature on the deposition of microcrystalline silicon is to know if there is an intrinsic effect of temperature, which is different of simply increasing  $P$  or  $n$ . To answer this question and to overcome the issue of  $P$ ,  $n$ , and  $T$  being linked by Equation (30), three series of samples have been studied as described below.

- Increase of the total pressure at constant gas temperature (200°C):

In this series, we study the effect of the total pressure from 1 Torr to 3.8 Torr by keeping the gas temperature at 200°C. The plasma conditions are given in Table 10.

$T_{sub}$ (°C)	$T_{RF}$ (°C)	$d_i$ (mm)	$P_r$ (Torr)	$SiF_4$ (sccm)	$H_2$ (sccm)	$Ar$ (sccm)	$P_w$ (W)	$t_d$ (sec)
150	200	10	1→3.8	3.6	5.3	88	20	1800

Table 10: Plasma conditions for pressure series at constant  $T_{RF}$ .

- Decrease of the gas temperature at constant pressure (3.8 Torr):

The gas temperature has been decreased from 200°C to 50°C and the pressure has been kept constant at 3.8 Torr. The plasma conditions are given in Table 11.

$T_{sub}$ (°C)	$T_{RF}$ (°C)	$d_i$ (mm)	$P_r$ (Torr)	$SiF_4$ (sccm)	$H_2$ (sccm)	$Ar$ (sccm)	$P_w$ (W)	$t_d$ (sec)
150	50→200	10	3.8	3.6	5.3	88	20	1800

Table 11: Plasma conditions for the  $T_{RF}$  series at constant pressure.

- Decrease of the gas temperature at constant gas density ( $7 \times 10^{16} \text{ cm}^{-3}$ ):

The gas temperature has been decreased from 200°C to 50°C and the gas density has been kept constant at  $7 \times 10^{16} \text{ cm}^{-3}$ . For each gas temperature, the pressure has been adjusted: the decrease of the gas temperature down to 50°C leads to the decrease of the pressure down to 2.35 Torr. The reference is the gas density at 200°C and 3.8 Torr. The plasma conditions are given in Table 12.

$T_{\text{sub}}$	$T_{\text{RF}}$	$d_i$	$P_r$	$\text{SiF}_4$	$\text{H}_2$	$\text{Ar}$	$P_w$	$t_d$
(°C)	(°C)	(mm)	(Torr)	(sccm)	(sccm)	(sccm)	(W)	(sec)
150	50	10	2.35	3.6	5.3	88	20	1800
	100		2.71					
	150		3.07					
	200		3.44					

Table 12: Plasma conditions for the  $T_{\text{RF}}$  series at constant gas density ( $7 \times 10^{16} \text{ cm}^{-3}$ ).

The inter-electrode distance has been set to 1 cm. As explained later in this chapter, the deposition rate depends on the product  $P \cdot d_i$  and a decrease in  $D_r$  is found above 6 Torr·cm. Above this value, potentially more complex mechanisms can take place such as negatively charged nanoparticles confinement and dust formation. As a precautionary measure, for this study we want to stay below this critical value.

Figure 29 shows the deposition rate as a function of the gas density (a), and as a function of the pressure (b). For the first series (in blue, full squares), the temperature is fixed at 200°C and the growth rates are small: from 1 Torr to 3.8 Torr,  $D_r$  increases from 0.2 Å/s to 0.5 Å/s. Concerning the second series (red full circles), the increase of gas temperature has a strong and beneficial impact. A deposition rate of 2.8 Å/s is obtained at 50 °C compared to 0.5 Å/s at 250 °C. One could argue that this increase is due to the increase of the gas density: it increases from  $7 \times 10^{16} \text{ cm}^{-3}$  at 250°C to  $11.3 \times 10^{16} \text{ cm}^{-3}$  at 50°C. However one should notice that the gas density has increased by less than a factor of 2 while the deposition rate increases by more than a factor of 5. Thus, high  $D_r$  cannot just be explained by gas density. Another way to demonstrate this point is to keep gas density constant, which is the purpose of the third series (green open circles). Moreover, by decreasing  $T$ , at constant gas density, the pressure is decreased. Nevertheless  $D_r$  increases from 0.5 Å/s at 200°C to 1.0 Å/s at 50°C.

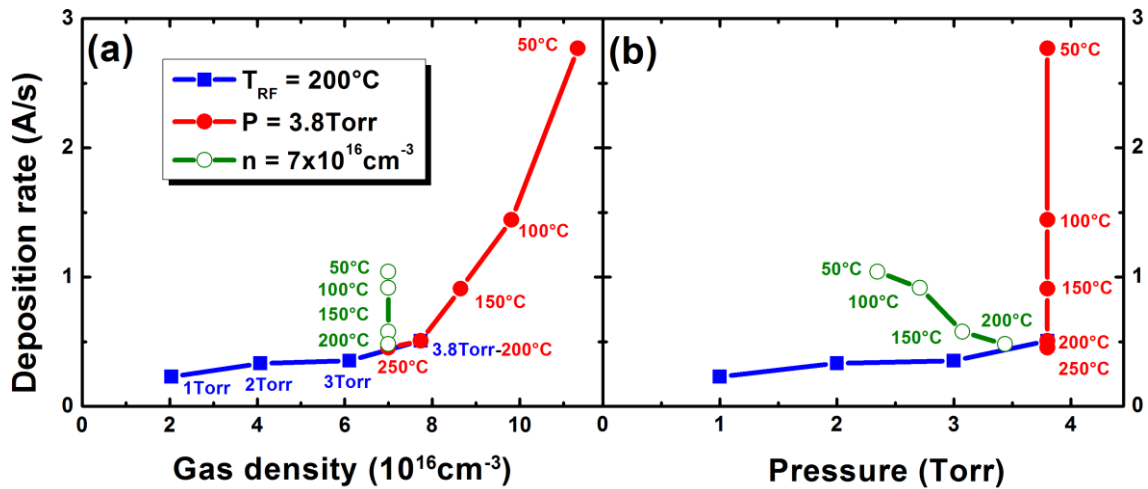


Figure 29: Deposition rate as a function of gas density (a) and pressure (b) for gas temperature series. The decrease of gas temperature favors high deposition rates.

Since neither  $P$  nor  $n$  explains the raise of  $D_r$  with the lowering of  $T$ , we turn into the contribution of plasma-generated nanoparticles to the growth rate. Low temperature could favor the nanoparticle growth and thus explain the effect of gas temperature. The nucleation of nanoparticles has been studied in  $\text{SiH}_4/\text{Ar}$  plasmas by the GREMI group [50][51][52]. The particle formation has been reported to be hindered by increasing the gas temperature. Therefore the statement of the nanoparticle contribution to the growth is consistent with our increase of  $D_r$  in the second and the third series. By forming a high density ( $\approx 10^{10} \text{ cm}^{-3}$ ) of nanoparticles, the plasma shifts from the  $\alpha$ -regime to the  $\gamma$ -regime, and the coupled RF power in the plasma has been reported to increase in dusty condition [53].

It should be mentioned that there is a gradient in temperature between the substrate (fixed at 150°C) and the RF electrode (varied from 50°C and 200°C). It has been reported in [54] that thermophoresis force resulting from the gradient of temperature pushed nanoparticles to low temperature surface. In our experiment, when  $T_{RF}$  is set to 200°C, the force is directed towards the substrate electrode, whereas when  $T_{RF}$  is set to 50°C, the force is directed towards the RF electrode. Therefore, a higher deposition rate was expected at 200°C than at 50°C. To our surprise, despite the possible thermophoresis force, the trend is just the opposite: the delay of the nanoparticle formation is dominant.

### 3.1.2 Early stage of deposition

The early stage of the growth has been studied by in-situ spectroscopic ellipsometry: the plasma has been switched on during a certain time, then it is switched off in order to perform spectroscopic ellipsometry measurement. This procedure has been repeated (every 30 s at the beginning) and for each deposition time, the thickness and the composition of film have been estimated from the fitting of ellipsometry spectrum. The process conditions are given in Table 13 and thicknesses and void fractions of the film are displayed in Figure 30.

$T_{sub}$	$T_{RF}$	$d_i$	$P_r$	$SiF_4$	$H_2$	$Ar$	$P_w$
(°C)	(°C)	(mm)	(Torr)	(sccm)	(sccm)	(sccm)	(W)
150	100	30	3.8	3.6	12	88	20

Table 13: Plasma conditions for the study of the early stage of the deposition.

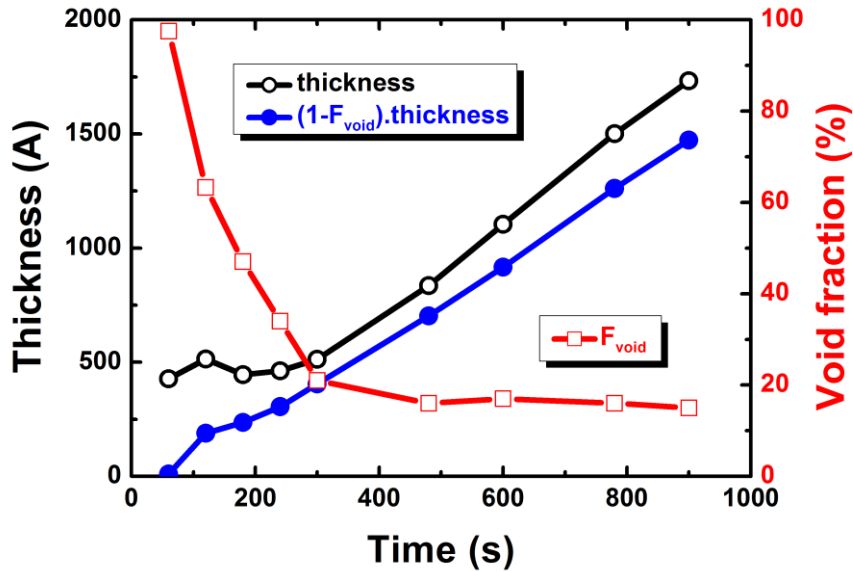


Figure 30: Thickness and void fraction as a function of the deposition time. The incubation time is 60 s and the layer is porous until 300 s. The growth rate is 2 Å/s.

Between 60 s and 300 s, the void fraction is high and decreases with time. At the beginning, the film is porous and becomes denser with time. After 300 s, the thickness increases with a slope (growth rate) of 2 Å/s and the void fraction stays around 20%. One can exclude this void fraction from the thickness by saying that only 80% of the nominal thickness is constituted of silicon. Therefore the thickness corrected from the void fraction is displayed in Figure 30 in blue. This notion of corrected thickness does have a meaning below 300 s: the quantity of deposited silicon is directly linked to this value and increases linearly above 60 s, irrespectively of the porous/dense transition occurring at 300 s. From this corrected thickness curve, we can clearly see that the incubation time is 60 s, which cannot be detected in the nominal thickness curve.

The ellipsometry spectrum (real and imaginary parts of the pseudo-dielectric function) of the layer deposited after 120 s is displayed in Figure 31. The two inflexion points found at 3.4 eV and 4.2 eV are

the signature of a crystalline material. Only microcrystalline and void materials are used to fit all the ellipsometry spectra corresponding to the data points in Figure 30 (from 60 s to 900 s). Indeed, given the high H<sub>2</sub> flow rate used for this series (12 sccm), a high concentration of atomic H is available at the substrate surface. Atomic H is responsible for the high incubation time and can explain why from the earliest stage of the growth, the silicon is found in crystalline phase.

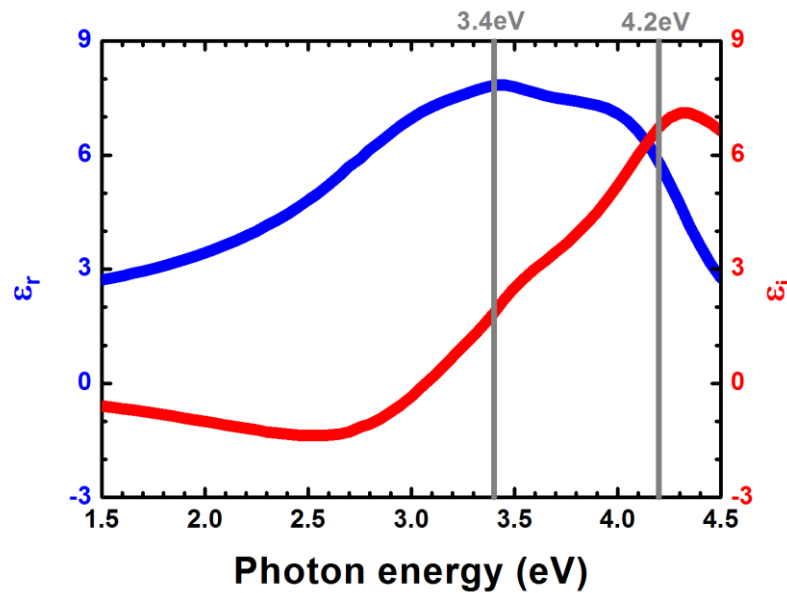


Figure 31: Real and imaginary parts of the pseudo-dielectric function measured by spectroscopic ellipsometry after 120 s of deposition.

Crystalline signatures are found around 3.4 eV and 4.2 eV.

In order to analyze the plasma-generated nanoparticles, a short deposition of 1 min has been done. The deposition conditions were such that the incubation time of the microcrystalline growth was high. To do so, a high H<sub>2</sub> flow rate of 15 sccm has been chosen. A high RF power of 50 W has been used to generate a high density of nanoparticles. The plasma conditions are given in Table 14. As shown in Figure 30, incubation time can be of the order of 1 min and more than 5 min could be required to obtain a dense film. At 15 sccm of H<sub>2</sub>, the situation is similar to 12 sccm. A TEM copper grid laid on the glass substrate was used to collect the plasma-generated nanoparticles as well as to characterize the nanoparticles using TEM in the bright field mode, which is displayed in Figure 32. A sparse distribution of nanoparticles is found with sizes below 30 nm. Moreover large aggregates with diameters of about 100 nm are also observed.

T <sub>sub</sub>	T <sub>RF</sub>	d <sub>i</sub>	Pr	SiF <sub>4</sub>	H <sub>2</sub>	Ar	Pw	t <sub>d</sub>
(°C)	(°C)	(mm)	(Torr)	(sccm)	(sccm)	(sccm)	(W)	(sec)
150	100	35	3.8	3.3	15	88	50	60

Table 14: Plasma conditions for study of nanoparticles by TEM image.

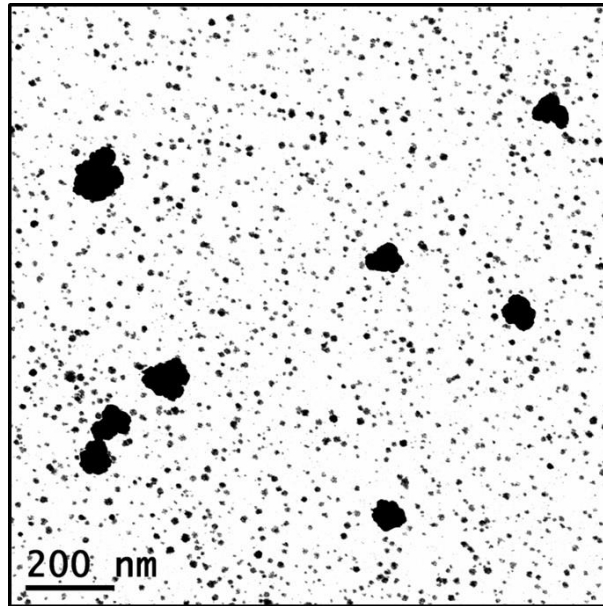


Figure 32: Bright field TEM image of plasma-generated nanoparticles collected on a copper grid after a discharge of 60 s.

The question of the origin of those nanoparticles and aggregates is of importance. Four alternatives are likely to happen:

- a. While the plasma is on, plasma-generated particles reach the substrate and stick to it.
- b. During the plasma and at time around the incubation time, growth seeds appear, are randomly distributed and their growth is determined by radicals (or by plasma-generated nanoparticles which is equivalent to (a)).
- c. When the plasma is turned off, all plasma-generated particles are allowed to stick on the substrate.
- d. Particles behave as dust, and reach the TEM grid thanks to convection (when plasma is off or simply when the chamber vacuum is broken for unloading the substrate).

For the aggregates, only hypotheses (c) and (d) can be considered because such large particles are inevitably negatively charged in the plasma and the plasma sheath above the substrate acts as a barrier. Precisely, by being trapped within the plasma, these particles have time to grow to become aggregates of 100 nm. Concerning nanoparticles, if hypothesis (b) is true, another 100 s will be sufficient to completely cover the surface, because, based on the plasma conditions, the deposition rate is  $2 \text{ \AA/s}$  (see Figure 23 at 50 W) and the typical distance between two seeds in Figure 32 is roughly 40 nm. Therefore during 100 s thanks to lateral growth, seeds will percolate and form a uniform and dense film. It is the reason why we discard the second hypothesis (b). Finally, both (a) and (c) predict that nanoparticles seen in Figure 32 are coming from the plasma.

These nanoparticles are plasma-generated and their diameter distribution is given in Figure 33b (an automatic graphical algorithm is used to detect and count each nanoparticle, except the aggregates). Their typical size is 6 nm but their number is decreasing with their size. Diameters up to 26 nm have been found. No nanoparticles are detected below 4 nm because of the limit of the detection technique (HR-TEM should be used to go below this size). From the diameter one can calculate the number of silicon atoms contained in one nanoparticle, as computed in Figure 33a. Then the number of silicon atoms deposited in 60 seconds (in Figure 32) as a function of the nanoparticle diameter can be estimated and is displayed in Figure 33b on the right axis in blue. Small nanoparticles (below 10 nm) are numerous but bring few silicon atoms to the surface. Large nanoparticles (above 20 nm) bring a lot of atoms but their number is low. The highest number of silicon atoms is brought by nanoparticles of

15 nm, which is the good balance between their number and their contribution in silicon atoms per unit of nanoparticle.

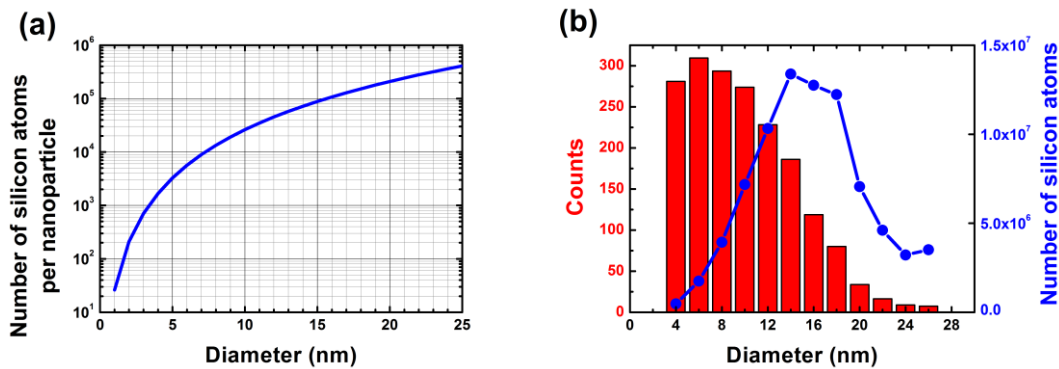


Figure 33: (a) Number of silicon atoms per nanoparticle as a function of the nanoparticle diameter. (b) Diameter distribution of nanoparticles seen in Figure 32 and the total number of silicon atoms as a function of the diameter.

The diffraction pattern of nanoparticles of Figure 32 shows that they are crystallized. Plasma-generated nanoparticles can be amorphous or crystalline. However in our plasma conditions the concentration of atomic H is high and surface crystallization can account for the crystalline nanoparticles seen in Figure 32.

Let us now estimate the contribution of nanoparticles to the deposition. A 5 nm diameter contains 3000 silicon atoms (see Figure 33a). Therefore the sticking of one such nanoparticle is three thousand times more efficient (in terms of deposition rate) than the sticking of a single radical to the growth surface. Of course the density of nanoparticles and radicals is not the same, but what matters is the number of silicon atoms. Moreover, the growth of nanoparticles in the plasma phase happens much faster than the deposition rate in the surface [55], starting by the higher temperature of nanoparticles in the case of a plasma phase growth [56][57][58]. From Figure 33b, very rough estimations can be done in the extreme cases that only hypothesis (a) is true or only hypothesis (c) is true.

- In the case of all nanoparticles stuck during the plasma discharge: from Figures 33a & 33b, one can estimate the total number of silicon atoms contained in the nanoparticles (aggregates excluded) at  $8 \times 10^7$  on the  $1.4 \times 1.4 \mu\text{m}^2$  area of Figure 32. By assuming a constant flux of incoming nanoparticles over the 60 s of deposition time, one can get that corresponding deposition rate is  $0.5 \text{ \AA/s}$  (density of silicon:  $5 \times 10^{22} \text{ at./cm}^3$ ). However the deposition rate is  $2 \text{ \AA/s}$ . Based on this rough estimation, 25 % of the deposition rate can be attributed to nanoparticles of diameter above 4 nm.
- In the case of all nanoparticles stuck just after the shutdown of the discharge: the total number of nanoparticles in Figure 32 is approximately 2000 for a surface of  $2 \mu\text{m}^2$ . The surface density of nanoparticles is then  $10^{11} \text{ cm}^{-2}$ . By neglecting the pumping after the plasma discharge and assuming that all nanoparticles in the volume ( $236 \text{ cm}^3$ ) are stuck uniformly on all the available surface ( $250 \text{ cm}^2$ ), the volume density of nanoparticles necessary to account for the surface density is  $1.1 \times 10^{11} \text{ cm}^{-3}$ . This value is above the electron density but is consistent with the literature [48].

The reality is of course more complex. However these simple calculations lead to coherent values. To summarize, our results are consistent with nanoparticles generated from the plasma phase. They play the crucial role of being the growth seeds in the early stage of the deposition.

### 3.1.3 Metallic grid

Large nanoparticles have a high probability to be negatively charged (mainly because the mobility of electrons is much higher than that of positive ions). Then by being negatively charged they cannot cross the plasma sheath and are trapped in the plasma bulk. Finally by being trapped they have a long residence time and can become larger and larger until being pumped. The pumping occurs through

four holes of 1 cm diameter drilled into the plasma confinement box (two for the in-situ ellipsometer beam and another two for OES measurements). There is a small pumping slit around the substrate holder but it can be neglected with respect to the size of the drilled holes.

In order to obstruct the pumping of negatively charged nanoparticles, a metallic grid can be installed in the holes to create a sheath above the mesh. The mesh pitch is 1 mm. It should be metallic such that the grid is grounded. A fine mesh will be efficient to trap negative species and a coarse one will be less efficient: pumping will be slowed but it will let some nanoparticles pass through the grid. We used a metallic grid with square gap of  $1 \times 1 \text{ mm}^2$ , which covers the cylindrical plasma confinement box. Figure 34a shows the grid installed on PHILIX reactor. The picture has been taken after a deposition. The yellow-orange parts are located exactly above the pumping holes (here corresponding the OES hole at the front (left in the picture) and the ellipsometer hole at the back (right in the picture)). Depositions on the holes are yellowish and are different from deposition on the rest of the grid (where there is no gas drag). The gas flow drags large nanoparticles through the holes and inevitably to the mesh. A glass substrate has been put just behind the grid covering the OES hole such that the gas drag is still occurring through this hole. The deposition on this substrate is shown in Figure 34b (the word "deposition" should be used here with caution because the adhesion is weak and particles only lay on the substrate). Individual spots are observed spaced of 1 mm in one direction (vertical on the picture) and elongated in the direction of the gas flow (horizontal on the picture). This picture shows that the mesh slows the pumping of the nanoparticles. But that the pumping occurs in the interstices of the mesh. Moreover, when the grid is installed, the pumping around the substrate holder is no more negligible and nanoparticles escape through this pumping direction: yellowish deposition is found around the substrate holder.

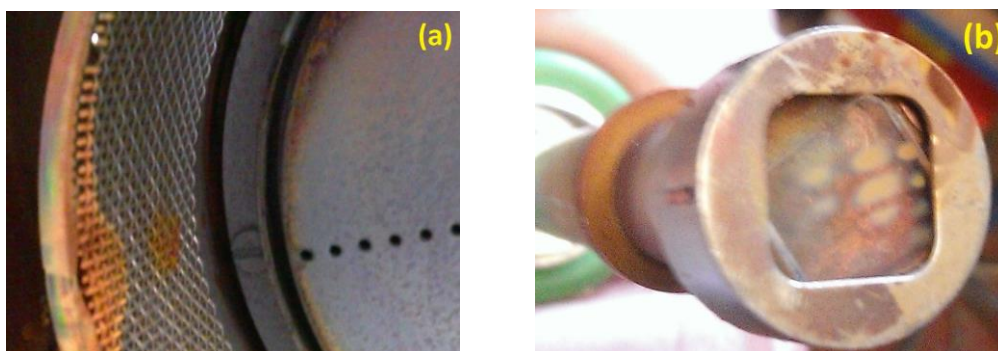


Figure 34: (a) Metallic grid and (b) deposition behind the pumping holes and the grid.

When the RF power is switched off, sheaths disappear and all nanoparticles can reach the substrate. Large nanoparticles are detectable by AFM and if they stick after the discharge, a non uniform layer is expected with a rather sparse distribution of particles. Let us compare the surface morphology of the layers deposited in exactly the same plasma conditions but one with the metallic grid to be compared to the other one without the mesh installed. In order to facilitate the comparison, amorphous conditions have been chosen instead of microcrystalline because roughness is known to be lower. Plasma conditions are given in Table 15. Figure 35a shows the surface morphology of the substrate when no mesh was installed. The surface is relatively flat (below 5 nm of variation) despite few particles randomly distributed. The surface morphology when the mesh is installed is displayed in Figure 35b where the background is flat (below 5 nm of variation) but where an important distribution of particles (laying on top of an amorphous layer) is found. Those particles are attributed to the ones trapped by plasma sheath and which have been deposited just after the stopping of RF power.

$T_{\text{sub}}$	$T_{\text{RF}}$	$d_i$	Pr	$\text{SiF}_4$	$\text{H}_2$	Ar	Pw	$t_d$
(°C)	(°C)	(mm)	(Torr)	(sccm)	(sccm)	(sccm)	(W)	(sec)
150	100	30	3.8	10	2	88	40	600

Table 15: Plasma conditions the metallic grid study.

A typical particle has been chosen in Figure 35b and its profile is plotted in Figure 36a (in red). The level of the background is at 10 nm and the pinnacle of the particles at 30 nm, leading to a height of 20 nm. Under the assumption that particles are spherical with a 20 nm radius, the theoretical profile should have a lateral dimension twice the vertical dimension (shown in blue in Figure 36a). The lateral difference the blue and the red curve is explained by the measurement technique: the AFM profile is the convolution of the surface morphology with the tip morphology. Indeed the size of the AFM tip is few tens of nanometers so that a lateral morphology of a 20 nm size particle cannot be resolved. The height distribution of particles of Figure 35b has been calculated and is displayed in Figure 36b. The mean height is 20 nm but small particles are also detected.

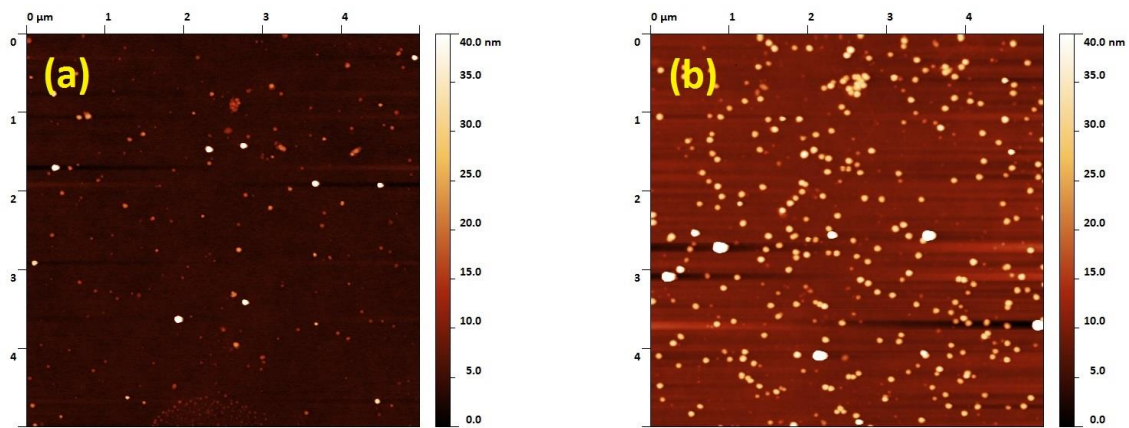


Figure 35: Surface morphology of samples (a) without and (b) with the metallic grid. A relatively flat surface is found for the sample deposited without and a sparse distribution of nanoparticles is obtained with the mesh.

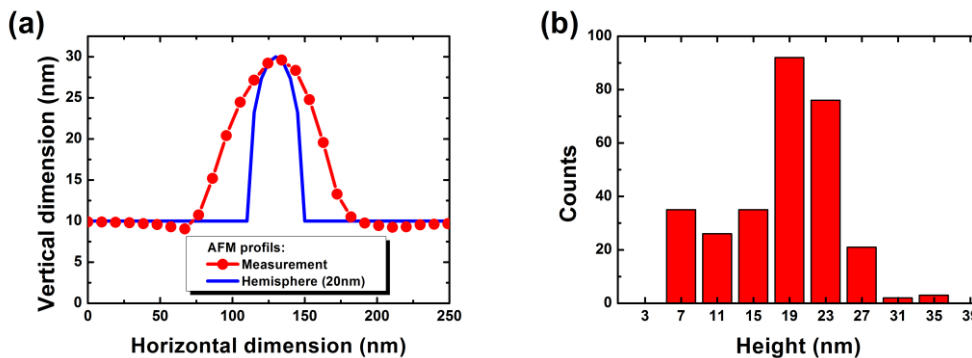


Figure 36: (a) AFM profile of one particle of Figure 35b; (b) Height distribution of the particles of Figure 35b.

The two films have been characterized by ellipsometry. The optical model for the fit consists of three layers: the glass substrate, the amorphous bulk and the roughness. The fitting results are given in Table 16.

(a) without grid				(b) with grid			
Roughness	10 Å	a-Si:H 50%	void 50%	Roughness	22 Å	a-Si:H 50%	void 50%
Bulk	306 Å	a-Si:H		Bulk	417 Å	a-Si:H	
Substrate	1 mm	Glass		Substrate	1 mm	Glass	

Table 16: Optical model deduced from ellipsometry for samples with and without the grid.

The deposition rate of the sample without the grid is 0.5 Å/s while it is 0.7 Å/s with the grid. The increase in the deposition rate can be understood by the formation of larger particles. Neutral particles can be pumped through the mesh. However particles can encounter charge fluctuation, and in particular negatively charged. These charged nanoparticles cannot be pumped through the mesh and their residence time are increased. The presence of the mesh fosters the formation of nanoparticles and therefore the deposition rate. It should be noted that the roughness is higher with the mesh than without. However the density of particles seen on Figure 35b is too small to contribute significantly to the roughness in the ellipsometry model.

It should be mentioned that in the presence of the metallic grid, self-sustained oscillations of  $V_{RF}$  have been observed despite their small amplitude (less than 1 V of the average  $V_{RF}$  of 100 V). The period was about 3 seconds. Self-sustained oscillations will be presented in another section of this chapter. The number of particles detected in Figure 35b is about 300. The area of AFM picture is 25  $\mu\text{m}^2$  leading to a surface density of  $1.2 \times 10^9 \text{ cm}^{-2}$ . By assuming that after the plasma extinction, all nanoparticles of the volume (236  $\text{cm}^3$ ) stick uniformly on all the surface (250  $\text{cm}^2$ ), an estimate of the particles volume density can be made. The large nanoparticles density is then  $1.3 \times 10^9 \text{ cm}^{-3}$ . This value is in order of magnitude of electron density. The probability of electron attachment on large nanoparticles (10-20 nm) is very high. The estimate of a large particles density is consistent with the plasma transition from  $\alpha$  regime to  $\gamma'$  regime [48].

The main conclusion from the metallic grid experiment is that negatively charged nanoparticles are trapped within the plasma where they can continue to grow bigger until being irretrievably pumped through the pumping holes of the plasma confinement box. Such a situation should be avoided because the deposition rate decreases and the waste of silicon precursors increases.

## 3.2 Effect of pressure and inter-electrode distance

### 3.2.1 Inter-electrode distance series

The geometry of the plasma chamber can be easily modified by translating the RF electrode with respect to the substrate holder, thus changing the inter-electrode distance (named " $d_i$ "). The plasma confinement box being grounded (like the substrate holder) the asymmetry of the plasma depends significantly on  $d_i$ . The RF electrode and the substrate holder are circular with a diameter of 10 cm and an area of 78.5  $\text{cm}^2$  (named " $A_{RF}$ "). The grounded electrode is composed of the substrate holder and of the lateral surface of a cylinder. Its base is  $A_{RF}$ , its height is  $d_i$ , and its area is named " $A_{GND}$ ". The following table shows the increase of the asymmetry with the increase of  $d_i$  from 5 mm to 45 mm. The asymmetry is evaluated by the ratio of the grounded and the RF electrode areas. As shown in Table 17, the ratio increases from 1.2 to 2.8.

$d_i$	(mm)	5	10	15	20	25	30	35	40	45
$A_{RF}$	( $\text{cm}^2$ )	78.5								
$A_{GND}$	( $\text{cm}^2$ )	94.2	110.0	125.7	141.4	157.1	172.8	188.5	204.2	219.9
$A_{GND}/A_{RF}$	(-)	1.2	1.4	1.6	1.8	2.0	2.2	2.4	2.6	2.8

Table 17: RF and grounded electrode areas as functions of the inter-electrode distance  $d_i$ .

The inter-electrode distance has a strong impact on the plasma parameters (in particular  $V_{DC}$  with the ratio of RF/grounded surfaces): the asymmetry increases with  $d_i$ , the volume is multiplied by a factor of 9 (proportional to  $d_i$ ), and the breakdown voltage is known (Paschen's law) to depend on the "pressure times  $d_i$ " parameter (named " $P \cdot d_i$ ").

Within an inter-electrode distance series, electrical measurements ( $V_{RF}$  and  $V_{DC}$ ) are difficult to interpret as the asymmetry changes (area ratio from 1.2 to 2.8). The  $V_{DC}$  should decrease (increase in absolute value) with the asymmetry but it does also depend on all other plasma properties. However the  $H_2$  depletion can help us to get “straightforward” information on the plasma chemistry. A  $d_i$  series has been performed under the plasma conditions of Table 18.

$T_{sub}$	$T_{RF}$	$d_i$	Pr	$SiF_4$	$H_2$	Ar	Pw	$t_d$
(°C)	(°C)	(mm)	(Torr)	(sccm)	(sccm)	(sccm)	(W)	(sec)
150	70	5→45	3.8	3.6	5.3	88	20	300

Table 18: Plasma conditions for the  $d_i$  series at 3.8 Torr.

The  $H_2$  depletion has been measured and the results are displayed in Figure 37 along with the change in the growth rate. The depositions have been made on the same substrate (exclusively for time saving – cooling/reloading/pumping/heating cycle taking at least 2 hours) and ellipsometry measurements have been performed between each plasma. Deposition rates have been estimated from the difference of thicknesses from one deposition to the previous one. Such estimated growth rates are plotted in Figure 37.

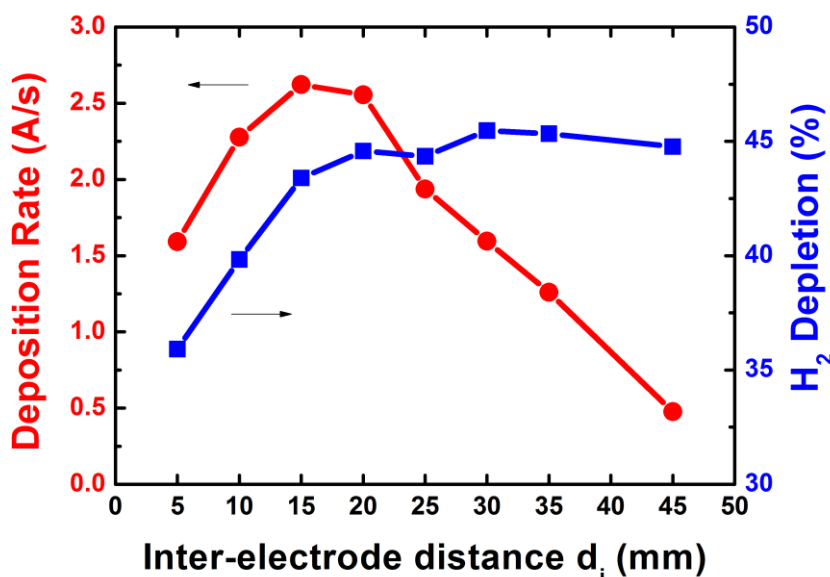


Figure 37: Deposition rate and  $H_2$  depletion as a function of the inter-electrode distance  $d_i$ .

The optimal deposition rate is found at 15 mm while the  $H_2$  depletion reaches a steady-value for  $d_i > 15$  mm.

The deposition rate increases from 1.6 Å/s to 2.6 Å/s in the range of 5-15 mm. At the same time the depletion increases from 36% to 43%. Following the argon series studied previously, a higher depletion can be associated to an increase in deposition rate. However the increase of depletion (+19%) cannot account for the large increase of the deposition rate (+63%). Moreover, above 15 mm, the growth rate decreases from 2.6 Å/s (at 15 mm) to 0.5 Å/s (at 45 mm) – a drop by a factor of 5. This drastic fall is not explained by the chemistry as the  $H_2$  depletion is constant around 45% between 15 mm and 45 mm.

Two other  $d_i$  series have been performed where pressure has been lowered to 2.5 Torr and 1.7 Torr. The comparison of the deposition rate is made with the previous series at 3.8 Torr. The plasma conditions are given in Table 19.

$T_{\text{sub}}$ (°C)	$T_{\text{RF}}$ (°C)	$d_i$ (mm)	Pr (Torr)	$\text{SiF}_4$ (sccm)	$\text{H}_2$ (sccm)	Ar (sccm)	Pw (W)	$t_d$ (sec)
150	70	5→45	1.7	3.6	5.3	88	20	300
			2.5					
			3.8					

Table 19: Plasma conditions for  $d_i$  series at 1.7 Torr, 2.5 Torr, and 3.8 Torr.

Figure 38 shows the deposition rate for the three plasma conditions (3.8 Torr, 2.5 Torr and 1.7 Torr) as a function of the inter-electrode distance (Figure 38a) and of the product pressure times inter-electrode distance (Figure 38b) – named “ $P \cdot d_i$ ” parameter. As in 3.8 Torr case, the deposition rate increases then decreases with  $d_i$  distance in 1.7 Torr case. The maximum growth rate is  $2.1 \text{ \AA/s}$  at 1.7 Torr, which is lower than  $2.6 \text{ \AA/s}$  at 3.8 Torr. The distance at which the maximum deposition rate is reached is greatly changed: 30 mm at 1.7 Torr and 15 mm at 3.8 Torr. However the factor 2 between 15 mm and 30 mm seems to be linked to the almost factor 2 between 1.7 Torr and 3.8 Torr. When plotted as function of  $P \cdot d_i$  parameter as shown in Figure 38b, the maximum deposition rate is obtained at 6 Torr·cm in both cases. Similar trend is found at 2.5 Torr. These results reinforce the idea that  $P \cdot d_i$  is the key physical parameter which controls the deposition rate.

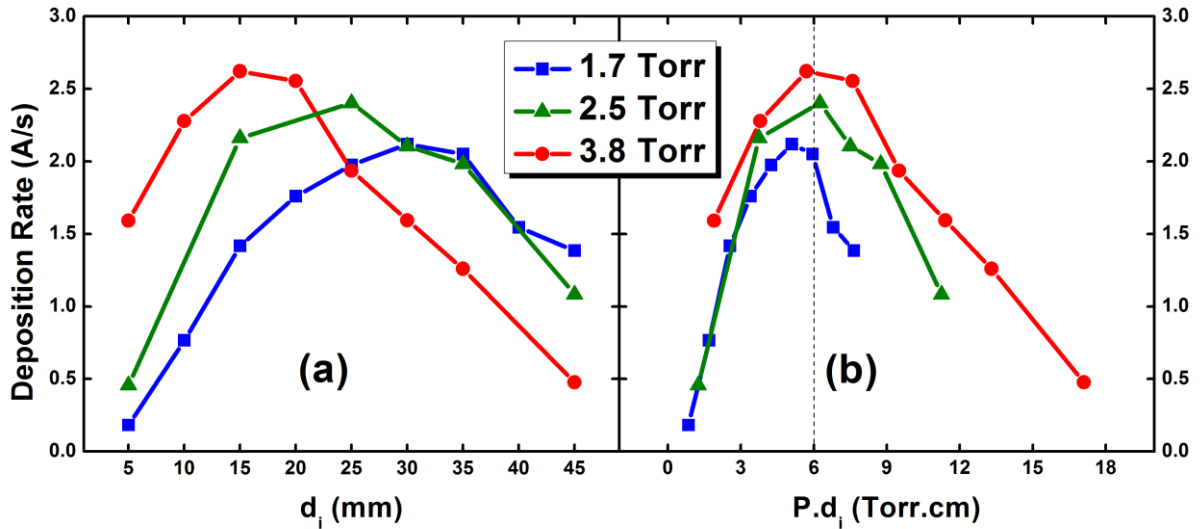


Figure 38: Deposition rate as a function of  $d_i$  (a) and  $P \cdot d_i$  (b) for various values of the total pressure: 3.8 Torr, 2.5 Torr and 1.7 Torr. The highest deposition rate is obtained at 6 Torr·cm in the three cases.

The trend of the deposition rate cannot be understood only by the depletion of  $\text{H}_2$ . More complex mechanisms must take place. For a constant pressure and a constant inter-electrode distance (and consequently a constant  $P \cdot d_i$ ) the deposition rate is proportional to the consumption of  $\text{H}_2$ . In reference to the phenomenological model of the previous section, let us call “ $A$ ” the number of precursors generated within the plasma. One can write Equation (31) where “ $C$ ” is the proportionality factor between growth rate and “ $A$ ” (the “ $C$ ” letter has been chosen in reference to “coupling”: how precursors turn into deposition). We have shown by Figure 38 that the coupling factor depends strongly on  $P \cdot d_i$ .

$$D_r = C(P \cdot d_i) \cdot A \quad (31)$$

From Figure 38b, we can observe that the trend of the deposition rate is narrow at 1.7 Torr and broader at 3.8 Torr. Therefore from a practical point of view, the optimization of the growth rate is easier at high pressure than at low pressure where a small variation of the  $P \cdot d_i$  product leads to steep variation of the deposition rate.

Figure 39 shows the H<sub>2</sub> depletion in the three series as a function of P·d<sub>i</sub> product. The H<sub>2</sub> flow rate is always 5.3 sccm therefore depletion and consumption are proportional and Figure 39 is representative of A. All the three curves overlap leading to the conclusion that A, itself, depends on P·d<sub>i</sub> and only on this product. On the contrary the deposition rate depends on P·d<sub>i</sub> but the maximum (obtained at 6 Torr·cm) depends on pressure too: 2.1 Å/s at 1.7 Torr, 2.4 Å/s at 2.5 Torr, and 2.6 Å/s at 3.8 Torr. Therefore the double dependence in P·d<sub>i</sub> and P is not related to A but to C, the coupling factor.

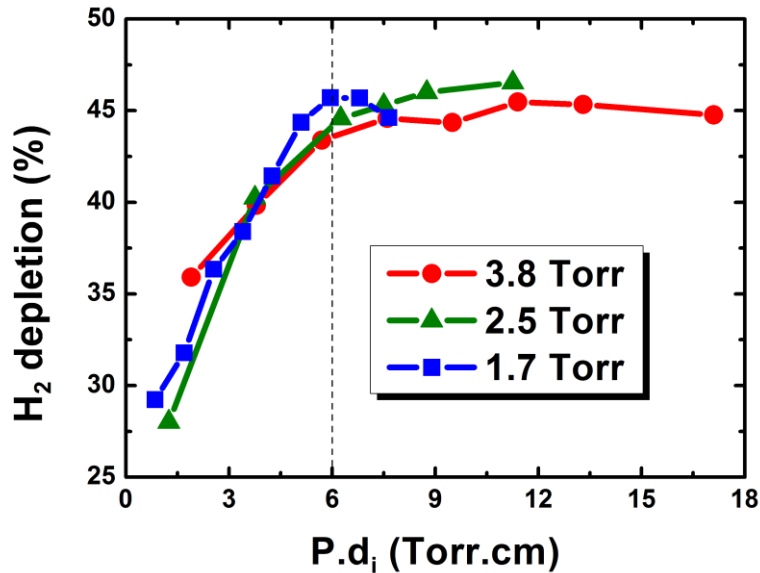


Figure 39: H<sub>2</sub> depletion as a function of P·d<sub>i</sub> at 3.8 Torr, 2.5 Torr and 1.7 Torr.

### 3.2.2 Where is my silicon?

The maximum H<sub>2</sub> depletion in Figure 39 is 45% for a H<sub>2</sub> flow rate of 5.3 sccm: the H<sub>2</sub> consumption is then 2.4 sccm. Given this consumption, what is the maximal deposition rate achievable is an interesting question. To get a silicon atom from a SiF<sub>4</sub> molecule, one should remove four fluorine atoms. Based on the phenomenological model, we will assume that fluorine is removed by HF. Therefore two H<sub>2</sub> molecules are required to form four HF and to obtain one silicon atom. 1 sccm of H<sub>2</sub> consumption is equivalent to 0.5 sccm of silicon atom. By assuming that the density of the silicon material is 5x10<sup>22</sup> at/cm<sup>3</sup>, which volume per second can be expected from 1 sccm of H<sub>2</sub> consumption? This volume per second will be expressed as the product of a surface by a deposition rate, it is the reason why the cm<sup>2</sup>·Å·s<sup>-1</sup> unit will be chosen. In standard conditions (of pressure and temperature), 0.5 cm<sup>3</sup>·min<sup>-1</sup> represents 2.2x10<sup>-5</sup> mol·min<sup>-1</sup> or 1.3x10<sup>19</sup> at·min<sup>-1</sup>, which is 2.2x10<sup>17</sup> at·s<sup>-1</sup>. The corresponding volume per second is then 4.3x10<sup>-6</sup>cm<sup>3</sup>·s<sup>-1</sup> or 430 cm<sup>2</sup>·Å·s<sup>-1</sup>.

For example, at d<sub>i</sub>=30 mm the area of the grounded and RF electrodes is 251.3 cm<sup>2</sup>. In the condition of Figure 37 the H<sub>2</sub> consumption is 2.4 sccm which leads to a volume per second of 1032 cm<sup>2</sup>·Å·s<sup>-1</sup>. By assuming a uniform deposition rate over the whole surface, the maximal deposition rate is 4.1 Å/s. The actual deposition rate is 1.5 Å/s. The waste is therefore evaluated at 2.6 Å/s, and only 37% of the dissociated silicon is found in the grown layer. This calculation can be performed for each d<sub>i</sub> and for the three pressures. The computed silicon wastes are displayed in Figure 40. Below 6 Torr·cm the waste is decreasing but it increases above 6 Torr·cm. The minimal waste is found to be 40% at 6 Torr·cm which corresponds to the maximum of the deposition rate in Figure 38b. This waste is only due to the coupling factor (not to A). Understanding the optimum of D<sub>r</sub> at 6 Torr·cm is the same as understanding the waste of silicon in the process. In order to account for the evolution of the silicon waste with P·d<sub>i</sub> product we propose two models: the dust model and the geometrical model.

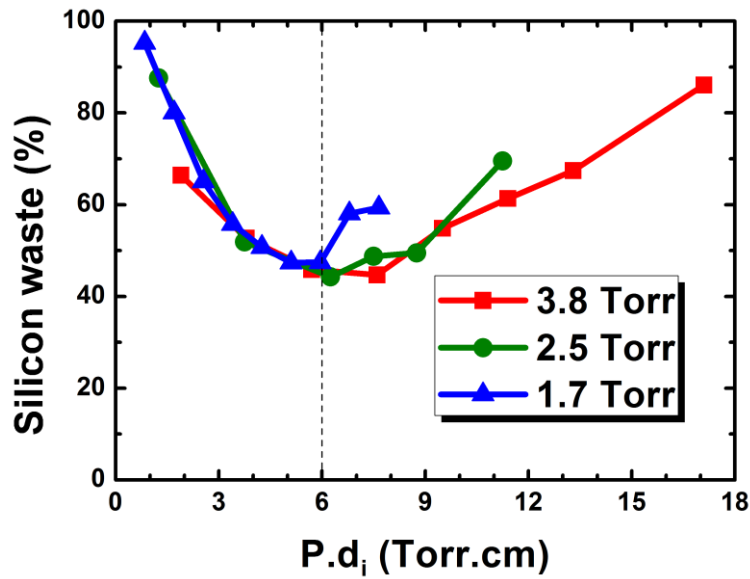


Figure 40: Silicon waste as a function of  $P \cdot d_i$  at 3.8 Torr, 2.5 Torr and 1.7 Torr.

### 3.2.3 Dust model

An explanation has been proposed by our group to account for the augmentation then the reduction of the growth rate as a function of the pressure or the inter-electrode distance  $d_i$ . Our plasma conditions are known to be dusty. The density of plasma-generated nanoparticles is known to increase with pressure and inter-electrode distance. With the assumption that nanoparticles contribute to the growth, the increase in deposition rate is read as the transition from a radical precursor regime to a nanoparticle precursor regime. When nanoparticle size reaches a critical value, they start to charge negatively and are irremediably confined/trapped by sheaths within the plasma bulk, before being finally pumped. We will call these large nanoparticles powders. By being trapped, powders do not contribute to the deposition rate. The reduction of the deposition rate with the increase in  $d_i$  is cleared up by the transition from nanoparticle precursor regime to powder precursor regime [59]. This model is named “dust model” and is summarized by three regimes: radical, nanoparticles and powders as depicted in Figure 41. The coupling factor is called  $C_{dust}$ .

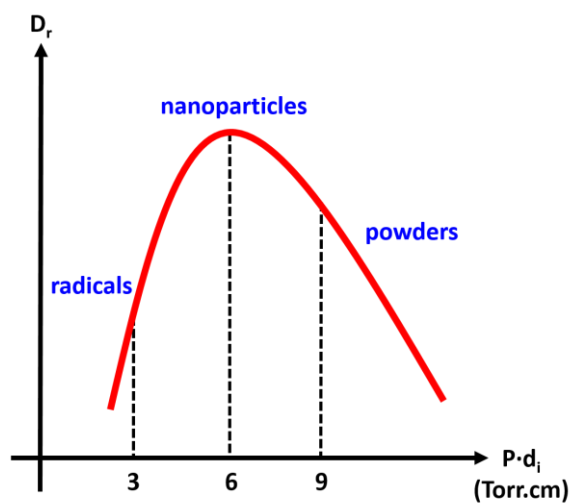


Figure 41: Schematic of the dust model. The trend of  $D_r$  is explained by the change in the plasma composition: three regimes: radicals, nanoparticles, and powders.

The  $P \cdot d_i$  parameter in the dust model controls the size of nanoparticles: above 6 Torr-cm they are trapped and have no chance to reach the growing surface. Experimentally a lot of powders are found on the cold walls of the reactor from the plasma to the pump. That silicon is obviously not used to grow layers. It contributes to increase the waste of silicon in Figure 40. The waste of silicon below 6 Torr-cm is attributed to the etching of radicals ( $\text{SiF}_x\text{H}_y$ ) or to the low sticking coefficient of species (radicals  $\text{SiF}_x\text{H}_y$  or of very small nanoparticles  $\text{Si}_2\text{F}_x\text{H}_y$ , ...). They are formed but they do not contribute to the growth and consequently contributes to the silicon waste. Moreover, in non-dusty  $\alpha$ -regime the RF power is less coupled (in comparison to dusty  $\gamma'$ -regime), which can account for the lower depletion in Figure 39 below 6 Torr-cm.

If the pressure is divided by 2, less collisions occur in the plasma. The doubling of the inter-electrode distance is then necessary to compensate the lowering of the average collision rate by pressure. By dividing  $P$  by two and multiplying  $d_i$  by two, same nanoparticles sizes are achieved and at 6 Torr-cm the critical size of negative charging is reached. This is the reason why  $P \cdot d_i$  should be the key parameter as found in Figure 38b.

### 3.2.4 Geometrical model

Another model can be proposed based on the geometry of the reactor. We will name this model as “geometrical model” and the coupling factor  $C_{\text{geom}}$ . The contribution of nanoparticles to the deposition rate is not questioned in the geometrical model but the increase and the decrease of  $D_r$  with  $P \cdot d_i$  does not rely on the presence of negatively charged nanoparticles. From 0 to 6 Torr-cm the plasma is changing since the  $\text{H}_2$  depletion can increase from 30% to 45% in Figure 39 at 1.7 Torr. However, this increase of the depletion cannot account for the increase of  $D_r$ . Something else is at stake. The fact that the depletion changed means that the cause of this variation could explain the significant increase of  $D_r$  from 0 to 2 Å/s at 1.7 Torr. The decrease of  $D_r$  above 6 Torr-cm can be understood as a decrease of the concentration of precursors close to the substrate: the depletion being constant and the volume being increased with the increase of  $d_i$ . The deposition rate could be proportional to the concentration and not to the total amount of precursors in the plasma: if  $d_i$  is 45 mm, precursors generated close to the RF electrode will have less chances of contributing to the growth on the grounded electrode. For instance, at 3.8 Torr from 15 mm to 45 mm the volume is tripled but the depletion is constant (Figure 39) and  $D_r$  decreases from 2.5 Å/s down to 0.5 Å/s (Figure 38a).

Figure 42 shows a schematic of the cross section of the cylindrical PECVD reactor where the RF electrode is located on the right hand-side and the substrate holder on the left hand-side. The grounded electrode is the substrate holder and the lateral side of the cylinder. We define the “useful volume”  $V_u$  as the volume of the plasma just in front of the substrate such that all the species inside this volume contribute to the deposition rate. Identically we define  $V_{u'}$  as the volume of species contributing to deposition on the side wall of the grounded electrode and  $V_{u''}$  as the volume of species contributing to the deposition on the RF electrode. Finally we define the “waste volume”  $V_w$  as the remaining volume where species will be pumped and will not contribute to deposition of any surfaces.

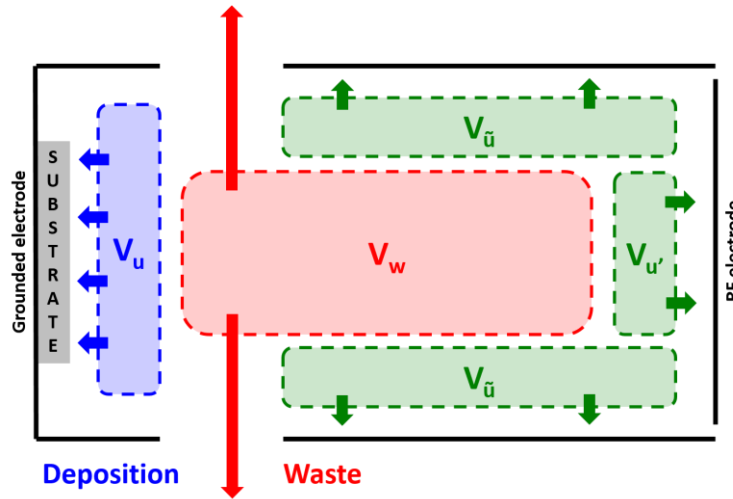


Figure 42: Schematic of volume definitions ( $V_u$ ,  $V_{\bar{u}}$ ,  $V_{u'}$ , and  $V_w$ ) of the geometrical model.

The total volume is  $V_{tot}=V_u+V_{\bar{u}}+V_{u'}+V_w$ . The useful volume  $V_u$  cannot be as large as wanted: it is limited by the diffusion of species in the gas. Therefore the size of the volume (in horizontal direction in Figure 42) is proportional to the mean free path. The mean free path is inversely proportional to the gas density, and thus to the total pressure. Figure 43 depicts the extension of  $V_u$  when  $d_i$  is increasing. The useful volume can decrease if the inter-electrode distance is too small: there is a competition between  $V_u$  and the other volumes (more specifically  $V_{u'}$ ). By increasing the distance,  $V_u$  is increased until the extension is limited by the mean free path. Above 6 Torr.cm  $V_{tot}$  linearly increases while  $V_u$  stays constant.

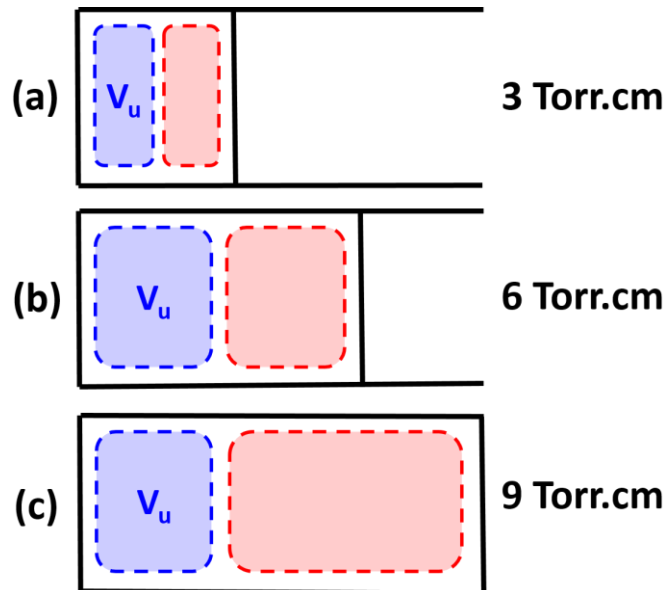


Figure 43: Extension of the useful volume  $V_u$  for various  $P.d_i$  values within the frame of the geometrical model.

Figure 44 summarizes the variations of the volumes as functions of  $P.d_i$ . Below 6 Torr.cm,  $V_u$  is proportional to  $P.d_i$  but we know that the  $H_2$  depletion is increasing with  $P.d_i$  (Figure 39). Therefore the deposition should increase with  $P.d_i$ . Above 6 Torr.cm,  $H_2$  depletion is constant. However  $V_{tot}$  is constant, thus the density of precursors is decreasing. Because  $V_u$  is constant, the deposition rate should decrease.  $C_{geom}$  is a function of  $V_u$  and  $V_{tot}$ .

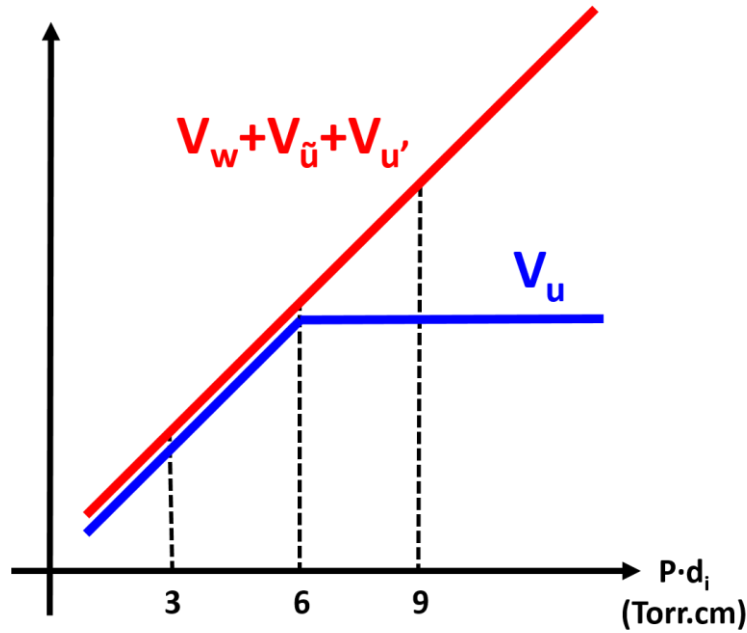


Figure 44: Variations of  $V_u$  and  $V_w + V_u + V_w$  as functions of  $P \cdot d_i$  in the frame of the geometrical model.

### 3.2.5 P·d<sub>i</sub> series for different plasma conditions

In this section more experiments are performed to confront the dust model and the geometrical.

- Gas temperature, pressure, and RF power series:

To continue the study, three new series have been performed: for the first series,  $d_i$  has been varied but the gas has been heated at 150°C instead of 70°C. Low gas temperature is known to promote the nucleation of nanoparticles in the plasma phase. Therefore an increase in  $T_{RF}$  should delay the nanoparticles formation [51][52] and the optimum might be expected (in the dust model) to shift to higher  $P \cdot d_i$  value. The second series consists on increasing the pressure from 1 Torr to 4 Torr (by steps of 500 mTorr) by keeping  $d_i$  constant at 30 mm. If  $P \cdot d_i$  is the physical key parameter, one should get the same behavior (increase then decrease of  $D_r$ ) for a pressure series as in inter-electrode distance series. The RF power has been increased at 40 W instead of 20 W in the third series and  $d_i$  has been varied again. The RF power should have a direct impact on the precursor density and therefore should change the growth rate and/or the density of nanoparticles. Plasma conditions are given in Table 20.

$T_{sub}$ (°C)	$T_{RF}$ (°C)	$d_i$ (mm)	Pr (Torr)	SiF <sub>4</sub> (sccm)	H <sub>2</sub> (sccm)	Ar (sccm)	Pw (W)	$t_d$ (sec)
150	70	5→45	3.8	3.6	5.3	88	20	300
	<b>150</b>	5→45	3.8				20	
	70	30	<b>1→4</b>				20	
	70	5→45	3.8				<b>40</b>	

Table 20: Plasma conditions for the  $P \cdot d_i$  series by changing  $T_{RF}$ , pressure and RF power.

The deposition rate for the three series is shown in Figure 45 along with the results from the previous series. Interestingly enough the optimum happens at 6 Torr·cm for the first series where  $T_{RF}$  was 150°C, despite the fact that nanoparticles formation is expected to be reduced. For the pressure series, a similar behavior is found as for the  $d_i$  series. This emphasizes that  $P \cdot d_i$  is really the key parameter to understand all these series. Moreover, the four series displayed in Figure 45 have the same optimum at 6 Torr·cm, confirming our statement. The increase of RF power does not affect the  $P \cdot d_i$  value at which the optimum occurs. Deposition rate reaches a higher value at 40 W due to the increase of the chemistry (C stays constant but A increases in Equation (31)).

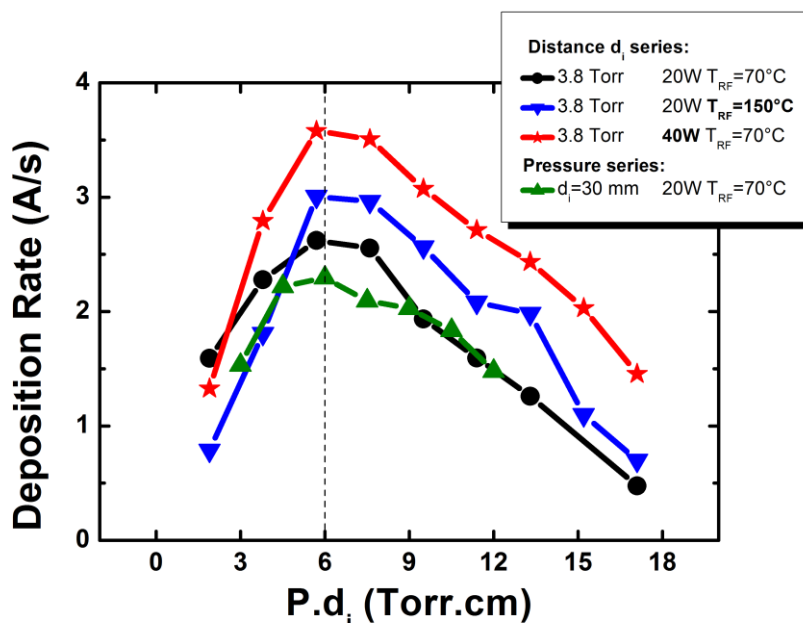


Figure 45: Deposition rate as a function of  $P \cdot d_i$  where pressure, RF power,  $d_i$  and  $T_{RF}$  have been varied.

- Gas residence time:

To further study the coupling factor, we address here the question of the gas residence time. Without the plasma, each particle entering the plasma box has a lifetime: the generation mechanism is the injection of  $\text{SiF}_4$ ,  $\text{H}_2$  and Ar gas, and the loss mechanism (in the absence of plasma) is only the pumping. The main component of the gas mixture is argon (usually partial pressures of  $\text{SiF}_4/\text{H}_2/\text{Ar}$  are respectively 200 mTorr, 200 mTorr and 3400 mTorr for a total pressure of 3.8 Torr). Therefore we will neglect the  $\text{SiF}_4/\text{H}_2$  flow rate compared to the Ar flow rate. The residence time is given by the ratio between the number of atoms within the plasma box (proportional to pressure, volume and inversely proportional to gas temperature, approximated here to the RF temperature) and the flow of atoms per second injected into the plasma box (easily computable from the Ar flow rate). The easiest way to change the residence time without changing  $P \cdot d_i$  is to vary the argon flow rate. We have seen in Figure 13 that the deposition rate does not significantly change between 44 sccm and 88 sccm of Ar flow rate. However the residence time should be divided by a factor of two. If the pumping is identical for all the species, the residence time is common to all and “gas” adjective is added to refer to that.

In the presence of plasma, the situation is noticeably more complex: new species are produced and their lifetime is not necessary given by the gas residence time. New loss mechanisms such as bulk dissociation, bulk recombination, or sticking on surfaces do occur. For charged species, it is even more complicated: positive species are accelerated towards the electrodes by the electric field while negative species are trapped by sheaths.

The gas residence time study is motivated by its direct relation with  $P \cdot d_i$ : gas residence time is proportional to pressure and volume and therefore to  $P \cdot d_i$ . A new  $P \cdot d_i$  series has been performed with an argon flow rate of 44 sccm in the previous plasma conditions of 1.7 Torr. Detailed conditions are given in Table 21. At 1.7 Torr and 70°C, from the ideal gas law, the density of molecules is  $4.77 \times 10^{16} \text{ at} \cdot \text{cm}^{-3}$ . For each sccm of total gas flow, there are  $4.48 \times 10^{18} \text{ at} \cdot \text{s}^{-1}$ . Residence time is then calculated given a volume and a total gas flow rate (approximated to the argon flow rate).

$T_{sub}$	$T_{RF}$	$d_i$	Pr	SiF <sub>4</sub>	H <sub>2</sub>	Ar	Pw	$t_d$
(°C)	(°C)	(mm)	(Torr)	(sccm)	(sccm)	(sccm)	(W)	(sec)
150	70	5→45	1.7	3.6	5.3	88	20	300
						44		

Table 21: Plasma conditions for the P-d<sub>i</sub> series when gas residence time is varied.

The deposition rate of the two series as well as the corresponding gas residence time are shown in Figure 46. The order of magnitude of the gas residence time is 100 ms. The deposition rate is almost the same at 44 sccm and at 88 sccm despite the fact that gas residence time is divided by two. The conclusion is that gas residence time does not affect the deposition rate and cannot explain the increase and the decrease of  $D_r$  with P-d<sub>i</sub>. The key parameter is the product P-d<sub>i</sub> and that is not because of the gas residence time.

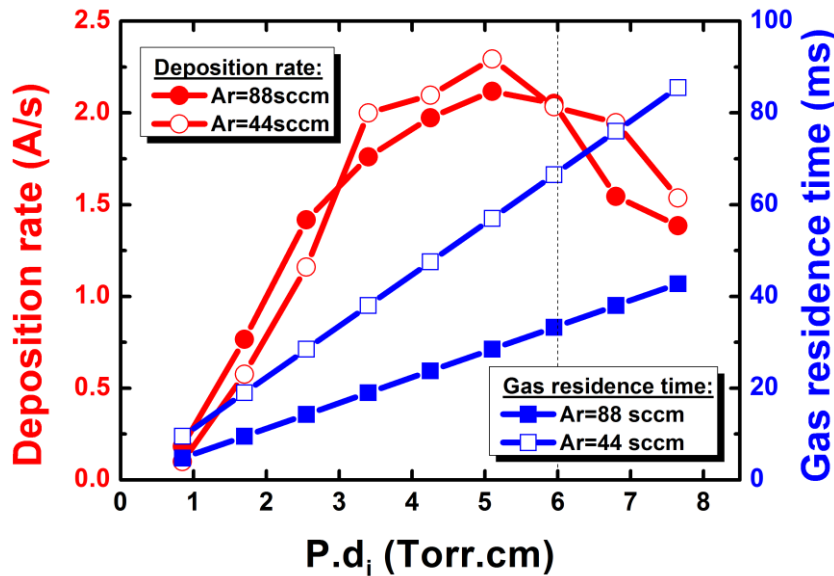


Figure 46: Deposition rate and residence time as a function of P-d<sub>i</sub> for Ar flow rate of 88 and 44 sccm.

- High depletion regime – amorphous layers:

In Figure 37, the 45% of depletion corresponds to 2.4 sccm of H<sub>2</sub> consumption. In the phenomenological model (below the transition), the deposition rate is proportional to the H<sub>2</sub> flow rate. In order to produce less dust, a decrease of H<sub>2</sub> flow rate has been applied but the nature of the material, according to the phenomenological model, becomes amorphous (high H<sub>2</sub> depletion regime). P-d<sub>i</sub> series have been performed for different SiF<sub>4</sub> flow rates as described in Table 22.

$T_{sub}$	$T_{RF}$	$d_i$	Pr	SiF <sub>4</sub>	H <sub>2</sub>	Ar	Pw	$t_d$
(°C)	(°C)	(mm)	(Torr)	(sccm)	(sccm)	(sccm)	(W)	(sec)
150	70	5→45	3.8	3.6	1.5	88	20	300
				3.6	1			
				10	1			

Table 22: Plasma conditions for the P-d<sub>i</sub> series in high depletion regime.

The deposition rate of the three P-d<sub>i</sub> series is shown in Figure 47a. For the amorphous layers, the growth rate rapidly increases and then decreases up to 12 Torr.cm. Above 12 Torr.cm, the deposition rate increases again but the layers are found to be porous. At 7.6 Torr.cm the void fraction of the layer (extracted from spectroscopic ellipsometry) is 8% and the roughness is estimated at 15 Å. At 15.2 Torr.cm the void fraction is 18% and the roughness 30 Å. The extracted thickness from ellipsometry does not take into account that less silicon is found in porous films. Therefore above

12 Torr-cm the growth rate is overestimated. At a  $\text{SiF}_4$  flow rate of 3.6 sccm, the deposition rate is higher for a  $\text{H}_2$  flow rate of 1.5 sccm (red squares) compared to 1 sccm (blue circles). The explanation is given by a higher  $\text{H}_2$  consumption (Figure 47b). At 1 sccm of  $\text{H}_2$  flow rate, if the  $\text{SiF}_4$  flow rate is increased from 3.6 sccm (blue circles) to 10 sccm (green triangles), the deposition rate decreases, which can be attributed to a higher etching by fluorinated species ( $\text{SiF}_x$  and F).

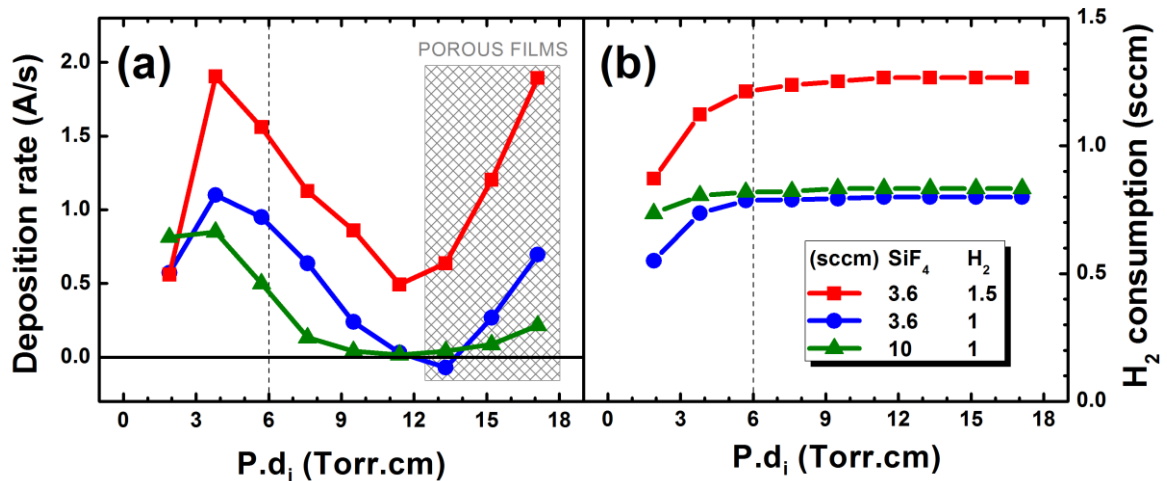


Figure 47: Deposition rate and  $\text{H}_2$  consumption as a function of  $P \cdot d_i$  for hydrogenated amorphous silicon conditions.

### 3.2.6 Pros and cons of dust and geometrical models

We have two concurrent models to explain  $P \cdot d_i$  series. None of them seems to be sufficient to explain all experiments presented above. They are concurrent but they are not, *a priori*, mutually exclusive. Nevertheless, with the two proposed models (dust and geometrical) we can argue about the pros and the cons based on experimental results.

- Pros of geometrical model:

The critical value of 6 Torr-cm is associated to the PHILIX reactor, and does not depend on the plasma conditions (except the pressure). This is consistent with all experiments, especially the increase of RF power from 20 W to 40 W. The value of 6 Torr-cm has also been found in another reactor of our laboratory [60] (ARCAM). The geometry of that reactors is similar to the one of PHILIX. Moreover the value has been obtained in a different chemistry ( $\text{SiH}_4/\text{H}_2$ ). That should confirm that the deposition rate trend is only related to geometry and not to the precise composition of the plasma (especially nanoparticles).

- Cons of geometrical model:

The explanation of the increase of the deposition rate is not satisfactory:  $V_u$  is linearly increasing with  $d_i$  and  $\text{H}_2$  depletion increases a little bit. The combination of the factor does not account for the steep increase of the deposition rate.

The explanation of the decrease is not sufficient either: both  $V_u$  and the  $\text{H}_2$  depletion are constant. The density of precursors over the volume drops by a factor of 3 from 15 mm to 45 mm in Figure 37. However a factor of 5 is found for the drop of the deposition rate.

- Pros of dust model:

The main advantage of the dust model is its clear explanation of the mechanisms of the decrease as well as the increase of the deposition rate. The formation of large and trapped particles is consistent with the waste of silicon computed in Figure 40. Radicals (which are fluorinated and have etching effect)

are also considered as waste, explaining the high waste at low  $P \cdot d_i$  values. Only nanoparticles are useful for the growth.

- Cons of dust model:

As the dust model was the “historical” explanation proposed for  $P \cdot d_i$  series, experiments have been performed to confirm or invalidate model predictions. What has been shown undermines the dust model.

The increase of the RF power creates more radicals. The deposition rate is higher at 40 W than at 20 W, whereas the maximum deposition rate is reached always at 6 Torr·cm. Within the dust model, this statement means that the sizes of nanoparticles only depend on  $P \cdot d_i$  parameter and not on the concentration of radicals. Therefore if the dust model is correct, we achieve a perfect decoupling between number of nanoparticles and their size distribution:  $P \cdot d_i$  governs the size distribution whereas all other parameters control the total number of nanoparticles. Which is equivalent of saying size distribution is given by  $C_{\text{dust}}$  and the total number by  $A$ . This decoupling is fully consistent with all optima found at 6 Torr·cm. However such a perfect decoupling is surprising because usually plasma physics is difficult and dust formation even more complex such that everything is entangled.

The  $H_2$  depletion starts to stabilize at 6 Torr·cm. The dust model should explain why the chemistry is affected by the transition from the radical regime to the nanoparticle regime, and moreover why the transition from nanoparticle regime to powder regime does not affect the depletion anymore. If regimes and chemistry are not correlated, it is difficult to believe that by luck the stabilization of the depletion happens precisely where nanoparticles start to charge.

From Figure 29 we know that a high gas temperature hindered the formation of nanoparticles. Accordingly below 6 Torr·cm in Figure 45 the deposition rate is higher at 70°C than at 150°C. However above 6 Torr·cm the situation is opposite. The temptation is to attribute the lower deposition rate at 70°C to a higher growth rate of nanoparticles which will have bigger sizes and then more nanoparticles will be trapped compared to the 150°C case. With this logic, the optimum should shift to a lower  $P \cdot d_i$  value (and size distribution should not only be determined by  $P \cdot d_i$ ).

The reason why nanoparticles have been invoked to explain the effect of  $d_i$ , is the absence of deposition in non-dusty plasma conditions. The idea behind the  $P \cdot d_i$  dependency is the shift to larger sizes in the nanoparticle size distribution with either a rise of  $P$  or a rise of  $d_i$ . Therefore the  $P \cdot d_i$  should appear as a good parameter estimating the nanoparticles sizes. High pressure is required to form nanoparticles, which is linked to the probability of collisions between species. The size of nanoparticles is directly determined by the number of collisions they undergo. In the dust model, this number increases with inter-electrode distance. The lifetime of nanoparticles depends on the loss mechanisms: they can stick to the surface or can be pumped away. If they are neutral, the lifetime could be given by the gas residence time, but if there are charged, Coulomb forces take place and lifetime is different from gas residence time (if positively charged then accelerated to electrodes; if negatively charged then trapped by sheaths). Therefore the number of collisions is given by the gas residence time and should depend on  $P \cdot d_i$ . The probability of collisions itself depends on  $P$ . Consequently a dependency in  $P^2 \cdot d_i$  should be expected and not  $P \cdot d_i$  as stated before. Moreover the experiment of Figure 46 shows that gas residence has no influence on the deposition rate and its optimum.

### 3.2.7 Perspectives

Further plasma studies must be performed and a more complete model should be found. Our study is only based on the  $H_2$  depletion to characterize the plasma chemistry but deeper and more comprehensive studies should be done to solve the  $P \cdot d_i$  series puzzle (the optimum at 6 Torr·cm). Other plasma characterization techniques should be used to figure out how plasmas behave at low and high  $P \cdot d_i$  values. The exact knowledge of the growth precursors is crucial and the role of etching should be deepened.

Unfortunately the quality of the microcrystalline silicon has not been addressed here. From our literature [59][61] the best material is obtained at 6 Torr·cm. The understanding of why the quality is enhanced and why it is deteriorated could give a powerful insight of what is going on in P·d<sub>i</sub> series.

From a practical point of view, the d<sub>i</sub> series study can be summarized as follow: for PHILIX reactor, the experimenter can choose the optimal inter-electrode distance to maximize the deposition rate such that P·d<sub>i</sub> is 6 Torr·cm.

### 3.3 Surface versus plasma crystallization

#### 3.3.1 Beyond the phenomenological model

The results of Figure 23 can be interpreted in the framework of the phenomenological model. However they revealed some unexpected material properties (crystalline fraction). This is not surprising as the model does not pretend to describe the full plasma chemistry and in particular it does not consider nanoparticles. In the phenomenological model, at low RF power we have a F-limited process (i.e. limited by the dissociation of SiF<sub>4</sub>) rather than a H<sub>2</sub>-limited process. It is the reason why the deposition rate does not depend on the H<sub>2</sub> flow rate at low RF power. At high RF power, the deposition rate saturates and the process becomes H<sub>2</sub> limited as depicted in Figure 23 at 35 W and 45 W for respectively a H<sub>2</sub> flow rate of 2 sccm and 3 sccm. In that way, the phenomenological model is helpful to account for experimental results.

Figure 48 gives again the deposition rate as a function of the RF power for two H<sub>2</sub> flow rates: 3 sccm and 10 sccm. Furthermore, the crystalline fraction deduced from ellipsometry fitting is shown. At low RF power the films are amorphous (10% of crystalline fraction), and by increasing it, the amorphous-to-microcrystalline transition occurs. For the same RF power, layers at high H<sub>2</sub> flow rate are more crystallized and grow faster, in line with the phenomenological model. However the amorphous-to-microcrystalline should appear while decreasing the RF power. With the model notation, the transition is given by the ratio B/A: high B (H<sub>2</sub> flow rate) or low A (RF power) favor the microcrystallinity to the detriment of the amorphous phase.

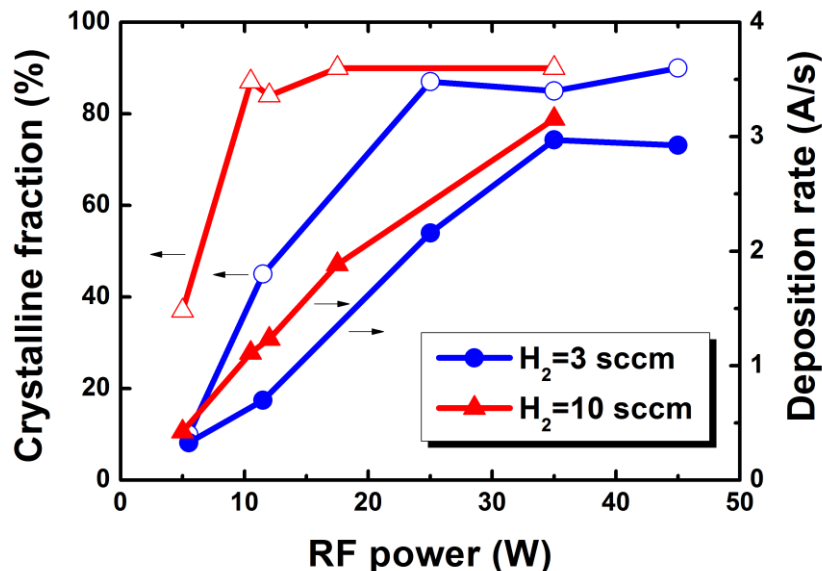


Figure 48: Crystalline fraction and deposition rate from ellipsometry as a function of RF power.

New experiments have been performed at 3 sccm of H<sub>2</sub> but with a broader RF power range (two years separate these experiments to the previous ones). The process conditions are given in the following table. The H<sub>2</sub> depletion has been measured and is displayed in Figure 49 as well as the layer crystalline fraction and the growth rate both determined by ellipsometry. From 25 W to 100 W the

deposition rate saturates in accordance with the saturation of the H<sub>2</sub> depletion. However microcrystalline layers are obtained on the contrary to Figures 15 & 17 where amorphous silicon is found at full H<sub>2</sub> depletion. Below 25 W the H<sub>2</sub> depletion is proportional to the RF power, as the growth rate is. However films are amorphous at low RF power (5 W) despite the excess of H<sub>2</sub>.

T <sub>sub</sub>	T <sub>RF</sub>	d <sub>i</sub>	Pr	SiF <sub>4</sub>	H <sub>2</sub>	Ar	Pw	t <sub>d</sub>
(°C)	(°C)	(mm)	(Torr)	(sccm)	(sccm)	(sccm)	(W)	(sec)
150	80	30	3.8	3.6	3	88	5→100	1800

Table 23: Plasma conditions for the RF power series.

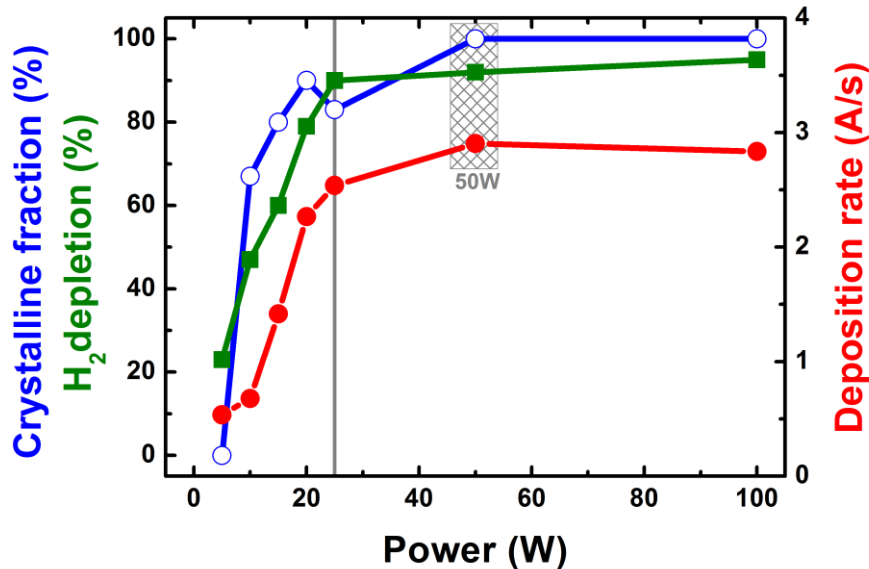


Figure 49: Crystalline fraction, H<sub>2</sub> depletion and deposition rate for RF power series.

The wrong prediction of the phenomenological model is twofold:

- Amorphous silicon is deposited at low H<sub>2</sub> depletion while microcrystalline silicon is expected.
- Microcrystalline silicon is obtained at high H<sub>2</sub> depletion while amorphous silicon is expected.

### 3.3.2 Crystallization of plasma-generated nanoparticles

Plasma-generated nanoparticles could be collected on glass substrates by putting the glass on a cold wall of the reactor along the pumping drag flow to maximize the quantity of nanoparticles. The obtained film is not dense and consists of dust sticking on the substrate. However Raman spectroscopy can be performed to assess the nature of the collected silicon. A blue laser (473 nm excitation) is preferred rather than red/IR laser (633 nm or 785 nm) for Raman spectroscopy because the penetration depth is shorter at this range of photon wavelength (or photon energy). Figure 50 shows the normalized Raman signal of the layer deposited on the substrate holder (as usual) and that of the plasma-generated nanoparticles at 50 W in the conditions of Figure 49. Concerning the layer, the crystalline peak at 520 cm<sup>-1</sup> is dominant compared to the amorphous peak at 480 cm<sup>-1</sup>. A highly crystallized layer is obtained at 50 W as confirmed by the crystalline fraction deduced by ellipsometry in Figure 49.

Concerning the Raman spectroscopy on nanoparticles, both amorphous and crystalline silicon peaks are present. The crystalline peak is shifted to lower wavenumbers (516 cm<sup>-1</sup>). This shift can be attributed to at least three phenomenon: (i) tensile stress [62]; (ii) increase of temperature due to laser irradiation heating [63]; and (iii) optical confinement effect [64][65]. The deconvolution of the three factors requires a painstaking study. The porous nanoparticles films are very sensitive to heating: an optical density filter is required to attenuate the power of the laser and to avoid laser crystallization. This phenomenon is irreversible and is detectable by the optical microscope of the Raman equipment:

a dark zone will appear. However by reducing the laser power, the Raman signal level will decrease too. We know that the nanoparticle layer is subject to heating, and possibly the crystalline peak seen in Figure 50 could simply result from a laser crystallization despite the precautions taken for the measurement. A less destructive technique is required to assess the crystallinity of nanoparticles such as TEM.

Crystallized nanoparticles could explain the growth of microcrystalline layers: some growth precursors are already crystalline when they reach the surface. Less hydrogen is then required to fully crystallize the layer. From the same reasoning, if the nanoparticles are amorphous more hydrogen is required to crystallize the huge amount of silicon carried from one nanoparticle (as evaluated in Figure 33a).

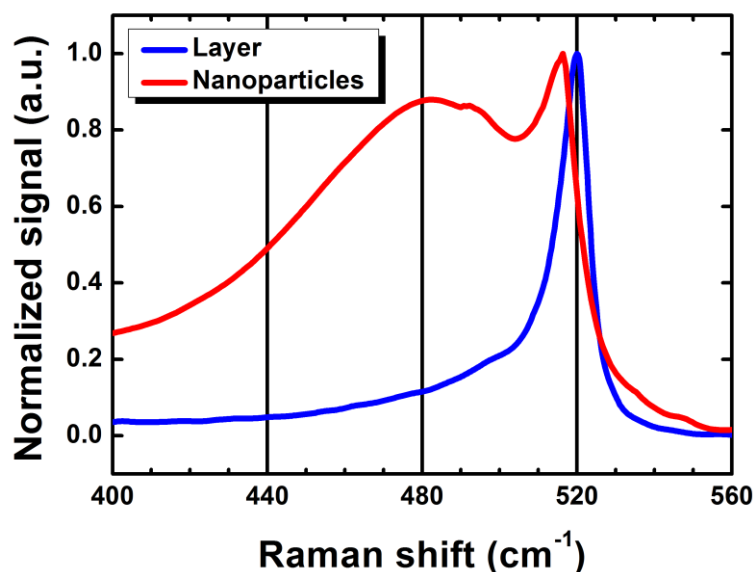


Figure 50: Raman signal of a silicon layer and of plasma-generated nanoparticles at 50 W, under the conditions of Table 23.

### 3.3.3 Mapping of plasma-generated nanoparticle crystallinity

In order to understand the relationship between amorphous/microcrystalline structure of the films and of the plasma-generated nanoparticles, a home-made approach has been used. It consists in the installation of TEM grids at two different locations: on the glass substrate in order to have more insights about the layer structure and on the exhaust line to collect nanoparticles generated (“synthesized”) by the plasma. A cold finger has been used to support the grid in the pumping line. It consists of a metallic rod with a 1x1 cm<sup>2</sup> substrate holder at the end which can be seen in Figure 34b. The rod is hollow to let water flowing and cooling the substrate. The substrate can be inserted in the middle of the pumping line (not laying on cold walls), approximately 10 cm from the plasma confinement box. Silicon collected on the cold finger only comes from plasma-generated nanoparticles without being exposed to ion bombardment or plasma environment. The presence of water cooling (about 15°C) helps nanoparticles of the gas flow to be attracted on the finger via thermophoresis force.

The advantage of this approach is the simplicity of its use as well as the absence of sample preparation between experiments and analysis (like FIB or polishing steps required for film cross section studies for instance). The grid is composed of a copper mesh with an amorphous carbon film on top of it. The mesh defines a matrix, each element being a square of 40x40 μm<sup>2</sup>. Within this square TEM and HR-TEM analysis can be performed. The amorphous carbon film is thin enough (15-30 nm) to be transparent to the electron beam. However, it represents an amorphous contribution which can be differentiated from an amorphous silicon layer by using advanced TEM techniques (EELS). An easy way to solve the problem is to use a holey-carbon film: the amorphous carbon film is not continuous and

some parts present holes with different sizes. An example is displayed in Figure 51a where the small dark spots are the nanoparticles.

By zooming on the edge of a hole, one can find aggregates of nanoparticles as depicted in Figure 51b. Each nanoparticle hangs with the others. On the left, they are attached to the carbon film substrate but on the right they are suspended (floating) in the vacuum of the electron microscope. Therefore the electron beam only sees the silicon and no carbon is detected in the hole. The electron microscope allows us to make local investigations of the silicon material without taking care of the carbon background. However since the nanoparticles are collected directly from the plasma, they are not well fixed on the carbon membrane. This will induce their vibration during the TEM experiments, especially when we want to record high magnification images (HR-TEM) in order to study the nanoparticle crystallographic structure. The origin of the binding between nanoparticles is an open question. We think it is linked to electrostatic forces such as dipole-dipole interactions. This behavior has been reported in chemical vapor deposition (without plasma) [66] in which the growth rate of nanorods was higher on floating substrate than on grounded substrate. The explanation is based on the attraction of small spheres by large spheres even if their signs are equal.

For the grid installed on the substrate within the plasma, a dense layer is obtained as shown Figure 51c. On the contrary, growth is observed on the carbon and lateral growth too. Again, the lateral growth on the edge of holes allows for a direct study of the layer without carbon background inconvenience. Note that no suspended nanoparticles are observed on this grid. The main drawback of the TEM grid is that layers are only studied from a top view. No information on depth profile can be given. As in Figure 51c, bulk layers are difficult to study: only average information can be extracted.

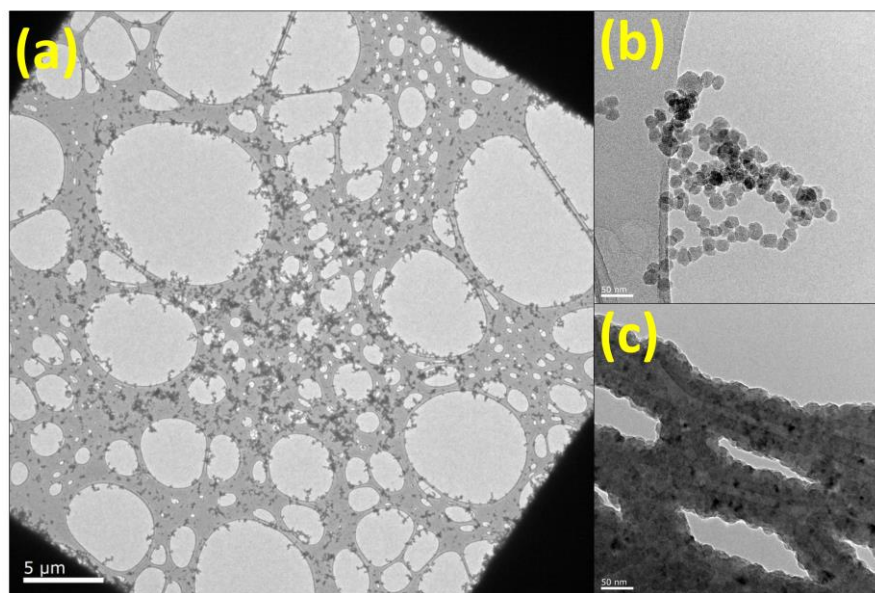


Figure 51: (a) One 40x40  $\mu\text{m}^2$  square of a holey TEM grid and the two locations: (a) (b) exhaust line and (c) plasma.

Layer and plasma-generated nanoparticles have been studied for five different plasma conditions given in Table 24. These conditions have been chosen such that the two important parameters are changed: the  $\text{H}_2$  flow rate and the RF power. As for the phenomenological model, the effect of the  $\text{H}_2$  flow rate has been studied (2, 5.3, and 15 sccm) while the RF power was kept constant at 20 W. Following experiments of the previous section (Figure 49), the RF power has been set to 50 W and 100 W while a low  $\text{H}_2$  flow rate of 3 sccm has been selected. Names are given (intuitively) for each condition as H02, H05, H15, W050, and W100.

name	T <sub>sub</sub> (°C)	T <sub>RF</sub> (°C)	d <sub>i</sub> (mm)	Pr (Torr)	SiF <sub>4</sub> (sccm)	H <sub>2</sub> (sccm)	Ar (sccm)	Pw (W)	t <sub>d</sub> (sec)	
H02	150	80	30	3.8	3.6	2	88	20	500	
H05						5.3				
H15						15				
W050						3				50
W100										100

Table 24: Plasma conditions for sample H02, H05, H15, W050, and W100.

Figures 52, 54 and 56 show the TEM images of conditions H02, H05, and H15 respectively. Left pictures (a) represent the grid installed on the substrate (within the plasma) while right pictures (b) correspond to the grid installed in the middle of the exhaust line collecting plasma-generated nanoparticles. Diffraction patterns are provided in Figures 53, 55, and 57. Crystalline silicon rings can be identified as the lattice constant of silicon is 5.43 Å (for instance in Figure 57):

- The first ring at 3.14 Å is associated with the (111) orientation.
- The second ring at 1.92 Å is associated with the (220) orientation.
- The third ring at 1.64 Å is associated with the (311) orientation.

For H02, H05, and H15 conditions, all collected nanoparticles are amorphous. This is deduced from TEM images and is corroborated with TEM diffraction patterns (Figure 55b). Their diameter ranges from 10 nm to 20 nm. Concerning the layers, amorphous silicon is found for H02 while microcrystalline silicon is deposited under H05 and H15 conditions. However H05's diffraction pattern (Figure 55a) shows an amorphous signature while H15's has a crystalline diffraction pattern (Figure 57). These findings are in agreement with the ellipsometry measurements on the glass substrate (on which the grid was laying) which indicate a mixture of 25% of amorphous silicon and 75% of microcrystalline silicon. Large aggregates of 50 nm are found in Figure 52a. This can reasonably be attributed to very large trapped nanoparticles collected during the extinction of the plasma as discussed and presented in Figures 32 and 35b. A continuous amorphous film is also present between these aggregates and mainly contributes to the amorphous diffraction pattern. Nanoparticles collected on the cold finger do not contribute to the deposition since they are found in the exhaust line.

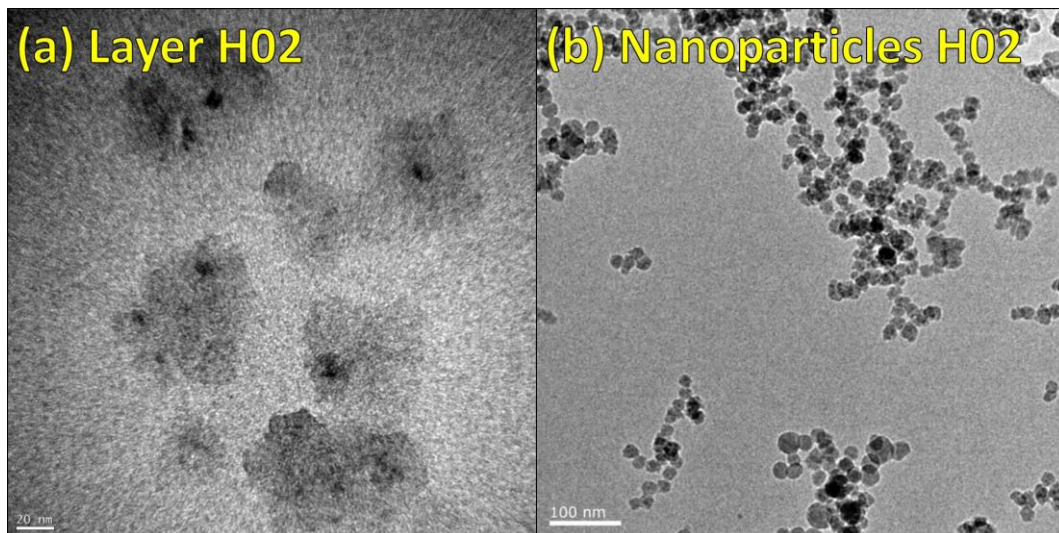


Figure 52: TEM images for H02 condition, of (a) the amorphous layer and (b) the amorphous nanoparticles collected on the cold finger installed in the exhaust line.

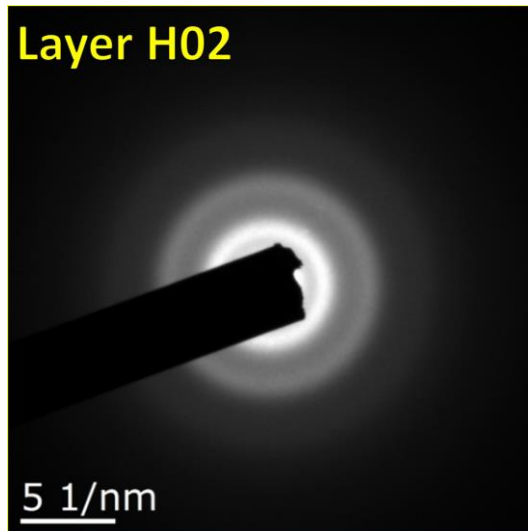


Figure 53: Diffraction pattern for H02 condition of the amorphous layer.

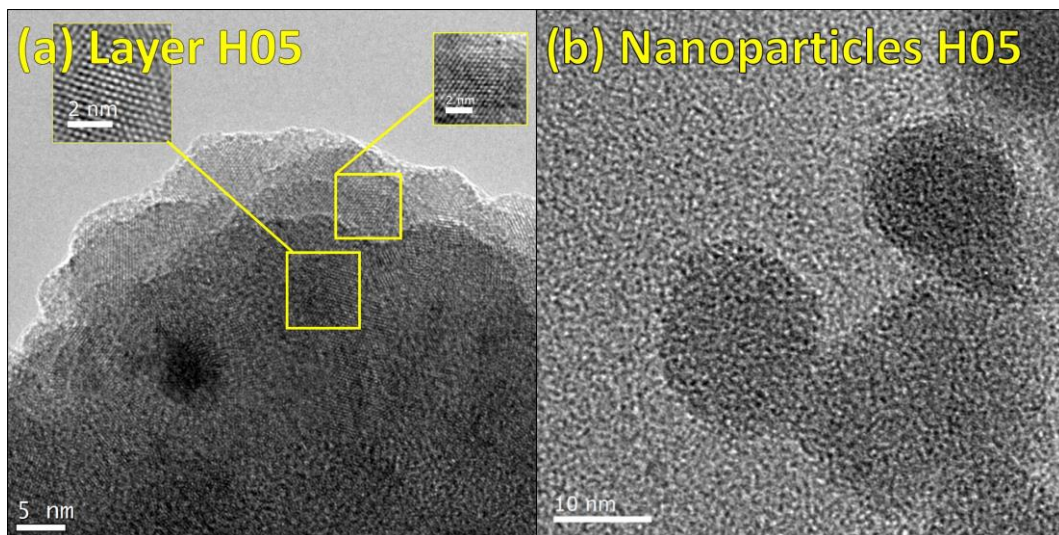


Figure 54: TEM images for H05 condition, of (a) the layer composed of a mixture of amorphous and microcrystalline phases and (b) the amorphous nanoparticles ( $\approx 10$  nm diameter) collected by the cold finger.

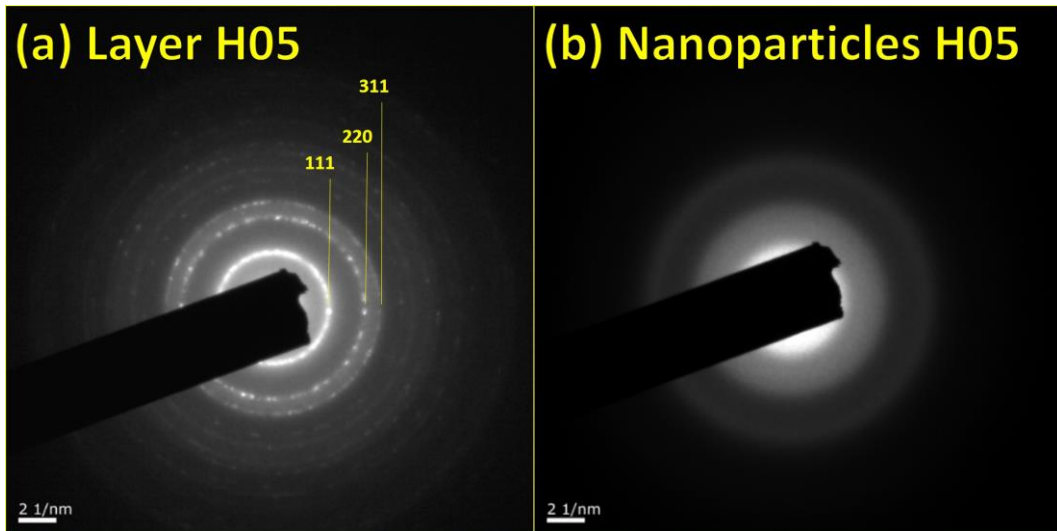


Figure 55: Diffraction patterns for H05 condition, of (a) the layer composed of a mixture of amorphous and microcrystalline and (b) the amorphous nanoparticles collected by the cold finger.

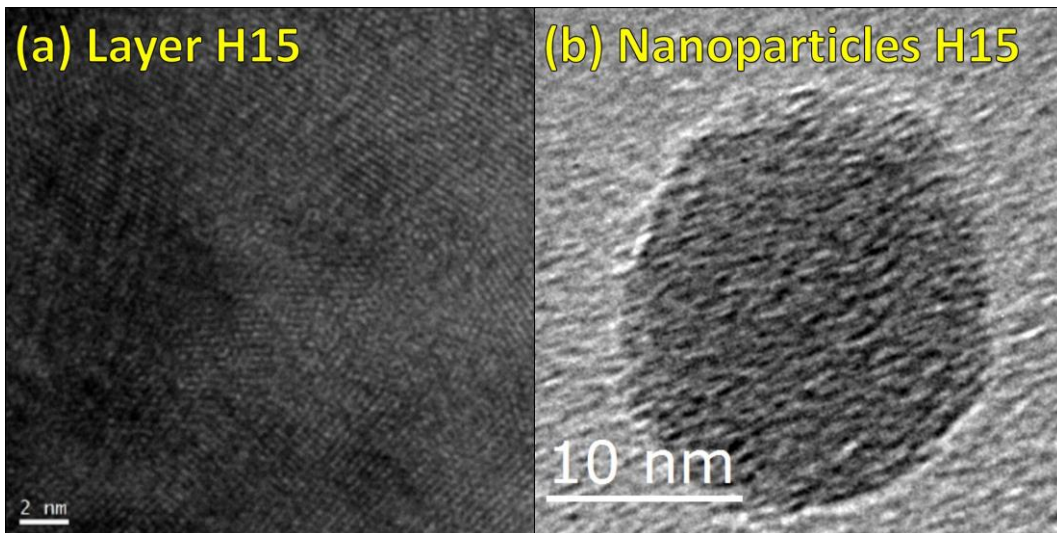


Figure 56: HR-TEM image for H15 condition, of (a) the microcrystalline layer and (b) the amorphous nanoparticles collected on the cold finger.

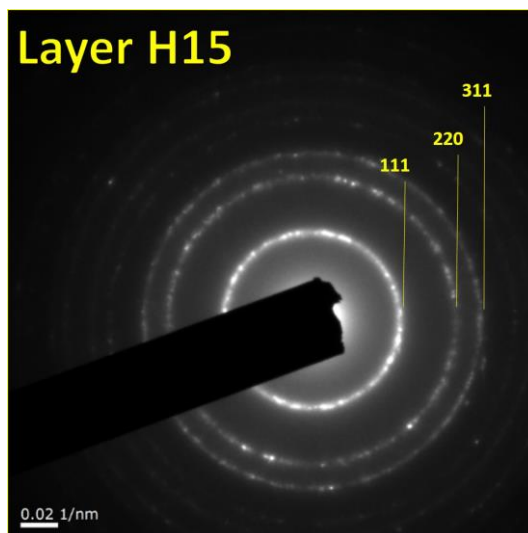


Figure 57: Diffraction pattern for H15 condition, of the microcrystalline layer.

TEM images of the H<sub>2</sub> flow rate series confirm the phenomenological model: at low H<sub>2</sub> flow rate (H02 condition) the films are amorphous while at high H<sub>2</sub> flow rate (H15 condition) the films are fully microcrystalline and finally at the transition (H05 condition) the layers are composed of a mixture of amorphous silicon and microcrystalline silicon. In all the cases, all nanoparticle are amorphous and therefore they cannot account for the crystallization of layers. Note that the size is independent of the H<sub>2</sub> flow rate. The surface crystallization of the film mediated by atomic hydrogen must take place via surface and subsurface reactions. Moreover large crystalline domains are found in H15 condition as depicted in Figure 58b. The inter-atomic distance is 3.2 Å which corresponds to cubic silicon.

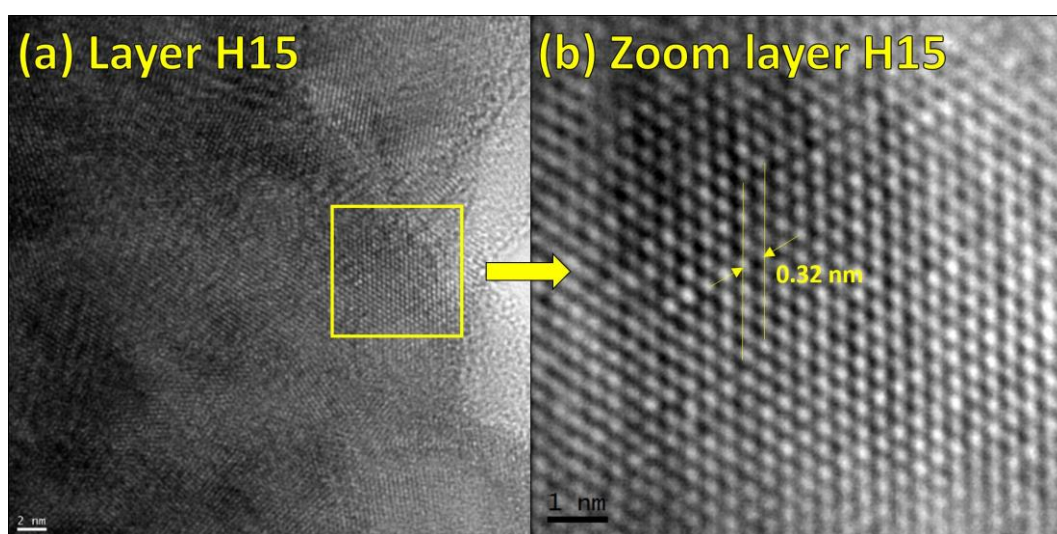


Figure 58: HR-TEM on the layer deposited under H15 condition. Crystalline domains of about 10 nm are found.

The thickness of the layer for the H05 condition is 76 nm as deduced from ellipsometry measurements on the glass substrate on which the copper grid is laying. This corresponds approximately to a deposition rate of 1.5 Å/s (consistent with Figure 48 at 20 W). This thickness is too big to allow a clear TEM characterization of the crystalline domains (many overlapping and embedded in the amorphous phase). A new deposition under the H05 condition has been performed during 120 s instead of 500 s. The measured thickness is 20 nm. Figure 59a shows the HR-TEM picture of the layer as well as its diffraction pattern (inset) in which spots are located on the crystalline ring of silicon (illustrating its crystalline structure). The FFT (Fourier transform) analysis of the high resolution TEM image clearly shows that several crystals are present. For these crystals, we have identified the {111} and the {200} spots. A single crystal orientation should contribute to only four spots. By selecting the

two spots separately with two masks (mask #1 and mask #2), images can be recomposed by iFFT (inverse Fourier transform). Figure 60a shows the recomposed image thanks to mask #1. Figure 60b shows the recomposed image thanks to mask #2. By overlapping the two recomposed images and using different color for each one (red for mask #1 and green for mask #2), the original image can be obtained where the two contributions can be identified, which is displayed in Figure 59b. Few-nanometer size crystalline domains are then unveiled in H05 condition.

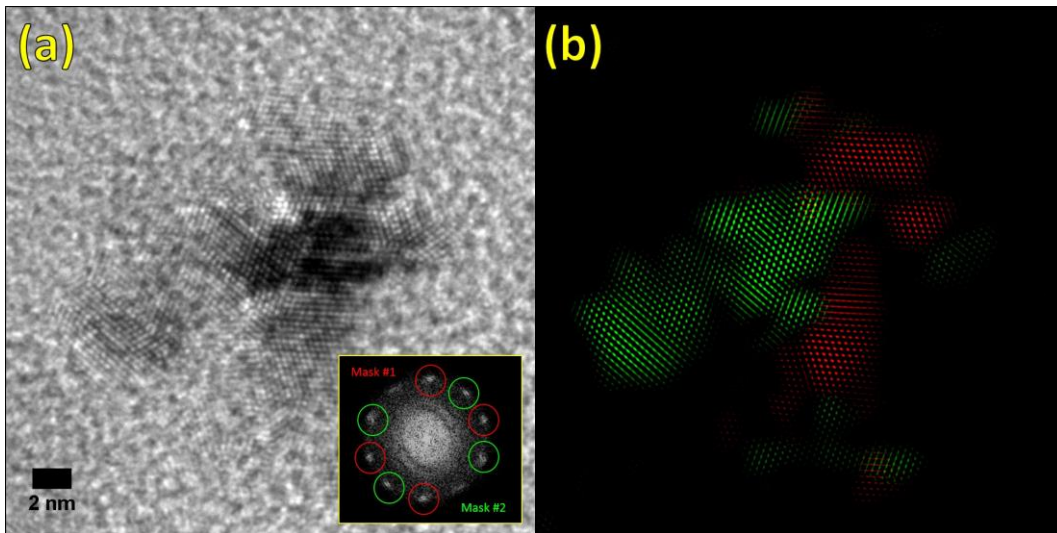


Figure 59: (a) HR-TEM on the layer in H10 condition with the diffraction pattern in the inset. Two orientations can be detected in (b) thanks to the inverse Fourier transform after proper masking of the diffraction pattern.

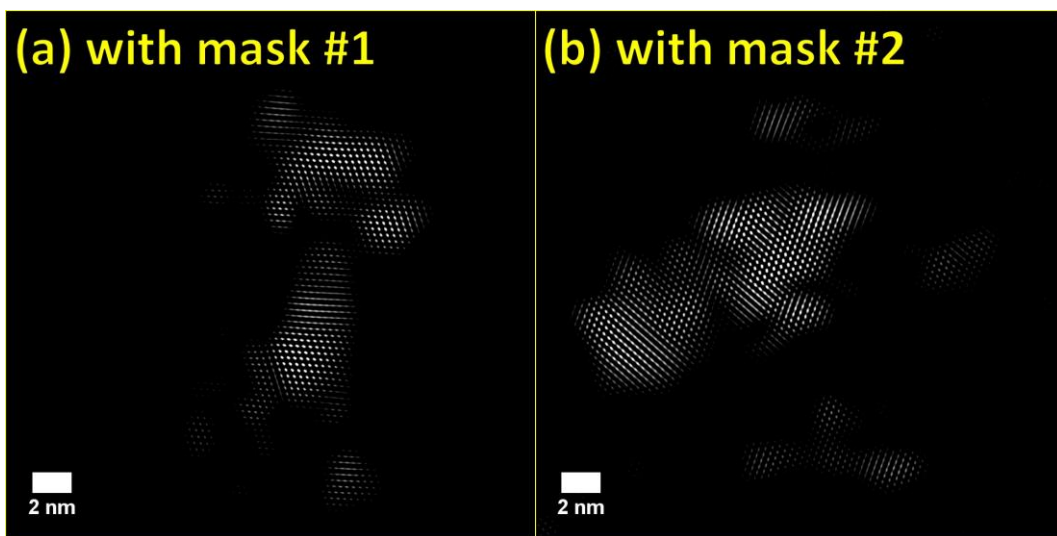


Figure 60: Inverse Fourier transform of TEM images (a) with the mask #1 and (b) with the mask #2.

Figures 61 and 63 show the TEM images of the samples deposited at high RF power (W050 and W100). For W050 condition, both amorphous and crystalline plasma-generated nanoparticles could be identified. The diffraction patterns of nanoparticles are given in Figures 62b and 64b. These results are completely consistent with the Raman spectroscopy analysis illustrated in Figure 50, confirming that the  $516\text{ cm}^{-1}$  crystalline peak is not due to laser irradiation-induced crystallization. Concerning the layer deposited in the same conditions, it is also found to be composed of a mixture of amorphous and microcrystalline silicon. At 100 W (W100 condition) all nanoparticles are crystalline. However the layer is a mixture of amorphous and microcrystalline silicon. The presence of an amorphous phase in W050 and W100 conditions is predicted by the phenomenological model ( $\text{H}_2$  depletion is above 90%, and

thus atomic hydrogen mainly binds to form HF instead of being a free radical to catalyze the crystallization). In the case of W050, amorphous nanoparticles can contribute to the amorphous phase of the layer. The microcrystalline phase can be associated to the crystallized nanoparticles. In the case of W100, nanoparticles (all crystallized) do not contribute to the amorphous phase but rather only to the microcrystalline phase of the layer.

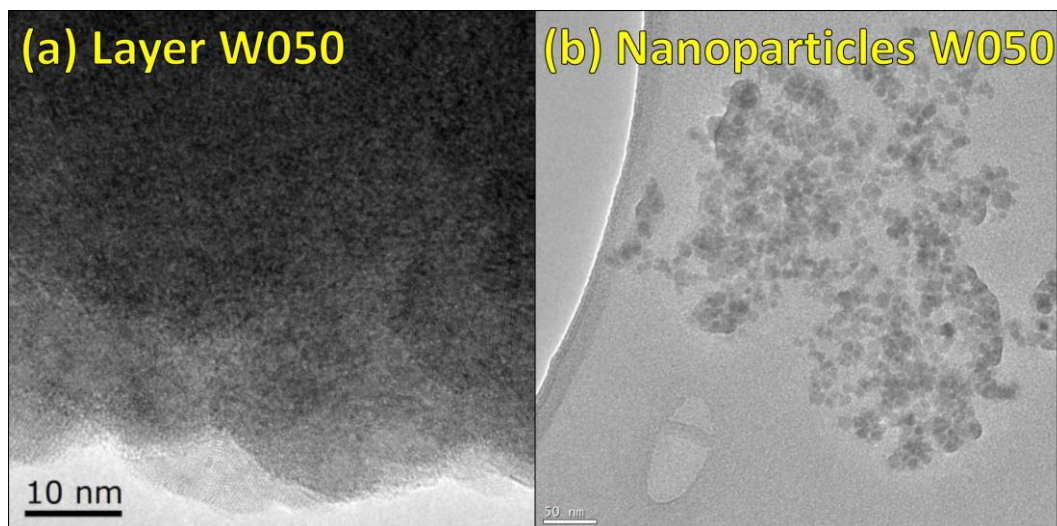


Figure 61: TEM images for W050 condition, of (a) the layer and (b) the nanoparticles of the cold finger. Both of them are a mixture of amorphous and microcrystalline silicon.

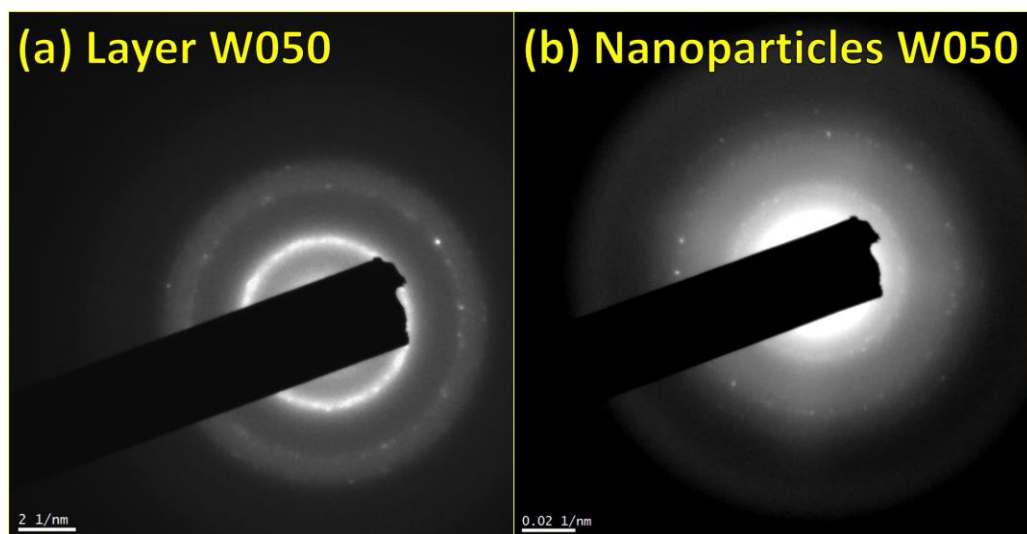


Figure 62: Diffraction patterns of the TEM images represented in Figure 61 for the sample synthesized under W050 condition, of (a) the layer and (b) the nanoparticles collected by the cold finger. The presence of a mixed structure of amorphous and microcrystalline silicon, for both (a) and (b), is revealed by the analysis of diffraction patterns.

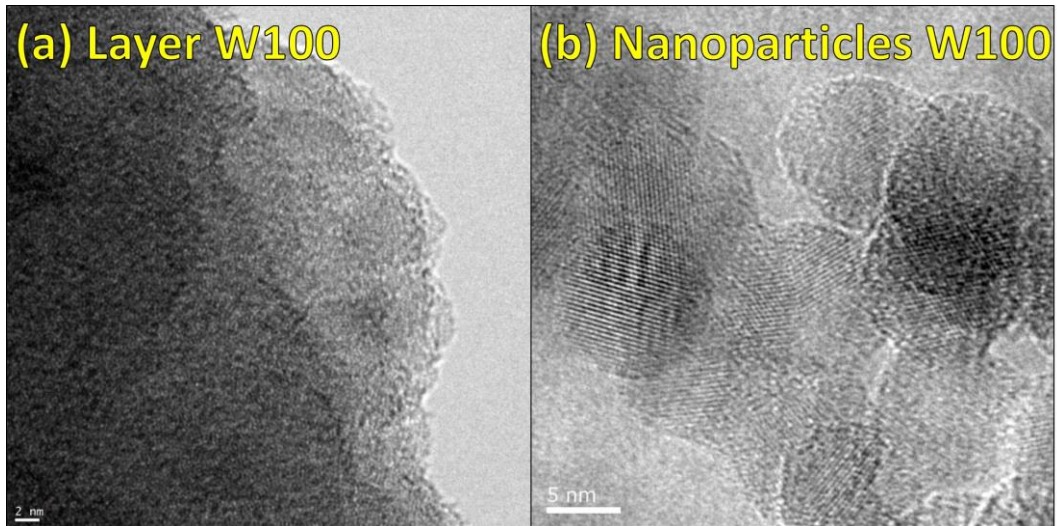


Figure 63: TEM images for W100 condition, of (a) the layer composed of a mixture of amorphous and microcrystalline silicon and (b) the crystalline nanoparticles of the cold finger.

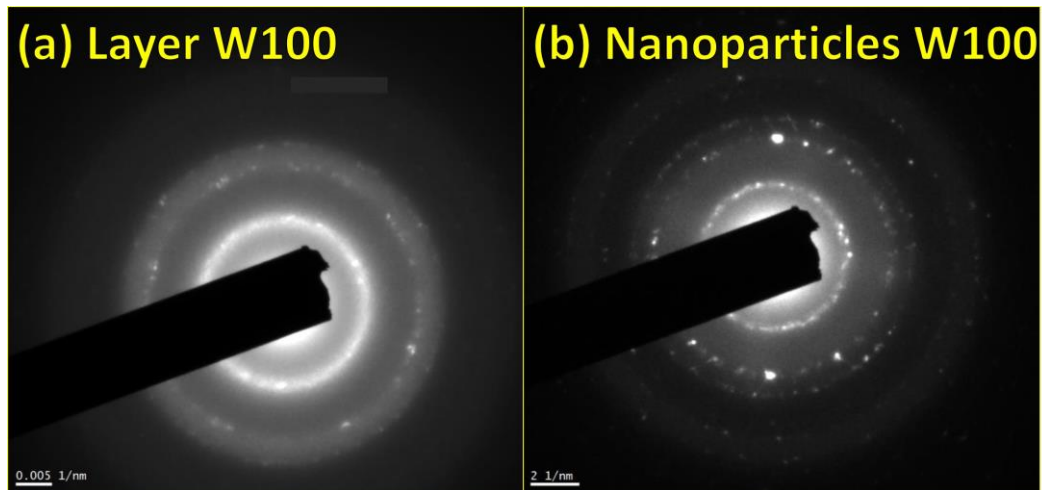


Figure 64: Diffraction patterns of the TEM images represented in Figure 63 for the sample synthesized under W100 condition, of (a) the layer composed of a mixture of amorphous and microcrystalline silicon and (b) the crystalline nanoparticles collected on the cold finger.

Figure 65 summarized some diffraction patterns taken on different areas of the layers and nanoparticles synthesized under W050 and W100 plasma conditions. The red arrows indicate the direction of the increase of crystalline fraction that can be estimated visually by comparing the intensities of the disks corresponding to the amorphous and the crystalline parts. As discussed above, the layer (a) seems more crystallized than the nanoparticles (b) synthesized under W050 condition, while the nanoparticles (d) are more crystalline than the layer (c) synthesized in W100 condition. Moreover the comparison between nanoparticles indicates that the ones made at 100 W (d) are more crystalline than the ones made at 50 W (b). These results made us conclude on the fact that a very high power seems to be needed to crystallize all the nanoparticles while an intermediate power will only crystallize a part of them.

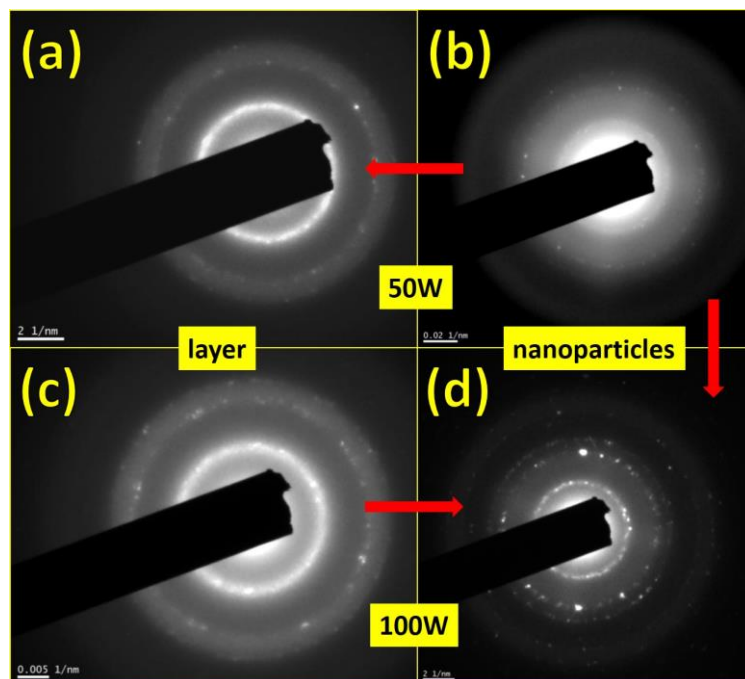


Figure 65: Diffraction pattern of (a) layer deposited at 50 W, (b) nanoparticles of the cold finger synthesized at 50 W, (c) layer deposited at 100 W, and (d) nanoparticles of the cold finger synthesized at 100 W. The red arrows indicate the increase of the crystalline fraction estimated visually from diffraction patterns.

In this section we have treated so far the H<sub>2</sub> flow rate series and the RF power series separately. By combining the two studies, one can invoke two types of crystallization to account for all experimental results: film crystallization through surface and subsurface reactions mediated by atomic hydrogen and plasma phase crystallization of nanoparticles. The detailed mechanisms of nanoparticle crystallization are not addressed here but some mechanisms have been proposed such as H-induced crystallization, electron-ion recombination, and heating above melting temperature [56][57][58][67]. The film crystallization is consistent with the phenomenological model. The findings of amorphous and crystalline nanoparticles are not new but it is worth noticing here that the conditions associated with each nature is now better known. Moreover, each type of crystallization is linked to one plasma parameter: the surface crystallization to H<sub>2</sub> flow rate and the plasma phase nanoparticles crystallization to the RF power.

Figure 66 maps the measured structure (amorphous or crystalline) as deduced from TEM measurements on layers and nanoparticles and the predictions of the phenomenological model (for the conditions H02, H05, H15, W050, and W100). The two types of crystallization (on the substrate or in the plasma) are represented by two different colors: red squares for surface crystallization and purple diamonds for plasma crystallization.

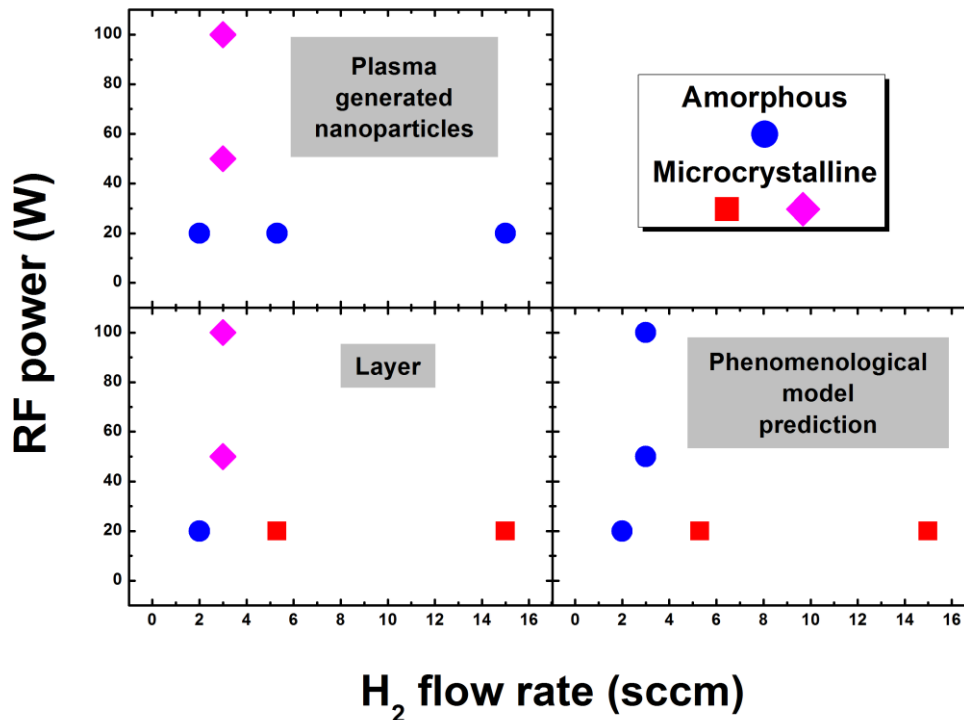
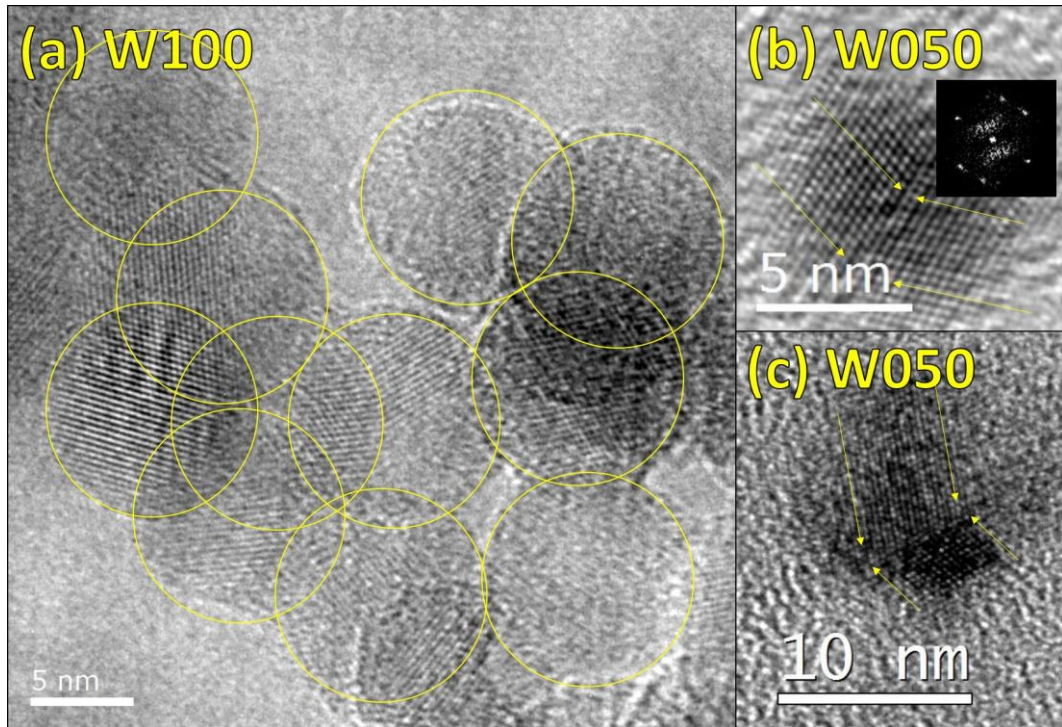


Figure 66: Amorphous or microcrystalline nature mapping of nanoparticles and layers compared to the model predictions, for H<sub>2</sub> flow rate and RF power series.

Let us afford an excessive simplification in order to outline the two main and concurrent crystallization mechanisms: surface crystallization due to atomic hydrogen. By doing so, crystallization can take place either by radicals or by nanoparticles. At low RF power, crystallization by radical occurs while crystallization by nanoparticles does not occur. However at high RF power, deposition from radicals should be amorphous but nanoparticles are crystalline, leading to a mixture of amorphous and microcrystalline silicon.

### 3.3.4 Morphology of nanoparticles

To conclude the TEM study on nanoparticles, we would like to emphasize the result of Figure 63b where spherical crystalline nanoparticles have been observed. The majority of the nanoparticles produced under W100 conditions present this morphology. The same picture is displayed in Figure 67a where yellow circles have been added highlighting all the nanoparticles. No stacking faults have been observed on the particles. On the contrary, when synthesized in W050 conditions, both types of nanoparticles (amorphous or microcrystalline) can be found. The main sizes of all the analyzed nanoparticles are 5-10 nm. The microcrystalline ones have irregular shapes. Moreover they undergo a poor crystallization and defects as twinned planes are often found as depicted in Figure 67b and 67c. An insufficient RF power (W050) hindered the nanoparticle crystallization, while sufficient RF power (W100) leads to perfect crystallization. Therefore, the crystallization is really due to RF power and the crystalline quality depends on it too.



**Figure 67: HR-TEM image of nanoparticles of the cold finger in (a) W100 condition and (b) (c) W050 condition. For W100, spherical perfect nanoparticles while for W050 irregular shapes and twinned planes are found. Yellow arrows are guides for the eyes and indicate the twinned planes.**

Nanoparticles produced under the condition of W100 but with a RF temperature set to 200°C (instead of 80°C) have been collected and studied by TEM. Figure 68a shows them: their shapes are irregular but close to spheres. The center is crystallized while the periphery is amorphous (oxidized or not). The corresponding diffraction pattern in Figure 68b demonstrates the crystalline structure of the nanoparticles. It also reveals that crystallization is better at 80°C than at 200°C: more crystalline rings can be observed in Figure 68b than in Figure 68c which is the diffraction pattern of nanoparticles at 80°C (and 100 W). Each ring corresponds to one lattice plane (3.14 Å for (111), 1.92 Å for (220), 1.64 Å for (311), etc.). As in the 80°C case, the layer is composed of a mixture of amorphous and microcrystalline silicon.

The sizes of nanoparticles are similar at 200°C and 80°C. We have previously stated that an increase of the RF temperature hinders the formation of nanoparticles, leading to a low deposition rates as shown in Figure 29 at high RF temperature. However, that is not inconsistent with the size similarity at 200°C and 80°C found in Figures 67a and 68a. Only large nanoparticles are collected on the cold finger. Small nanoparticles are neutral and contributed to the growth. The formation of these small nanoparticles does depend on the gas temperature. However, as explained in [48], the fast coagulation phenomenon does not depend on temperature but only on the 2 nm nanoparticles concentration (about  $10^{10}$ - $10^{11}$ cm<sup>-3</sup>). Large nanoparticles are then formed and their size is temperature independent. The  $\alpha$ - $\gamma'$  transition occurs when nanoparticle size exceeds the critical value of 6 nm [48]. TEM images show plasma-generated nanoparticles of 10 nm, demonstrating the  $\gamma'$  regime of our SiF<sub>4</sub>/H<sub>2</sub>/Ar plasmas in the steady state. It should be pointed out here that in [48] the plasma chemistry was SiH<sub>4</sub>/Ar, but results should in some extent be considered as valid for our fluorinated chemistry.

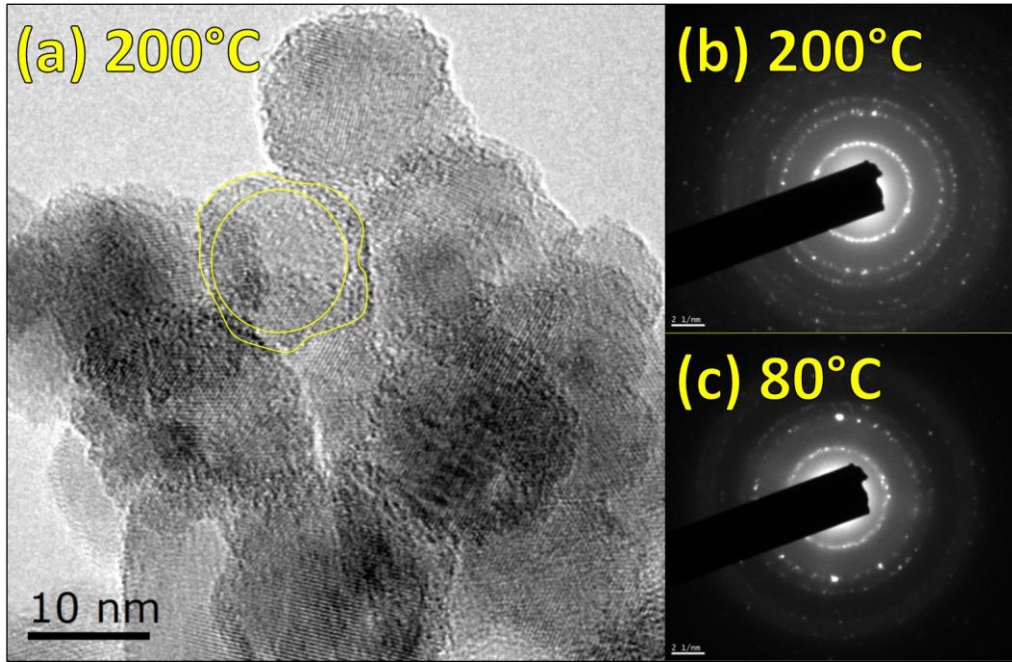


Figure 68: (a) HR-TEM image of nanoparticles of the cold finger at 100 W and 200°C with its diffraction pattern in (b). For the comparison, diffraction pattern of nanoparticles at 100 W and 80°C is given in (c).

### 3.4 Self-sustained plasma oscillations

#### 3.4.1 Overview

After switching on the RF power, the plasma appears and a few seconds later a steady state is reached: electrical ( $V_{DC}$  and  $V_{RF}$ ) and optical (OES signals) parameters are constant in time. Steady state is by far the most often encountered situation. However, under some conditions, no-steady state happens: discharge parameters fluctuate with a period of a few seconds. Plasma instabilities have been widely studied in dusty plasmas [68][69]. In our  $\text{SiF}_4/\text{H}_2/\text{Ar}$  for instance, the argon emission line at 750 nm can oscillate as shown in Figure 69. The envelope of beats is constant for the upper bound, but decreases for the lower bound as shown in the inset of the figure. By taking the maximum signal as a reference, the amplitude of the oscillations represents at the beginning 10% of the maximum. 300 s later it represents 30% of the maximum. That shows that this oscillating phenomenon can be significant and can only be explained by important changes in plasma parameters ( $n_e$ ,  $T_e$ , ect.) and plasma chemistry (radicals, nanoparticles, ect.).

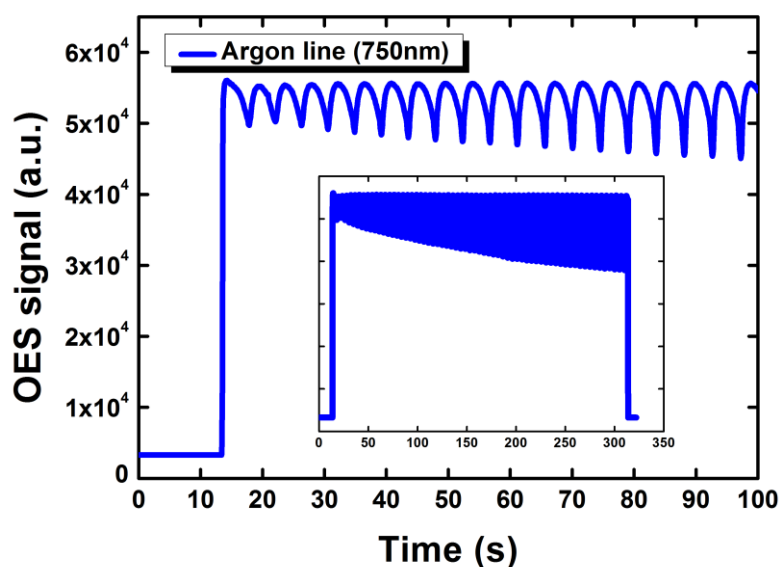


Figure 69: Example of oscillations of OES Argon signal at 750 nm.  
The inset shows the signal on a longer time scale.

This kind of oscillations have been reported by our group in [49], where they are called “very low frequency oscillations”. One can find in [49] a detailed literature review of a wide range of plasma oscillation frequencies. Oscillations have been observed for different chemistries:  $\text{SiH}_4/\text{H}_2$ ,  $\text{GeH}_4/\text{H}_2/\text{Ar}$ , and  $\text{SiF}_4/\text{H}_2/\text{Ar}$ . The explanation of these oscillations is related to the  $\alpha$ - $\gamma'$  transition. When  $\gamma'$  regime is reached, the electron density drastically decreases due to electron attachment on nanoparticles and to balance this diminution, electron temperature increases [49]. However the loss of electrons translates into less radical formation, thus hindering nanoparticles growth. That describes the first part of the cycle. The second one consists in a decrease of nanoparticles concentrations and consequently electron density returns to higher values and more radicals are formed. These oscillations will sustain, no external oscillator is required. Explanations from experimental artefacts (oscillations of butterfly valve, mass flow controller, ect.) have been properly discarded. These fluctuations are intrinsic to the plasma and are called self-sustained oscillations.

Contrary to what reported in [49], all parameters always oscillate with the same frequency. The period ranges from 1 s to 10 s. The waveform is not unique as well as the envelop function and their amplitude. Figure 70 shows a non-exhaustive zoology of waveforms we can encounter. In case (a), small oscillations can be seen at the beginning but vanish and a steady state is reached. After 2 min, the steady state is broken and the system starts to oscillate with a relative amplitude of 10% and a period of 3.3 s. In case (b), the plasma directly oscillates from it start. Relative amplitude is 10%, but after 2 min, it increases up to 15%, and 3 min later up to 20%. The period is estimated at 5.6 s. In case (c), after 1 min of stable oscillations, the plasma starts to fluctuate chaotically but periodically. The relative amplitude is 15% while the period is 6.3 s. Finally, in case (d), small oscillations are found with a relative amplitude of 3% and a period of 5.4 s.

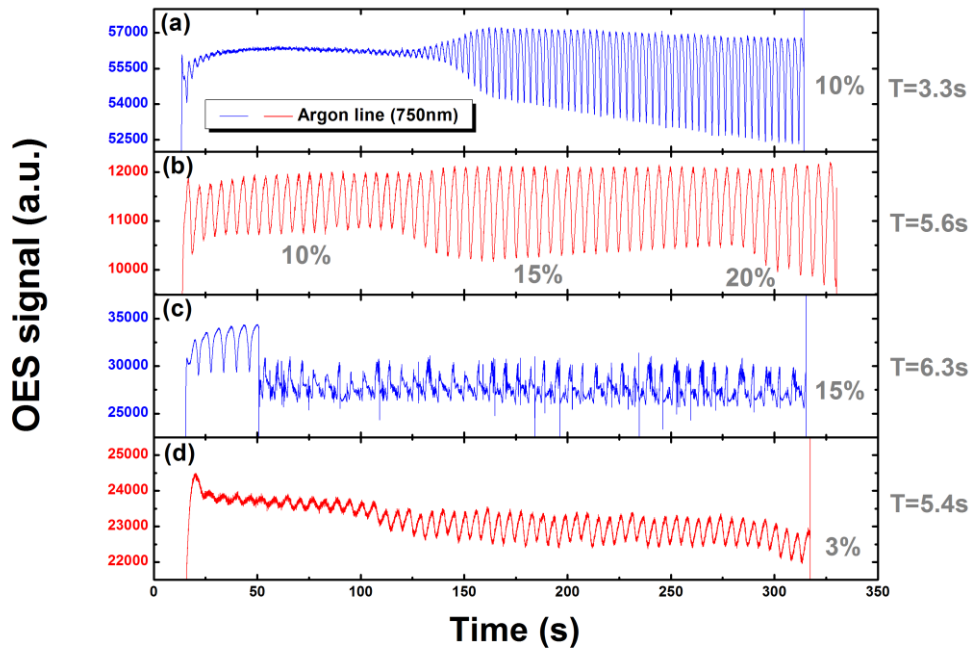


Figure 70: Different self-sustained oscillation waveforms.

Relative amplitudes and periods are given in percentage of the total amplitude and in seconds respectively.

### 3.4.2 Detailed analysis of the OES oscillations

As shown in Figure 70, the 750 nm argon line oscillates in time. Indeed, the whole optical emission spectrum fluctuates. Based on the SiF<sub>4</sub>/H<sub>2</sub> plasma OES spectrum study in [32], an emission line can be associated to an excited species. One species can have multiple lines depending on the possible transitions between energy states. Generally, there is no straightforward relation between emission line intensity and the related species concentration in the plasma because the density of excited species is a non-linear function of the electron density ( $n_e$ ), of the electron temperature ( $T_e$ ), of the excitation cross-section, and of the radiative emission decay time.

We focus on specific emission lines of SiF<sub>4</sub>/H<sub>2</sub>/Ar chemistry: SiF at 443 nm, SiF<sub>2</sub> at 395 nm, SiF<sub>3</sub> at 240 nm, H<sub>2</sub> at 602 nm, H<sub>α</sub> at 656 nm, H<sub>β</sub> at 486 nm, and Ar at 750 nm. Normalized OES emission of all these lines are displayed in Figure 71 and sorted by their molecule origin (SiF<sub>4</sub>, H<sub>2</sub> or Ar). By taking argon line as a reference, two groups of species can be formed: ones oscillating in phase and others oscillating in opposite phase. Only H<sub>2</sub> is in-phase with argon while H<sub>α</sub>, H<sub>β</sub>, SiF, SiF<sub>2</sub>, and SiF<sub>3</sub> are in antiphase. SiF<sub>2</sub> and H<sub>α</sub> signals seem to belong to antiphase. However a small decrease can be seen just before the maximum of SiF<sub>3</sub> signal. The minimum of Ar and H<sub>2</sub> corresponds to the maximum of SiF, SiF<sub>3</sub> as depicted in Figure 71 with the gray vertical lines. The reciprocal is not true: minimum of SiF and SiF<sub>3</sub> does not match the maximum of Ar and H<sub>2</sub>. That demonstrates the complexity of underlying process. Moreover the phase shift  $\phi$  between RF current and RF voltage is displayed in Figure 71. It is intimately related to the real part of the plasma impedance which is itself related to the composition of the plasma. The resistive part is proportional to the electron collision frequency [52] and in dusty plasmas, collisions between electrons and nanoparticles are important. The term is proportional to the density of nanoparticles and to the mean electron thermal velocity [52] which is an increasing function of  $T_e$ .

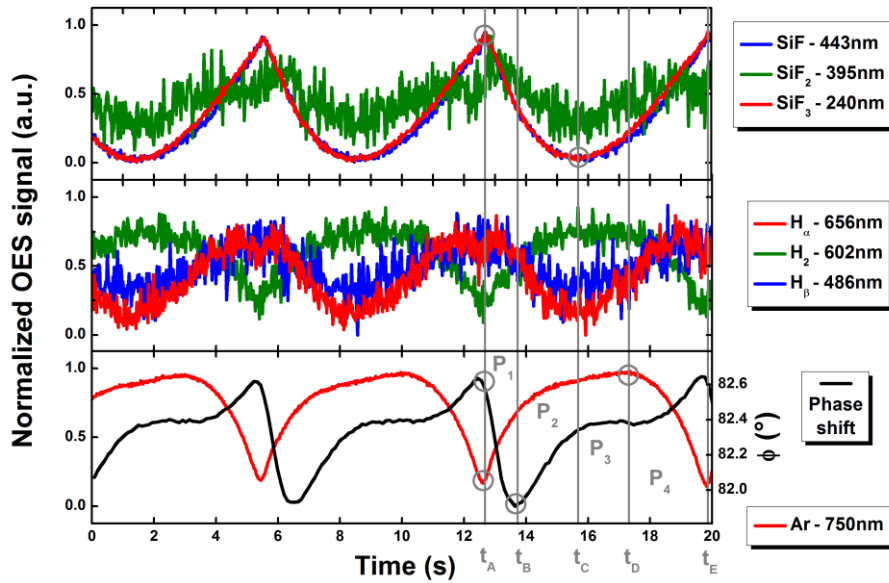


Figure 71: Oscillations of different OES lines: SiF, SiF<sub>2</sub>, SiF<sub>3</sub>, H<sub>2</sub>, H<sub>α</sub>, H<sub>β</sub> and Ar.

We define five times for each period of  $\approx 6.5$  seconds in the waveform:

- $t_A$  when SiF and  $\phi$  are maximum while Ar is minimum.
- $t_B$  when  $\phi$  is minimum (more resistive plasma).
- $t_C$  when SiF is minimum.
- $t_D$  when Ar is maximum.
- $t_E$  defined similarly to  $t_A$ .  $t_E - t_A$  represent the period of the oscillations.

Such time scale allows us to define four phases in the waveforms:

- P<sub>1</sub> between  $t_A$  and  $t_B$ .
- P<sub>2</sub> between  $t_B$  and  $t_C$ .
- P<sub>3</sub> between  $t_C$  and  $t_D$ .
- P<sub>4</sub> between  $t_D$  and  $t_E$ .

Figure 72 shows the phase portrait of the two dynamic variables: Ar and SiF. The time has disappeared and the time evolution happens following the curve of SiF signal as a function of Ar signal. The curves have been divided into four parts corresponding exactly to P<sub>1</sub>, P<sub>2</sub>, P<sub>3</sub>, and P<sub>4</sub>.

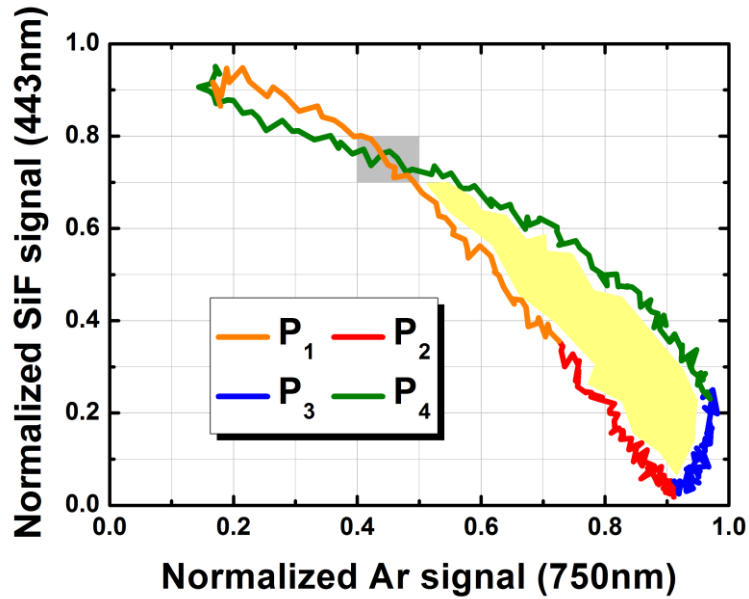


Figure 72: Phase portrait of one waveform: SiF (443 nm) as a function of Ar (750 nm).

The form of the curve is elongated showing a strong correlation between Ar and SiF. The elongation has a negative slope due to the opposite phase between Ar and SiF oscillations. However SiF is not simply the opposite of Ar signal: the curve is not a straight line. The yellow area confined within the curve demonstrates that the correlation is not full. Both are functions of two independent dynamical variables. The knowledge of these independent variables is difficult. Reference [49] suggests that large nanoparticles density and electron temperature are the two important dynamics variables. Furthermore, because of the crossing in phase portrait of trajectory in  $P_1$  and  $P_4$  (gray background square), the number of all independent dynamics variables could not be only two. There is at least another dynamic parameter explaining why for the same Ar and SiF signal values the system follows two different trajectories.

Figure 73 shows the phase portrait of  $H_\alpha$  and SiF lines. Again the curve is divided in four parts. The  $H_\alpha$  line is stable in the  $P_1$  part while Ar is increasing. In the  $P_2$  part,  $H_\alpha$  starts to decrease while Ar continues to increase. That is different from SiF behavior of Figure 72 where SiF decrease in  $P_1$  and  $P_2$  part while Ar increases. However the  $H_\alpha$  behavior is similar to SiF in  $P_3$  and  $P_4$  parts.

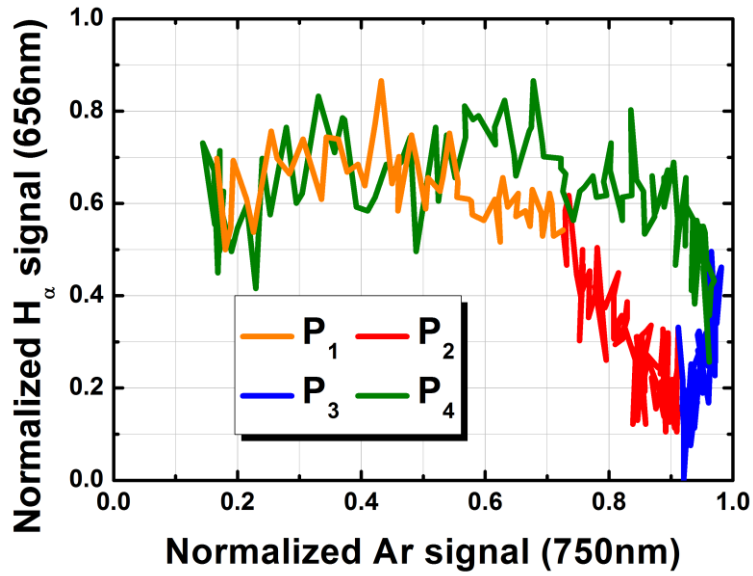


Figure 73: Phase portrait of one waveform:  $H_{\alpha}$  (656 nm) as a function of Ar (750 nm).

The variations of Ar, SiF and  $H_{\alpha}$  lines and of  $\phi$  are summarized in Table 25. The argon signal does not increase of a lot in  $P_2$  and  $P_3$  parts.

Part	$P_1$	$P_2$	$P_3$	$P_4$	$P_1$
Ar	↗	=	=	↘	↗
SiF	↘		↗		↘
$H_{\alpha}$	=	↘	↗		=
$\phi$	↘	↗	=	↗	↘

Table 25: Variations of Ar, SiF,  $H_{\alpha}$ , and  $\phi$  during one period of oscillation.

The oscillation mechanism of [49] is in line with the description of the  $\alpha$ - $\gamma'$  transition of [48]. The first step is the formation of small nanoparticles of 2 nm diameter. The second step is the coagulation of these small nanoparticles into large nanoparticles. During this step, the growth of nanoparticles is negligible. The merging of two nanoparticles keeps constant the total volume but decreases the developed (external) surface. Therefore during the coagulation phase, whole volume is constant and whole developed surface is decreasing. The third step happens when nanoparticles diameter reaches 6 nm [48]. Plasma parameters drastically change:  $n_e$  drops by a factor of 10 and  $T_e$  triples (from 2 eV to 6 eV). These changes are due to the intense electron attachment on 6 nm diameter nanoparticles, and characterizes the  $\alpha$ - $\gamma'$  transition. The increase of electron temperature is the compensation of the new loss mechanism [48].

The argon signal is a function of  $n_e$  and  $T_e$ . However the signal is only proportional to  $n_e$  whereas it is exponentially increasing with the inverse of  $T_e$ . The dependency in  $T_e$  is stronger. We assume that the argon signal increases when  $T_e$  is high and inversely that it decreases when  $T_e$  is low. Therefore, under this assumption, during part  $P_1$ ,  $T_e$  is increasing. According to [48][52], the increase in  $T_e$  is due to the decrease in  $n_e$  which is itself due to attachment on nanoparticles. That is consistent with the

increase of the resistive part of the plasma impedance since we measure a decrease of  $\phi$  in part  $P_1$ . The other variations in parts  $P_2$ ,  $P_3$  and  $P_4$  for the argon signal are difficult to interpret. That applies also to SiF and  $H_\alpha$ . What we can see it that  $\phi$  increases between  $P_2$  and  $P_4$ . That increase can be due to a decrease of the density of nanoparticles by their pumping or their deposition on surface, or by their coagulation: the number of nanoparticles decreases whereas their total volume is constant [48].

Other evolutions can be found for Ar/SiF phase portrait in different plasma conditions as ones for Figure 70a which phase diagram is displayed in Figure 74b. Between 50 s and 75 s the steady state is represented by a point in the portrait. When the plasma starts to oscillate, Ar and SiF signals begin to draw an elongate ellipse which passes through the steady state point. The ellipse becomes bigger and bigger after each oscillation until a limit cycle is reached (between 175 s and 200 s, drawn in red color in Figures 74a and 74b).

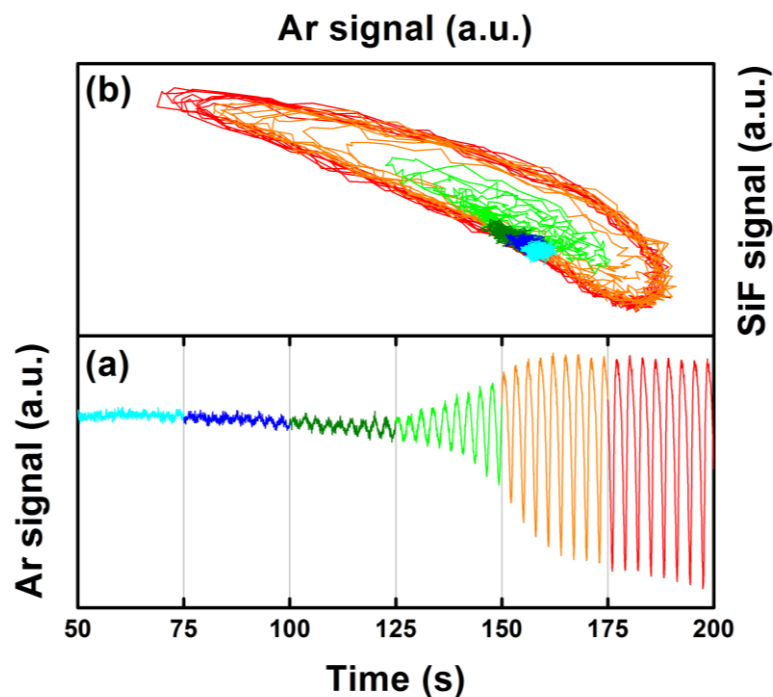


Figure 74: Phase portrait (a) of Ar/SiF signal of oscillations (b) (same as in Figure 70a).

### 3.4.3 Toy model

In reference [49], a simulation of the growth of nanoparticles was proposed. The ingredients of the simulation are (i) nucleation of 1 nm diameter nanoparticles, (ii) growth of nanoparticles up to 80 nm, (iii) finite residence time of nanoparticles (due to pumping) and finally (iv) electron attachment on large nanoparticles (above a given diameter threshold). The electron attachment acts like a negative feedback loop, producing oscillations in some conditions. Precisely low residence time leads to damped oscillations whereas high residence time produces self-sustained oscillations.

The advantage of this simulation is the reproduction of oscillation or damping. The drawback is the non-analytical solution of the equations. Only simulation can be done. Another approach is to choose a simpler model sufficiently “rich” to reproduce oscillation/damping transition. The equations are linear but non-linearity will not change the fundamental idea behind the transition from steady state plasma conditions to self-sustained oscillation conditions. Moreover, the model is made of equations with a physical meaning. We call the model “toy model” as it allow us to play with basic concepts.

Let us consider three species X, Y, Z representing respectively radicals, small nanoparticles and large nanoparticles. We allow reactions which consume species and create new species. We assume a continuous supply of X species which is described by Equation (32). In this set of reactions (32-39), the

rate of each reaction is displayed on top of the arrow starting from reactants and ending with products. Small nanoparticles (Y species) are formed from radicals (X species). The corresponding reaction is given in Equation (33) where the reaction rate is called  $\alpha$ . Similarly, large nanoparticles (Z species) are grown from small nanoparticles (Y species) and the associated reaction is Equation (34). For a simple model, the same reaction rate is chosen – which is a strong assumption but we adopt it for the sake of simplicity. In Equation (35), Z species can form another species called “T” in which we are not interested to (the primary reason of this reaction will be understood afterwards as it allows the toy model to be analytically solved). Electron attachment is modeled as follow: each Z species will decrease the electron density and therefore less radicals will be produced. The X species are then coupled to the Z species. It is equivalent to state that there is a reaction where Z is the reactant and where the product is the same Z species and the loss of one X species, written  $-X$ . Equation (36) represents the electron attachment on large nanoparticles and the coupling factor is named  $\gamma$  (in reference to the phenomenon responsible to the transition from  $\alpha$  to  $\gamma'$  regime). Finally, we introduce pumping of all species which can be written as Equations (37), (38), and (39). Letter “P” refers to pumping. The rate is the inverse of a time, because strongly related to a residence time. Note that the rate is different for Z species. To simplify again, we will consider  $\tau$  and  $\tau'$  as equal, but we will discuss the case of inequality as well.



We use for the model exactly the same ingredients as the simulation of reference [49]: (i) nucleation of small nanoparticles by Equation (33), (ii) growth of large nanoparticles by Equation (34), (iii) finite residence time by Equations (37)-(38)-(39), and finally (iv) negative feedback loop of electron attachment on large nanoparticles by Equation (36).

Based on this set of reactions, we are able to write the associated dynamic equations. The concentrations of X, Y, and Z species are noted respectively  $x$ ,  $y$  and  $z$ . On the reactants side of all the reactions, only one species at maximum appears. There is no two-body reaction. Therefore the differential equations are all linear as given by Equations (40), (41), and (42).

$$\dot{x} = \Phi - \alpha \cdot x - x/\tau - \gamma \cdot z \quad (40)$$

$$\dot{y} = \alpha \cdot x - \alpha \cdot y - y/\tau \quad (41)$$

$$\dot{z} = \alpha \cdot y - \alpha \cdot z - z/\tau' \quad (42)$$

These three equations form a linear system of ordinary differential equations (ODE). The steady state solution ( $x_{ss}$ ,  $y_{ss}$ , and  $z_{ss}$ ) is easy to find. Let us set  $\beta = \alpha + 1/\tau$ . Equations (43), (44), and (45) give respectively  $x_{ss}$ ,  $y_{ss}$ , and  $z_{ss}$ . Without coupling ( $\gamma=0$ ), they simplify into respectively  $\beta \cdot \Phi$ ,  $\alpha \cdot \Phi$ , and  $\alpha^2/\beta \cdot \Phi$ . An increase of the residence time ( $\tau$ ) or of growth rate of particles ( $\alpha$ ) produces more large nanoparticles compared to radical, and leads to dustier plasma conditions.

With coupling ( $\gamma \neq 0$ ), the concentration of all species decreases compared to the non-coupling case: electron trapping on large nanoparticles is detrimental to the global number of species.

$$x_{ss} = \beta^3 \cdot \frac{\Phi}{\beta^2 + \gamma \cdot \alpha^2} \quad (43)$$

$$y_{ss} = \alpha \cdot \beta^2 \cdot \frac{\Phi}{\beta^2 + \gamma \cdot \alpha^2} \quad (44)$$

$$z_{ss} = \alpha^2 \cdot \beta \cdot \frac{\Phi}{\beta^2 + \gamma \cdot \alpha^2} \quad (45)$$

Mathematically the steady-state solution verifies all the equations. However the crucial point is the question of the stability of this solution: if the plasma is close to that solution, does the system return back to the steady state point, or does it deviate indefinitely?. In fact the stability condition of the steady state solution will give us the transition from damping to oscillation. As soon as the steady-state solution is stable, the plasma will converge (after a transient regime) to a steady-state. When the steady stage solution becomes unstable, the plasma will converge to a limit cycle. It is worth noticing here that our model is simple and ODE are linear. Therefore no limit cycle will be seen. By adding non-linearity, limit cycles will appear. We can reasonably believe in plasma physics, non-linearities are the rule and not the exception. By adding non-linearity, no analytical solution can be found. However the spirit of the limit cycle is kept: the crucial point to check is the stability of the steady state solution. A good example of dynamics equations with non-linearity and with a transition from steady-state solution and self-sustained oscillations is the autocatalytic reaction named "Brusselator" (whose explanation can be easily found on the internet).

To assess the stability question of the steady-state solution, one can use the Jacobian matrix of the system, representing the partial derivatives (in  $x$ ,  $y$ , and  $z$ ) of time-derivative of  $x$ ,  $y$ , and  $z$  as defined in Equation (46). From a mathematical point of view, the (complex) eigenvalues of the Jacobian matrix will decide on the stability or not of the steady-state solution. If the real parts of all the three eigenvalues are strictly negative, stability will be encountered. However, if at least one has a positive real part, the solution will not be stable.

$$J = \begin{pmatrix} \frac{\partial \dot{x}}{\partial x} & \frac{\partial \dot{x}}{\partial y} & \frac{\partial \dot{x}}{\partial z} \\ \frac{\partial \dot{y}}{\partial x} & \frac{\partial \dot{y}}{\partial y} & \frac{\partial \dot{y}}{\partial z} \\ \frac{\partial \dot{z}}{\partial x} & \frac{\partial \dot{z}}{\partial y} & \frac{\partial \dot{z}}{\partial z} \end{pmatrix} \quad (46)$$

From equations (40), (41), and (42), one can calculate the Jacobian matrix and found Equation (47). Its characteristic polynomial is given in Equation (48) and its roots are exactly the eigenvalue of the

matrix. We take  $\tau' = \tau$ . The roots of this polynomial ( $\lambda_0$ ,  $\lambda_1$ , and  $\lambda_2$ ) are very simple (we have been rewarded from all the simplifications we have made!) and are given by Equation (49) where  $j$  stands for  $\exp(2i\pi/3)$  verifying  $j^3=1$ .

$$J = \begin{pmatrix} -\frac{1}{\tau} - \alpha & 0 & -\gamma \\ -\alpha & -\frac{1}{\tau} - \alpha & 0 \\ 0 & -\alpha & -\frac{1}{\tau'} - \alpha \end{pmatrix} = \begin{pmatrix} -\beta & 0 & -\gamma \\ -\alpha & -\beta & 0 \\ 0 & -\alpha & -\beta \end{pmatrix} \quad (47)$$

$$P_c(\lambda) = \det(\lambda \cdot Id - J) = (\lambda + \beta)^3 + \alpha \cdot \gamma^2 \quad (48)$$

$$\lambda_k = -\beta - j^k \cdot \sqrt[3]{\gamma \cdot \alpha^2}, k \in \{0,1,2\} \quad (49)$$

By deviating from the steady state, the evolution of the deviation will be ruled by the three functions:  $\exp(-\lambda_0 \cdot t)$ ,  $\exp(-\lambda_1 \cdot t)$ , and  $\exp(-\lambda_2 \cdot t)$ . In the case of no coupling ( $\gamma=0$ ), roots are obviously all real and negative ( $\tau$  and  $\alpha$  are positive). Therefore the three functions will promptly decrease to 0 and the system will go back to the steady-state. Any deviation will be naturally suppressed. With coupling,  $\lambda_0$  is always negative ( $j^0=1$  and  $\gamma$  is positive). Therefore the instability will be due to either  $\lambda_1$  or  $\lambda_2$ . Their real part and imaginary part are given in Equations (50) and (51).

$$\text{Re}(\lambda_k) = -\beta + \frac{1}{2} \cdot \sqrt[3]{\gamma \cdot \alpha^2}, k \in \{1,2\} \quad (50)$$

$$\text{Im}(\lambda_k) = \pm \frac{\sqrt{3}}{2} \cdot \sqrt[3]{\gamma \cdot \alpha^2}, k \in \{1,2\} \quad (51)$$

Damping oscillations will be found if the real part is negative (damping) and the angular frequency of the oscillation will be given by the imaginary part. If the real part is positive, damping will disappear and divergence will be seen in the toy model. However, as explained above, in real life non-linearity will carry the plasma to a limit cycle (nonetheless non-steady state). It is worth noticing that the angular frequency increases with  $\gamma$  and  $\alpha$ . The coupling parameter is reasonably a fixed parameter, electron attachment is intrinsic to physics of clusters and therefore does not depend on plasma parameters. However the growth rate of nanoparticles ( $\alpha$ ) can vary by acting on the RF power of the plasma. From Equation (51) the angular frequency increases with RF power, which is consistent with the decrease of oscillation period with the RF power reported in [49].

Stabilization towards a steady state solution is helped by a low residence time (high pumping speed):  $-1/\tau$  (and  $\beta$  too) will decrease to very negative values. This behavior is identical to the simulation of reference [49]. Another stabilization factor is a high growth rate ( $\alpha$ ), and interestingly enough, quicker damping is associated to faster oscillations.

A stability condition can be calculated from Equation (50) where eigenvalues should be negative. The condition is given in Equation (52). The right side of this equation is a function of  $\alpha$  which is increasing from  $\alpha=0$  to  $\alpha=\gamma/27$  to reach  $\gamma/54$ . Above  $\alpha=\gamma/27$ , it decreases. It reaches 0 at  $\alpha=\gamma/8$  but continues to decrease.

$$\frac{1}{\tau} > \frac{1}{2} \cdot \sqrt[3]{\gamma \cdot \alpha^2} - \alpha \quad (52)$$

Figure 75 shows the mapping of the stability in the  $(\alpha, \tau)$  plan. For a given  $\alpha$  above  $\gamma/8$ , a steady-state solution is obtained for all residence time ( $\tau$ ) values. For a given  $\alpha$  below  $\gamma/8$ , stability is found for low residence time. For a given  $\tau$  below  $54/\gamma$ , the plasma is stable for all  $\alpha$  values, whereas for a given  $\gamma$  above  $54/\gamma$ , the plasma is only stable for low of high values of  $\alpha$ . Intermediate values lead to instability.

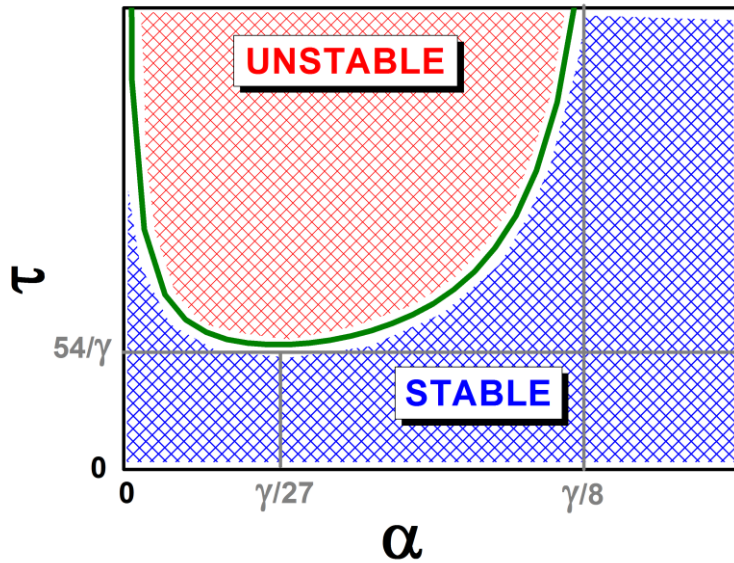


Figure 75: Stability mapping of the steady state solution of the toy model.

We reach now the limit of the simplified model. The toy model sheds light on the complexity of instability conditions: only a limited part of the  $(\alpha, \tau)$  plan is associated with instability. From the experimental point of view, no mapping of oscillating conditions has been performed. The toy model can explain very well the difficulty of such study.

By combining the toy model with non-linearity, only two regimes can be seen: self-sustained oscillations or damping oscillations. The regime of damping without oscillation cannot be seen. In fact, if  $\tau' \neq \tau$ , the roots of the characteristics polynomial can be all negative and real. In the case of  $\tau' = \tau$ , there is always one real root, and two complex roots. The imaginary part being responsible of oscillations, few oscillations will always be present with damping. Therefore in the real world, three regimes of plasma can be found: (i) pure damping, (ii) damping oscillation, and (iii) limit cycle. Table 26 summarizes the conditions to get each regime.

Case	(i)	(ii)	(iii)
Type within toy model	Pure Damping	Damping Oscillation	Diverging
Type in real world	Converging to steady state	Converging to steady state with few oscillations	Limit cycle
Eigenvalues	$\lambda_0 < 0$ $\text{Re}(\lambda_{1,2}) < 0$ $\text{Im}(\lambda_{1,2}) = 0$	$\lambda_0 < 0$ $\text{Re}(\lambda_{1,2}) < 0$ $\text{Im}(\lambda_{1,2}) \neq 0$	$\lambda_0 < 0$ $\text{Re}(\lambda_{1,2}) > 0$ $\text{Im}(\lambda_{1,2}) \neq 0$

Table 26: Conditions on eigenvalues to get damping or oscillating regimes.

And the three cases are found experimentally (for example on the Ar signal) as shown in Figure 76.

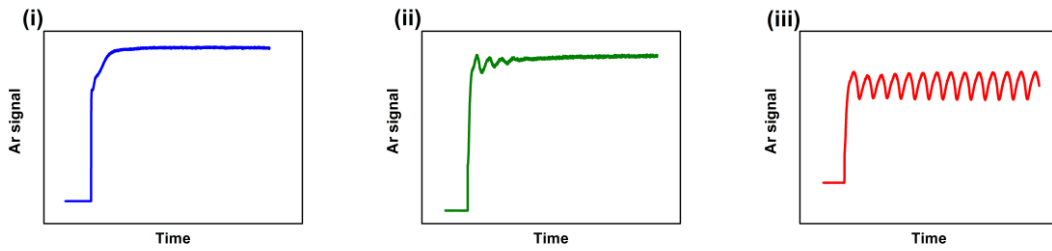


Figure 76: Experimental evidences on the Ar signal of (i) pure damping, (ii) damping oscillation, and (iii) limit cycle.

As shown in Figure 75, by changing continuously the plasma parameters, it is not possible to go from (i) to (iii) without passing through (ii). Figure 77 shows a typical example of plasma (experimental data) which displays a (i) regime at its start (first minute) and suddenly after another minute of stable steady state, begins to oscillate following (ii) regime. The damping of the oscillations is as long as two minutes. The plasma returns to another stable steady state. The phase shift between RF voltage and RF current at 13.56 MHz is also shown in Figure 77. One should get  $90^\circ$  in a purely capacitively discharge. However the real part of the plasma impedance is non-null, and in particular dusty condition increases the resistive part of the impedance. In Figure 77 between the two steady states, phase shift have dropped from  $83^\circ$  to  $81.5^\circ$  confirming a change towards a dustier plasma conditions.

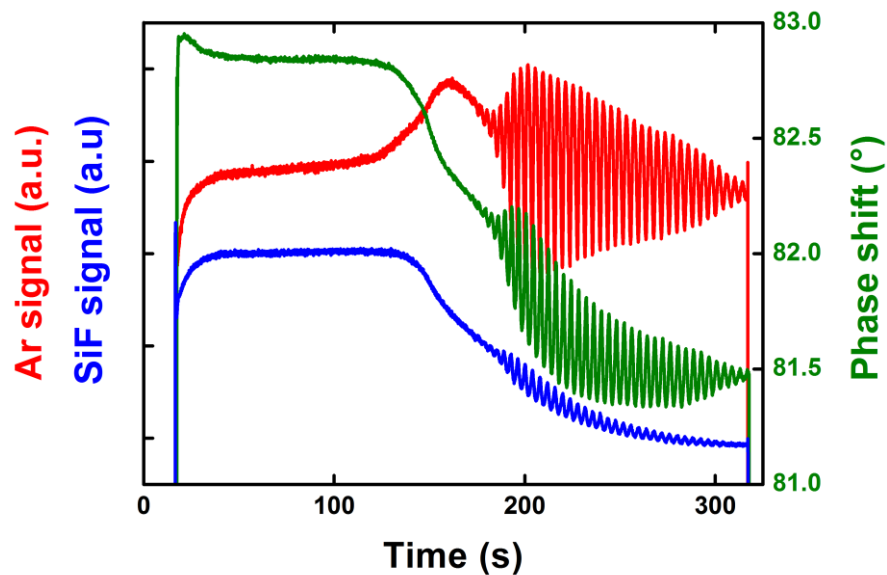


Figure 77: Example of transition from regime (i) to regime (ii) in Ar/SiF signals and phase shift.

Figure 78 shows a transition from regime (ii) to regime (iii). Until 50 s, the plasma evolution follows damping oscillations and reaches a stable steady state. After 100 s, the plasma shifts to a limit cycle. Neither SiF signal nor phase shift are, in average, changing. The plasma condition does not become dustier. Another ingredient shifts the system from (ii) regime to (iii) regime.

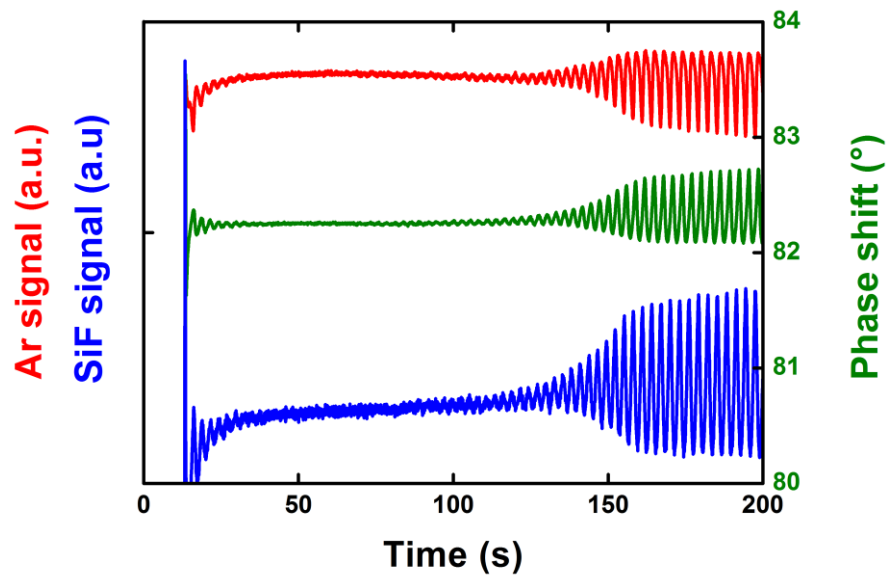


Figure 78: Example of transition from regime (ii) to regime (iii) in Ar/SiF signals and phase shift.

### 3.4.4 Forced oscillations

In self-sustained conditions, the plasma acts like a free oscillator with its own frequency. An external excitation can be applied to this free oscillator. The easiest way is to modulate the RF power of the plasma. For example instead of using a constant 30 W RF power, one can vary the RF power from 20 W to 40 W for a given repetition period. The idea behind the external excitation is the resonance phenomenon. The best example in electronics is an RLC circuit driven by a sinusoidal force: after a transient period, the system oscillates at the frequency of the external excitation. However the amplitude of the oscillation will encounter a maximum at the resonance defined by the equality of internal and external frequencies. In our case of oscillating plasmas, the dynamics of the system is much more complex than the linear differential equation of a RLC circuit.

We have shown in the previous section that Ar and SiF signals were oscillating in opposite phase. As shown in Figure 79a, in steady state plasma conditions, the modulation of the RF power results in an oscillation of Ar and SiF signals in phase. Figure 79b shows these signals at constant RF power but in self-sustained oscillation plasma conditions.

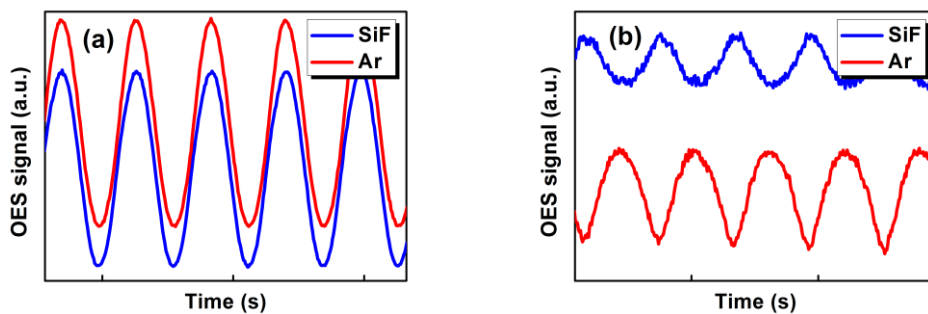


Figure 79: Ar and SiF signals for (a) steady state plasma condition and modulated RF power, and (b) oscillating plasma condition and constant RF power.

By combining oscillating plasma condition and modulated RF power, a lot of unexpected signals have been found as depicted in Figures 80 (a), (b), (c) and (d). The intermediate situation between phase and anti-phase is obtained in Figure 80a where SiF and Ar signals are in quadrature. The modulation period has been chosen close the self-sustained oscillation period. By having different

periods (being off resonance), situation of Figure 80b is obtained. By modulating faster than the self-oscillations, case of Figure 80c is get: the Ar signal fluctuates at the modulation frequency and beats are found with the self-sustained oscillation period. Finally, sometimes it is possible to decrease the fluctuation amplitude of Ar as seen in Figure 80d. It worth noticing that SiF signal merely follows the RF power and mainly Ar signal encounters the combination of external modulation and internal oscillations (quadrature, beats, canceling, etc.)

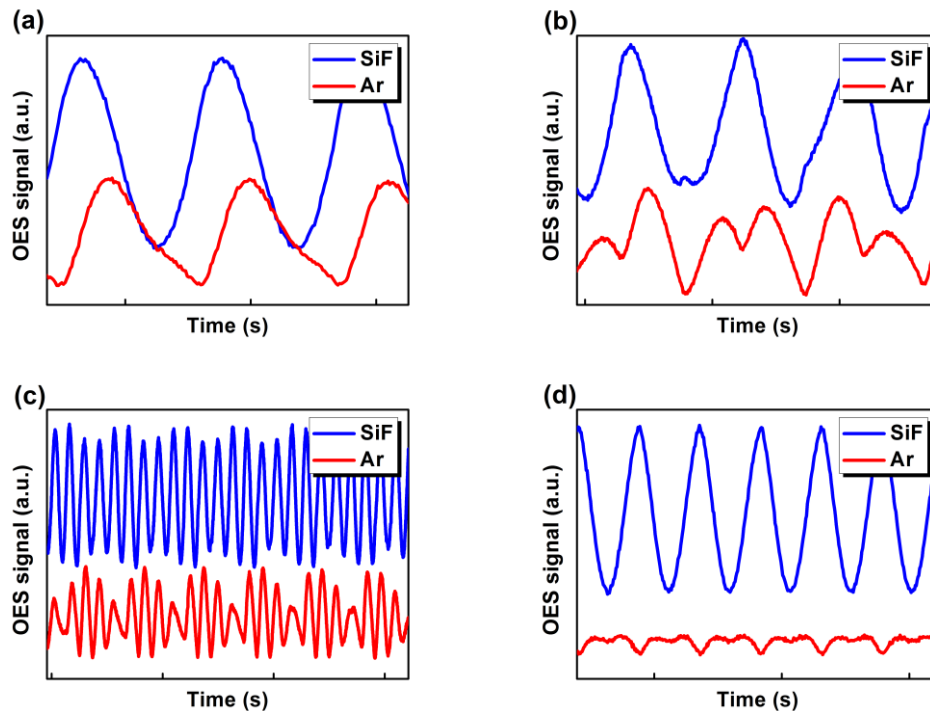


Figure 80: Ar and SiF signals in oscillating plasma condition and modulated RF power.

The results on forced oscillations demonstrate the inherent oscillating mechanisms of the plasma chemistry (nanoparticles, trapping,  $\alpha$ - $\gamma'$  transition etc.). The presence of forced oscillations does not change the internal oscillator: the two oscillations will be superposed.

### 3.5 Chapter key results

To summarize this chapter, few and yet important messages need to be conveyed. Dusty plasma conditions occur at high pressure but mostly at low gas temperature:

- The plasma-generated nanoparticles do contribute to the growth of the silicon film as the deposition rate increases with the decrease of the gas temperature. The presence of nanoparticles could have a dramatic impact of the plasma itself: sometimes self-oscillations of all the plasma parameters are encountered.
- Small nanoparticles undergo charge fluctuations and tend to get negatively charged as their size increases, which has the disadvantage of trapping the big nanoparticles into the plasma. These nanoparticles do not contribute to the growth and should be considered as waste. We have found that the lowest silicon waste is achieved at the P-d<sub>i</sub> product of 6 Torr-cm where the deposition rate is maximum.
- The plasma-generated nanoparticles are generally amorphous but at high RF power density, their crystallization may occur. Two types of layer crystallization have therefore been identified: crystallization at the surface, which is mediated by atomic hydrogen (usually obtained at high H<sub>2</sub> flow rate) and crystallization in the plasma phase, through the crystallization of nanoparticles (usually obtained at high RF power).



# 4. Material properties

## Contents

---

<b>4.1 Crystalline silicon</b> .....	<b>106</b>
4.1.1 Bragg Brentano XRD .....	106
4.1.2 Grazing Incidence XRD .....	106
<b>4.2 Raman spectroscopy</b> .....	<b>107</b>
4.2.1 Overview .....	107
4.2.2 Deconvolution .....	108
4.2.3 Definitions of crystallinity-related fractions .....	112
4.2.4 Mapping of the crystallinity with Raman measurements .....	113
<b>4.3 Hydrogen incorporation</b> .....	<b>114</b>
4.3.1 FTIR and exodiffusion .....	114
4.3.2 H <sub>2</sub> flow rate series .....	118
4.3.3 RF power series .....	121
<b>4.4 Material quality</b> .....	<b>122</b>
4.4.1 SIMS .....	122
4.4.2 Defect density from FTPS measurements .....	125
<b>4.5 Chapter key results</b> .....	<b>127</b>

---

In the previous chapters we have presented new and original results leading to a better understanding of the plasma chemistry related to both chemical reactions (formation of HF for instance) and complex nanoparticle growths. However our target is solar cells. In order to build a bridge between plasmas and solar cells, the material properties should be addressed. This is a subject in itself. In this chapter we will focus on some film properties. In particular we will focus on the crystallinity of the films, their composition and the defect density. For the composition we shall focus on hydrogen bonding and content as well as on oxygen or fluorine. The structure of the material can be amorphous or microcrystalline, but the microcrystallinity has to be characterized as this term encompasses a lot of different types of material. For instance the crystallite size can differ from one material to another. The material can be characterized by its bandgap and its defect density within the bandgap, responsible of undesired electron-hole pair recombination.

This chapter deals with all these characterizations to sketch a partial yet useful picture of our material. It is organized as follow:

- Investigation of the crystalline structure by X-ray diffraction
- Micro-structure of the material by Raman spectroscopy
- Study of the hydrogen content and bonding by FTIR and exodiffusion
- Analysis of the material quality by contaminant concentration and defect density

## 4.1 Crystalline silicon

### 4.1.1 Bragg Brentano XRD

X-ray diffraction has been used to characterize the crystalline orientation of the microcrystalline silicon. Figure 81 shows the XRD pattern (in Bragg-Brentano configuration) of the microcrystalline silicon in a solar cell structure. Several peaks are found corresponding either to the silicon or to the zinc-oxide and the silver used to sandwich the intrinsic microcrystalline layer. For silicon, 111, 220, and 311 orientations are found. The intensity of the 311 peak is slightly higher than the two others. The spectrum shows that the films are crystalline but no preferential orientation are found.

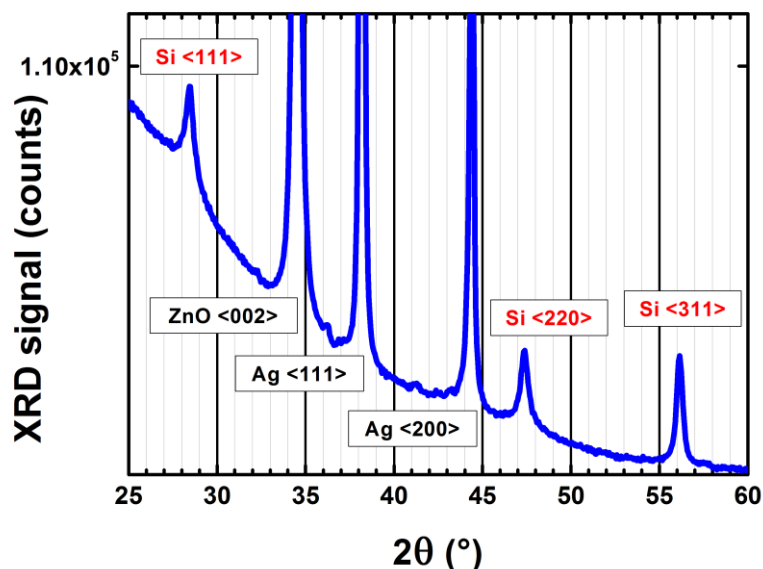


Figure 81: XRD pattern in Bragg-Brentano configuration of a solar cell.

### 4.1.2 Grazing Incidence XRD

In grazing incidence (GI) configuration, the X-ray path in silicon is higher than in Bragg-Brentano (BB) configuration. Therefore the XRD signal will increase in GI case. The intensity of signal is an issue when the samples are deposited on glass substrates where the thickness is no more than 500 nm to avoid

peeling off. The issue of the GI configuration is that the reference plane for the orientation is rotating with angle (in BB configuration the reference plane for the orientation is the substrate plane). There a 311 preferential orientation in a GI-XRD pattern is not a 311 preferential orientation in a BB-XRD pattern.

We perform GI-XRD on two samples representing the two types of crystallization identified in the previous chapter i.e. through surface reactions or through the deposition of silicon nanocrystals. Conditions are reminded in Table 27 where deposition time is higher than what has been done previously because thick layers are wanted. The H05 condition corresponds to the surface crystallization induced by atomic hydrogen while W050 corresponds to plasma-generated nanoparticle crystallization.

Name	T <sub>sub</sub>	T <sub>RF</sub>	d <sub>i</sub>	Pr	SiF <sub>4</sub>	H <sub>2</sub>	Ar	Pw	t <sub>d</sub>
(-)	(°C)	(°C)	(mm)	(Torr)	(sccm)	(sccm)	(sccm)	(W)	(sec)
H05	150	80	30	3.8	3.6	5.3	88	20	7200
W050						3		50	1800

Table 27: Plasma conditions (H05 and W050) for the sample measured in GI-XRD.

Figure 82 shows the GI-XRD pattern of microcrystalline silicon deposited in H05 and W050 conditions. The H05 condition is similar to the condition used for the deposition of solar cell in Figure 81. In H05 case, the 311 peak is pronounced and the 111 peak is not the highest peak. That is also seen in Figure 81 with the BB configuration.

In W050 case the 311 peak is smaller than the 111 peak and the relative intensities of 111, 220, and 311 peaks are similar to these obtained in silicon powder, demonstrating no-preferential orientation in W050 condition. The relative peak intensities of silicon powders are 100% for <111>, 60% for <220>, 35% for <311>, 8% for <400>, 13% for <331>, and 17% for <422>. The randomness of the orientation can be understood as crystalline nanoparticles arriving on the substrate with a random orientation.

By comparing H05 and W050, the width of the 311 peak is smaller in H05 than in W050 (FWHM estimated by fitting with a Lorentzian curve: 0.91° for H05 and 2.0° for W050), therefore from Scherrer equation the size of crystallites giving the 311 signal is higher in H05 than in W050. That is consistent with the height of the peak: the high and narrow 311 peak in H05 condition is related to large crystalline domains.

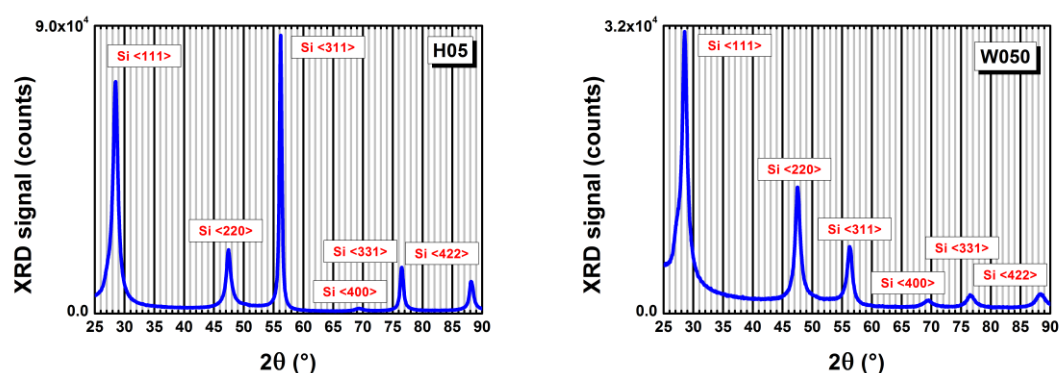


Figure 82: XRD patterns in grazing incidence configuration of microcrystalline silicon deposited on glass under H05 and W050 conditions.

## 4.2 Raman spectroscopy

### 4.2.1 Overview

Raman spectroscopy is a powerful technique to characterize silicon-silicon bonds. Generally a photon is elastically scattered by the matter (microcrystalline silicon in our case): it corresponds to the Rayleigh scattering. However sometimes inelastic scattering occurs due to what is called Raman

scattering: the scattered photon does not have exactly the same energy as the incident one. The incident photon reacts with a phonon (collective vibration mode of the network) and can lose or gain energy. The energy difference corresponds precisely to the energy of the phonon (energy continuity). The phonon is characteristic of the material. However the phenomenon is a very inefficient process and Raman scattering happens approximately every  $10^7$  Rayleigh scatterings. A high flux of incident photons is therefore required to detect some photons scattered by Raman process. It is the reason why a laser is used as excitation source. The description of different types of phonons (LO, TO, LA, TA, etc.) is out the scope of this thesis. A phonon of amorphous silicon is found at  $480\text{ cm}^{-1}$  (TO mode), whereas a phonon of crystalline silicon is found at  $520\text{ cm}^{-1}$  [70].

Microcrystalline silicon films can be deposited on glass substrates or on textured zinc-oxide (ZnO:Al). Usually glass substrates are used to perform plasma studies but for the final application of PIN thin film solar cells, the substrate is the beginning of the solar cell stack. Texturing has a beneficial effect on the adhesion of microcrystalline silicon: 1 micron-thick microcrystalline deposited on glass will often peel off when the sample is removed from the reactor whereas several-micron-thick microcrystalline films can be grown on textured ZnO without peeling. We will restrict our study to microcrystalline silicon deposited on textured ZnO. Indeed our samples are the solar cell themselves.

#### 4.2.2 Deconvolution

Figure 83a shows the Raman spectra of two microcrystalline silicon films: one is a mixture between amorphous and crystalline silicon and the other one is fully crystallized. Two peaks are roughly found: the amorphous peak at  $480\text{ cm}^{-1}$  and the crystalline peak at  $520\text{ cm}^{-1}$ . The peaks are approximated by Gaussian curves. However, the amorphous peak is not a Gaussian curve because its Raman signal does not converge to zero below  $400\text{ cm}^{-1}$  and above  $560\text{ cm}^{-1}$  as seen in Figure 83a. The reason is that other phonons contribute to the signal between  $400\text{ cm}^{-1}$  and  $560\text{ cm}^{-1}$ . A baseline is therefore required before trying to deconvolute the Raman spectrum. The way the baseline is defined will influence the position/width/height of each peak of the deconvolution. We decide here to choose the same baseline method for all the samples. The baseline is defined between  $380\text{ cm}^{-1}$  and  $560\text{ cm}^{-1}$  as a straight line as shown in Figure 83a. We are aware that the chosen baseline method is very simple and is not the most accurate way to isolate the amorphous and crystalline peaks. While the choice can affect the absolute values of the various peaks, we expect it will not affect the general trends we are interested in and will not undermine the forthcoming conclusions. Figure 83b shows the Raman spectra after the baseline has been subtracted. The baseline in fully crystallized microcrystalline case is less problematic as the spectra is close to zero below  $440\text{ cm}^{-1}$  and above  $560\text{ cm}^{-1}$ .

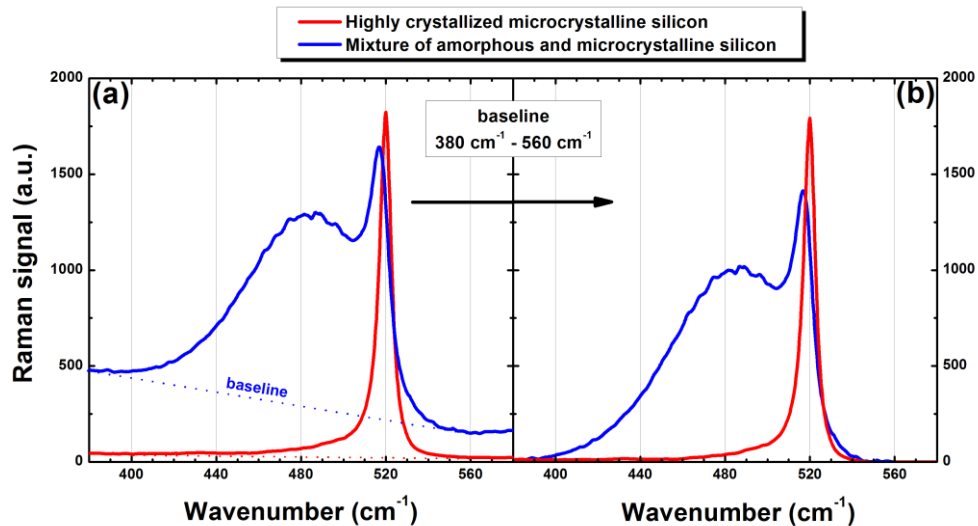


Figure 83: (a) Raman spectroscopy of microcrystalline silicon. (b) After the baseline subtraction.

Figure 84a shows the deconvolution of the Raman spectra of the  $\mu\text{c-Si:H}$  samples with two Gaussian curves: one for the amorphous part and one for the crystalline part. Globally the fitting seems correct: the position of the amorphous peak is around  $480\text{ cm}^{-1}$  and the position of the crystalline peak about  $520\text{ cm}^{-1}$ . However it has been reported that grain boundaries give separate Raman signal located around  $500\text{ cm}^{-1}$  [71]. The deconvolution with three Gaussian curves is shown in Figure 84b. The addition of an intermediate peak shifts the amorphous peak to a lower position (from  $482\text{ cm}^{-1}$  to  $475\text{ cm}^{-1}$ ). The grain boundaries peak is located at  $502\text{ cm}^{-1}$ . The crystalline peak is located at  $517\text{ cm}^{-1}$ . As we will see later, we associate this peak either to the crystalline phase or the “crystallites” (small crystalline domains) [65]. The reason is that in this material, since we have a significant amorphous fraction, we expect to find the crystallized part in the form of small crystallites instead of larger crystalline domains. The Raman signal of the crystallites is a little bit shifted to lower wavenumber values ( $517\text{ cm}^{-1}$  in the deconvolution with two or three Gaussian curves) with respect to the crystalline silicon ( $520\text{ cm}^{-1}$ ). To summarize, the  $\mu\text{c-Si:H}$  samples are deconvoluted into three peaks: amorphous, grain boundaries, and crystallite/crystalline. Their location is respectively  $475\text{ cm}^{-1}$ ,  $502\text{ cm}^{-1}$ , and  $517\text{ cm}^{-1}$ , while their widths are respectively  $52\text{ cm}^{-1}$ ,  $29\text{ cm}^{-1}$ , and  $8.5\text{ cm}^{-1}$ . The FWHM is proportional to the width with the factor  $\sqrt{2 \cdot \ln(2)} \approx 1.177$ . The width is naturally strongly correlated to the disorder of the Si-Si bond category: crystallites are more ordered than the grain boundaries, which are themselves more ordered than the amorphous part. In a disordered material, the random distribution of the Si-Si bonds leads to a widening of the energy distribution of phonons (therefore to wider peak). Our deconvolution into three peaks respects this logic.

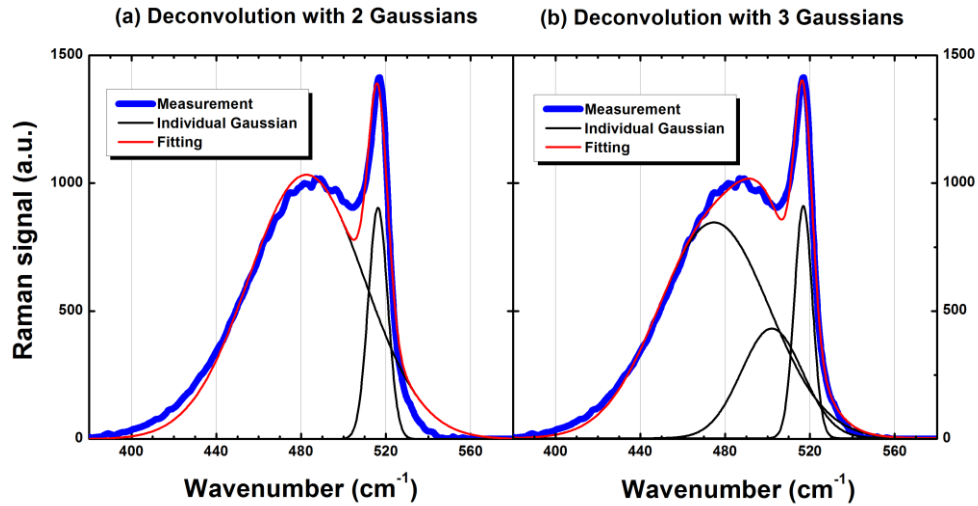


Figure 84: Fitting of a-Si:H/ $\mu$ c-Si:H mixture Raman spectrum.

Figure 85a shows the deconvolution of the fully crystallized film with one Gaussian curve (note the change of the wavenumber scale). The measurement shows a peak at  $520\text{ cm}^{-1}$  as for crystalline silicon wafer. However it does not perfectly fit with only one Gaussian: there is a shoulder between  $500\text{ cm}^{-1}$  and  $515\text{ cm}^{-1}$  which is not embedded in the Gaussian crystalline peak. The deconvolution with two Gaussian peaks is presented in Figure 85b. The position of the crystallite and crystalline peaks are respectively  $517\text{ cm}^{-1}$  and  $520\text{ cm}^{-1}$  with a width of respectively  $18\text{ cm}^{-1}$  and  $5\text{ cm}^{-1}$ . In comparison, the width of a crystalline silicon wafer is  $4.6\text{ cm}^{-1}$  if deconvoluted with one Gaussian (corresponding to a FWHM of  $5.5\text{ cm}^{-1}$ ). Nevertheless, we see here that the deconvolution in two Gaussian curves (crystallite and crystalline) is not satisfactory to reproduce the shape of the shoulder.

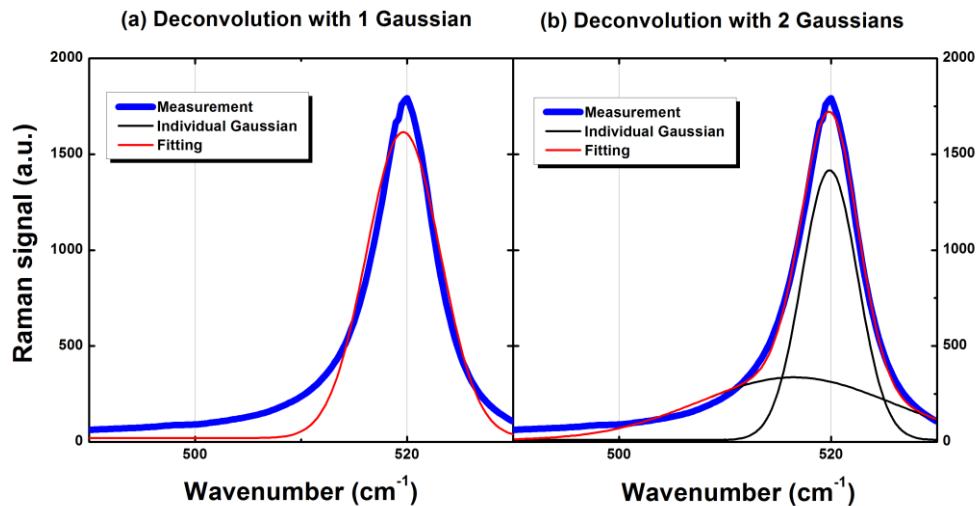


Figure 85: Fitting of fully crystallized  $\mu$ c-Si:H Raman spectrum.

Figure 86 shows the deconvolution of the Raman spectrum of the fully crystalline sample into three Gaussian curves: the grain boundaries, the crystallites, and the crystalline peaks. Their position are respectively  $504\text{ cm}^{-1}$ ,  $519\text{ cm}^{-1}$ , and  $520\text{ cm}^{-1}$  with the width of respectively  $34\text{ cm}^{-1}$ ,  $11\text{ cm}^{-1}$ , and  $4.4\text{ cm}^{-1}$ . The shoulder is well fitted, however some wariness should be taken concerning the physical meaning of the deconvoluted peaks, showing the limit of the deconvolution: the crystalline width is lower than the crystalline silicon wafer (meaning that it is better crystalline than a crystalline wafer...). No amorphous peak (at  $480\text{ cm}^{-1}$ ) is required to fit the spectrum.

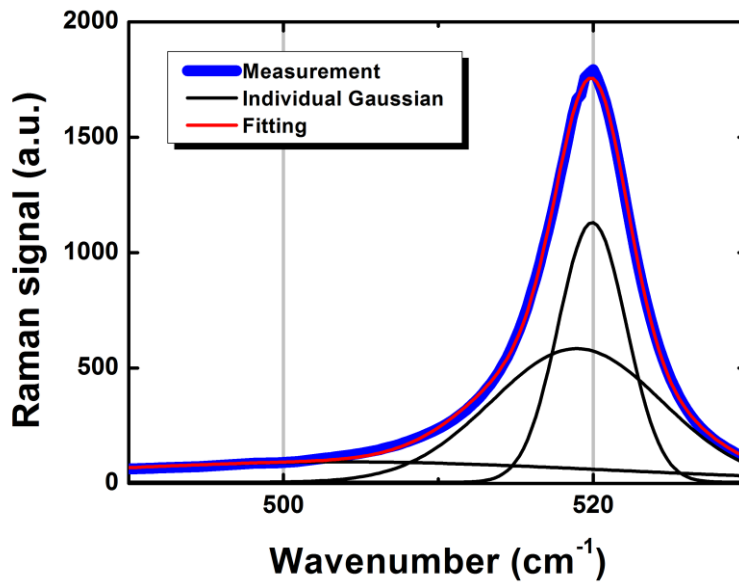


Figure 86: Fitting of fully crystallized  $\mu\text{c-Si:H}$  Raman spectrum with three Gaussians.

The deconvolution of Raman spectra into multiple Gaussian peaks is always a tradeoff between accuracy of the fitting and the physical meaning of each peak. From a mathematical point of view, the more peaks involved, the better the fitting. The case of a mixture of a-Si:H and  $\mu\text{c-Si:H}$  is a good example: we manage to fit with three Gaussian curves and each curve has a physical meaning (amorphous, grain boundaries, and crystallite). However the fitting with four Gaussian curves (by adding a crystalline peak at  $520\text{ cm}^{-1}$ ) does not work because the system is over-determined: from this measurement we cannot discriminate between the crystallite peaks and the crystalline peak. We have to live with that. Table 28 summarizes the different peaks found in our microcrystalline silicon. The intensity of each peak is noted  $I_A$  for the amorphous peak,  $I_{GB}$  for the grain boundaries peak,  $I_{SC}$  for the small crystallite peak, and  $I_C$  for the crystalline peak.

Name	Amorphous	Grain Boundaries	Small Crystallites	Crystalline
Notation	$I_A$	$I_{GB}$	$I_{SC}$	$I_C$
Position	$\approx 480\text{ cm}^{-1}$	$\approx 500\text{ cm}^{-1}$	$\approx 510\text{-}518\text{ cm}^{-1}$	$\approx 520\text{ cm}^{-1}$
Width	$\approx 50\text{ cm}^{-1}$	$\approx 30\text{ cm}^{-1}$	$\approx 10\text{ cm}^{-1}$	$\approx 5\text{ cm}^{-1}$
FWHM	$\approx 60\text{ cm}^{-1}$	$\approx 35\text{ cm}^{-1}$	$\approx 12\text{ cm}^{-1}$	$\approx 6\text{ cm}^{-1}$

Table 28: Typical position and FWHM of the four peaks used in the deconvolution.

Up to now, we only use three curves to deconvolute the Raman spectra of microcrystalline silicon. The amorphous peak is not required in a fully crystallized layer and the crystalline peak is not needed in an a-Si:H/ $\mu\text{c-Si:H}$  mixture layer. However, for materials less crystallized than that shown in Figure 85 but with less amorphous fraction than Figure 84, the four peaks are required to fit the measured Raman spectrum. Table 29 summarizes when the peaks are used in the fitting procedure.

Sample	$I_A$	$I_{GB}$	$I_{SC}$	$I_C$
a-Si:H with a fraction of $\mu\text{c-Si:H}$	yes	yes	yes	<del>yes</del>
$\mu\text{c-Si:H}$ with a fraction of a-Si:H	yes	yes	yes	yes
$\mu\text{c-Si:H}$ without a-Si:H	<del>yes</del>	yes	yes	yes

Table 29: Selected peaks used for the deconvolution depending of the material.

Figure 87 shows the fitting with four Gaussian curves of microcrystalline silicon well crystallized but with a little amount of amorphous silicon. The position of the amorphous, grain boundaries, small crystallite and crystalline peaks are respectively  $475\text{ cm}^{-1}$ ,  $502\text{ cm}^{-1}$ ,  $515\text{ cm}^{-1}$ , and  $519\text{ cm}^{-1}$ . The

associated widths are respectively  $57\text{ cm}^{-1}$ ,  $31\text{ cm}^{-1}$ ,  $12\text{ cm}^{-1}$ , and  $6.2\text{ cm}^{-1}$ . The inset of Figure 87 shows the discrepancy of the fitting when only three curves are used and highlights the importance of the four peaks.

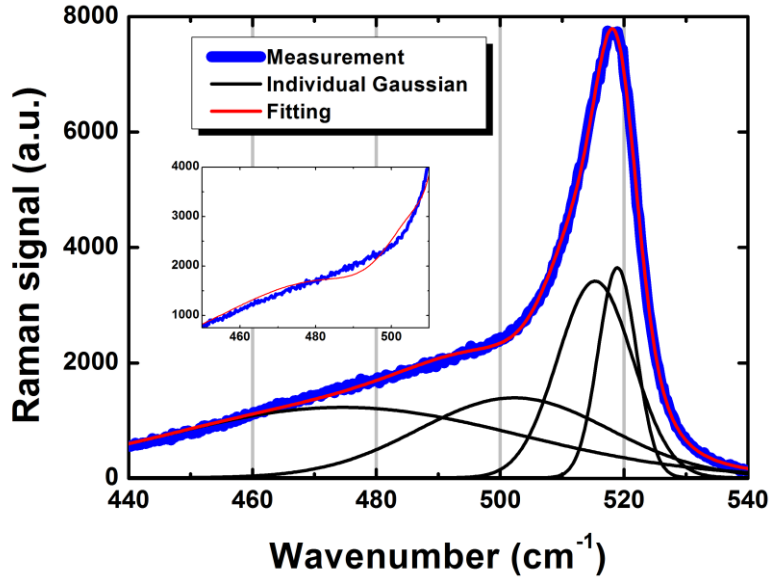


Figure 87: Fitting of  $\mu\text{c-Si:H}$  with a little bit of  $\text{a-Si:H}$  Raman spectrum with four Gaussians. The inset shows a discrepancy around  $500\text{ cm}^{-1}$  when the fitting uses the three Gaussian curves.

#### 4.2.3 Definitions of crystallinity-related fractions

Based on the deconvolution into four peaks presented above, and following the conventions in the literature [9][71], we define the crystalline fraction (noted  $X_c$ ) of the layer as given by Equation (53). The only peak which does not contribute to the crystalline fraction is the amorphous peak (which is of course used in the denominator for the normalization).

$$X_c = \frac{I_{GB} + I_{SC} + I_C}{I_A + I_{GB} + I_{SC} + I_C} \quad (53)$$

With this definition of the crystalline fraction, we can perform the deconvolution of the Raman spectra of all the intrinsic microcrystalline films used in our large set of PIN solar cells. Figure 88 shows the position of the grain boundaries (GB) peak as a function of the crystalline fraction. Our set of solar cells covers a range of crystalline fractions from 70% to 100% whereas the GB peak is located between  $495\text{ cm}^{-1}$  and  $505\text{ cm}^{-1}$ . This is consistent with previous observations [9][72] where two types of grain boundaries have been identified:

- Grain boundaries of type I: GB between microcrystalline grains and the amorphous phase, having a peak location around  $494\text{ cm}^{-1}$ .
- Grain boundaries of type II: GB between microcrystalline grains themselves, with a signature around  $507\text{ cm}^{-1}$ .

By decreasing the amorphous fraction from 30% to 0%, the grain boundaries type changes from type I to type II. One could argue about the scatter of the data points in Figure 88. Layers with  $X_c$  below 80% have been plotted in blue circles while layers with  $X_c$  above 80% are displayed with red losenges. We suggest that the signature at  $500\text{ cm}^{-1}$  is distinct from the amorphous phase and is associated with column boundaries. In average we measured a position of  $502\text{ cm}^{-1}$  for  $X_c > 80\%$  samples and a position of  $498\text{ cm}^{-1}$  for  $X_c < 80\%$  samples. The difference is only  $4\text{ cm}^{-1}$  and consequently the distinction between type I and type II is hard to bring to light. Moreover, since the difference of the peak position between the two types of grain boundaries ( $494\text{ cm}^{-1}$  and  $507\text{ cm}^{-1}$ ) is approximately  $13\text{ cm}^{-1}$ , the method of the

baseline is very important and can influence the peak position. The important message that we want to convey is that fully crystallized layer can be fabricated (no amorphous phase,  $I_A=0\%$ ) and that a GB peak is needed at  $500\text{ cm}^{-1}$  to fit the Raman spectrum. This peak is the signal of boundaries of type II – boundaries between crystallite.

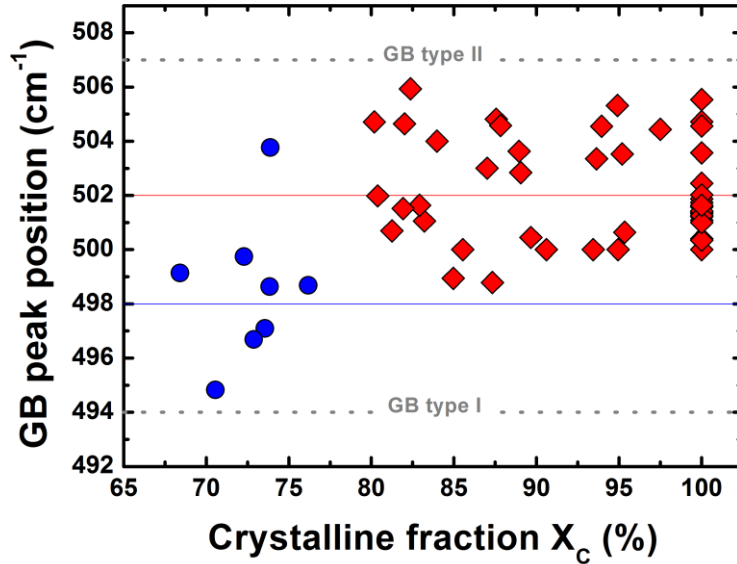


Figure 88: Grain boundaries peak position as a function of the crystalline fraction  $X_c$ . The position of grain boundaries of type I and type II are taken from [72].

It can be seen in Figure 88 that a fully crystallized layer (with our definition of crystalline fraction) can be achieved. The corresponding solar cells, as it will be explained in the next chapter, have excellent performances. To deepen the understanding on this subset of solar cells, we define in Equation (54) the grain boundaries fraction, likewise the definition of the crystalline fraction. Among the 100% crystalline fraction solar cells ( $I_A=0\%$ ), the GB fraction can vary between 0% and 30%.

$$X_{GB} = \frac{I_{GB}}{I_{GB}+I_{SC}+I_C} \quad (54)$$

We also define the crystallite fraction  $X_{cry}$  by Equation (55). When  $I_A=0\%$ , we have of course the relation  $X_C=X_{GB}+X_{cry}$ . As it will be shown in the next chapter, for samples with  $X_C=100\%$ , we can have  $X_{cry}$  varying between 70% and 100%.

$$X_{cry} = \frac{I_{SC}+I_C}{I_A+I_{GB}+I_{SC}+I_C} \quad (55)$$

#### 4.2.4 Mapping of the crystallinity with Raman measurements

To clarify the identification of the  $500\text{ cm}^{-1}$  peak, a 2D Raman mapping has been performed on a sample where no amorphous phase was detected ( $I_A=0\%$ ). By naming  $S_{Raman}$  the measured Raman signal, we define the ratio R by Equation (56). The numerator represents the grains boundaries peak and the denominator the small crystallite and crystalline peaks. The ration R should vary likewise  $X_{GB}$ .

$$R = \frac{\int_{495\text{cm}^{-1}}^{505\text{cm}^{-1}} S_{Raman}(\omega) \cdot d\omega}{\int_{510\text{cm}^{-1}}^{525\text{cm}^{-1}} S_{Raman}(\omega) \cdot d\omega} \quad (56)$$

Figure 89 shows the ratio R. One clearly sees that the  $500\text{ cm}^{-1}$  contribution is more pronounced in the region corresponding to a tissue, in which are imbedded into 1 to 2  $\mu\text{m}$  size islands (in cyan/green

in the Figure 89) with a smaller  $500\text{ cm}^{-1}$  contribution. This observation leads us to associate the additional peak at  $500\text{ cm}^{-1}$  with the column boundaries.

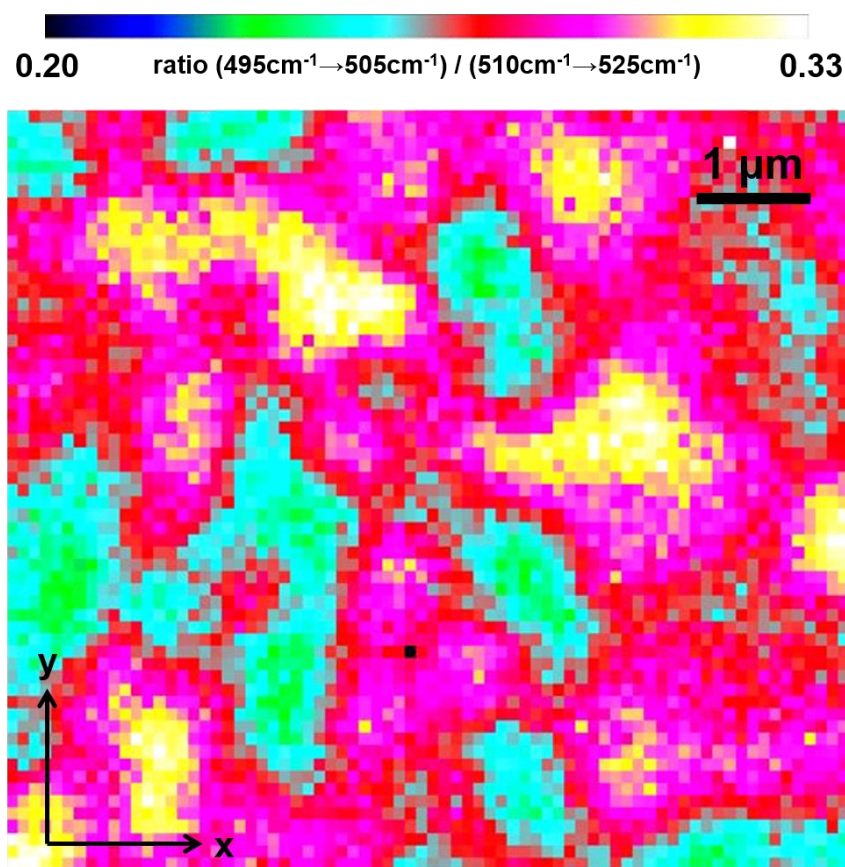


Figure 89: Mapping of the ratio R in a microcrystalline layer without amorphous phase.

## 4.3 Hydrogen incorporation

### 4.3.1 FTIR and exodiffusion

Exodiffusion is a technique where the sample is heated from room temperature up to  $800^\circ\text{C}$  in vacuum. The ramp of temperature is  $10^\circ\text{C}/\text{min}$ . A mass spectrometer measures the  $\text{H}_2^+$  partial pressure to estimate how many  $\text{H}_2$  molecules have escaped from the layer because of heating. This technique is also called Thermal Desorption Spectroscopy [73][74].

Two layers have been deposited: one amorphous (at 2 sccm of  $\text{H}_2$  flow rate) and one microcrystalline (at 8 sccm of  $\text{H}_2$  flow rate). Plasma conditions are given in Table 30. The substrate is composed of silicon nitride  $\text{SiN}_x$  deposited on top of an intrinsic crystalline wafer. The reason of the thin  $\text{SiN}_x$  layer is to avoid a possible epitaxial growth: we want to study amorphous silicon like deposited on glass (however glass substrate we use is not transparent in IR range). The stack (i)c-Si +  $\text{SiN}_x$  is transparent in the range around  $1900\text{--}2200\text{ cm}^{-1}$ . Therefore the absorption in this range is only due to the amorphous and microcrystalline layers.

$T_{\text{sub}}$ ( $^\circ\text{C}$ )	$T_{\text{RF}}$ ( $^\circ\text{C}$ )	$d_i$ (mm)	Pr (Torr)	$\text{SiF}_4$ (sccm)	$\text{H}_2$ (sccm)	Ar (sccm)	Pw (W)	$t_d$ (sec)
150	200	30	3.8	10	2	88	40	600
					8			

Table 30: Plasma conditions for FTIR and exodiffusion studies.

Figure 90 shows the exodiffusion spectra of the amorphous and microcrystalline samples used in FTIR measurement of Figure 91. Two peaks are obtained around 300°C and 400°C. Hydrogen atoms are present in different bonding configurations and environments as they are released dependently of the annealing temperature, showing different easiness of the thermal desorption. We will name these two peaks weak and tight bonded hydrogen for respectively the 300°C peak and the 400°C (written WBH and TBH respectively) after the reference [75]. Very weak hydrogen peaks are also detected around 200°C. The layers here are very thin, and this peak is not observed on the exodiffusion spectra of thick layers as shown later in Figure 93.

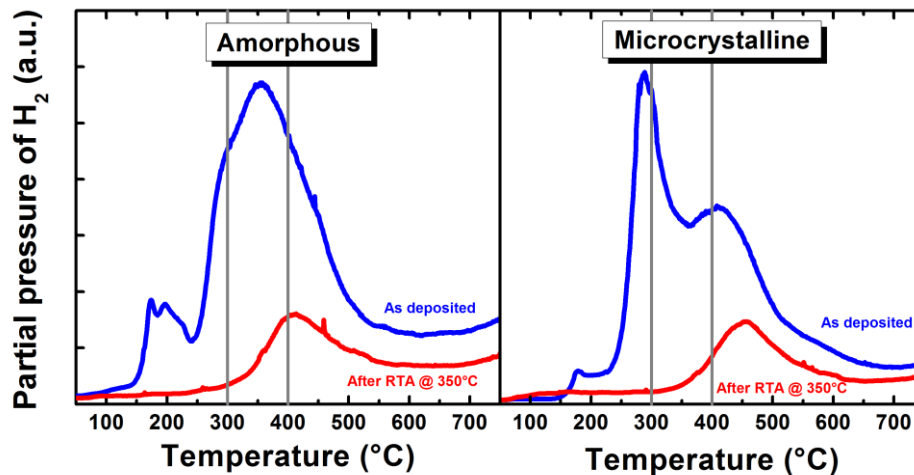


Figure 90: Exodiffusion spectra for amorphous and microcrystalline samples before and after a rapid thermal annealing at 350°C.

Another tool to characterize the hydrogen bonding is the absorption of infra-red photons by the material: IR light excites the bonds between hydrogen and silicon. Si-H and SiH<sub>2</sub> stretching modes are absorbed around, respectively, 2000 cm<sup>-1</sup> and 2100 cm<sup>-1</sup> [70]. Fourier Transform Infrared Spectroscopy (FTIR) is a technique which allows the measurement of the absorption of a sample in IR range. In transmission configuration, a polychromatic beam is sent to the sample and its transmission is measured. The measured transmission is global and corresponds to the whole beam. Any absorption will decrease the transmission. The input beam spectrum is continuously changed by a Michelson interferometer and thanks to a Fourier transform, one can get the transmission as a function of the photon energy from the global transmissions of each different input spectrum.

Figure 91 shows the FTIR spectra of the two samples from 1500 cm<sup>-1</sup> to 2500 cm<sup>-1</sup> (blue curves). The broad variation of the transmission is due to IR interferences between interfaces of the stack (i)c-Si + SiN<sub>x</sub> + layer. The hydrogen contribution from the SiN<sub>x</sub> layer is negligible because of its small thickness (few nanometers). Between 1800 cm<sup>-1</sup> and 2200 cm<sup>-1</sup> an absorption peak is found due to absorption of the IR beam by Si-H and Si-H<sub>2</sub> bonds.

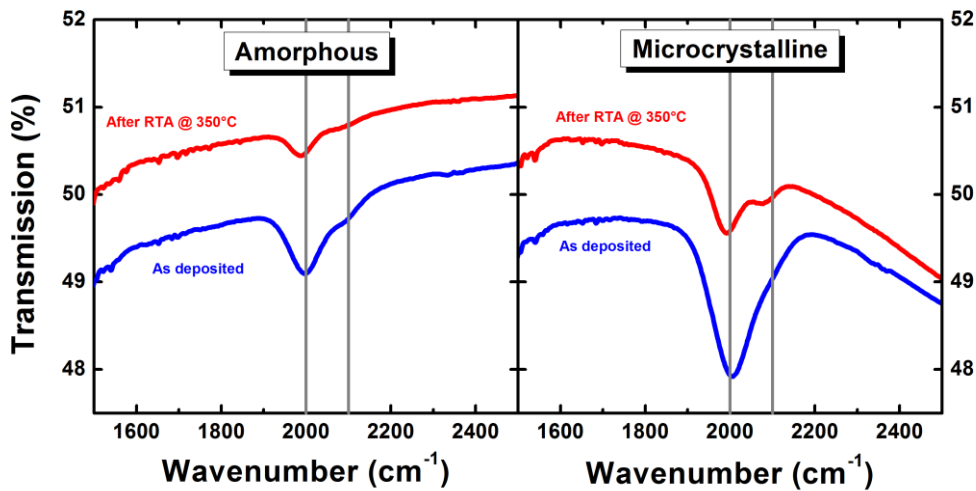


Figure 91: Transmission spectra measured by FTIR for amorphous and microcrystalline samples before and after a rapid thermal annealing at 350°C.

To estimate the absorption, we should subtract the measured transmission with the expected transmission without the absorption effect (only the IR interference). To do so, we interpolate between 1800  $\text{cm}^{-1}$  and 2200  $\text{cm}^{-1}$  by a straight line. Absorptions are given in Figure 92. In order to deconvolute the absorption, two Gaussian curves are used. The position of the Si-H (resp. Si-H<sub>2</sub>) peak is noted P<sub>1</sub> (resp. P<sub>2</sub>), its height H<sub>1</sub> (resp. H<sub>2</sub>), its width W<sub>1</sub> (resp. W<sub>2</sub>) and its area A<sub>1</sub> (resp. A<sub>2</sub>). Two Gaussian curves are sufficient to fit FTIR spectra.

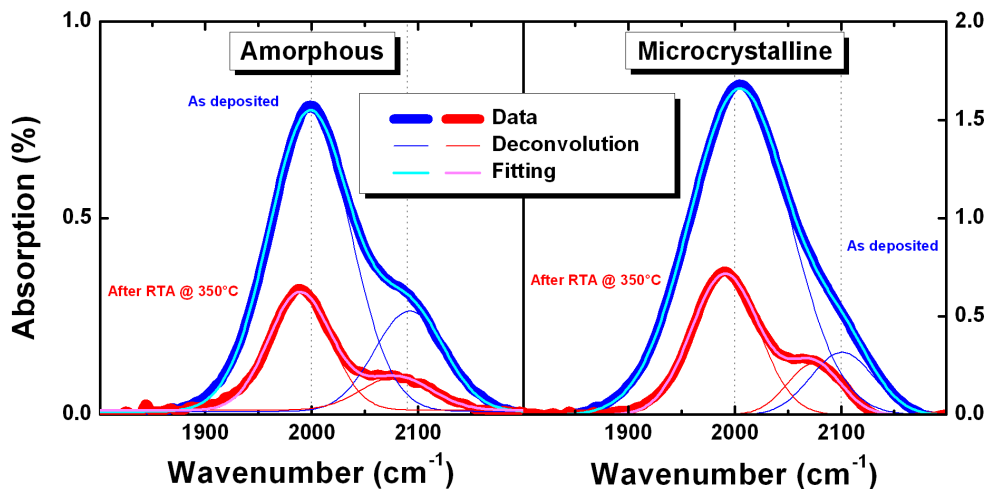


Figure 92: Absorptions extracted from FTIR for amorphous and microcrystalline samples before and RTA at 350°C.

To further analyze the exodiffusion spectra, a correlation between exodiffusion weak/tight bond peaks and FTIR Si-H/Si-H<sub>2</sub> bonds is studied. Following the idea of reference [76], samples are annealed at 350°C: a Rapid Thermal Annealing (RTA) equipment is used and the annealing duration is 15 min. Exodiffusion spectra are shown in Figure 90 for amorphous and microcrystalline samples after the RTA step. By heating up to 350°C, all weakly bonded hydrogen is removed from the sample. Only tightly hydrogen is kept. By such treatment, one can study only the tight peak.

FTIR measurements can then be performed on the annealed samples. They are shown in Figures 91 and 92. The transmission baseline is changed after the RTA because IR interference is modified: by removing hydrogen, the index of the layer is changed. Therefore Fresnel's reflection/transmission coefficients are different at the SiN<sub>x</sub>/layer and layer/air interfaces.

The hydrogen content on the films is proportional to the total signal (integration below the curve) of FTIR and of exodiffusion. The signals are integrated and the result is displayed in Table 31. The estimation of hydrogen loss is consistent between FTIR and exodiffusion: the loss is around 65-70%.

	Integrated signals (a.u.)			
	Amorphous		Microcrystalline	
	FTIR	Exodiffusion	FTIR	Exodiffusion
As deposited	97.3	$1.60 \times 10^{-7}$	218	$2.06 \times 10^{-7}$
After RTA @350°C	33.1	$5.00 \times 10^{-8}$	72.5	$6.56 \times 10^{-8}$
Hydrogen loss	-66%	-69%	-67%	-68%

**Table 31: Comparison of the hydrogen loss after RTA estimated by FTIR and by exodiffusion.**

Absorption spectra of samples after RTA can be deconvoluted into two peaks. Table 32 summarizes the FTIR deconvolution parameter for the amorphous and the microcrystalline samples before and after the annealing step.

Sample:	Amorphous		Microcrystalline	
Annealing:	-	RTA @350°C	-	RTA @350°C
P <sub>1</sub> (cm <sup>-1</sup> )	1998	1989	2005	1991
P <sub>2</sub> (cm <sup>-1</sup> )	2092	2080	2101	2074
H <sub>1</sub> (%)	0.76	0.30	1.66	0.72
H <sub>2</sub> (%)	0.26	0.09	0.32	0.26
W <sub>1</sub> (cm <sup>-1</sup> )	77	58	94	63
W <sub>2</sub> (cm <sup>-1</sup> )	66	66	60	50
A <sub>1</sub> (%.cm <sup>-1</sup> )	73	22	196	57
A <sub>2</sub> (%.cm <sup>-1</sup> )	21	7	24	17
A <sub>1</sub> /(A <sub>1</sub> +A <sub>2</sub> )	78%	76%	89%	77%

**Table 32: Fit parameters of FTIR spectra.**

Literature is prolific on positions of Si-H and Si-H<sub>2</sub> peaks, because their position depends on the environment configuration of the bonds [77]. For example in the case of Si-H, the environment of the silicon atom or the hydrogen atom depend on the spatial configuration of neighborhood (void, silicon atoms, hydrogen atoms). If more configurations exist in a material, the FTIR peak will be broader.

Before continuing the discussion, let us introduce a notation for the four different hydrogen bonds we have identified so far in our amorphous and microcrystalline material. Two categories were created from the exodiffusion measurement: weakly bonded hydrogen or tightly bonded hydrogen. From FTIR spectra, two other categories were found: Si-H bond or Si-H<sub>2</sub> bond. Therefore a hydrogen bond is identified by two characteristics: weak/tight and Si-H/SiH<sub>2</sub>. Table 33 gives the name of each configuration.

	Si-H	Si-H <sub>2</sub>
Weak	B <sub>w1</sub>	B <sub>w2</sub>
Tight	B <sub>t1</sub>	B <sub>t2</sub>

**Table 33: Name of the four types of bonds.**

If the weak/tight characteristics are uncorrelated to the Si-H/Si-H<sub>2</sub> characteristics, we should have the relations on peak position  $P(B_{w1})=P(B_{t1})$  and  $P(B_{w2})=P(B_{t2})$  and the relations on peak width  $W(B_{w1})=W(B_{t1})$  and  $W(B_{w2})=W(B_{t2})$ . After RTA, only tight bonds are present. As shown in the amorphous case we have  $P(B_{t1})=1989 \text{ cm}^{-1}$ ,  $P(B_{t2})=2080 \text{ cm}^{-1}$ ,  $W(B_{t1})=58 \text{ cm}^{-1}$ , and  $W(B_{t2})=66 \text{ cm}^{-1}$ . Before RTA, both weak and tight bonds are present. Therefore  $P(B_{w1}+B_{t1})=1998 \text{ cm}^{-1}$ ,  $P(B_{w2}+B_{t2})=2092 \text{ cm}^{-1}$ ,  $W(B_{w1}+B_{t1})=77 \text{ cm}^{-1}$ , and  $W(B_{w2}+B_{t2})=66 \text{ cm}^{-1}$ . We can conclude that  $P(B_{t1})$  is lower than  $P(B_{w1})$  by

$10\text{ cm}^{-1}$ , and  $P(B_{t2})$  is lower than  $P(B_{w2})$  by  $10\text{ cm}^{-1}$  as well. The reasoning is more delicate for the width comparison: the Si-H peak can't be deconvoluted into one Gaussian curve (position  $P_1$  and width  $W_1$ ) but should be deconvoluted with two Gaussian curves with parameter  $P(B_{w1})$  and  $W(B_{w1})$  for the first, and  $P(B_{s1})$  and  $W(B_{s1})$  for the second. But since peak positions are different and proportions of  $B_{w1}$  and  $B_{w2}$  bonds are not identical, it is very difficult to estimate what would be the equivalent position and width of the summation of the two Gaussians (which is moreover mathematically not correct). Therefore no comparison can be done between  $W(B_{w1})$  and  $W(B_{t1})$ , even if  $W(B_{w1}+B_{t1}) > W(B_{t1})$ . Same problem is encountered for the Si-H<sub>2</sub> peak.

The conclusion is that  $P(B_{s1}) < P(B_{w1})$  and  $P(B_{s2}) < P(B_{w2})$  (both by  $10\text{ cm}^{-1}$ ). This demonstrates that weakly bonded hydrogen and tightly bonded hydrogen do not have same environment resulting in a peak shifting in FTIR. This is both true for Si-H or Si-H<sub>2</sub> and amorphous or microcrystalline cases. Further investigations should be performed to deepen the understanding.

#### 4.3.2 H<sub>2</sub> flow rate series

A H<sub>2</sub> flow rate series has been presented in Chapter 2. For the same plasma conditions, given in Table 34, exodiffusion measurements have been performed to address the question of the hydrogen configuration.

T <sub>sub</sub> (°C)	T <sub>RF</sub> (°C)	d <sub>i</sub> (mm)	Pr (Torr)	SiF <sub>4</sub> (sccm)	H <sub>2</sub> (sccm)	Ar (sccm)	Pw (W)	t <sub>d</sub> (sec)
150	200	30	3.8	10	1	88	40	1800
					5			
					9			

Table 34: Plasma conditions for the H<sub>2</sub> flow rate series studied by exodiffusion.

Figure 93 shows the three exodiffusion spectra corresponding to the conditions of Table 34. At 1 sccm, the layer is amorphous and the exodiffusion spectra display a WBH height lower than the TBH. The position of the weak peak is around 300°C whereas the position of the tight peak is  $\approx 480^\circ\text{C}$ . At 2 sccm, the amorphous-to-microcrystalline transition occurs and the WBH height is higher than the TBH height (contrary to the 1 sccm amorphous case). The position of the WBH is again 300°C but the position of the TBH is shifted to higher temperature at 480°C. At 9 sccm, the film is fully microcrystalline and the WBH height is lower than the TBH height. The WBH position is always 300°C whereas the TBH position is shifted again at above 480°C.

The total area below the exodiffusion spectra is proportional to the quantity of hydrogen contained in the film. To get the concentration of hydrogen, one should divide this quantity by the volume of the layer. The surface is similar for each sample: it is always half of a 5x5 cm<sup>2</sup> glass substrate. The thickness of layers strongly depends on the H<sub>2</sub> flow, in line with the phenomenological model. In the amorphous regime, deposition rate is proportional to the H<sub>2</sub> flow rate, whereas above the amorphous-to-microcrystalline transition, the deposition is relatively constant (there is a small etching effect by atomic hydrogen). Therefore the exodiffusion of the 1 sccm sample seems low but its thickness is low too leading to a high concentration of hydrogen. On the contrary, the exodiffusion of the 9 sccm sample is low but the sample is thicker leading to a low concentration of hydrogen. At the transition, the exodiffusion of the 5 sccm sample is very high but the thickness is similar to the one at 9 sccm. Therefore the concentration of hydrogen is very high.

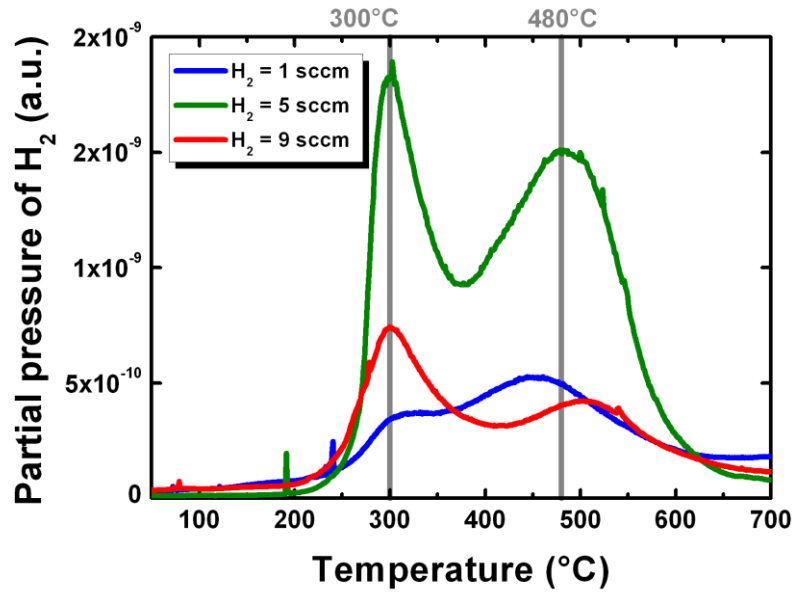


Figure 93: Exodiffusion spectra of three silicon films: amorphous at 1 sccm, a mixture of amorphous and crystalline phases at 5 sccm, and fully crystallized material at 9 sccm.

The hydrogen concentration is estimated from the normalization of the whole hydrogen (detected by exodiffusion) by the thickness of the layer (measured by ellipsometry). Figure 94 shows the hydrogen concentration as a function of the  $H_2$  flow rate. From 1 sccm to 4 sccm of the  $H_2$  flow rate, this concentration is relatively constant, but at the transition (5 sccm), there is a peak in the level of hydrogen in the films. Above the transition, between 6 sccm and 10 sccm, the hydrogen concentration is lower than the one before the transition: microcrystalline layers have less hydrogen than the amorphous films (by about a factor of two). Interestingly enough, at the transition there is a peak of hydrogen concentration. This is consistent with the general picture of H-mediated crystallization. We know that the crystallization is a phase transition where atomic hydrogen plays a key role. Therefore, the hydrogen peak is not unexpected.

Figure 95 shows the ratio between the WBH versus the TBH. The ratio is increasing with the  $H_2$  flow rate meaning that the more microcrystalline the higher the weak peak and the lower the strong peak. In other words, hydrogen content is lower in microcrystalline films and is incorporated as a weakly bonded hydrogen most likely at grain boundaries.

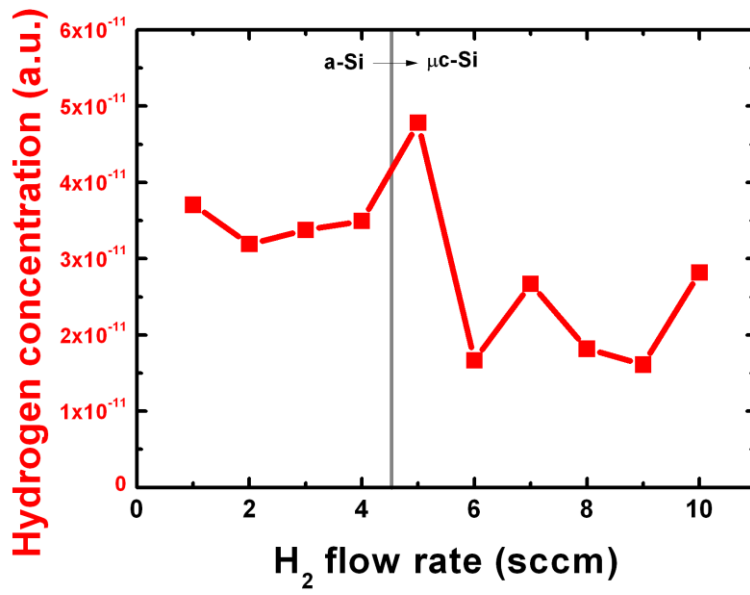


Figure 94: Hydrogen concentration deduced from exodiffusion measurements as a function of the  $H_2$  flow rate.

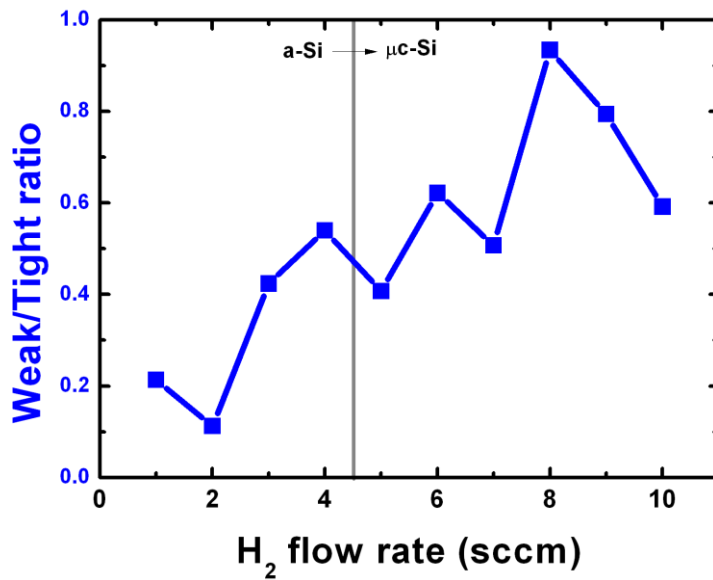


Figure 95: Ratio between weak and tight peak from exodiffusion as a function of the  $H_2$  flow rate.

### 4.3.3 RF power series

We have demonstrated the feasibility of the crystallization of plasma-generated nanoparticles by increasing the RF power like in plasma conditions of Table 35. A fourth plasma condition has been added for the comparison.

$T_{\text{sub}}$ (°C)	$T_{\text{RF}}$ (°C)	$d_i$ (mm)	$P_r$ (Torr)	$\text{SiF}_4$ (sccm)	$\text{H}_2$ (sccm)	$\text{Ar}$ (sccm)	$P_w$ (W)	$t_d$ (sec)
150	80	30	3.8	3.6	3	88	10	1800
					3		25	
					3		100	
					6		20	

Table 35: Plasma conditions for the RF power series studied by exodiffusion.

As described in Figure 49, the sample at 10 W was found to be a mixture of amorphous and microcrystalline silicon. The depletion was low, therefore, microcrystalline silicon should be expected, but amorphous nanoparticles are coming from the plasma and are difficult to crystallize due to the huge amount of silicon provided by each nanoparticle. The 100 W sample was found microcrystalline due to the contribution of already crystallized plasma-generated nanoparticles.

Figure 96 shows the exodiffusion spectra of the 10 W, 25 W, and 100 W samples of the RF power series in comparison with the microcrystalline sample deposited at 6 sccm of  $\text{H}_2$  flow rate and 20 W of RF power. The spectra have been normalized by the thickness of each sample. The area below the curves is proportional to the hydrogen concentration of the films.

From the exodiffusion spectra, the 25 W sample looks more amorphous than the 10 W because the amplitude of the tight peak is higher than the weak peak. This can be attributed to the increase of the  $\text{H}_2$  depletion with the increasing RF power. By increasing the RF power from 10 W to 100 W, the hydrogen concentration decreases as it can be visually seen in Figure 96. Hydrogen concentration at  $\text{H}_2=3$  sccm and 100 W is even lower than in the microcrystalline silicon deposition at  $\text{H}_2=6$  sccm and 20 W which has undergone a surface/sub-surface crystallization by atomic hydrogen with amorphous nanoparticles. The low hydrogen content for the 100 W sample is consistent with a growth model based on crystallized silicon particles which should bring a very low hydrogen concentration (pure crystalline particles without hydrogen) and where the  $\text{H}_2$  depletion is very high ( $\text{H}_2$ -limited regime).

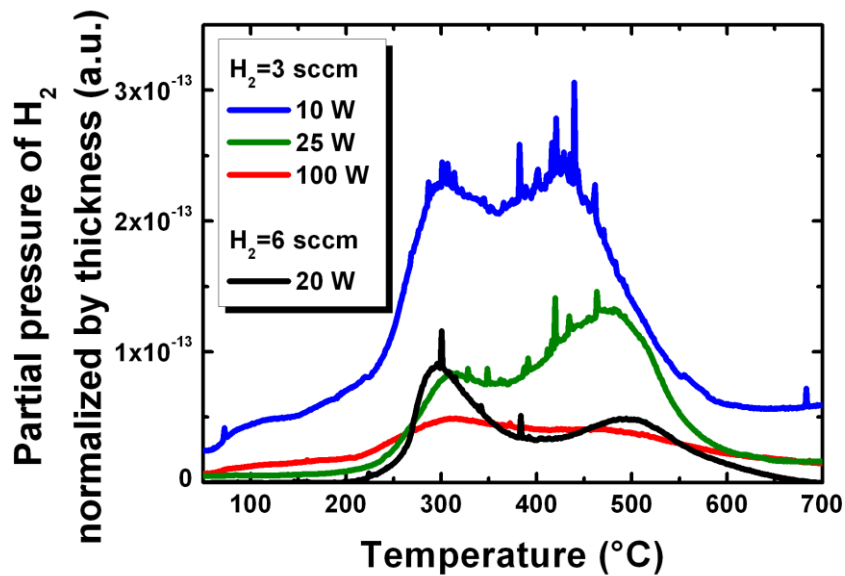


Figure 96: Exodiffusion spectra normalized by the thickness of layers.

## 4.4 Material quality

### 4.4.1 SIMS

Besides the nanostructure and the microstructure of the material, the electronic properties of microcrystalline silicon are very sensitive to the contamination by impurities. In order to assess the quality of our materials, the question of their composition is of importance. The main atom is of course silicon. However other elements are expected such as hydrogen or fluorine coming from the  $\text{SiF}_4$  and  $\text{H}_2$  gas. The microcrystalline silicon should be intrinsic and phosphorus and boron are not expected in our layers. Elements like oxygen or carbon are considered as impurities.

Secondary Ion Mass Spectroscopy (SIMS) is a technique which sputters the sample with an ion beam. The sputtered material is analyzed by a mass spectrometer. The technique can be quantitative if adequate calibration is done. For our measurement,  $\text{Cs}^+$  ions have been used with an energy of 10 keV. A SIMS profile shows the concentration of the elements contained in the sample as a function the sputtering depth. These concentrations are calibrated thanks to standards.

SIMS profiles have been measured on solar cell stacks because what really matters is the intrinsic microcrystalline silicon deposition into the PIN stack. The deposition conditions of solar cells differs from the conditions on glass (usually used for plasma studies): the substrate is the ZnO with a thin layer of (p) $\mu\text{c-Si:H}$ . Moreover the ZnO is textured and the growth is different from the flat substrate because the stress release will be modified. As it will be described in the next chapter, the solar cell stack (except metallization) consists (from the bottom to the top) of glass (substrate), ZnO:Al (transparent conductive oxide), (p) $\mu\text{c-Si:H}$  (P-layer), (i) $\mu\text{c-Si:F,H}$  (I-layer), (n)a-Si:H (N-layer), ITO (transparent conductive oxide and intermediate index layer). Only the intrinsic layer is fabricated from  $\text{SiF}_4/\text{H}_2/\text{Ar}$  gas mixtures. The SIMS profile will start the sputtering from the top to the bottom of the stack until reaching the substrate. It is worth noticing that ZnO is textured with a pattern size ( $\approx 0.5 \mu\text{m}$ ) smaller than the SIMS beam size ( $8 \mu\text{m}$  or  $30 \mu\text{m}$  diameter depending on the analyzed species). Therefore the SIMS profile will average all the material found in depth, and in particular boron of the P-layer will be detected on a depth similar to the texturing ( $1 \mu\text{m}$ ) while its thickness is much lower (20 nm).

Two solar cells have been selected, differing by their crystalline fraction deduced from Raman spectroscopy. The two solar cells show a crystalline fraction of 100% and 80% respectively. Table 36 summarizes the solar cell properties.

Crystalline fraction of (i) $\mu\text{c-Si:H}$ layer (%)	Thickness of (i) $\mu\text{c-Si:H}$ layer ( $\mu\text{m}$ )	$J_{\text{sc}}$ ( $\text{mA/cm}^2$ )	$V_{\text{oc}}$ (mV)	FF (%)	$\eta$ (%)
80	3.0	21.7	580	64	8.1
100	1.8	25.4	536	68	9.2

Table 36: Description of solar cells analyzed by SIMS.

Figure 97 shows the SIMS profiles of hydrogen (H), fluorine (F), phosphorus (P), and boron (B) elements of the 100% microcrystalline solar cell. The concentration of dopants (P and B) is very low within the bulk of the I-layer (depth between 0.1  $\mu\text{m}$  and 1.5  $\mu\text{m}$ ). The hydrogen concentration is  $2 \times 10^{21} \text{ cm}^{-3}$ . By taking  $5 \times 10^{22} \text{ cm}^{-3}$  as the density of our material, there is 4% of hydrogen in the material. The fluorine concentration is  $3 \times 10^{19} \text{ cm}^{-3}$ , representing 0.06% of the total atoms.

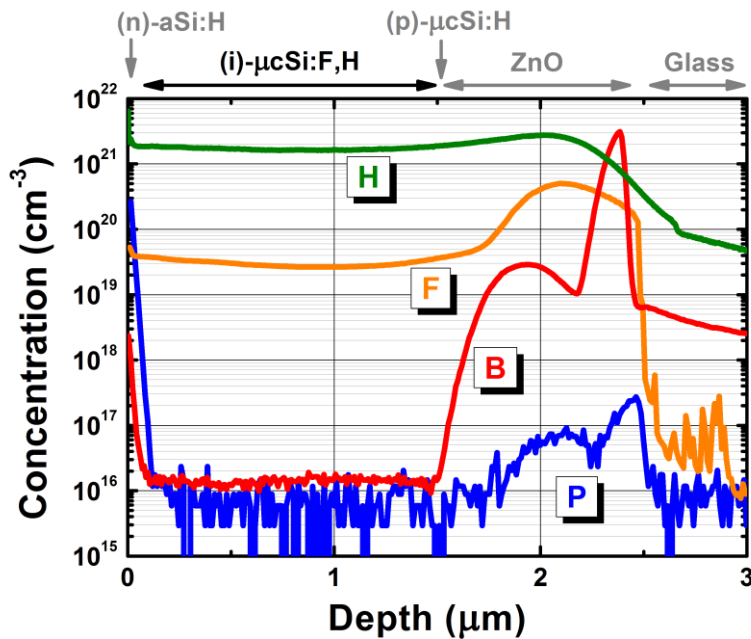


Figure 97: H, F, B, and P SIMS profiles of 100% microcrystalline silicon solar cell.

Figure 98 shows the SIMS profile of the 80% microcrystalline solar cell. Again the dopant concentrations are very low. The hydrogen concentration is  $4 \times 10^{21} \text{ cm}^{-3}$  and the fluorine concentration is  $5 \times 10^{19} \text{ cm}^{-3}$ . They correspond respectively to 8% and 0.1% of the total density. Table 37 summarizes the H and F concentrations extracted from SIMS profiles of the two samples. The doubling of the hydrogen content is attributed to the 20% of amorphous phase.

Sample	H concentration	F concentration
80%	8%	0.1%
100%	4%	0.06%

Table 37: H and F concentrations estimated by SIMS.

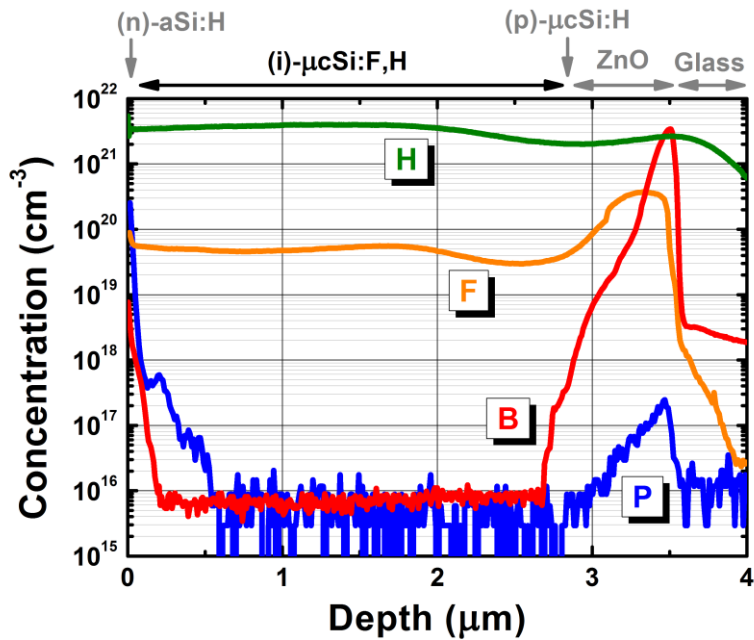


Figure 98: H, F, B, and P SIMS profiles of 80% microcrystalline silicon solar cell.

The fluorine concentration deduced from the SIMS analysis is low compared to hydrogen. In comparison, Ovshinsky and Madan reported in 1978 a fluorine content of 2% to 6% depending on the ratio of  $\text{SiF}_4/\text{H}_2$  and a hydrogen content about 0.5% for amorphous films [27]. These results can be enlightened by the phenomenological model. Few years later, Ovshinsky and Madan published another paper [28] where plasma conditions were given: the RF power was 50 W but a  $\text{SiF}_4/\text{H}_2$  ratio varied from 10 to 99. This means that they were far away from the transition (B very small compared to A in Figure 20) where all the hydrogen is depleted to form HF but where a lot of fluorine atoms are free (not scavenged) to go onto the growing surface. This could explain the significant difference between their fluorine content of more than 1% with our fluorine content of less than 0.1%.

Figure 99 shows the SIMS profiles of carbon and oxygen elements, which have not been calibrated. The raw signal is in counts per second which is still proportional to the element concentration for a given material (the calibration does take into account the differential sputtering rate of each element in each material). The comparison stands between the 80% and the 100% microcrystalline solar cell. In the intrinsic microcrystalline layer, the carbon and oxygen contents are identical. The plasma conditions giving the two samples are very close because the 80% sample is obtained by being near the transition. The similar oxygen and carbon concentration is understandable and, unlike hydrogen or fluorine, they are not involved in the amorphous to microcrystalline transition: their concentration is independent of the  $\text{H}_2$  flow rate.

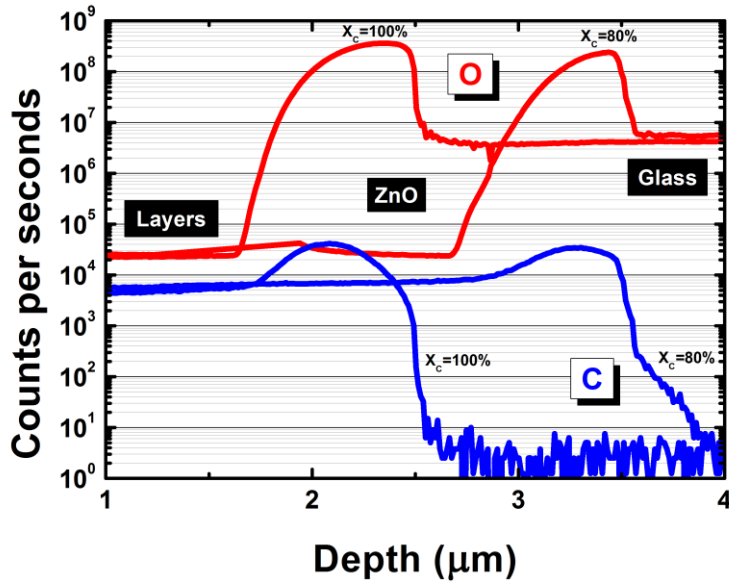


Figure 99: C and O SIMS profiles of the 80% and 100% microcrystalline silicon solar cell. The profiles are not calibrated.

#### 4.4.2 Defect density from FTPS measurements

Fourier Transform Photocurrent Spectroscopy (FTPS) is a technique through which one can estimate the absorption coefficient with high accuracy. The absorption of a semi-conductor below its bandgap is very useful as it is linked to the presence of defects: if a photon is absorbed below the bandgap, it proves that an electron state exist below the bandgap thus acting as a trapping and/or a recombination center. FTPS measurements have been performed by the group of the Institute of Physics in Prague in Czech Republic (Jakub Holovský, Adam Purkrt, and Milan Vaněček). We are interested in microcrystalline silicon deposited in solar cell conditions which is different of what we can get from deposition on glass. It is the reason why FTPS measurements have been done on the solar cell stack. Three stacks have been measured: one solar cell having a fully intrinsic microcrystalline layer, while the two others have a crystalline fraction ( $X_c$ ) of about 70% and an amorphous fraction of about 30%. Solar cell properties are given in Table 38.

Name	Thickness (nm)	$X_c$ (%)	$V_{oc}$ (mV)
70% Thin	700	74	594
70% Thick	2200	71	594
100%	2100	100	530

Table 38: Solar cell characteristics for FTPS measurements.

In terms of solar cell characteristics, the presence of 30% of amorphous silicon has a significant impact on the open-circuit voltage ( $V_{oc}$ ) and external quantum efficiency (EQE). Figure 100 shows the EQE of the three solar cells. The fully crystallized solar cell has a  $V_{oc}$  of 530 mV and its EQE decreases to zero at 1100 nm which corresponds to the bandgap of crystalline silicon. The two solar cells with 30% of intrinsic amorphous silicon have a  $V_{oc}$  of 594 mV and their EQE decreases to zero at 1000 nm. The 70% crystallized and thick sample absorbs less red light than the 100% crystallized sample despite their same thickness. This is consistent with previous results from Moreno *et al.* [78].

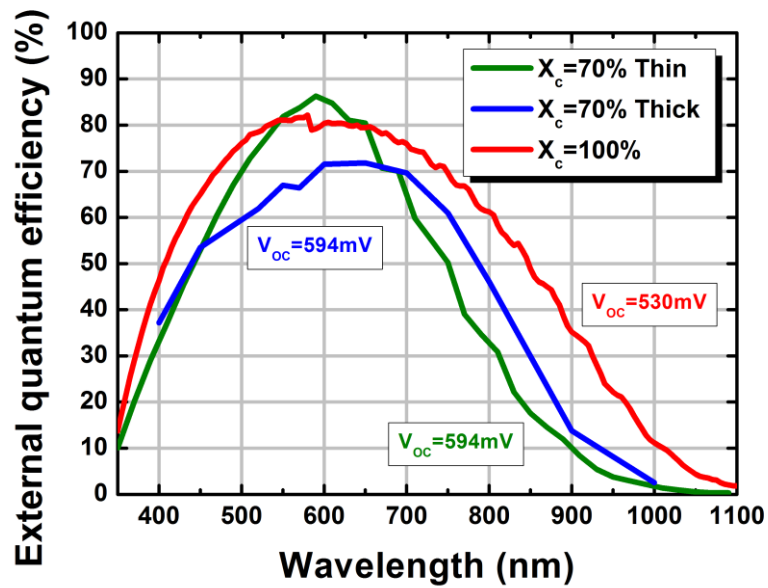


Figure 100: EQE of the three solar cells measured in FTPS.

Figure 101 shows the FTPS measurements of the three solar cells. A crystalline silicon wafer has been taken as a reference for the absorption coefficient of fully crystallized silicon. The reference point is taken at 1.35 eV with an absorption coefficient ( $\alpha$ ) of  $250 \text{ cm}^{-1}$ . The bulk quality is usually associated to the absorption coefficient at 0.8 eV. The Urbach slope value is evaluated from the steepest part of the Urbach edge and is linked with the disorder of the material.

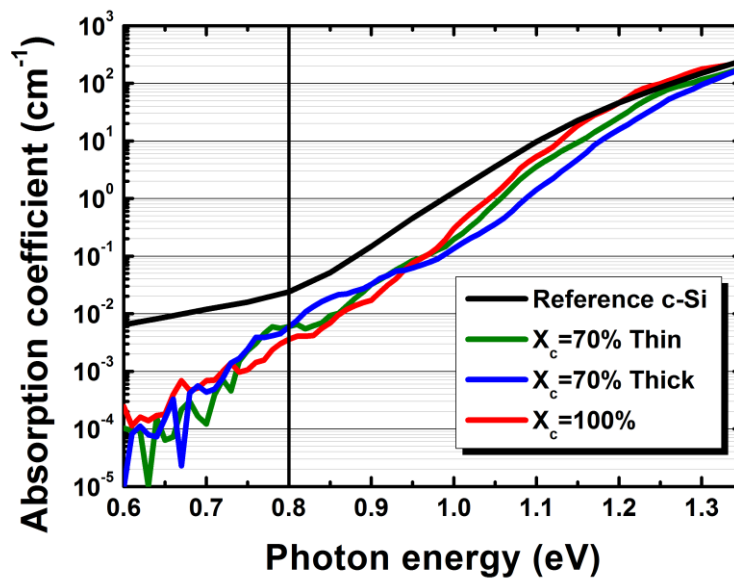


Figure 101: FTPS measurements of the three solar cells.

Table 39 summarizes the values of  $\alpha$  at 0.8 eV and the Urbach energy for the three samples. The lowest  $\alpha$  at 0.8 eV is obtained with the 100% crystallized layer at  $3 \times 10^{-3} \text{ cm}^{-1}$ , which can be translated into a defect density of  $5.1 \times 10^{14} \text{ cm}^{-3}$  according to the coefficient  $1.7 \times 10^{17} \text{ cm}^{-2}$  provided in [79]. This low defect density is correlated to the low Urbach energy of 38.4 meV related to low disorder materials. This value of defect density is similar to one published in [80] by EPFL group. The 70% crystallized layers also have a low defect density but which is higher than in the 100% crystallized case. The amorphous part is therefore more defective than the crystalline part (and its grain boundaries). The higher

absorption coefficients are correlated to higher Urbach slopes by a few meV. Moreover Figure 101 shows a shift in the absorption edge (at  $\alpha=10^0 \text{ cm}^{-1}$ ) to higher energy suggesting a wider gap of about 100 meV. That is fully consistent and correlated to EQE curves of Figure 100 where the two 70% crystallized sample curves decrease at 1000 nm instead of 1100 nm (case of the 100% crystallized sample), which is of the order of 100 meV too. The bandgap of partially crystallized samples (1.2 eV) is nonetheless much smaller than bandgap of amorphous silicon (1.7-1.9 eV).

Sample	$\alpha$ @ 0.8 eV ( $\text{cm}^{-1}$ )	Urbach energy (meV)	Defect density ( $\text{cm}^{-3}$ )
70% Thin	$0.005 \pm 0.002$	$37.3 \pm 2$	$8.5 \times 10^{14}$
70% Thick	$0.007 \pm 0.002$	$38.4 \pm 0.5$	$1.2 \times 10^{15}$
100%	$0.003 \pm 0.0005$	$34.7 \pm 0.5$	$5.1 \times 10^{14}$

**Table 39: Absorption coefficient at 0.8 eV and the Urbach energy deduced from by FTPS measurements.**

For the three samples, such low defect densities are the probable source of the excellent  $V_{oc}$  obtained in our PIN solar cells: 530 mV for 100% crystallized and 594 mV for 70% crystallized intrinsic layer.

## 4.5 Chapter key results

The material studies presented in this chapter have revealed the complexity of the material as well as its main characteristics. XRD patterns have demonstrated that for the microcrystalline films originating from plasma-generated nanoparticles, a random orientation was found, whereas preferential orientation has been measured in the films where the crystallization is mediated by surface and subsurface reactions. Raman spectroscopy has been used to bring into light the amorphous tissue, the crystalline domains, the small crystallites, and the grain boundaries. Each of them contributes to a specific identified peak in the Raman spectra. We have defined the crystalline fraction  $X_c$ , the crystallite fraction  $X_{cry}$ , and the grain boundaries fraction  $X_{GB}$ . We will see on the next chapter that all of them are important to understand the solar cell performances.

Concomitant to the complex structure of the material, hydrogen is embedded under various configurations: FTIR revealed the Si-H bonding as well as the Si-H<sub>2</sub> bonding, but exodiffusion measurements suggested that Weakly Bonded Hydrogen (WBH) is located on the grain boundaries as the increase of the H<sub>2</sub> flow rate leads to an increase of the WBH and to a decrease of the Tightly Bonded Hydrogen (TBH). From SIMS measurements we determined a hydrogen concentration at 4% for microcrystalline silicon with  $X_c=100\%$ , whereas the fluorine concentration has been estimated at a value below 0.1%.

By working at the amorphous-to-microcrystalline plasma conditions, a defect density as low as  $5.1 \times 10^{14} \text{ cm}^{-3}$  has been achieved. The next chapter will show how this low defect density can be turned into high solar cell performances. Correlation between material characterizations (described in this chapter) and solar cell performances will be done.



# 5. Solar cells

## Contents

---

<b>5.1 Description of the P-I-N stacks.....</b>	<b>130</b>
5.1.1 Solar cell stack .....	130
5.1.2 ZnO.....	131
5.1.3 TEM cross section picture of the PIN solar cells.....	131
5.1.4 Metallization.....	134
5.1.5 Plasma conditions for the intrinsic microcrystalline silicon layer .....	135
5.1.6 Solar cell characterizations.....	135
<b>5.2 Correlation between solar cell characteristics and material properties.....</b>	<b>135</b>
5.2.1 Fully crystallized versus partially crystallized I-layer .....	135
5.2.2 $V_{OC}$ versus $X_C$ and $X_{cry}$ .....	139
5.2.3 $V_{OC}$ & $J_0$ versus $X_{GB}$ at $X_C=100\%$ .....	140
5.2.4 Spectral response at 800 nm versus the I-layer thickness for $X_C=100\%$ I-layer .....	142
<b>5.3 Focus on our record solar cells .....</b>	<b>143</b>
5.3.1 Thick intrinsic microcrystalline layer: 3.8 $\mu\text{m}$ with $X_C<100\%$ .....	143
5.3.2 High efficiency solar cell: 3.4 micron-thick with $X_C<100\%$ .....	144
5.3.3 Highest efficiency solar cell: 1.8 micron-thick with $X_C=100\%$ .....	145
5.3.4 Summary of the solar cells.....	145
<b>5.4 Chapter key results .....</b>	<b>146</b>

---

## 5.1 Description of the P-I-N stacks

### 5.1.1 Solar cell stack

The solar cells are fabricated layer by layer and the reactor used to deposit the layers is changing at each step. The main layer is the (i) $\mu\text{c-Si:H,F}$  and is deposited in PHILIX reactor. That reactor used for plasma and material studies in the previous chapters does not have dopant gas lines, therefore a different reactor is used for doped layers. That is most likely detrimental to the interfaces and therefore to the solar cell performances. Figure 102 shows the schematic of our PIN solar cell structure.

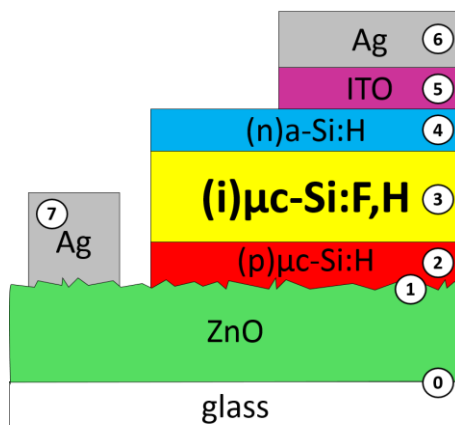


Figure 102: Schematic of the PIN solar cell structure.

- **Step #0 – glass and ZnO:** the zinc-oxide deposited on glass substrate comes from Jülich Forschungszentrum. It is fabricated by magnetron sputtering and is doped with aluminum (Al). The substrate is cleaved into  $2.5 \times 2.5 \text{ cm}^2$  samples. The ZnO is used as a front contact.
- **Step #1 – texturing:** the surface is textured by a hydrochloric (HCl) acid bath during 60 seconds. The acid is highly diluted in deionized (DI) water (concentration of 0.5%). After the bath, the sample is dipped into DI water to remove all the etchants from the surface, thus stopping the etching reaction. Then the sample is immersed in an isopropyl solution to remove the water from the surface. Finally, the isopropyl is removed from the sample surface by drying it with nitrogen gas flow (alcohol being a volatile species).
- **Step #2 – P-doped layer:** the textured sample is loaded into a PECVD reactor named “ARCAM”. A detailed description of this reactor can be found in [40]. The P-doped layer is made of microcrystalline silicon from a  $\text{SiH}_4/\text{H}_2/\text{B}_2\text{H}_6$  gas mixture plasma. The thickness of the P layer is 10-30 nm.
- **Step #3 – Intrinsic layer:** the sample is loaded in our “PHILIX” reactor. Intrinsic microcrystalline silicon is deposited with gas mixtures of  $\text{SiF}_4$ ,  $\text{H}_2$ , and Ar. When the sample is loaded, pumping is launched and heating starts (substrate holder at  $150^\circ\text{C}$  and RF electrode at  $80^\circ\text{C}$ ). The plasma is only ignited when the base pressure is below  $2 \times 10^{-6}$  mbar (in order to minimize oxygen concentration within the reactor). After deposition, the reactor is cooled down and the sample is unloaded only when the temperature is below  $70^\circ\text{C}$ . That is to avoid excessive thermal shock during the opening of the reactor to the ambient air.
- **Step #4 – N-doped layer:** the sample is again loaded in “ARCAM” reactor. The N layer is made of amorphous silicon. The dopant gas is  $\text{PH}_3$ . The thickness is about 10-30 nm.
- **Step #5 – ITO:** indium-tin-oxide (ITO) is sputtered from an ITO target to the sample with a plasma of Ar and  $\text{O}_2$  gas. The thickness is about 80 nm. A mask is used to deposit ITO only on specific areas defining our solar cells. The mask is composed of six circles with a surface of

0.126 cm<sup>2</sup>. Therefore in one sample there are six solar cells. The typical sheet resistance of our ITO is 55 Ω/□ (measured on glass substrate).

- Step #6 – Ag for back contact: on top of ITO, silver (Ag) is evaporated (same mask as for ITO is used for the process step). A nominal thickness of 250 nm of silver is typically deposited. The silver purpose is twofold: it is used as a back contact to collect electrons arriving through the N-layer and it is used as a back reflector for red and infrared photons.
- Step #7 – Ag for front contact: the ZnO is used to collect holes coming from the P-layer. However ZnO is hidden by the stacking. In order to reach the ZnO, the PIN stack is scratched with a diamond pen around the solar cells (the six circles). Furrows are thereby created, revealing the ZnO. Silver paste (mixture of silver and toluene solvent) is spread out onto the furrows.
- Step #8 – annealing: the final step is an annealing of the sample at 150°C during 30 min. It allows the drying of the silver front contact and the reduction of the contact resistance at the semiconductor/ITO/metal interfaces.

The ITO is used as an intermediate material between (n)a-Si:H layer and silver contact, in order to reflect light instead of being lost in the metal. The N-layer is amorphous but not microcrystalline. The main reason for this choice is the easiness of the solar cell surface definition: since the lateral conductivity of the amorphous silicon (N-doped) is low, one can neglect the collection of electrons outside the cylinder below the ITO+Ag circle. The illumination comes from the whole glass surface and all the intrinsic microcrystalline silicon is illuminated. However only the cylinder below the contact defines the area of the solar cells. The other reason for the use of N-doped amorphous silicon instead of microcrystalline silicon is the heterojunction effect at I/N interface which should reduce recombination of holes at this interface.

### 5.1.2 ZnO

Figure 103 shows a SEM (Scan Electron Microscopy) image of the textured ZnO layer. A lunar shape is found with crater diameters about of 1 μm and therefore a depth of 0.5 μm.

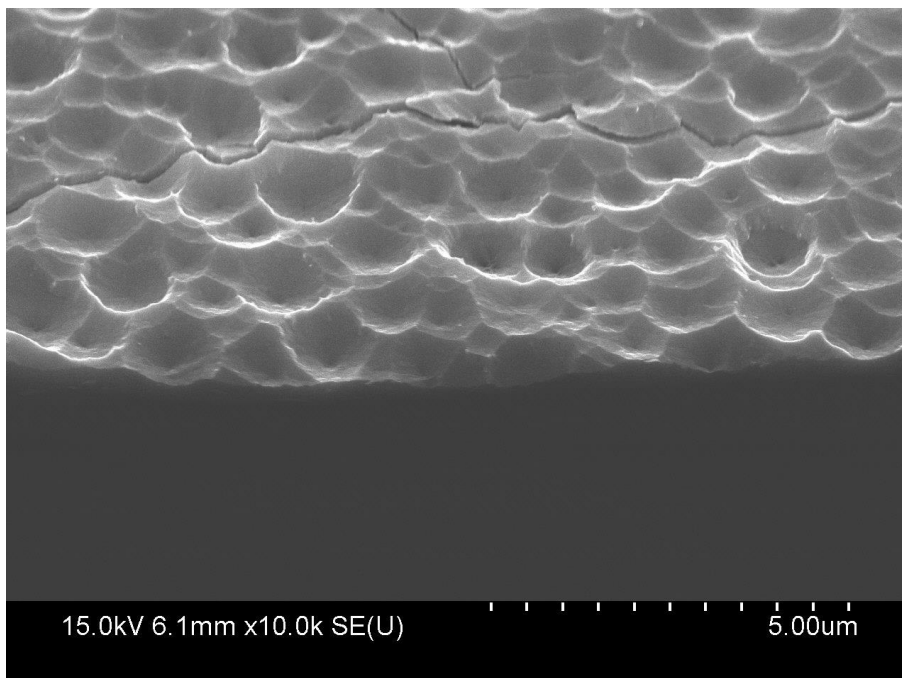


Figure 103: SEM image of textured ZnO.

### 5.1.3 TEM cross section picture of the PIN solar cells

Figure 104 shows a TEM cross section of the solar cell stack. The cross section has been made by the FIB (focus ion beam) technique at IEMN at Lille by David Troadec. On the bottom, one can see the ZnO in black which is textured with a pyramidal shape. The contrast within the ZnO shows the

crystalline columns of the microcrystalline structure of the ZnO. The bright part on top of the ZnO corresponds to the intrinsic microcrystalline silicon with a thickness of about 3  $\mu\text{m}$ .

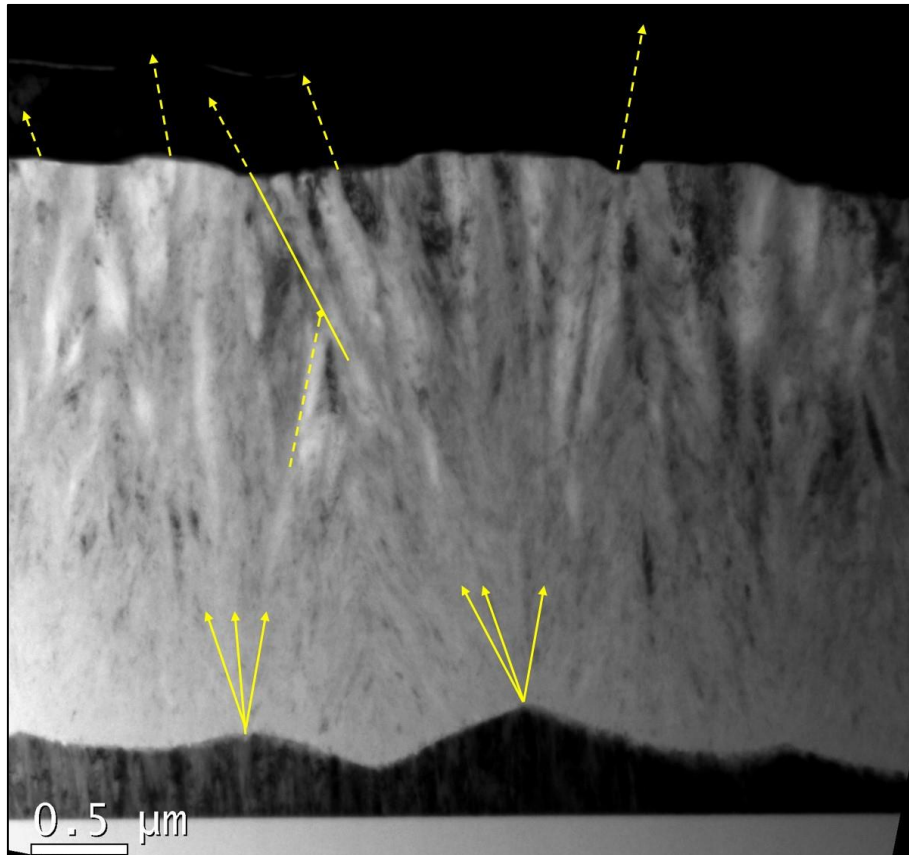


Figure 104: TEM image of a solar cell in cross section.

The structure of the microcrystalline silicon seems to be linked with the textured shape of the ZnO. On top of the microcrystalline silicon, column boundaries are found and these boundaries draw cones. By extrapolating these boundaries until the ZnO, it seems that the origin of the cones coincides with the top of the pyramids.

By measuring the diffraction pattern of the stack, several diffraction rings can be identified. Due to the microcrystalline phase (random azimuthal angle), rings are found instead of spots. By selecting one ring, a dark field TEM image can be obtained as displayed in Figure 105. In this Figure, we can see that the selected ring corresponds to the orientation of some columns in the ZnO, as well as some crystalline domains in the microcrystalline silicon region.

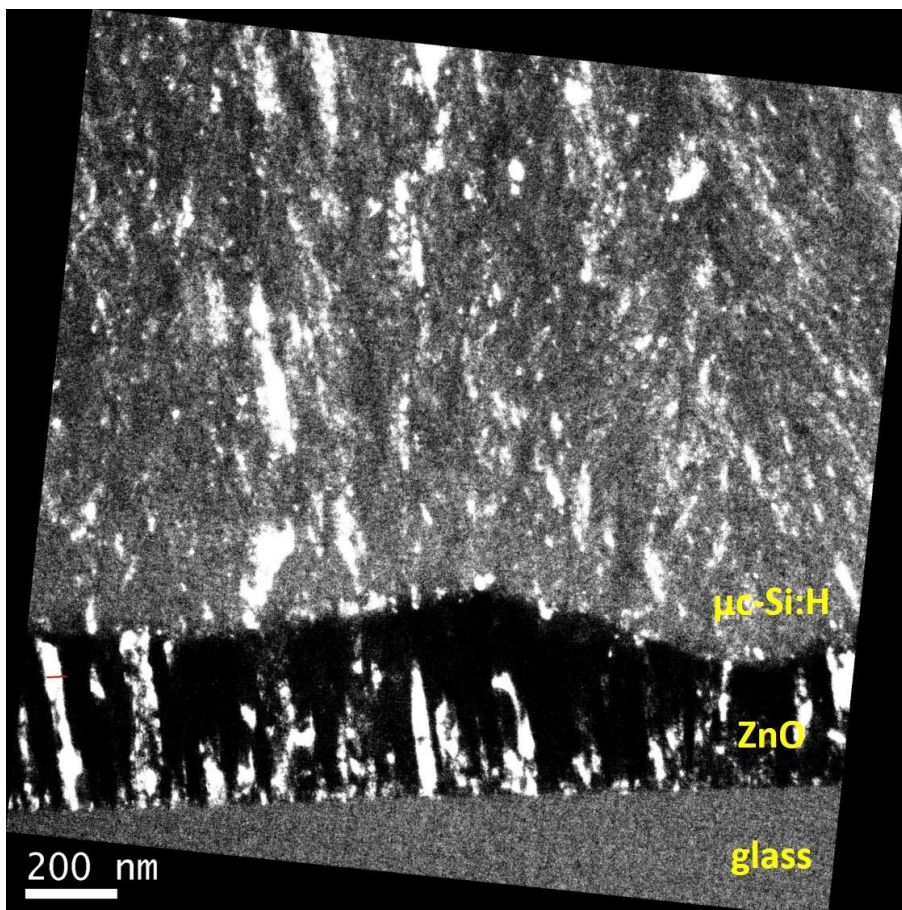


Figure 105: Dark field TEM image of a solar cell in cross section.

What is very interesting in this dark field image is the presence of elongated bright domains within the microcrystalline silicon phase. The elongation is in the direction of the growth (from bottom to top of the picture). Since it is the dark field image of a ring (in the Fourier space), we cannot directly conclude that one domain is made of only one crystalline orientation. However if several orientations constitute one domain, then there is no reason why all these orientations will contribute exactly to the same ring. Therefore we suggest that each bright domain is made of one crystalline orientation but that between domains the orientation is random (explaining the ring shape in the Fourier space).

The bright domains are larger than the crystallite size (several tens of nanometers compared to about 5-10 nm). The mechanisms leading to these large single-oriented domains should be addressed. However this is a difficult question requiring more studies. We propose that the mechanism is linked to epitaxial growth of silicon on top of small single-oriented domains. The epitaxy starts on small microcrystalline silicon grains. The small grain plays the role of a crystalline wafer. We call this process “local-epitaxy” [81] or “self-epitaxy” because the epitaxy happens on the crystallites of the microcrystalline silicon itself (there is no monocrystalline wafer, only small crystalline domains). The resulting material contains large grains. This hypothesis is not only based on the dark field image of Figure 105. Indeed, it is also correlated with: (i) the highest solar cell efficiencies are obtained at the amorphous-to-microcrystalline transition (lowest value of  $H_2$  flow rate giving microcrystalline silicon); (ii) amorphous plasma conditions lead to epitaxy on crystalline silicon wafer [82][37]; (iii) large grain microcrystalline silicon which is obtained at the transition [78]; (iv) in Figure 82a the GI-XRD pattern which shows a more intense 311 peak compared to the 111 and the 220 peaks, in a plasma condition close to the one used for the solar cell of Figures 104 and 105; (v) as it will be shown below, our solar cell performances are excellent [83][84] especially for the open-circuit voltage, despite the non-optimization of the layers and the interfaces and the vacuum-break between each layer.

#### 5.1.4 Metallization

Figure 106 shows a top view of a typical solar cell. The sample is a 2.5x2.5 cm<sup>2</sup> square where six solar cells are defined by the six ITO+Ag circles. We can see ten smaller solar cells but there are not used. The front contacts are seen in three parts: two lines parallel to the ruler in the middle and in the top, and one with a square shape encircling one solar cell. The front and back contacts are made of silver and look metallic. The orange part on the four corners is due to the four blades holding the sample in the PHILIX reactor during the (i) $\mu$ c-Si:H,F deposition. The grey part is the color of thick microcrystalline deposited on textured ZnO.

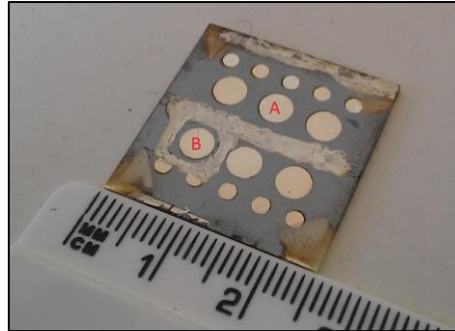


Figure 106: Picture of the top of a typical solar cell. The front contact is made of silver paste.

Under operation, holes are collected from the P-layer to the Ag front contact through the ZnO. The collection is not perfect and some Joule losses are encountered. In order to visualize these losses, an IR camera (“CA1884 RayCam” from Chauvin Arnoux) has been used to have a cartography of the hot regions. We are interested in the comparison of the front contact furrow geometry: the line or the square. Figure 107 shows the camera snapshots of the IR light of the solar cells of Figure 106 under bias (“A” and “B” in Figure 106).

In Figure 107a, the line-shaped front contact is used with cell “A” and the current flows from all the surface to the silver line. All the electrons of the ZnO (over the whole cell area) have to be collected by the silver contact. The electrons at the opposite side of the silver line have to travel a long distance into the ZnO before reaching the silver. This is an issue since the resistivity is higher in ZnO than in silver. In average, a higher series resistance will be incurred.

In Figure 107b, the square-shaped contact is used with cell “B” and the electrons are collected all around the silver front contact. The electrons will travel a short distance via the ZnO. Into the silver contact they will travel a long distance, which is not an issue since the conductivity is much higher in silver than in ZnO.

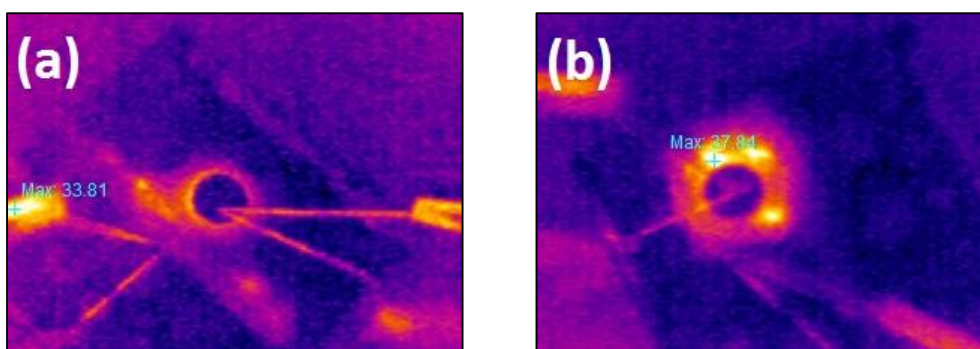


Figure 107: Infrared camera snapshots of a solar cell under bias with (a) the line-shaped and (b) the square-shaped front contact.

### 5.1.5 Plasma conditions for the intrinsic microcrystalline silicon layer

In this thesis, we focus on the intrinsic microcrystalline silicon layer made from SiF<sub>4</sub> precursors. The plasma conditions have been changed but not with big variations. Various layers have been obtained with respect to crystalline fraction, grain boundaries fraction, and material quality. We do recognize that many steps of the process are not totally reproducible and that it is difficult to predict the material nature and quality. That is of course not unexpected because we deposit our intrinsic layer during a long time and many issues can be encountered during this deposition time. To grow a 3 μm thick layer, about 6 hours are required. Moreover, the best solar cells are obtained close to the transition, and it is always difficult to work close to a transition: we do not know in advance if we will shift into the amorphous regime.

It should also be pointed out that the solar cells have been fabricated before the understanding of the SiF<sub>4</sub>/H<sub>2</sub>/Ar chemistry by the RGA and the phenomenological model. The structuration of this thesis does not reproduce the chronology of the events.

Table 40 shows the typical plasma conditions used to grow the microcrystalline silicon from SiF<sub>4</sub>/H<sub>2</sub>/Ar gas mixtures.

T <sub>sub</sub>	T <sub>RF</sub>	d <sub>i</sub>	Pr	SiF <sub>4</sub>	H <sub>2</sub>	Ar	Pw
(°C)	(°C)	(mm)	(Torr)	(sccm)	(sccm)	(sccm)	(W)
150	80	30	3.8	3.6	5.3	88	20

Table 40: Typical plasma conditions for the deposition of μc-Si:H,F used in PIN solar cells.

### 5.1.6 Solar cell characterizations

After the annealing step, the solar cells are characterized to evaluate their performances. The External Quantum Efficiency (EQE) is measured between 350 nm and 1100 nm under short-circuit. From the EQE and by integrating the EQE curve, we estimate the short-circuit current (J<sub>sc</sub>). Two other EQE curves are measured for each solar cell: with a reverse bias of -0.5 V and with a forward bias of +0.2 V. To assess the quality of our solar cells, we compare the EQE curves under reverse bias, no bias, and forward bias. In crystalline silicon solar cells the diffusion of carriers is the most important, but in thin film microcrystalline silicon the drift of the carriers is the main transport mechanism to collect electrons on the N-side and holes on the P-side. By assuming that the electric field is constant across the I-layer thickness, the reverse bias increases the internal electric field and enhances the collection of carriers. Conversely, the forward bias decreases the internal electric field and degrades the collection of carriers. The important parameter is the “collection length” compared to the thickness of the I-layer. This collection length depends on the internal electric field. For a solar cell which is not limited by the carrier collection, the thickness of the I-layer is lower than the collection length. Therefore if the EQE in the forward bias decreases with respect to the short circuit case (no bias), then we know that the I-layer is too thick and we are limited by the carrier collection through the I-layer.

Current density versus voltage (J-V) curve is then measured. The distance between the lamp and the sample is adjusted such that the measured J<sub>sc</sub> matches the estimated J<sub>sc</sub> from EQE. It is worth noticing that our J-V curves are measured with two probes. A four probes measurement might be useful to eliminate part of the series resistance due to the probe-silver contacts.

## 5.2 Correlation between solar cell characteristics and material properties

### 5.2.1 Fully crystallized versus partially crystallized I-layer

We have a set of solar cells and we want to correlate their performance with their material properties. We have shown in the previous chapter how to deconvolute Raman spectra into four peaks: amorphous, grain boundaries, crystallite, and crystalline peaks. Table 41 displays a subset of our solar cells where the crystalline fraction of the (i)μc-Si:F,H layer is given as well as the V<sub>oc</sub> and the J<sub>sc</sub>. The Full Width at Half Maximum (FWHM) of the crystalline peak (around 520 cm<sup>-1</sup>) is also given. Four solar

cells (A, B, C, and D) have a crystalline fraction around 70% and three solar cells (X, Y, and Z) are fully crystallized. A crystalline wafer (W) is also analyzed by Raman spectroscopy as reference.

Name	$X_c$ (%)	$V_{oc}$ (mV)	$J_{sc}$ (mA/cm <sup>2</sup> )	Thickness (nm)	$FWHM_{520}$ (cm <sup>-1</sup> )
A	72	623	18.5	1980	7.8
B	73	613	18.2	2000	7.8
C	71	594	18.5	2190	7.9
D	74	594	16.8	700	8.6
W=wafer	100				4.5
X	94	493	20.2	3000	5.0
Y	100	530	22.9	2100	3.2
Z	100	485	21.2	3050	4.9

Table 41:  $FWHM_{520}$  of selected samples compared with their  $X_c$ ,  $V_{oc}$ ,  $J_{sc}$ .

A, B, C, and D solar cells have a  $V_{oc}$  around 600 mV and a  $J_{sc}$  around 18 mA/cm<sup>2</sup> which is correlated with the 30% of amorphous tissue. X, Y, and Z solar cells have a  $V_{oc}$  around 500 mV and a  $J_{sc}$  around 21 mA/cm<sup>2</sup>. The difference of 100 mV in  $V_{oc}$  between the two categories has already been correlated with a shift of the bandgap of 100 mV in Figure 101 (FTPS measurements). The counterpart of an increase of the  $V_{oc}$  is a decrease of the  $J_{sc}$ : if the bandgap is lower, more photons can be collected. The EQE corresponding to solar cells A, B, X, and Y are shown in Figure 108. The difference between fully and partially crystallized layers can be seen at 1000 nm in the IR range, close to bandgap. The absorption is low for partially crystallized layer (higher bandgap) and the absorption is still sufficient to produce an EQE of 10% at 1000 nm because the layers are fully crystallized (lower bandgap).

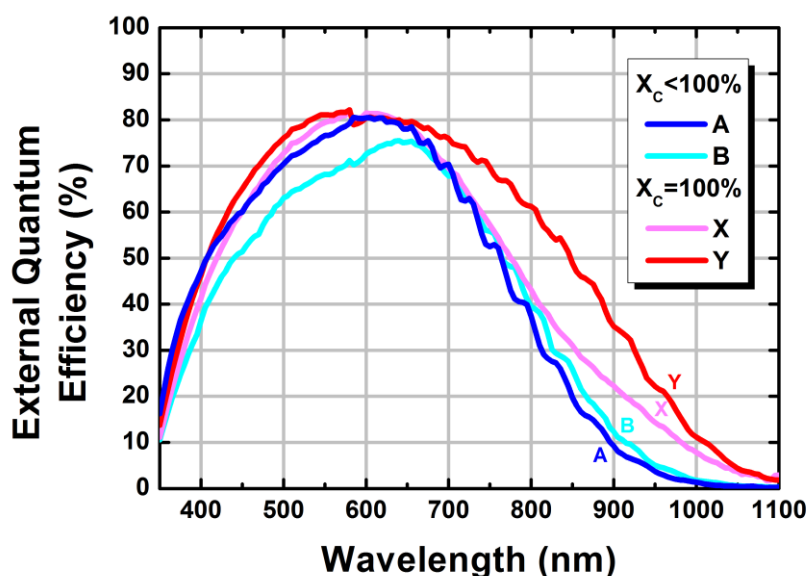


Figure 108: EQE curves of A, B, X, and Y solar cells.

The FWHM of the crystalline peak for partially crystallized layers is about 8 cm<sup>-1</sup>, whereas for fully crystallized layers it is below 5 cm<sup>-1</sup>. For comparison, the crystalline wafer has a FWHM of 4.5 cm<sup>-1</sup>. The solar cell Y has a FWHM of 3.2 cm<sup>-1</sup> which is below 4.5 cm<sup>-1</sup>. That is not possible because it would mean that the microcrystalline layer is more crystallized than the wafer. Most likely this is an artefact of the fitting procedure in four Gaussian curves. The widening of the crystalline peak in the partially crystallized layer has been associated to optical confinement due to the presence of small crystallites into an amorphous tissue. Before continuing on that study, we want to be sure that the widening of the crystalline peak is not an artefact of the fitting procedure.

Another way to estimate the width of the crystalline peak is to begin from the definition of the FWHM: we calculate the maximum signal of the Raman spectrum and look where the curves cross the value of half the maximum. Figure 109 shows the geometrical construction to estimate the FWHM: after normalizing the Raman signal to 1, the crystalline peak position is easily estimated where the signal is maximum. By looking at which Raman shift the curve reaches the value of 0.5, we can estimate the Half Width at Half Maximum (HWHM). The HWHM is only taken on the right side of the crystalline peak as the other peaks have a contribution in low Raman shift region (left part). The FWHM is then simply twice the HWHM. This estimation of the FWHM can be done automatically by a program (a MATLAB script for example) following the algorithm described above.

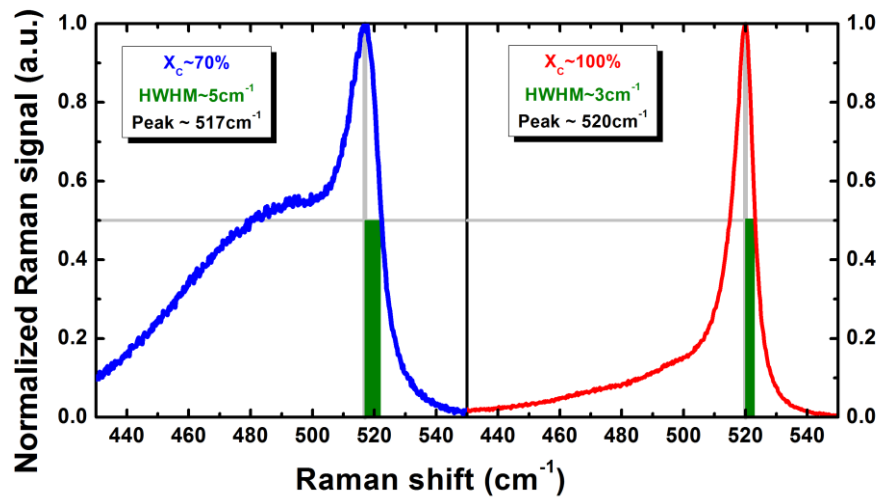


Figure 109: Geometrical construction used by the algorithm which leads to an estimation of the position and the HWHM of the crystalline peak.

Figure 110a shows the comparison between the crystalline peak position estimated by the fitting in four Gaussian curves and by the algorithm (Raman shift where Raman signal is the maximum). The correlation is good, meaning that there is no artefact of the fitting procedure on the crystalline peak position. Figure 110b shows the FWHM given by the fitting as a function of the FWHM given by the algorithm based on HWHM. The red line symbolizes the equality between the two values. One can see that the fitting always gives a FWHM lower than the algorithm. This can be understood as we use two Gaussian curves close to  $520 \text{ cm}^{-1}$ : the crystalline peak and the crystallite peak. Consequently the fitting procedure distributes the width into the two peaks. By looking carefully on the distribution of the data points in Figure 110b, one can observe that the peak position values seem to be discretized. This is only an artefact of the algorithm computing HWHM: close to  $520 \text{ cm}^{-1}$ , the Raman spectrum is measured every  $\delta=0.264 \text{ cm}^{-1}$ . The algorithm only takes the wavenumber where the next point has a signal below 0.5. Therefore, no interpolation is made and the position of the crossing at 0.5 is given with an error of  $\pm\delta/2$ . The same applies for the crystalline peak position and therefore the HWHM is given  $\pm\delta$ . Consequently the FWHM is given  $\pm 2\cdot\delta$ , which is approximately what we see on the Figure 110b (a discretization of about  $0.528 \text{ cm}^{-1}$ ). Despite the discretization and the fitting artefact of the crystalline peak width, the two methods to estimated FWHM are correlated: the two values increase proportionally. Based on these two correlations (peak position and peak width), we trust our fitting procedure even if we are aware of some fitting artefacts.

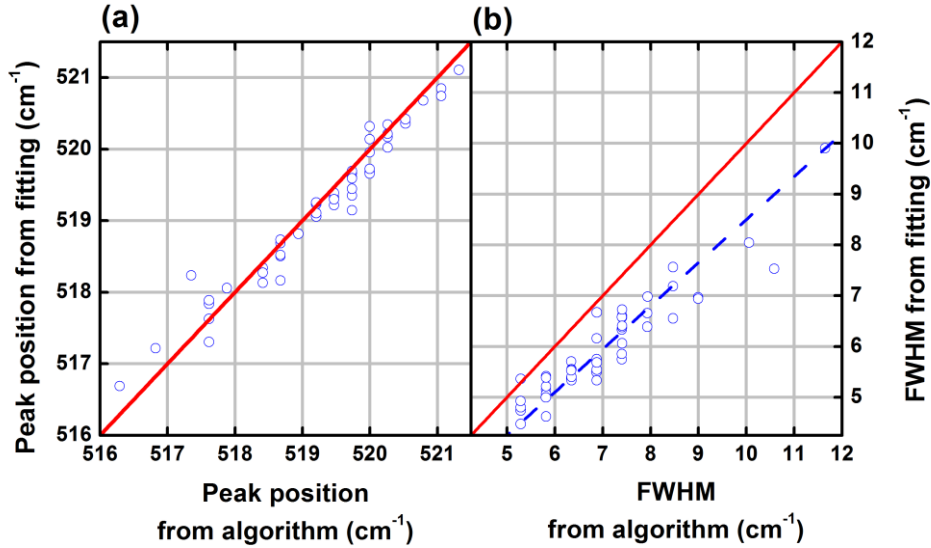


Figure 110: Correlation between the fitting and the algorithm in the estimation of (a) the crystalline peak position and (b) the FWHM of the crystalline peak. The blue dashed-line is a guide for the eyes.

The widening of the crystalline peak has been studied in [65] and has been associated to phonon confinement. Concomitant to the widening, a shift in the peak position is also found. Equations (57) and (58), taken from the reference [65], express respectively the Raman shift and the FWHM of the crystalline peak as a function of D - the diameter of the crystallites.

$$\Delta\omega(\text{cm}^{-1}) = -97.462 \cdot \left(\frac{0.543}{D(\text{nm})}\right)^{1.39} \quad (57)$$

$$\text{FWHM}(\text{cm}^{-1}) = 2 \cdot \frac{D(\text{nm})+3.1309}{0.81004 \cdot D(\text{nm})-1.6053} \quad (58)$$

We use the position and the FWHM of the crystalline peak given by the fitting procedure. From the peak shift and Equation (57) we can estimate the diameter of the crystallites. The reference peak position is taken at 521  $\text{cm}^{-1}$ . Figure 111 shows the FWHM extracted from the fitting as a function of the crystallite diameter. The Equation (58) is plotted in red line. The red line seems to fit well the blue data points. However it should be pointed out that if the peak shift is calculated from another reference (not 521  $\text{cm}^{-1}$ ), then discrepancy between red line and data point will be seen. Moreover one could argue that the FWHM from the algorithm should be taken instead of the one from the fitting which is higher. The estimated crystallite diameters range from 5 nm to 20 nm. The data point from 5 nm and 10 nm is consistent with our TEM investigations of crystalline domain of such dimensions. However we are doubtful about a crystallite diameter of 20 nm. It might be too large. Large diameters are linked to a large scattering of the data points.

The relative variation of the FWHM and the Raman shift is consistent with the model of phonon confinement. It reinforces the visual picture of our material: (small or large) crystallites embedded in an amorphous tissue. The tissue can be reduced to grain boundaries for fully crystallized layers. Interestingly even for the lowest amorphous fraction, the boundaries seem to be passivated since high  $V_{oc}$  is obtained for such layers [85].

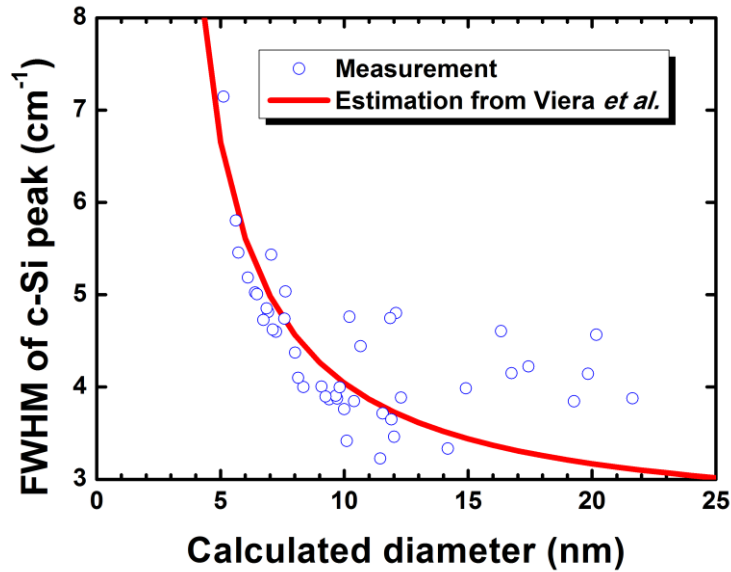


Figure 111: FWHM as a function of the crystallite diameter estimated from Equation (57).

### 5.2.2 $V_{OC}$ versus $X_C$ and $X_{cry}$

We have seen that the  $V_{OC}$  is higher by about 100 mV for solar cells with 70% crystallized intrinsic layer compared to 100% crystallized layer. Figure 112a shows the  $V_{OC}$  as a function of the crystalline fraction  $X_C$  for our set of solar cells. The red points correspond to the subset of solar cells with fully crystallized I-layer. Despite the scatter in the data point, the  $V_{OC}$  decreases with the increase of  $X_C$ . However, obtained  $V_{OC}$  are higher than the ones reported in [9] by EPFL group on a similar cell structure. The green line represents their dependency for a silane and hydrogen gas chemistry. Similar dependency has been obtained by FZ Jülich group in HWCVD [20].

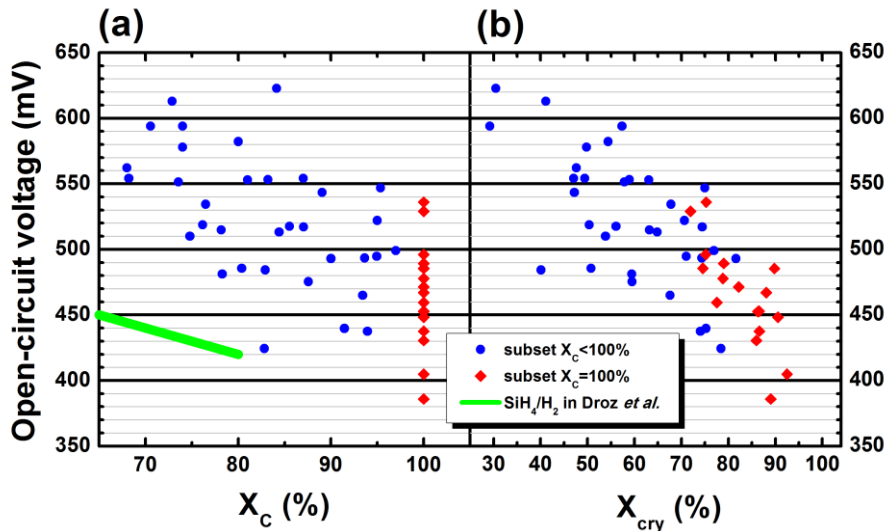


Figure 112:  $V_{OC}$  dependency with  $X_C$  and  $X_{cry}$ .

Figure 112b shows the dependency of the  $V_{OC}$  with the  $X_{cry}$  parameter. The data points are redistributed but the same trend is observed: the decrease of the  $V_{OC}$  when crystallite fraction  $X_{cry}$  increases. However the choice of  $X_{cry}$  rather than  $X_C$  leads to less scatter in the data, suggesting that the grain boundary phase (with a Raman signature most often located between  $500\text{ cm}^{-1}$  and  $507\text{ cm}^{-1}$ ) is a key contributor of the passivation of crystallite domains. It has been recently reported that one

order of magnitude of defect density can be responsible of a decrease of 100 mV in  $V_{OC}$  [86]. Such high obtained  $V_{OC}$  shall be related to a low defect density.

### 5.2.3 $V_{OC}$ & $J_0$ versus $X_{GB}$ at $X_C=100\%$

By taking the subset of fully crystallized layers in Figure 112b, and changing from  $X_{cry}$  to  $X_{GB}$  ( $X_{cry}+X_{GB}=1$  because amorphous fraction is zero) we obtained the increase of the  $V_{OC}$  with the increase of  $X_{GB}$  as depicted in Figure 113. The dark saturation current is also plotted and it decreases with the increase of  $X_{GB}$ . A low  $J_0$  is related to a good diode and therefore contributes to the increase of the  $V_{OC}$ .

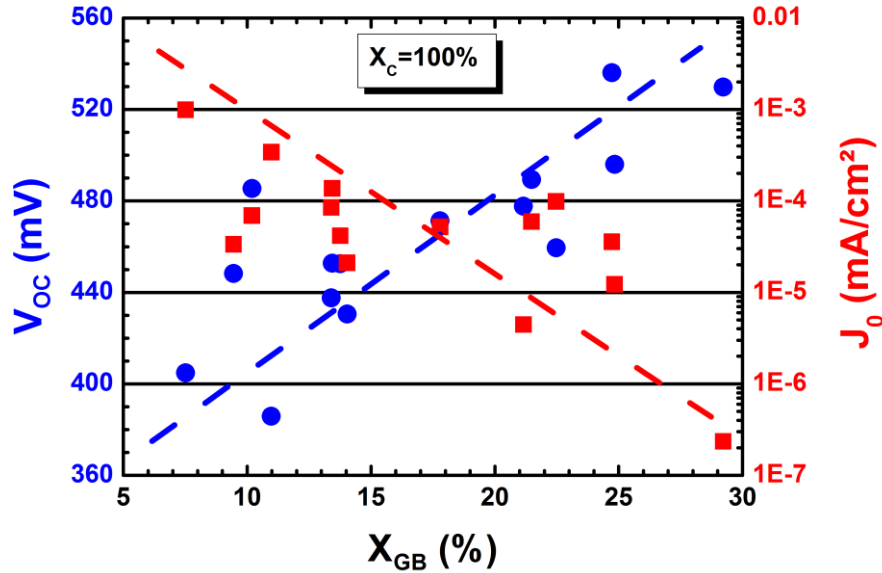


Figure 113:  $V_{OC}$  and  $J_0$  as a function of the grain boundaries fraction for the subset of fully crystallized solar cells. Dashed lines are guides for the eyes.

Larger grain boundary fraction could be understood as an indication of higher density films with a better passivation and less oxygen and diffusion at column boundaries. In addition, type-II grain boundaries located above  $500 \text{ cm}^{-1}$ , which is the case for all of our fully crystallized samples, are also reported to show higher correlation lengths and less recombination compared with type-I boundaries with a Raman signature at around  $495 \text{ cm}^{-1}$  [72]. Recombination is directly linked to an increase of  $J_0$ . All these elements support the increase of  $V_{OC}$  with grain boundary fraction in fully crystallized samples.

For the selected subset of solar cells, dark J-V curves can be measured and dark saturation current  $J_0$  and ideality factor  $n$  can be estimated. However if the superposition principle (that J-V curve under illumination is given by the dark J-V curve translated by the photogenerated current density) stands, then the  $V_{OC}$  should verify the Equation (59).

$$V_{OC} = \frac{n \cdot kT}{q} \cdot \ln \left( 1 + \frac{J_{sc}}{J_0} \right) \quad (59)$$

However in our solar cells, the  $V_{OC}$ ,  $J_{sc}$  and  $n$  values do not satisfy Equation (59). The measured  $V_{OC}$  is always below the “theoretical”  $V_{OC}$  given by Equation (59). This discrepancy, evaluated by the difference between the measured  $V_{OC}$  under light and the  $V_{OC}$  expected from Equation (59), is displayed in Figure 114. Again there is scatter in the data but the discrepancy decreases with the increase of  $X_{GB}$ : at low grain boundaries fraction, the passivation is less efficient and higher recombination is encountered. However the increase of  $J_0$  is not sufficient to explain all the decrease of the  $V_{OC}$  as the  $V_{OC}$  should decrease following the Equation (59). The discrepancy represents all the voltage losses not related to the  $J_0$ .

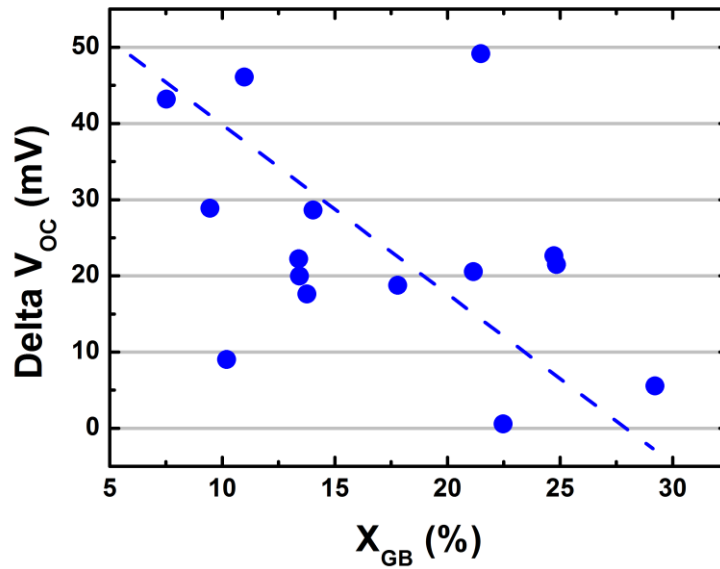


Figure 114: The discrepancy between the measured  $V_{OC}$  and the  $V_{OC}$  computed from  $(J_0, n)$  parameters as a function of the grain boundaries fraction  $X_{GB}$ . Dashed line is a guide for the eyes.

For example, a shunt resistance is responsible for a decrease of the  $V_{OC}$  and is extrinsic of the diode characteristics  $(J_0, n)$ . A lower bound of the shunt resistance is given by the differential resistance at the short-circuit condition in J-V curve, which is named “ $R_{SC}$ ”. In Figure 115,  $R_{SC}$  is plotted as a function of the measured  $V_{OC}$ .  $R_{SC}$  is high when  $V_{OC}$  is high too, meaning that solar cell performances ( $V_{OC}$ ) are limited by low shunt resistance.

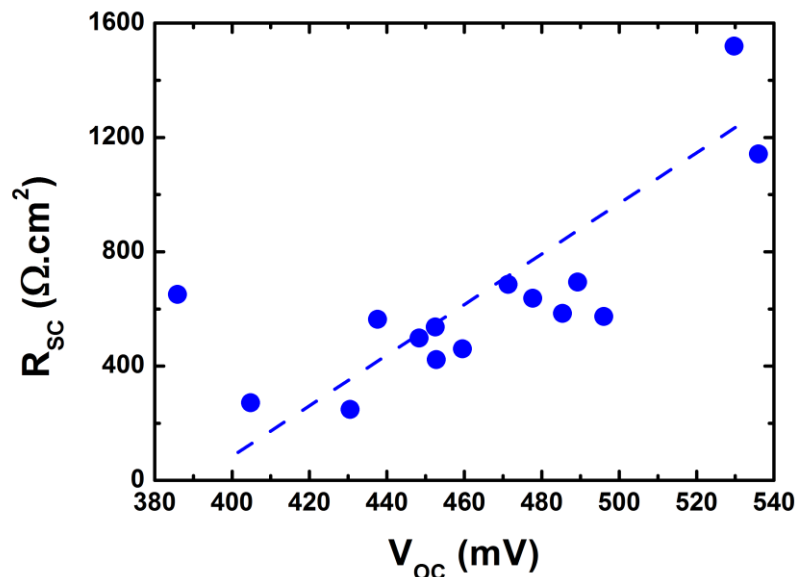


Figure 115: Differential resistance at the short-circuit condition  $R_{SC}$  as a function of the open-circuit voltage  $V_{OC}$  showing that solar cells might be limited by low shunt resistance. Dashed line is a guide for the eyes.

At low  $V_{OC}$ , we have low passivation by grain boundaries (Figure 113) and therefore high  $J_0$  but also low shunt resistance explaining the increase of the discrepancy at low  $X_{GB}$  in Figure 114. The impact on the  $V_{OC}$  of the decrease of the passivation is twofold: by  $J_0$  through Equation (59) and by shunt resistance.

#### 5.2.4 Spectral response at 800 nm versus the I-layer thickness for $X_c=100\%$ I-layer

To increase the  $J_{SC}$ , thick I-layers are required. However the solar cell efficiency does depend on  $J_{SC}$  and  $V_{OC}$ . As we have already shown, crystallized grain boundaries increase the  $V_{OC}$  and decrease the  $J_{SC}$ . Therefore, to study the impact of the thickness on the  $J_{SC}$ , we only select fully crystallized layers with  $X_c=100\%$ . The  $J_{SC}$  can be estimated from the integration of the EQE curves over the whole solar spectrum. However what happens in the UV range of the EQE is related to front absorption and not in relation with the thickness of the I-layer. On the contrary, the IR range of the EQE is strongly related to the absorption of red/IR photons over all the thickness of the microcrystalline silicon. Instead of comparing  $J_{SC}$  with the thickness, we prefer to compare the EQE at a given red/IR wavelength with the thickness. We choose 800 nm as the reference wavelength.

Figure 116 shows the EQE at 800 nm of our fully crystallized solar cells as a function of their I-layer thickness. The EQE at 800 nm ranges from 55% to 75% when the thickness ranges from 1  $\mu\text{m}$  to 5.5  $\mu\text{m}$ . As expected, the EQE at 800 nm increases with the thickness.

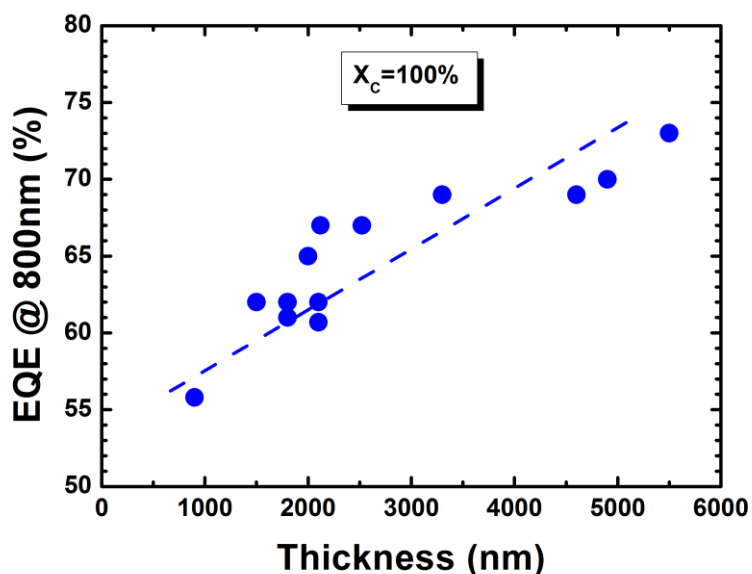


Figure 116: EQE at 800 nm as a function of the thickness of the I-layer.

The EQE at 800 nm increases linearly without a sign of saturation. The absorption coefficient  $\alpha$  at 800 nm of crystalline silicon is  $1000\text{ cm}^{-1}$ . That corresponds to an absorption depth of 10  $\mu\text{m}$ . Our thicknesses are below 10  $\mu\text{m}$  explaining why we are still in a linear regime between absorption and thickness.

We can have a closer look of the EQE curve of the thickest solar cell (I-layer of 5.5  $\mu\text{m}$ ) in Figure 117. The EQE at 800 nm reaches 73%. Moreover, the EQE at 1000 nm is as high as 20%.

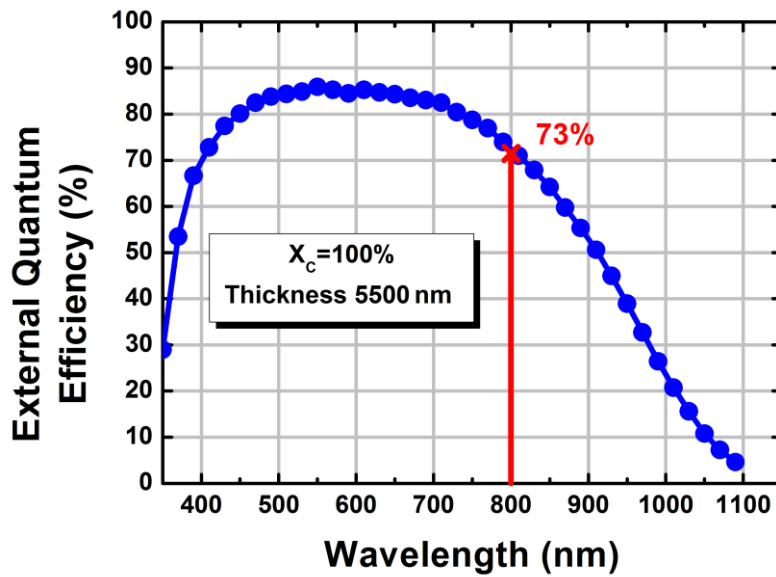


Figure 117: EQE curve of our thickest solar cell with an I-layer of 5.5  $\mu\text{m}$ . The EQE at 800 nm is as high as 73% and the EQE at 1000 nm is as good as 20%.

### 5.3 Focus on our record solar cells

We focus in this section on three noteworthy solar cells because of their high performance. Table 42 summarizes the characteristics of the I-layer.

$X_c$	Thickness
(%)	( $\mu\text{m}$ )
89	3.8
80	3.4
100	1.8

Table 42: I-layer characteristics of the three best solar cells.

#### 5.3.1 Thick intrinsic microcrystalline layer: 3.8 $\mu\text{m}$ with $X_c < 100\%$

Figure 118 shows the J-V curve and the EQE of our thickest solar cell which is partially crystallized ( $X_c=89\%$ ). The EQE is as high as 90% between 600 nm and 700 nm and is still 15% at 1000 nm. Such an EQE leads to a high  $J_{sc}$  of 26.6  $\text{mA}/\text{cm}^2$ . The EQE under forward bias is close to the one with no bias showing that the carrier collection over 3.8  $\mu\text{m}$  is pretty satisfactory.

The EQE reaches 90% but we need to be careful with this high value because there is reflection between the air and the glass in the front which can be more than 10%. Indeed, with the same EQE equipment, we measured crystalline silicon solar cell EQE and got 105%, which means that there might be a shift of 5% the EQE.

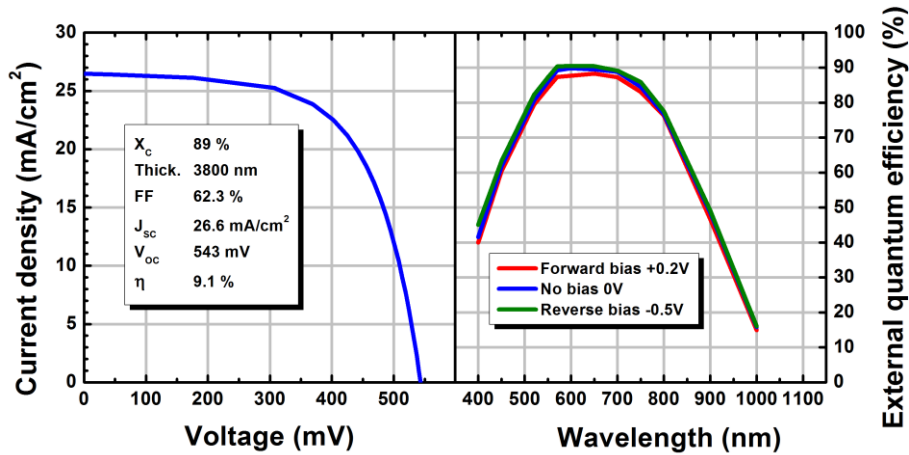


Figure 118: J-V curve and EQE of the thickest (3.8  $\mu\text{m}$ ) solar cell partially crystallized (89%).

### 5.3.2 High efficiency solar cell: 3.4 micron-thick with $X_c < 100\%$

Figure 119 shows the J-V-curve and the EQE of our best solar cell which is partially crystallized ( $X_c=80\%$ ). From EQE curves, the carrier collection is excellent over the 3.4  $\mu\text{m}$  of the I-layer. The  $J_{sc}$  is 24.1 mA/cm<sup>2</sup> and the  $V_{oc}$  is as high as 553 mV. The efficiency is 9.2%.

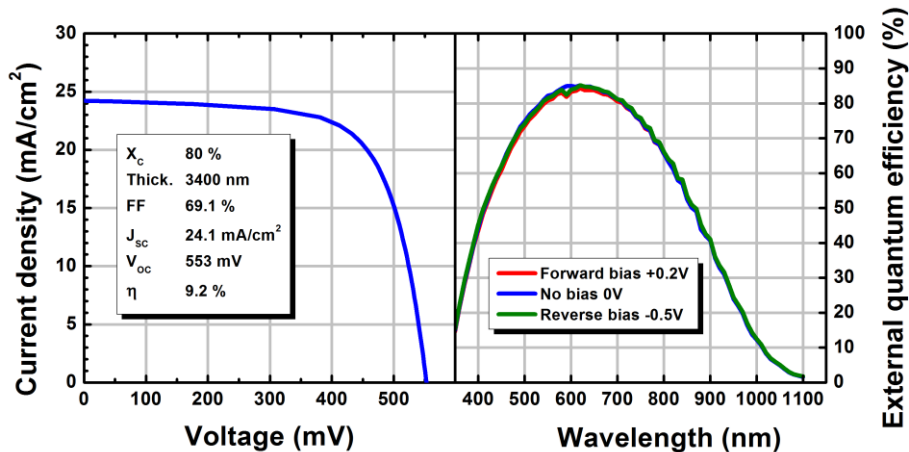


Figure 119: J-V curve and EQE of the best (9.2%) solar cell partially crystallized (80%).

Figure 120 shows the dark J-V curve of the solar cell. ( $J_0, n$ ) parameters are estimated from the fitting of the dark J-V curve in the linear part (at the  $V_{oc}$ ). The dark saturation current of the solar cell is  $9.42 \times 10^{-6}$  mA/cm<sup>2</sup> with an ideality factor of 1.59. Following the Equation (59), the theoretical  $V_{oc}$  should be 610 mV. However the measured  $V_{oc}$  is 553 mV. The discrepancy in  $V_{oc}$  is 57 mV. Equivalently, the current density in the dark at the  $V_{oc}$  is 6.5 mA/cm<sup>2</sup>, which should be the  $J_{sc}$  according to Equation (59). However the  $J_{sc}$  is 24.1 mA/cm<sup>2</sup>. The discrepancy between  $J_{sc}$  and  $J_{dark}(V_{oc})$  is 17.6 mA/cm<sup>2</sup>. At open-circuit, all the generated carriers should recombine in the device such that no current flows from the N-side to the P-side. The recombination by the diode ( $J_0, n$ ) represents 6.5 mA/cm<sup>2</sup> over the total recombination of 24.1 mA/cm<sup>2</sup> (that to say 27%). The other recombinations (such as shunt resistance) represent 17.6 mA/cm<sup>2</sup> over the total recombination of 24.1 mA/cm<sup>2</sup> (that to say 73%). Therefore the best way to improve our solar cell efficiency is to work on reducing shunt resistance.

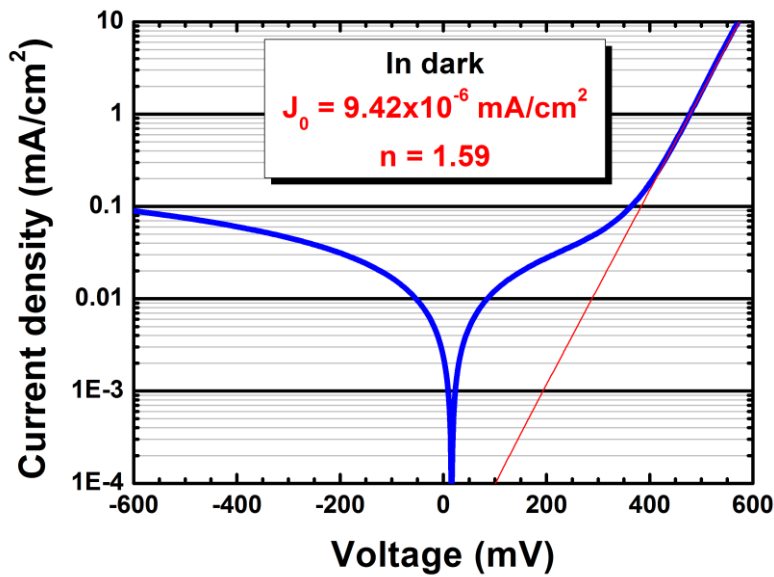


Figure 120: Dark J-V curve of the solar cell.

### 5.3.3 Highest efficiency solar cell: 1.8 micron-thick with $X_c=100\%$

Figure 121 shows the J-V-curve and the EQE of our best solar cell which is fully crystallized ( $X_c=100\%$ ). From EQE under bias, the carrier collection seems quite independent of the applied bias. The  $J_{sc}$  is as high as  $25.4 \text{ mA/cm}^2$  with a  $V_{oc}$  of 536 mV even for a fully crystallized I-layer. We reach the efficiency of 9.2%. For this solar cell, (p) $\mu\text{c-SiO}_x\text{:H}$  has been used and the EQE at 400 nm is 60%.

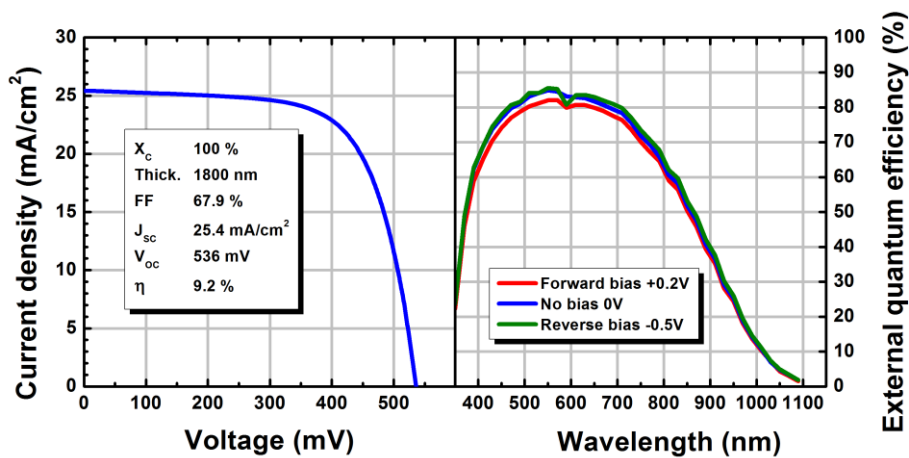


Figure 121: J-V curve and EQE of the best (9.2%) solar cell fully crystallized.

### 5.3.4 Summary of the solar cells

Table 43 summarizes the solar cell performances presented above.

Specificity	$X_c$	Thickness	FF	$V_{oc}$	$J_{sc}$	$\eta$
	(%)	( $\mu\text{m}$ )	(%)	(mV)	( $\text{mA/cm}^2$ )	(%)
Thickest	89	3.8	62.3	543	26.6	9.1
Best	80	3.4	69.1	553	24.1	9.2
Best	100	1.8	67.9	536	25.4	9.2

Table 43: Summary of the performances of the selected solar cells.

We can conclude from these performances that from  $\text{SiF}_4/\text{H}_2/\text{Ar}$  chemistry, a high  $V_{oc}$  can be achieved even for fully crystallized layers. Several microns of I-layer can be used if the layer is fully

crystallized but with a sufficient amount of grain boundaries to passivate the crystallites. We challenge the common consensus that the optimum of microcrystalline solar cell should be at the material transition between amorphous and microcrystalline transition: our target is to use fully crystallized layer for the I-layer, and since it is crystallized, very thick layers can be used to absorb IR photons and thus increasing the  $J_{SC}$ . The presence of 30% of amorphous tissue is no required to passivate crystallites and to obtain high  $V_{OC}$ . We demonstrate that crystallized grain boundaries are needed, thus shifting the common tradeoff toward better crystallized I-layers.

However, we claimed that our best microcrystalline is also obtained at the amorphous-to-microcrystalline transition. We do distinguish between plasma transition and material transition: the  $H_2$  flow rate is adjusted such that the plasma conditions are at the transition, but the resulting material is fully crystallized (thus it is not at the material transition).

We showed that our solar cell performances are strongly limited by shunt resistances and interfaces. Further studies should be performed in order to have appropriate interfaces and hopefully a better solar cell structure:

- anti-reflection coating (ARC)
- double front texturing
- (p) $\mu\text{c-SiO}_x\text{:H}$
- (n) $\mu\text{c-SiO}_x\text{:H}$
- N-I-P instead of P-I-N
- back texturing
- new back reflector
- 4-probe measurement instead of 2-probe measurement
- Etc.

## 5.4 Chapter key results

We have demonstrated in this chapter that a high  $V_{OC}$  can be obtained for fully crystallized layer when using the  $\text{SiF}_4/\text{H}_2/\text{Ar}$  chemistry compared to the  $\text{SiH}_4/\text{H}_2$  chemistry.  $V_{OC}$  is decreasing with the increase of  $X_C$ , but we showed that the dependence of  $V_{OC}$  with  $X_{cry}$  is stronger than with  $X_C$ . In the case of  $X_C=100\%$ ,  $X_{cry}+X_{GB}=1$  and the grain boundary fraction is crucial as its highest  $V_{OC}$  are achieved at high  $X_{GB}$ .

The detailed analysis of our solar cells showed that their performances are limited by  $J_0$  and shunt resistance. Despite the absence of optimization of interfaces, a solar cell with a I-layer of  $5.5 \mu\text{m}$  have been realized and its EQE reached 73% at 800 nm, demonstrating the feasibility of thick I-layer without losing carrier collection.

Our current record efficiency is 9.2%, which has been achieved by two types of solar cells: one with a fully crystallized I-layer ( $X_C=100\%$ ) and a  $V_{OC}$  of 536 mV, and another one with an I-layer at  $X_C=80\%$  and a  $V_{OC}$  of 553 mV. These high  $V_{OC}$  for thick I-layers are an achievement demonstrating the advantage of  $\text{SiF}_4/\text{H}_2/\text{Ar}$  chemistry and of the new paradigm stipulating that fully crystallized and thick microcrystalline layers should be used in P-I-N solar cells.

# 6. Conclusions and perspectives

## Contents

---

6.1 Achievements.....	148
6.2 Perspectives on SiF <sub>4</sub> /H <sub>2</sub> /Ar plasmas.....	149
6.3 Strategies to improve microcrystalline silicon solar cell efficiencies.....	149

---

## 6.1 Achievements

Throughout this thesis, we have met the challenges related to the understanding of the SiF<sub>4</sub>/H<sub>2</sub>/Ar plasma by a simple yet powerful phenomenological model. The key phenomenon happening in such plasmas is the formation of HF molecules via the spontaneous reaction of atomic F with molecular H<sub>2</sub>. The direct consequence is the identification of the **H<sub>2</sub>-limited regime** and the **F-limited regime**. For given plasma conditions, the knowledge of the type of regime (H<sub>2</sub>- or F-limited) can be determined by a simple measurement of the H<sub>2</sub> depletion by a Residual Gas Analyzer (RGA). It allows us to tune very easily the amorphous-to-microcrystalline transition as well as to have a practical way to increase deposition rate by simultaneously increasing the RF power and the H<sub>2</sub> flow rate. It turns out that the deposition rate scales with the H<sub>2</sub> consumption which again can be easily measured with the RGA. Moreover, we demonstrate the feasibility of the transfer from PHILIX reactor to CLUSTER reactor with only the help of a RGA.

The dusty nature of our plasma has been investigated and has shown that the contribution of plasma-generated nanoparticles is important for the plasma (self-sustained oscillations may occur) as well as for the film properties (deposition rate increases with low gas temperature). We put into light two modes of crystallization: the first mode is called “**surface crystallization**”, i.e. by the crystallization mediated by atomic hydrogen on the surface and sub-surface, and the second mode is called “**plasma crystallization**”, i.e. by crystallized plasma-generated nanoparticles. The first mode is mainly activated by an increase of the H<sub>2</sub> flow rate, whereas the second mode happens at high RF power density. In the case of plasma crystallization, the vector of the crystalline nature of the grown film is the plasma-generated nanoparticles which is correlated with a random orientation of the small crystallites. However, in the case of surface crystallization (and with amorphous plasma-generated nanoparticles), a preferential orientation is obtained with large grains. This type of crystallization should be preferred to get high quality microcrystalline silicon.

Our best microcrystalline silicon material is obtained with amorphous nanoparticles at the lowest H<sub>2</sub> flow rate leading to the microcrystalline phase. The resulting material can be fully crystallized. We call this “**plasma transition**” because it corresponds to a transition on a plasma parameter (which is the knob of the H<sub>2</sub> mass flow controller). That is in contrast with the amorphous-to-microcrystalline transition of the grown material where the crystalline fraction should vary between 50% and 70%. Sometimes, the H<sub>2</sub> flow rate should be tuned during the plasma to keep the deposited material at the amorphous-to-microcrystalline transition. We call this “**material transition**”.

Material characterizations have shown a complex structure of the μc-Si:H,F films: amorphous tissue, crystallites, and grain boundaries. A **defect density as low as 5.1x10<sup>14</sup> cm<sup>-3</sup>** has been achieved, which is correlated with an excellent solar cell V<sub>oc</sub>. For fully crystallized I-layers, we found that V<sub>oc</sub> was increasing with the grain boundaries fraction which leads us to suggest that an amorphous tissue is not necessary to passivate the crystallites, contrariwise to the general consensus on microcrystalline silicon deposited from SiH<sub>4</sub>/H<sub>2</sub>.

A solar cell with a fully crystallized I-layer of 5.5 μm has been fabricated showing good collection properties with an **EQE of 73% at 800 nm**. PIN solar cells with **an efficiency of 9.2%** have been obtained. **V<sub>oc</sub> as high as 536 mV** was achieved with a fully crystallized I-layer (X<sub>c</sub>=100%) and **V<sub>oc</sub> as high as 553 mV** with an I-layer with X<sub>c</sub>=80%.

## 6.2 Perspectives on SiF<sub>4</sub>/H<sub>2</sub>/Ar plasmas

Microcrystalline silicon solar cells is a suitable application for the SiF<sub>4</sub>/H<sub>2</sub>/Ar chemistry. However, it is worth looking at the application of amorphous silicon as it is easily deposited by choosing a low H<sub>2</sub> flow rate (H<sub>2</sub>-limited regime). The target is **to deposit a-Si:H with a lower amount of hydrogen** compared to a-Si:H deposited from SiH<sub>4</sub>/H<sub>2</sub> gas mixture. The idea behind this goal is the scavenging of hydrogen by atomic fluorine in amorphous plasma conditions (H<sub>2</sub>-limited).

**Silicon epitaxy is another promising application of SiF<sub>4</sub>/H<sub>2</sub>/Ar plasma**, since the trend is to use thinner and thinner wafers (40 μm or 10 μm) for high efficiency crystalline silicon solar cells. The main asset of the fluorinated chemistry is the understanding of the plasma provided by our phenomenological model.

## 6.3 Strategies to improve microcrystalline silicon solar cell efficiencies

By combining all the understanding and the knowledge accumulated during this thesis, a noteworthy efficiency improvement should be easy to reach. The microcrystalline silicon for the I-layer should be deposited in specific conditions:

- i. **Adequate H<sub>2</sub> flow rate:** as low as possible while still being compatible with a microcrystalline growth.
- ii. **Low RF power** to have a low ion bombardment energy (IBE).
- iii. **P·d<sub>i</sub>=6 Torr·cm** to increase the deposition rate and improve the material quality. The solar cells presented in this thesis have been fabricated with an I-layer deposited at P·d<sub>i</sub>=12 Torr·cm.

Large grain microcrystalline silicon is obtained in these conditions. Our group is currently intensively studying the low temperature silicon epitaxy in SiH<sub>4</sub>/H<sub>2</sub> and SiF<sub>4</sub>/H<sub>2</sub>/Ar mixtures. The rule of thumb for good epitaxy is indeed (i) and (ii). The correspondence between epitaxy conditions and large grain microcrystalline conditions is of importance through the “local-epitaxy” (or “self-epitaxy”): by being close to the amorphous transition (condition (i)), epitaxy can occur on a small crystalline grain and thus lead to the growth of a large grains.

In addition with this plasma condition for the I-layer, one should work on the solar cell structure: use thinner P-layer, use oxide doped-layer, and change from superstrate to substrate configuration.



# 7. Publications

## 7.1 Leading author

- **Deposition of high-efficiency microcrystalline silicon solar cells using SiF<sub>4</sub>/H<sub>2</sub>/Ar mixtures.**  
IEEE Journal of Photovoltaics, DOI: 10.1109/JPHOTOV.2012.2221683
  - Jean-Christophe DORNSTETTER
  - Samir KASOUIT
  - Pere ROCA I CABARROCAS
- **Material and growth mechanism studies of microcrystalline silicon deposited from SiF<sub>4</sub>/H<sub>2</sub>/Ar gas mixtures.**  
Canadian Journal of Physics, DOI: 10.1139/CJP-2013-0606
  - Jean-Christophe DORNSTETTER
  - Junkang WANG
  - Bastien BRUNEAU
  - Erik V. JOHNSON
  - Pere ROCA I CABARROCAS
- **Understanding the amorphous-to-microcrystalline silicon transition in SiF<sub>4</sub>/H<sub>2</sub>/Ar gas mixtures.**  
Journal of Chemical Physics, DOI: 10.1063/1.4883503
  - Jean-Christophe DORNSTETTER
  - Bastien BRUNEAU
  - Pavel BULKIN
  - Erik V. JOHNSON
  - Pere ROCA I CABARROCAS

## 7.2 Co-author

- **Growth mechanisms study of microcrystalline silicon deposited by SiH<sub>4</sub>/H<sub>2</sub> plasma using tailored voltage waveforms.**  
Journal of Applied Physics, DOI: 10.1063/1.4866693
  - Bastien BRUNEAU
  - Junkang WANG
  - Jean-Christophe DORNSTETTER
  - Erik V. JOHNSON
- **Ion energy threshold in low temperature silicon epitaxy for thin film crystalline photovoltaics.**  
IEEE Journal of Photovoltaics, DOI: 10.1109/JPHOTOV.2014.2357256
  - Bastien BRUNEAU
  - Romain CARIOU
  - Jean-Christophe DORNSTETTER
  - Michael LEPECQ
  - Jean-Luc MAURICE
  - Pere ROCA I CABARROCAS
  - Erik V. JOHNSON
- **Effect of ion energy on microcrystalline silicon material and devices: a study using tailored voltage waveforms.**  
IEEE Journal of Photovoltaics, DOI: 10.1109/JPHOTOV.2014.2357259
  - Bastien BRUNEAU
  - Michael LEPECQ
  - Junkang WANG
  - Jean-Christophe DORNSTETTER
  - Jean-Luc MAURICE
  - Erik V. JOHNSON



## 8. Bibliography

- [1] Kapur, Moslehi, Deshpande, Rana, Kramer, Seutter, Deshazer, Coutant, Calcaterra, Kommera, Su, Grupp, Tamilmani, Dutton, Stalcup, Du, and Wingert, "A Manufacturable, Non-plated, Non-Ag Metallization based 20.44% Efficient, 243 cm<sup>2</sup> Area, Back Contacted Solar Cell on 40 μm Thick Mono-Crystalline Silicon," *28th EUPVSEC Proceedings*, 2013.
- [2] S. Vepřek and V. Mareček, "The preparation of thin layers of Ge and Si by chemical hydrogen plasma transport," *Solid-State Electronics*, vol. 11, no. 7, pp. 683–684, 1968.
- [3] A. Matsuda, "Growth mechanism of microcrystalline silicon obtained from reactive plasmas," *Thin Solid Films*, vol. 337, pp. 1–6, 1999.
- [4] P. Roca i Cabarrocas, "Deposition Techniques and Processes Involved in the Growth of Amorphous and Microcrystalline Silicon Thin Films," in *Physics and Technology of Amorphous-Crystalline Heterostructure Silicon Solar Cells*, W. G. J. H. M. van Sark, L. Korte, and F. Roca, Eds. Springer Berlin Heidelberg, 2012, pp. 131–160.
- [5] O. Vetterl, F. Finger, R. Carius, P. Hapke, L. Houben, O. Kluth, A. Lambertz, A. Mück, B. Rech, and H. Wagner, "Intrinsic microcrystalline silicon: A new material for photovoltaics," *Solar Energy Materials and Solar Cells*, vol. 62, no. 1–2, pp. 97–108, 2000.
- [6] A. A. Howling, B. Strahm, and C. Hollenstein, "Non-intrusive plasma diagnostics for the deposition of large area thin film silicon," *Thin Solid Films*, vol. 517, no. 23, pp. 6218–6224, 2009.
- [7] M. Kondo, M. Fukawa, L. Guo, and A. Matsuda, "High rate growth of microcrystalline silicon at low temperatures," *Journal of Non-Crystalline Solids*, vol. 266–269, Part 1, pp. 84–89, 2000.
- [8] S. Michard, M. Meier, B. Grootoink, O. Astakhov, A. Gordijn, and F. Finger, "High deposition rate processes for the fabrication of microcrystalline silicon thin films," *Materials Science and Engineering: B*, vol. 178, no. 9, pp. 691–694, 2013.
- [9] C. Droz, E. Vallat-Sauvain, J. Bailat, L. Feitknecht, J. Meier, and A. Shah, "Relationship between Raman crystallinity and open-circuit voltage in microcrystalline silicon solar cells," *Solar Energy Materials and Solar Cells*, vol. 81, no. 1, pp. 61–71, 2004.
- [10] W. Futako, K. Yoshino, C. M. Fortmann, and I. Shimizu, "Wide band gap amorphous silicon thin films prepared by chemical annealing," *Journal of Applied Physics*, vol. 85, no. 2, pp. 812–818, 1999.
- [11] J. Meier, S. Dubail, J. Cuperus, U. Kroll, R. Platz, P. Torres, J. A. Anna Selvan, P. Pernet, N. Beck, N. Pellaton Vaucher, C. Hof, D. Fischer, H. Keppner, and A. Shah, "Recent progress in micromorph solar cells," *Journal of Non-Crystalline Solids*, vol. 227–230, Part 2, pp. 1250–1256, 1998.
- [12] S. Veprek, F.-A. Sarott, and Z. Iqbal, "Effect of grain boundaries on the Raman spectra, optical absorption, and elastic light scattering in nanometer-sized crystalline silicon," *Phys. Rev. B*, vol. 36, no. 6, pp. 3344–3350, 1987.
- [13] B. Rezek, J. Stuchlík, A. Fejfar, and J. Kočka, "Local characterization of electronic transport in microcrystalline silicon thin films with submicron resolution," *Applied Physics Letters*, vol. 74, no. 10, pp. 1475–1477, 1999.
- [14] N. Layadi, P. Roca i Cabarrocas, B. Drévilion, and I. Solomon, "Real-time spectroscopic ellipsometry study of the growth of amorphous and microcrystalline silicon thin films prepared by alternating silicon deposition and hydrogen plasma treatment," *Physical Review B*, vol. 52, no. 7, p. 5136, 1995.
- [15] S. Hamma and P. Roca i Cabarrocas, "In situ correlation between the optical and electrical properties of thin intrinsic and n-type microcrystalline silicon films," *Journal of Applied Physics*, vol. 81, no. 11, pp. 7282–7288, 1997.
- [16] J. Y. W. Seto, "The electrical properties of polycrystalline silicon films," *Journal of Applied Physics*, vol. 46, no. 12, pp. 5247–5254, Dec. 1975.
- [17] C. Droz, M. Goerlitzer, N. Wyrsh, and A. Shah, "Electronic transport in hydrogenated microcrystalline silicon: similarities with amorphous silicon," *Journal of Non-Crystalline Solids*, vol. 266–269, Part 1, pp. 319–324, 2000.
- [18] R. Brenot, R. Vanderhaghen, B. Drévilion, P. Roca i Cabarrocas, R. Rogel, and T. Mohammed-Brahim, "Transport mechanisms in hydrogenated microcrystalline silicon," *Thin Solid Films*, vol. 383, no. 1–2, pp. 53–56, 2001.

- [19] O. Astakhov, R. Carius, F. Finger, Y. Petrusenko, V. Borysenko, and D. Barankov, "Relationship between defect density and charge carrier transport in amorphous and microcrystalline silicon," *Phys. Rev. B*, vol. 79, no. 10, p. 104205, 2009.
- [20] S. Klein, F. Finger, R. Carius, and J. Lossen, "Improved deposition rates for  $\mu\text{c-Si:H}$  at low substrate temperature," *Thin Solid Films*, vol. 501, no. 1–2, pp. 43–46, 2006.
- [21] S. Hänni, G. Bugnon, G. Parascandolo, M. Boccard, J. Escarré, M. Despeisse, F. Meillaud, and C. Ballif, "High-efficiency microcrystalline silicon single-junction solar cells," *Progress in Photovoltaics: Research and Applications*, vol. 21, no. 5, pp. 821–826, 2013.
- [22] S. Hänni, D. T. L. Alexander, L. Ding, G. Bugnon, M. Boccard, C. Battaglia, P. Cuony, J. Escarré, G. Parascandolo, S. Nicolay, M. Cantoni, M. Despeisse, F. Meillaud, and C. Ballif, "On the Interplay Between Microstructure and Interfaces in High-Efficiency Microcrystalline Silicon Solar Cells," *IEEE Journal of Photovoltaics*, vol. 3, pp. 11–16, 2013.
- [23] M. A. Green, K. Emery, Y. Hishikawa, W. Warta, and E. D. Dunlop, "Solar cell efficiency tables (version 44)," *Prog. Photovolt: Res. Appl.*, vol. 22, no. 7, pp. 701–710, 2014.
- [24] H. Sai, T. Koida, T. Matsui, I. Yoshida, K. Saito, and M. Kondo, "Microcrystalline Silicon Solar Cells with 10.5% Efficiency Realized by Improved Photon Absorption via Periodic Textures and Highly Transparent Conductive Oxide," *Appl. Phys. Express*, vol. 6, no. 10, p. 104101, 2013.
- [25] B. Yan, G. Yue, L. Sivec, J. Yang, S. Guha, and C.-S. Jiang, "Innovative dual function nc-SiO<sub>x</sub>:H layer leading to a >16% efficient multi-junction thin-film silicon solar cell," *Applied Physics Letters*, vol. 99, no. 11, p. 113512, 2011.
- [26] S. Guha, J. Yang, and B. Yan, "High efficiency multi-junction thin film silicon cells incorporating nanocrystalline silicon," *Solar Energy Materials and Solar Cells*, vol. 119, pp. 1–11, 2013.
- [27] A. Madan and S. Ovshinsky, "A new amorphous silicon-based alloy for electronic applications," *Nature*, vol. 276, pp. 482–484, 1978.
- [28] A. Madan and S. R. Ovshinsky, "Properties of amorphous Si:F:H alloys," *Journal of Non-Crystalline Solids*, vol. 35–36, Part 1, pp. 171–181, 1980.
- [29] I. Shimizu, "Reactions on substrate for preparation of silicon-networks from precursors, SiFnHm(n+m<3)," *Journal of Non-Crystalline Solids*, vol. 97–98, Part 1, pp. 257–260, 1987.
- [30] S. Oda, S. Ishihara, N. Shibata, H. Shirai, A. Miyauchi, K. Fukuda, A. Tanabe, H. Ohtoshi, J. Hanna, and I. Shimizu, "The Role of Hydrogen Radicals in the Growth of a-Si and Related Alloys," *Japanese Journal of Applied Physics*, vol. 25, no. Part 2, No. 3, pp. L188–L190, 1986.
- [31] G. Bruno, P. Capezzuto, M. M. Giangregorio, G. V. Bianco, and M. Losurdo, "From amorphous to microcrystalline silicon: Moving from one to the other by halogenated silicon plasma chemistry," *Philosophical Magazine*, vol. 89, no. 28–30, pp. 2469–2489, 2009.
- [32] G. Bruno, P. Capezzuto, and G. Cicala, "rf glow discharge of SiF<sub>4</sub>-H<sub>2</sub> mixtures: Diagnostics and modeling of the a-Si plasma deposition process," *Journal of Applied Physics*, vol. 69, no. 10, pp. 7256–7266, 1991.
- [33] G. Cicala, P. Capezzuto, and G. Bruno, "Microcrystalline silicon by plasma enhanced chemical vapor deposition from silicon tetrafluoride," *Journal of Vacuum Science & Technology A*, vol. 19, no. 2, pp. 515–523, 2001.
- [34] M. Lejeune, W. Beyer, R. Carius, J. Müller, and B. Rech, "Silicontetrachloride based microcrystalline silicon for application in thin film silicon solar cells," *Thin Solid Films*, vol. 451–452, pp. 280–284, 2004.
- [35] W. Beyer, R. Carius, M. Lejeune, J. Müller, B. Rech, and U. Zastrow, "Deposition and properties of microcrystalline silicon from chlorosilane precursor gases," *Journal of Non-Crystalline Solids*, vol. 338–340, pp. 147–150, 2004.
- [36] S. Kasouit, S. Kumar, R. Vanderhaghen, P. Roca i Cabarrocas, and I. French, "Fluorine and hydrogen effects on the growth and transport properties of microcrystalline silicon from SiF<sub>4</sub> precursor," *Journal of Non-Crystalline Solids*, vol. 299–302, Part 1, pp. 113–117, 2002.
- [37] Moreno and P. R. i Cabarrocas, "Ultra-thin crystalline silicon films produced by plasma assisted epitaxial growth on silicon wafers and their transfer to foreign substrates," *EPJ Photovoltaics*, vol. 1, p. 6, 2010.

- [38] Torres Rios, Djeridane, Reydet, Reyal, and Roca i Cabarrocas, "Epitaxial Growth of Crystalline Silicon on N42 Alloys by PECVD at 175 °C for Low Cost and High Efficiency Solar Cells," *26th EUPVSEC Proceedings*, 2011.
- [39] O. Vetterl, A. Lambertz, A. Dasgupta, F. Finger, B. Rech, O. Kluth, and H. Wagner, "Thickness dependence of microcrystalline silicon solar cell properties," *Solar Energy Materials and Solar Cells*, vol. 66, p. 345, 2001.
- [40] P. Roca i Cabarrocas, J. B. Chévrier, J. Huc, A. Lloret, J. Y. Parey, and J. P. M. Schmitt, "A fully automated hot-wall multiplasma-monochamber reactor for thin film deposition," *Journal of Vacuum Science & Technology A*, vol. 9, no. 4, pp. 2331–2341, 1991.
- [41] L. Kroely, S. K. Ram, P. Bulkin, and P. R. i Cabarrocas, "Microcrystalline silicon films and solar cells deposited at high rate by Matrix Distributed Electron Cyclotron Resonance (MDECR) plasma," *Phys. Status Solidi (c)*, vol. 7, no. 3–4, pp. 517–520, 2010.
- [42] C. W. Bauschlicher and P. R. Taylor, "Full CI studies of the collinear transition state for the reaction  $F+H_2 \rightarrow HF+H$ ," *The Journal of Chemical Physics*, vol. 86, no. 2, pp. 858–861, 1987.
- [43] A. A. H. L. Sansonnens, "The Role of Metastable Atoms in Argon-Diluted Silane Radiofrequency Plasmas," 1994.
- [44] M. J. Kushner, "A model for the discharge kinetics and plasma chemistry during plasma enhanced chemical vapor deposition of amorphous silicon," *Journal of Applied Physics*, vol. 63, no. 8, pp. 2532–2551, 1988.
- [45] G. Cicala, M. Losurdo, P. Capezzuto, and G. Bruno, "Time-resolved optical emission spectroscopy of modulated plasmas for amorphous silicon deposition," *Plasma Sources Sci. Technol.*, vol. 1, no. 3, p. 156, 1992.
- [46] S. Kasouit, J. Damon-Lacoste, R. Vanderhaghen, and P. Roca i Cabarrocas, "Contribution of plasma generated nanocrystals to the growth of microcrystalline silicon thin films," *Journal of Non-Crystalline Solids*, vol. 338–340, pp. 86–90, 2004.
- [47] P. Roca i Cabarrocas, N. Layadi, T. Heitz, B. Drévillon, and I. Solomon, "Substrate selectivity in the formation of microcrystalline silicon: Mechanisms and technological consequences," *Applied Physics Letters*, vol. 66, no. 26, pp. 3609–3611, 1995.
- [48] A. A. Fridman, L. Boufendi, T. Hbid, B. V. Potapkin, and A. Bouchoule, "Dusty plasma formation: Physics and critical phenomena. Theoretical approach," *Journal of Applied Physics*, vol. 79, no. 3, pp. 1303–1314, 1996.
- [49] E. V. Johnson, Y. Djeridane, A. Abramov, and P. Roca i Cabarrocas, "Experiment and modelling of very low frequency oscillations in RF-PECVD: a signature for nanocrystal dynamics," *Plasma Sources Sci. Technol.*, vol. 17, no. 3, p. 035029, 2008.
- [50] L. Boufendi and A. Bouchoule, "Particle nucleation and growth in a low-pressure argon-silane discharge," *Plasma Sources Sci. Technol.*, vol. 3, no. 3, p. 262, 1994.
- [51] L. Boufendi, J. Hermann, A. Bouchoule, B. Dubreuil, E. Stoffels, W. W. Stoffels, and M. L. de Giorgi, "Study of initial dust formation in an Ar-SiH<sub>4</sub> discharge by laser induced particle explosive evaporation," *Journal of Applied Physics*, vol. 76, no. 1, pp. 148–153, 1994.
- [52] L. Boufendi, J. Gaudin, S. Huet, G. Viera, and M. Dudemaine, "Detection of particles of less than 5 nm in diameter formed in an argon–silane capacitively coupled radio-frequency discharge," *Applied Physics Letters*, vol. 79, no. 26, pp. 4301–4303, 2001.
- [53] C. Bohm and J. Perrin, "Spatially resolved optical emission and electrical properties of SiH<sub>4</sub> RF discharges at 13.56 MHz in a symmetric parallel-plate configuration," *J. Phys. D: Appl. Phys.*, vol. 24, no. 6, p. 865, 1991.
- [54] A. Fontcuberta i Morral and P. Roca i Cabarrocas, "Shedding light on the growth of amorphous, polymorphous, protocrystalline and microcrystalline silicon thin films," *Thin Solid Films*, vol. 383, no. 1–2, pp. 161–164, 2001.
- [55] T. Nguyen-Tran, P. R. i Cabarrocas, and G. Patriarche, "Study of radial growth rate and size control of silicon nanocrystals in square-wave-modulated silane plasmas," *Applied Physics Letters*, vol. 91, no. 11, p. 111501, 2007.

- [56] U. Kortshagen, "Nonthermal plasma synthesis of semiconductor nanocrystals," *J. Phys. D: Appl. Phys.*, vol. 42, no. 11, p. 113001, 2009.
- [57] N. J. Kramer, R. J. Anthony, M. Mamunuru, E. S. Aydil, and U. R. Kortshagen, "Plasma-induced crystallization of silicon nanoparticles," *J. Phys. D: Appl. Phys.*, vol. 47, no. 7, p. 075202, 2014.
- [58] H.-L. Thi Le, N. C. Forero-Martinez, and H. Vach, "Heating and melting of plasma-born hydrogenated silicon clusters by reactions with atomic hydrogen," *Phys. Status Solidi A*, vol. 211, no. 2, pp. 294–300, 2014.
- [59] P. Roca i Cabarrocas, Y. Djeridane, V. D. Bui, Y. Bonnassieux, and A. Abramov, "Critical issues in plasma deposition of microcrystalline silicon for thin film transistors," *Solid-State Electronics*, vol. 52, no. 3, pp. 422–426, 2008.
- [60] P. Roca i Cabarrocas, T. Nguyen-Tran, Y. Djeridane, A. Abramov, E. Johnson, and G. Patriarche, "Synthesis of silicon nanocrystals in silane plasmas for nanoelectronics and large area electronic devices," *J. Phys. D: Appl. Phys.*, vol. 40, no. 8, p. 2258, 2007.
- [61] V. Suendo, A. V. Kharchenko, and P. Roca i Cabarrocas, "The effects of RF plasma excitation frequency and doping gas on the deposition of polymorphous silicon thin films," *Thin Solid Films*, vol. 451–452, pp. 259–263, 2004.
- [62] V. Paillard, P. Puech, and P. Roca i Cabarrocas, "Measurement of stress gradients in hydrogenated microcrystalline silicon thin films using Raman spectroscopy," *Journal of Non-Crystalline Solids*, vol. 299–302, Part 1, pp. 280–283, 2002.
- [63] R. Tsu and J. G. Hernandez, "Temperature dependence of silicon Raman lines," *Applied Physics Letters*, vol. 41, no. 11, pp. 1016–1018, 1982.
- [64] V. Paillard, P. Puech, M. A. Laguna, R. Carles, B. Kohn, and F. Huisken, "Improved one-phonon confinement model for an accurate size determination of silicon nanocrystals," *Journal of Applied Physics*, vol. 86, no. 4, pp. 1921–1924, 1999.
- [65] G. Viera, S. Huet, and L. Boufendi, "Crystal size and temperature measurements in nanostructured silicon using Raman spectroscopy," *Journal of Applied Physics*, vol. 90, no. 8, pp. 4175–4183, 2001.
- [66] W.-K. Youn, S.-S. Lee, J.-Y. Lee, C.-S. Kim, N.-M. Hwang, and S. Iijima, "Comparison of the Deposition Behavior of Charged Silicon Nanoparticles between Floating and Grounded Substrates," *J. Phys. Chem. C*, vol. 118, no. 22, pp. 11946–11953, 2014.
- [67] Q. Brulin, N. Ning, and H. Vach, "Hydrogen-induced crystallization of amorphous silicon clusters in a plasma reactor," *Journal of Non-Crystalline Solids*, vol. 352, no. 9–20, pp. 1055–1058, 2006.
- [68] M. Cavarroc, M. C. Jouanny, K. Radouane, M. Mikikian, and L. Boufendi, "Self-excited instability occurring during the nanoparticle formation in an Ar–SiH<sub>4</sub> low pressure radio frequency plasma," *Journal of Applied Physics*, vol. 99, no. 6, p. 064301, 2006.
- [69] A. Bouchoule, *Dusty plasmas: physics, chemistry, and technological impacts in plasma processing*. Wiley, 1999.
- [70] S. Lebib and P. Roca i Cabarrocas, "Effects of ion energy on the crystal size and hydrogen bonding in plasma-deposited nanocrystalline silicon thin films," *Journal of Applied Physics*, vol. 97, no. 10, p. 104334, 2005.
- [71] D. Han, J. D. Lorentzen, J. Weinberg-Wolf, L. E. McNeil, and Q. Wang, "Raman study of thin films of amorphous-to-microcrystalline silicon prepared by hot-wire chemical vapor deposition," *Journal of Applied Physics*, vol. 94, no. 5, pp. 2930–2936, 2003.
- [72] G. Yue, J. D. Lorentzen, J. Lin, D. Han, and Q. Wang, "Photoluminescence and Raman studies in thin-film materials: Transition from amorphous to microcrystalline silicon," *Applied Physics Letters*, vol. 75, no. 4, pp. 492–494, 1999.
- [73] W. Beyer, "Hydrogen effusion: a probe for surface desorption and diffusion," *Physica B: Condensed Matter*, vol. 170, no. 1–4, pp. 105–114, 1991.
- [74] C. Rath, J. Farjas, P. Roura, F. Kail, P. Roca i Cabarrocas, and E. Bertran, "Thermally Induced Structural Transformations on Polymorphous Silicon," *Journal of Materials Research*, vol. 20, no. 09, pp. 2562–2567, 2005.
- [75] G. Sardin and J. L. Morenza, "Unifying model of thermal and light-induced degradations of a-Si:H," *Solar Energy Materials*, vol. 20, no. 3, pp. 189–197, 1990.

- [76] G. Talukder, J. C. L. Cornish, P. Jennings, G. T. Hefter, B. W. Clare, and J. Livingstone, "Effects of annealing on infrared and thermal-effusion spectra of sputtered a-Si:H alloys," *Journal of Applied Physics*, vol. 71, no. 1, pp. 403–409, 1992.
- [77] A. H. M. Smets and M. C. M. van de Sanden, "Relation of the Si-H stretching frequency to the nanostructural Si-H bulk environment," *Phys. Rev. B*, vol. 76, no. 7, p. 073202, 2007.
- [78] M. Moreno, R. Boubekri, and P. Roca i Cabarrocas, "Study of the effects of different fractions of large grains of  $\mu\text{c-Si:H:F}$  films on the infrared absorption on thin film solar cells," *Solar Energy Materials and Solar Cells*, vol. 100, pp. 16–20, 2012.
- [79] M. Vaněček, A. Poruba, Z. Remeš, J. Rosa, S. Kamba, V. Vorlíček, J. Meier, and A. Shah, "Electron spin resonance and optical characterization of defects in microcrystalline silicon," *Journal of Non-Crystalline Solids*, vol. 266–269, pp. 519–523, 2000.
- [80] G. Bugnon, G. Parascandolo, T. Söderström, P. Cuony, M. Despeisse, S. Hänni, J. Holovský, F. Meillaud, and C. Ballif, "A New View of Microcrystalline Silicon: The Role of Plasma Processing in Achieving a Dense and Stable Absorber Material for Photovoltaic Applications," *Advanced Functional Materials*, vol. 22, pp. 3665–3671, 2012.
- [81] L. Houben, C. Scholten, M. Luysberg, O. Vetterl, F. Finger, and R. Carius, "Growth of microcrystalline nip Si solar cells: role of local epitaxy," *Journal of Non-Crystalline Solids*, vol. 299–302, Part 2, pp. 1189–1193, 2002.
- [82] M. Moreno, G. Patriarche, and P. Roca i Cabarrocas, "Fine-tuning of the interface in high-quality epitaxial silicon films deposited by plasma-enhanced chemical vapor deposition at 200 °C," *Journal of Materials Research*, vol. 28, no. 13, pp. 1626–1632, 2013.
- [83] J.-C. Dornstetter, S. Kasout, and P. Roca i Cabarrocas, "Deposition of High-Efficiency Microcrystalline Silicon Solar Cells Using  $\text{SiF}_4/\text{H}_2/\text{Ar}$  Mixtures," *IEEE Journal of Photovoltaics*, vol. 3, pp. 581–586, 2013.
- [84] J.-C. Dornstetter, J. Wang, B. Bruneau, E. V. Johnson, and P. Roca i Cabarrocas, "Material and growth mechanism studies of microcrystalline silicon deposited from  $\text{SiF}_4/\text{H}_2/\text{Ar}$  gas mixtures," *Can. J. Phys.*, pp. 1–4, 2014.
- [85] Q. Zhang, E. V. Johnson, Y. Djeridane, A. Abramov, and P. R. i Cabarrocas, "Decoupling crystalline volume fraction and VOC in microcrystalline silicon pin solar cells by using a  $\mu\text{c-Si:F:H}$  intrinsic layer," *phys. stat. sol. (RRL)*, vol. 2, no. 4, pp. 154–156, 2008.
- [86] O. Astakhov, V. Smirnov, R. Carius, B. E. Pieters, Y. Petrusenko, V. Borysenko, and F. Finger, "Relationship between absorber layer defect density and performance of a-Si:H and  $\mu\text{c-Si:H}$  solar cells studied over a wide range of defect densities generated by 2 MeV electron bombardment," *Solar Energy Materials and Solar Cells*, vol. 129, pp. 17–31, 2014.



## List of Figures

Figure 1: World energy consumption in 2013 by types of fuels. ....	16
Figure 2: Energy consumption in 2013 by types of fuels for USE, China, Brazil, and France. ....	17
Figure 3: Growth of the world consumption of energy between 2003 and 2013. ....	18
Figure 4: Growth of the world consumption of renewable energy between 2003 and 2013. ....	18
Figure 5: World map of the DNI (SolarGIS © 2014 GeoModel Solar). ....	19
Figure 6: Historic of record cell efficiencies by NREL. ....	20
Figure 7: Picture of PHILIX reactor with the chamber is opened. ....	24
Figure 8: Schematic of PHILIX reactor with the RGA. ....	29
Figure 9: Signals detected by QMS at 40 amu ( $\text{Ar}^+$ ) and 20 amu ( $\text{Ar}^{++}$ and $\text{HF}^+$ ). ....	30
Figure 10: $\text{HF}^+$ signal detected by QMS. ....	31
Figure 11: RGA signals at 40, 2 and 20 amu as a function of time. ....	32
Figure 12: HF signal versus $\text{H}_2$ depletion for many different plasma conditions. ....	33
Figure 13: $\text{H}_2$ depletion and deposition rate for argon flow rate series. ....	35
Figure 14: $V_{\text{RF}}$ and $V_{\text{DC}}$ for argon flow rate series. ....	36
Figure 15: Film composition deduced by ellipsometry as a function of the $\text{H}_2$ flow rate. ....	37
Figure 16: Deposition rate and $V_{\text{DC}}$ as functions of the $\text{H}_2$ flow rate. ....	38
Figure 17: (a) Depletion of $\text{H}_2$ and production of HF and (b) the hydrogen consumption as a function of the $\text{H}_2$ flow rate. ....	39
Figure 18: OES signals of SiF (440nm), H $\alpha$ (656nm), and Ar (750nm) as functions of the $\text{H}_2$ flow rate. ....	40
Figure 19: $\text{H}_2$ consumption as a function of the $\text{H}_2$ flow rate for various values of the RF power and $\text{SiF}_4$ flow rate. ....	41
Figure 20: Concentrations of the six species included in the phenomenological model as functions of the B parameter. ....	44
Figure 21: $[\text{SiF}_3]-[\text{F}]$ concentration and $[\text{H}]/([\text{SiF}_3]-[\text{F}])$ ratio versus the B parameter. ....	45
Figure 22: Modeled $\text{H}_2$ consumption as a function of the parameter B. ....	46
Figure 23: Deposition rate as a function of the RF power. ....	47
Figure 24: OES argon signal and $V_{\text{DC}}$ as functions of the $\text{H}_2$ flow rate for different plasma conditions. ....	48
Figure 25: Depletion and consumption of $\text{H}_2$ as functions of the $\text{H}_2$ flow rate measured by RGA on CLUSTER-PL8 reactor. ....	50
Figure 26: Optimization of the $\text{H}_2$ consumption as a function of the Ar flow rate, the $\text{SiF}_4$ flow rate, the RF power and the pressure. ....	52
Figure 27: QMS signal at different mass-to-charge ratio in a $\text{SiF}_4/\text{H}_2/\text{Ar}$ gas mixture. ....	52
Figure 28: $\text{SiF}_4$ consumption versus $\text{H}_2$ consumption. ....	53
Figure 29: Deposition rate as a function of gas density (a) and pressure (b) for gas temperature series. ....	57
Figure 30: Thickness and void fraction as a function of the deposition time. ....	58
Figure 31: Real and imaginary parts of the pseudo-dielectric function measured by spectroscopic ellipsometry after 120 s of deposition. ....	59
Figure 32: Bright field TEM image of plasma-generated nanoparticles collected on a copper grid after a discharge of 60 s. ....	60
Figure 33: (a) Number of silicon atoms per nanoparticle as a function of the nanoparticle diameter. (b) Diameter distribution of nanoparticles seen in Figure 32 and the total number of silicon atoms as a function of the diameter. ....	61
Figure 34: (a) Metallic grid and (b) deposition behind the pumping holes and the grid. ....	62
Figure 35: Surface morphology of samples (a) without and (b) with the metallic grid. ....	63
Figure 36: (a) AFM profile of one particle of Figure 35b; (b) Height distribution of the particles of Figure 35b. ....	63
Figure 37: Deposition rate and $\text{H}_2$ depletion as a function of the inter-electrode distance $d_i$ . ....	65

Figure 38: Deposition rate as a function of $d_i$ (a) and $P \cdot d_i$ (b) for various values of the total pressure: 3.8 Torr, 2.5 Torr and 1.7 Torr. The highest deposition rate is obtained at 6 Torr-cm in the three cases.	66
Figure 39: $H_2$ depletion as a function of $P \cdot d_i$ at 3.8 Torr, 2.5 Torr and 1.7 Torr.	67
Figure 40: Silicon waste as a function of $P \cdot d_i$ at 3.8 Torr, 2.5 Torr and 1.7 Torr.	68
Figure 41: Schematic of the dust model. The trend of $D_r$ is explained by the change in the plasma composition: three regimes: radicals, nanoparticles, and powders.	68
Figure 42: Schematic of volume definitions ( $V_u$ , $V_{\bar{u}}$ , $V_{u'}$ , and $V_w$ ) of the geometrical model.	70
Figure 43: Extension of the useful volume $V_u$ for various $P \cdot d_i$ values within the frame of the geometrical model.	70
Figure 44: Variations of $V_u$ and $V_{\bar{u}} + V_{u'} + V_w$ as functions of $P \cdot d_i$ in the frame of the geometrical model.	71
Figure 45: Deposition rate as a function of $P \cdot d_i$ where pressure, RF power, $d_i$ and $T_{RF}$ have been varied.	72
Figure 46: Deposition rate and residence time as a function of $P \cdot d_i$ for Ar flow rate of 88 and 44 sccm.	73
Figure 47: Deposition rate and $H_2$ consumption as a function of $P \cdot d_i$ for hydrogenated amorphous silicon conditions.	74
Figure 48: Crystalline fraction and deposition rate from ellipsometry as a function of RF power.	76
Figure 49: Crystalline fraction, $H_2$ depletion and deposition rate for RF power series.	77
Figure 50: Raman signal of a silicon layer and of plasma-generated nanoparticles at 50 W, under the conditions of Table 23.	78
Figure 51: (a) One $40 \times 40 \mu m^2$ square of a holey TEM grid and the two locations: (a) (b) exhaust line and (c) plasma.	79
Figure 52: TEM images for H02 condition, of (a) the amorphous layer and (b) the amorphous nanoparticles collected on the cold finger installed in the exhaust line.	80
Figure 53: Diffraction pattern for H02 condition of the amorphous layer.	81
Figure 54: TEM images for H05 condition, of (a) the layer composed of a mixture of amorphous and microcrystalline phases and (b) the amorphous nanoparticles ( $\approx 10$ nm diameter) collected by the cold finger.	81
Figure 55: Diffraction patterns for H05 condition, of (a) the layer composed of a mixture of amorphous and microcrystalline and (b) the amorphous nanoparticles collected by the cold finger.	82
Figure 56: HR-TEM image for H15 condition, of (a) the microcrystalline layer and (b) the amorphous nanoparticles collected on the cold finger.	82
Figure 57: Diffraction pattern for H15 condition, of the microcrystalline layer.	83
Figure 58: HR-TEM on the layer deposited under H15 condition. Crystalline domains of about 10 nm are found.	83
Figure 59: (a) HR-TEM on the layer in H10 condition with the diffraction pattern in the inset. Two orientations can be detected in (b) thanks to the inverse Fourier transform after proper masking of the diffraction pattern.	84
Figure 60: Inverse Fourier transform of TEM images (a) with the mask #1 and (b) with the mask #2.	84
Figure 61: TEM images for W050 condition, of (a) the layer and (b) the nanoparticles of the cold finger.	85
Figure 62: Diffraction patterns of the TEM images represented in Figure 61 for the sample synthesized under W050 condition, of (a) the layer and (b) the nanoparticles collected by the cold finger.	85
Figure 63: TEM images for W100 condition, of (a) the layer composed of a mixture of amorphous and microcrystalline silicon and (b) the crystalline nanoparticles of the cold finger.	86
Figure 64: Diffraction patterns of the TEM images represented in Figure 63 for the sample synthesized under W100 condition, of (a) the layer composed of a mixture of amorphous and microcrystalline silicon and (b) the crystalline nanoparticles collected on the cold finger.	86

Figure 65: Diffraction pattern of (a) layer deposited at 50 W, (b) nanoparticles of the cold finger synthesized at 50 W, (c) layer deposited at 100 W, and (d) nanoparticles of the cold finger synthesized at 100 W. ....	87
Figure 66: Amorphous or microcrystalline nature mapping of nanoparticles and layers compared to the model predictions, for H <sub>2</sub> flow rate and RF power series. ....	88
Figure 67: HR-TEM image of nanoparticles of the cold finger in (a) W100 condition and (b) (c) W050 condition. ....	89
Figure 68: (a) HR-TEM image of nanoparticles of the cold finger at 100 W and 200°C with its diffraction pattern in (b). ....	90
Figure 69: Example of oscillations of OES Argon signal at 750 nm. ....	91
Figure 70: Different self-sustained oscillation waveforms. ....	92
Figure 71: Oscillations of different OES lines: SiF, SiF <sub>2</sub> , SiF <sub>3</sub> , H <sub>2</sub> , H <sub>α</sub> , H <sub>β</sub> and Ar. ....	93
Figure 72: Phase portrait of one waveform: SiF (443 nm) as a function of Ar (750 nm). ....	94
Figure 73: Phase portrait of one waveform: H <sub>α</sub> (656 nm) as a function of Ar (750 nm). ....	95
Figure 74: Phase portrait (a) of Ar/SiF signal of oscillations (b) (same as in Figure 70a). ....	96
Figure 75: Stability mapping of the steady state solution of the toy model. ....	100
Figure 76: Experimental evidences on the Ar signal of (i) pure damping, (ii) damping oscillation, and (iii) limit cycle. ....	101
Figure 77: Example of transition from regime (i) to regime (ii) in Ar/SiF signals and phase shift. ....	101
Figure 78: Example of transition from regime (ii) to regime (iii) in Ar/SiF signals and phase shift. ....	102
Figure 79: Ar and SiF signals for (a) steady state plasma condition and modulated RF power, and (b) oscillating plasma condition and constant RF power. ....	102
Figure 80: Ar and SiF signals in oscillating plasma condition and modulated RF power. ....	103
Figure 81: XRD pattern in Bragg-Brentano configuration of a solar cell. ....	106
Figure 82: XRD patterns in grazing incidence configuration of microcrystalline silicon deposited on glass under H05 and W050 conditions. ....	107
Figure 83: (a) Raman spectroscopy of microcrystalline silicon. (b) After the baseline subtraction. ....	109
Figure 84: Fitting of a-Si:H/μc-Si:H mixture Raman spectrum. ....	110
Figure 85: Fitting of fully crystallized μc-Si:H Raman spectrum. ....	110
Figure 86: Fitting of fully crystallized μc-Si:H Raman spectrum with three Gaussians. ....	111
Figure 87: Fitting of μc-Si:H with a little bit of a-Si:H Raman spectrum with four Gaussians. ....	112
Figure 88: Grain boundaries peak position as a function of the crystalline fraction X <sub>c</sub> . The position of grain boundaries of type I and type II are taken from [72]. ....	113
Figure 89: Mapping of the ratio R in a microcrystalline layer without amorphous phase. ....	114
Figure 90: Exodiffusion spectra for amorphous and microcrystalline samples before and after a rapid thermal annealing at 350°C. ....	115
Figure 91: Transmission spectra measured by FTIR for amorphous and microcrystalline samples before and after a rapid thermal annealing at 350°C. ....	116
Figure 92: Absorptions extracted from FTIR for amorphous and microcrystalline samples before and RTA at 350°C. ....	116
Figure 93: Exodiffusion spectra of three silicon films: amorphous at 1 sccm, a mixture of amorphous and crystalline phases at 5 sccm, and fully crystallized material at 9 sccm. ....	119
Figure 94: Hydrogen concentration deduced from exodiffusion measurements as a function of the H <sub>2</sub> flow rate. ....	120
Figure 95: Ratio between weak and tight peak from exodiffusion as a function of the H <sub>2</sub> flow rate. ....	120
Figure 96: Exodiffusion spectra normalized by the thickness of layers. ....	122
Figure 97: H, F, B, and P SIMS profiles of 100% microcrystalline silicon solar cell. ....	123
Figure 98: H, F, B, and P SIMS profiles of 80% microcrystalline silicon solar cell. ....	124
Figure 99: C and O SIMS profiles of the 80% and 100% microcrystalline silicon solar cell. ....	125

Figure 100: EQE of the three solar cells measured in FTPS.....	126
Figure 101: FTPS measurements of the three solar cells.....	126
Figure 102: Schematic of the PIN solar cell structure. ....	130
Figure 103: SEM image of textured ZnO. ....	131
Figure 104: TEM image of a solar cell in cross section.....	132
Figure 105: Dark field TEM image of a solar cell in cross section. ....	133
Figure 106: Picture of the top of a typical solar cell. The front contact is made of silver paste....	134
Figure 107: Infrared camera snapshots of a solar cell under bias with (a) the line-shaped and (b) the square-shaped front contact.....	134
Figure 108: EQE curves of A, B, X, and Y solar cells.....	136
Figure 109: Geometrical construction used by the algorithm which leads to an estimation of the position and the HWHM of the crystalline peak. ....	137
Figure 110: Correlation between the fitting and the algorithm in the estimation of (a) the crystalline peak position and (b) the FWHM of the crystalline peak. The blue dashed-line is a guide for the eyes. ....	138
Figure 111: FWHM as a function of the crystallite diameter estimated from Equation (57). ....	139
Figure 112: $V_{OC}$ dependency with $X_C$ and $X_{CRY}$ . ....	139
Figure 113: $V_{OC}$ and $J_0$ as a function of the grain boundaries fraction for the subset of fully crystallized solar cells.....	140
Figure 114: The discrepancy between the measured $V_{OC}$ and the $V_{OC}$ computed from ( $J_0, n$ ) parameters as a function of the grain boundaries fraction $X_{GB}$ . ....	141
Figure 115: Differential resistance at the short-circuit condition $R_{SC}$ as a function of the open-circuit voltage $V_{OC}$ showing that solar cells might be limited by low shunt resistance.....	141
Figure 116: EQE at 800 nm as a function of the thickness of the I-layer. ....	142
Figure 117: EQE curve of our thickest solar cell with an I-layer of 5.5 $\mu\text{m}$ . ....	143
Figure 118: J-V curve and EQE of the thickest (3.8 $\mu\text{m}$ ) solar cell partially crystallized (89%). ....	144
Figure 119: J-V curve and EQE of the best (9.2%) solar cell partially crystallized (80%).....	144
Figure 120: Dark J-V curve of the solar cell. ....	145
Figure 121: J-V curve and EQE of the best (9.2%) solar cell fully crystallized. ....	145

## List of Tables

Table 1: Plasma conditions for the argon flow rate series.....	35
Table 2: Plasma conditions for the H <sub>2</sub> flow rate series. ....	37
Table 3: Plasma conditions for study of H <sub>2</sub> consumption. ....	40
Table 4: Plasma conditions for study of RF power series to test the prediction of the model.....	46
Table 5: Plasma conditions for the transfer from PHILIX to CLUSTER reactors. ....	49
Table 6: Plasma conditions for the pressure series in the CLUSTER reactor. ....	50
Table 7: Plasma conditions for the Ar flow rate series in the CLUSTER reactor. ....	51
Table 8: Plasma conditions for the SiF <sub>4</sub> flow rate series in the CLUSTER reactor. ....	51
Table 9: Plasma conditions for the RF power series in the CLUSTER reactor. ....	51
Table 10: Plasma conditions for pressure series at constant T <sub>RF</sub> . ....	56
Table 11: Plasma conditions for the T <sub>RF</sub> series at constant pressure.....	56
Table 12: Plasma conditions for the T <sub>RF</sub> series at constant gas density (7x10 <sup>16</sup> cm <sup>-3</sup> ). ....	57
Table 13: Plasma conditions for the study of the early stage of the deposition. ....	58
Table 14: Plasma conditions for study of nanoparticles by TEM image. ....	59
Table 15: Plasma conditions the metallic grid study.....	63
Table 16: Optical model deduced from ellipsometry for samples with and without the grid.....	64
Table 17: RF and grounded electrode areas as functions of the inter-electrode distance d <sub>i</sub> . ....	64
Table 18: Plasma conditions for the d <sub>i</sub> series at 3.8 Torr. ....	65
Table 19: Plasma conditions for d <sub>i</sub> series at 1.7 Torr, 2.5 Torr, and 3.8 Torr. ....	66
Table 20: Plasma conditions for the P·d <sub>i</sub> series by changing T <sub>RF</sub> , pressure and RF power.....	71
Table 21: Plasma conditions for the P·d <sub>i</sub> series when gas residence time is varied. ....	73
Table 22: Plasma conditions for the P·d <sub>i</sub> series in high depletion regime. ....	73
Table 23: Plasma conditions for the RF power series. ....	77
Table 24: Plasma conditions for sample H02, H05, H15, W050, and W100. ....	80
Table 25: Variations of Ar, SiF, H <sub>α</sub> , and φ during one period of oscillation.....	95
Table 26: Conditions on eigenvalues to get damping or oscillating regimes.....	100
Table 27: Plasma conditions (H05 and W050) for the sample measured in GI-XRD. ....	107
Table 28: Typical position and FWHM of the four peaks used in the deconvolution.....	111
Table 29: Selected peaks used for the deconvolution depending of the material. ....	111
Table 30: Plasma conditions for FTIR and exodiffusion studies.....	114
Table 31: Comparison of the hydrogen loss after RTA estimated by FTIR and by exodiffusion. ...	117
Table 32: Fit parameters of FTIR spectra. ....	117
Table 33: Name of the four types of bonds. ....	117
Table 34: Plasma conditions for the H <sub>2</sub> flow rate series studied by exodiffusion.....	118
Table 35: Plasma conditions for the RF power series studied by exodiffusion.....	121
Table 36: Description of solar cells analyzed by SIMS.....	123
Table 37: H and F concentrations estimated by SIMS.....	123
Table 38: Solar cell characteristics for FTPS measurements.....	125
Table 39: Absorption coefficient at 0.8 eV and the Urbach energy deduced from by FTPS measurements.....	127
Table 40: Typical plasma conditions for the deposition of μc-Si:H,F used in PIN solar cells. ....	135
Table 41: FWHM <sub>520</sub> of selected samples compared with their X <sub>C</sub> , V <sub>OC</sub> , J <sub>SC</sub> .....	136
Table 42: I-layer characteristics of the three best solar cells.....	143
Table 43: Summary of the performances of the selected solar cells.....	145





# Microcrystalline silicon deposited from SiF<sub>4</sub>/H<sub>2</sub>/Ar plasmas and its application to photovoltaics

Jean-Christophe Dornstetter  
under the supervision of Pr. Pere Roca i Cabarrocas

---

## Summary:

Silicon tetrafluoride is a good candidate to replace silane as silicon precursor in plasmas used to deposit thin films. It has been demonstrated by previous Ph.D. thesis at LPICM that microcrystalline silicon, grown from SiF<sub>4</sub>/H<sub>2</sub>/Ar gas mixtures, leads to excellent thin film transistors. This thesis is dedicated to another application: photovoltaic devices. A new challenge arises because several micron thick layers are required in microcrystalline silicon thin film PIN solar cells. Therefore a better and deeper understanding of SiF<sub>4</sub>/H<sub>2</sub>/Ar plasmas is necessary to optimize the deposition rate of microcrystalline silicon.

SiF<sub>4</sub>/H<sub>2</sub>/Ar plasmas have been studied thanks to mass spectrometry and the specificity of such gas mixtures is demonstrated to be the formation HF molecules via the recombination of atomic F and molecular H<sub>2</sub>. We found that a H<sub>2</sub>-limited process is associated to amorphous growth and all H<sub>2</sub> is used to form HF. On the contrary, an excess of H<sub>2</sub> leads to microcrystalline growth. A simple yet accurate model, strongly based on experimental data, has been developed to explain the amorphous-to-microcrystalline transition and enables a controlled tuning of plasma parameters leading to an increase of deposition rate. Moreover, the contribution of plasma generated nanoparticles has been clarified, in particular their crystallization in the plasma phase. The microcrystalline silicon, fabricated from SiF<sub>4</sub>/H<sub>2</sub>/Ar, is a high quality material: a density of defects as low as  $3 \times 10^{-3} \text{cm}^{-1}$  has been deduced from absorption below the bandgap (at 0.8eV). By using the fluorinated chemistry for the deposition of the intrinsic absorber layers in thin film PIN solar cells, open-circuit voltage as high as 536mV has been obtained for highly crystallized layers, leading to an efficiency of 9.2%.

---

## Résumé:

Le tétrafluorure de silicium est une excellente alternative pour remplacer le silane comme précurseur dans les plasmas de dépôt de couches minces. Il a été montré dans les précédentes thèses du LPICM que le silicium microcristallin, crû par des mélanges de SiF<sub>4</sub>/H<sub>2</sub>/Ar, conduit à d'excellents transistors en couches minces. Cette thèse est consacrée à une autre application : les dispositifs photovoltaïques. Un nouveau défi apparaît du fait que l'épaisseur nécessaire des couches est de plusieurs microns. C'est pourquoi une compréhension des plasmas de SiF<sub>4</sub>/H<sub>2</sub>/Ar meilleure et plus approfondie est requise pour optimiser la vitesse de dépôt du silicium microcristallin.

Les plasmas de SiF<sub>4</sub>/H<sub>2</sub>/Ar ont été étudiés par spectroscopie de masse et il a été démontré que la spécificité de tels mélanges est la formation de molécules de HF par la recombinaison de fluor atomique avec l'hydrogène moléculaire. Nous avons montré que dans des conditions où le H<sub>2</sub> est limitant, la couche obtenue est amorphe et l'hydrogène est principalement utilisé pour former du HF. Inversement, un excès de H<sub>2</sub> mène à des couches microcristallines. Un modèle simple mais fidèle, basé sur nos données expérimentales, a été développé pour expliquer la transition amorphe vers microcristallin. Ce modèle nous permet d'augmenter la vitesse de croissance de nos couches par un ajustement raisonné des paramètres du plasma. De plus, la contribution des nanoparticules générées en phase plasma a été clarifiée comme par exemple les conditions de leur cristallisation en phase plasma. Le silicium microcristallin fabriqué à partir de SiF<sub>4</sub>/H<sub>2</sub>/Ar est de haute qualité : une densité de défauts aussi basse que  $3 \times 10^{-3} \text{cm}^{-1}$  a été déduite par absorption sous la bande interdite (précisément à 0.8eV). En utilisant une chimie fluorée pour le dépôt de la couche intrinsèque absorbante dans des cellules PIN en couches minces, une tension en circuit ouvert aussi élevée que 536mV a été obtenue avec des couches bien cristallisées, aboutissant à des rendements de 9.2%.